SISSA
Scuola
Internazionale
Superiore di
Studi Avanzati

Mott transition, topology, and magnetism of interacting fermions in confined geometries

candidate: **Karla Jana Baumann**
supervisor: Massimo Capone

PHD thesis in: **Theory and Numerical Simulation of Condensed Matter**
August 2020

Dedicated to the loving memory of Karel Linhart.
10.08.1925 – 10.08.2000

ABSTRACT

This thesis reports original research on strongly interacting fermions described by Hubbard-like models which can be realized with ultracold atom experiments. In particular, two main directions have been pursued: (i) the control of magnetic and topological properties in a honeycomb lattice through a suitable tuning of the trapping potential, and (ii) the possibility to observe orbital-selective Mott physics in a multicomponent Fermi system where the SU(N) symmetry is broken in a controlled way. The first line of research is based on the idea that increasing the strength of a trapping potential, one can trap a strongly interacting fermions in a limited portion of space, thereby changing their average density and the related magnetic properties. In particular it was demonstrated that this confinement protocol can be used to designeffective "nanoflakes" which are reminiscent of a solid-state proposal [1]. The second step was to extend the same philosophy to the so-called Kane-Mele model, a spinful version of the paradigmatic model proposed by Haldane which presents quantum Hall states. This model can be realized with cold-atom systems using artificial gauge fields. In this thesis we consider a Kane-Mele-Hubbard model where the electronic structure of the Kane-Mele model is supplemented by the onsite Hubbard interaction, allowing us to study the interplay between the correlations and magnetism induced by the repulsion, with the non-trivial topological properties. Also for this model, we follow the strategy discussed above, namely the possibility to engineer an effective "nanoflake" by tuning the lattice potential. The final outcome in this case is even reacher, because it leads, among other results, to a situation where the effective flake hosts an inhomogeneous state which presents at the same time topologically non-trivial properties and magnetism, realizing a spin-Chern insulator [2]. Besides the remarkable application for topological matter, artificial gauge fields, which rely on the coupling of spin states, offer also great insides into mutli-orbital physics. In the second main research line reported in the thesis we study in collaboration with the experimental group of Leonardo Fallani, the controlled symmetry breaking on a ^{173}Yb many-body system, where coupling between spin states is exploited to simulate the mechanism relevant for the physics of multi-orbital materials, such as iron-based superconductors. In order to reveal this mechanism in cold atoms we focus on interacting $SU(3)$ lattice fermions where the $SU(3)$ spin symmetry is explicitly broken by a Raman coupling between the spin states. Combining experiments and theory, we demonstrate that this setup reveals orbital-selective physics and it shows that the $SU(3)$-symmetry-breaking Raman coupling favours Mott localization and selective properties [3]. Our results show a clear evidence of orbital-selective correlations, which reflect in contrasting transport properties in different orbitals, the extreme case being an orbital-selective Mott state where only some of the orbitals are Mott localized while others remain metallic. Moreover, the coupling between spin states favors Mott localization with respect to the symmetric case, hence it reduces the critical interaction needed for a full Mott localization.

PUBLICATIONS

1. **K. Baumann**, A.Valli, A. Amaricci, M. Capone "Inducing and controlling magnetism in the honeycomb lattice through harmonic trapping potential", *Phys. Rev. A* **101**, *033611* (2020)

2. **K. Baumann**, A. Amaricci, A.Valli, M. Capone "Governing magnetic order and topology in artificial interacting Kane-Mele system", *in preparation* (2020)

3. L. Livi, L. Franchi, D. Tusi, **K. Baumann**, L. Del Re, M. Capone, J. Catani, L. Fallani "Direct observation of orbital-selective localization in interacting SU(N) lattice fermions via controlled symmetry breaking", *in preparation* (2020)

CONTENTS

1

INTRODUCTION

1.1 INTRODUCTION

Strong correlation are at the basis of fundamental processes in condensed matter and beyond, which makes their study exceptionally impactful. We think about strong correlations when the collective behavior of a many-particles system can not be obtained as the result of the individual properties of single particles, but only as a collective phenomenon, in which the behavior of each constituent is indeed correlated with the others.

A conceptually simple, yet powerful, model to describe interacting particles on a lattice is the celebrated Hubbard model [1], a minimal model featuring a hopping term and a local repulsion which has been exploited to study Mott localization [2, 3], quantum magnetism [4], unconventional superconductivity [5] and numerous more phenomena. Initially, the Hubbard model was proposed in order to approximate the physics governing solid-state systems, but the complexity and complication of real materials limits the application of the model when it comes to concrete evaluation of observables. Moreover, simple modifications of the model can lead to novel phenomena which sometimes are not accessible in a solid-state framework.

The famous idea by R. Feynman [6] to engineer synthetic quantum systems to explore quantum phenomena predicted by theoretical models and to simulate the model itself is becoming more and more a concrete perspective, thanks to the development of different platform for synthetic matter, among which the most established is represented by trapped ultracold atoms [7–9]. The field of cold atoms has rapidly developed thanks to incredible progress in cooling atoms through laser manipulation down to nanokelvin regimes, where the quantum nature of systems becomes accessible. Due to refined measurement techniques and and the ability to provide a controlled and clean framework, quantum simulation with ultracold atomic gases became a powerful model system to test former predictions and to realize new physics. Moreover, ultracold atoms allow for the direct verification of most elementary mechanisms, as opposed to solid-state platforms where a large number of degrees of freedom precludes the direct probe of simple paradigmatic phenomena.

In order to create synthetic solids where ultracold atoms replace conduction electrons, periodic potentials are created by using counterpropagating laser beams. The artificial crystals are called optical lattices and confine neutral atoms cooled down to very low temperatures allowing to simulate and examine condensed matter model Hamiltonians. Different geometies and dimensionalities can be explored, starting from a

square/cubic lattice in 2 or 3 dimensions, honeycomb lattices [10], kagome lattice [10] or quasi 1-dimensional chains [11].

The atomic clouds are additionally trapped by an external confining harmonic potential which plays a major role in cold atomic experiments. In most cold atomic experiments the harmonic trap is present which makes in turn the theoretical study of lattice problems with harmonic potential very important.

In this work we propose to use the harmonic trap also as a tool to create many states of matter for example inducing interfaces with coexisting phase or realizing a phase transition by simply manipulating the potential depth.

In the case of the Hubbard model one can simulate the metal to insulator transition (MIT) [12–19] by not only changing the interaction strength, but also the trapping potential strength. Typically the MIT is observed at half-filling upon increasing the interaction among particles; in this scenario the transition is controlled by the two model energy scales, the kinetic energy, and the onsite Coulomb repulsion. When studying the MIT in ultracold gas experiments, the harmonic potential competes with the other energy scales potentially affecting the Mott transition.

The first natural effect of the trapping potential is an inhomogeneous density distribution controlled by the optical trap. The density is a crucial control parameter in the MIT since the conventional Mott insulating state only emerges when we have one fermion per site on average. this leads to the possibility to have different degree of localization and different magnetic properties in different regions of a system with charge modulation.

For example by realizing honeycomb lattices the study of artificial graphene became accessible. Graphene is a very unique material with extraordinary mechanical, thermal and transport properties. Solid state graphene systems have very peculiar and elusive magnetic properties. These properties are challenging to induce in real graphene sheets, while in small nano structures magnetic states are easier promoted due to the presence of edges which enhance the effect of correlation, yet they are difficult to synthesize in from real materials.

In this thesis we apply the idea to control the physics of a quantum system by tuning the trapping potential to the honeycomb lattice, and we show that it is actually possible to generate effective small "nanoflakes" and control their magnetic state.

Moreover, the new generation of cold atomic experiments allows the access to an increased number of observables [20–22], which for example allowed the implementation of the Haldane model, which is considered to be hard to realize in condensed matter systems. The Haldane model has a unique band structure and host topologically nontrivial states called quantum Hall state. Quantum Hall states are naturally generated in two-dimensional lattices in a large magnetic fields. In cold atomic experiments, magnetic fields can not be applied for this purpose since the atoms are neutral and no Lorentz force can be experienced.

Fortunately, experimental techniques were developed to overcome this limitation, which rely on the simulation of the effect of real magnetic fields. These artificial magnetic fields [23–30] pushed the community towards the observation of topological states of matter and the effect of spin-orbit coupling (SOC).

On the honeycomb lattice, this means to simulate the Kane-Mele model [31, 32], a spinful version of the Haldane model displaying quantum Hall states. In this thesis we consider a Kane-Mele-Hubbard model [33] where the electronic structure of the

KM model is supplemented by the onsite Hubbard interaction, allowing us to study the interplay between the correlations and magnetism induced by the repulsion, with the non-trivial topological properties. Also for this model, we follow the strategy discussed above, namely the possibility to engineer an effective "nanoflake" by tuning the lattice potential, and we discuss how this inhomogeneous state can host topological and magnetic properties.

Besides the remarkable application for topological matter, artificial gauge fields, which rely on the coupling of spin states, offer also great insides into mutli-orbital physics. In this thesis we study in collaboration with the experimental group of Leonardo Fallani, the controlled symmetry breaking on a ^{173}Yb many-body system [17, 34], where coupling between spin states is exploited to simulate the mechanism relevant for the physics of multi-orbital materials, such as iron-based superconductors.
One of the most intrigiung features of multi component systems is the orbital selectivity characterized by the possibility for electrons to show contrasting transport properties in different orbitals. e.g, entering a Mott insulating state in one orbital, while remaining metallic in the other orbital [35–41]. On top of the selectivity the coupling between spin states can induce a Mott insulating state at a weaker interaction strength, hence increase the degree of correlation. In order to reveal this mechanism in cold atoms we focus on interacting $SU(3)$ lattice fermions, modeled by the $SU(3)$ Hubbard model with tunable coupling between the spin states. Here $SU(3)$ refers to the spin symmetry and denotes the presence of three spin states. Combining experiments and theory, we demonstrate that this setup reveals orbital-selective physics and it shows that the $SU(3)$-symmetry-breaking Raman coupling favours Mott localization and selective properties.

1.2 CONTENT OF THE THESIS

This thesis is organized as follows:

- **Chapter 2** introduces ultracold atoms in optical lattice and describes fundamental tools to engineer the theoretical models and proposals discussed in this thesis. Emphasis in this chapter is put on alkaline-earth-;like atoms and in particular Ytterbium, presenting the techniques employed to explore the properties of ^{173}Yb. This includes the introduction of Feshbach resonances used to control interactions among particles, Raman coupling employed to manipulate and couple spin states and how artificial magnetic fields and topological matter can be realized. In addtion we discuss an example of a synthetic Hall ribbon relevant for Chapter 6 and the experimental realization of a $SU(N)$ Mott insulator relevant for Chapters 7 and 8.

- **Chapter 3** is devoted to the Hubbard model and the methods that we use for its solution. We discuss some basic concepts to characterize the fluid and insulating states of the model and the Mott transition connecting them. We introduce Dynamical mean-field theory (DMFT) [42] a powerful method to capture the metal to Mott insulator transition (MIT) and derive the equations. We present some details of our implmentation based on the exact diagonalization of the auxiliary Anderson Impurity Model. Then we discuss a real-space extension of DMFT

(RDMFT) [43–46] suitable for inhomogeneous system such as ultracold atomic experiments with optical trap, also here deriving the main equations. After establishing the technical background, we discuss the basics of Mott transition and give a concrete example of a cold atom simulation of the transition using RDMFT.

- **Chapter 4** is devoted to strong coupling expansions [47] of the Hubbard model and the Kane-Mele Hubbard model and we derive effective Hamiltonians, which will be used in the discussions of the following Chapters.

- **Chapter 5** discusses the results about controlling and inducing magnetism on the honeycomb lattice. First we introduce graphene nanoflakes by examining their basic properties and elaborate on the size effects and then demonstrate how to simulate their magnetic properties in cold atomic experiments using a harmonic potential . We solve this system using RDMFT. We introduce the concept of effective edges induced by the optical trap and their role in the magnetic state. We present different magnetic states potentially realizable optical lattices.

- **Chapter 6** introduces the Kane-Mele Hubbard model and its topological and magnetic properties. We explain how topological order can be detected in inhomogenous systems by means of the local Chern marker []. Then we examine the magnetic and topological state on a graphene nanoflake upon changing the spin-orbit coupling and the interaction strength at half-filling. We propose an experimental scheme to simulate the topological and magnetic nanoflake in cold atoms exploiting harmonic potentials. We extend the analysis to different fillings and derive and effective theory explaining the rich magnetic states we observe.

- **Chapter 7** is an introduction to multi-orbital physics including an experimentally feasible proposal for $SU(3)$ Raman coupled Hubbard model to study orbital selective Mott transitions. This chapter builds the foundation for Chapter 8 where a very similar model is studied and compared with new experiments.

- **Chapter 8** represents one of the main works carried out in this PhD thesis. It discusses the experimental realization of the proposal on orbital selectivity presented in Chapter 7, though slightly modified. The modification is a non-trivial extension where only two out of three flavors are coupled due to experimental benefits. This modification in the coupling requires a new theoretical understanding which is presented in this chapter. After we discussed an ideal model system of the experimental Hamiltonian, we directly simulate the experimental set up and compare the measurements obtained by the experimental group with our theoretical calculations. Remarkably, we demonstrate, that the proposal on orbital selectivity of chapter 7 has been succesfully implemented.

- **Conclusions** are finally given, wrapping up the main results of the thesis.

2

QUANTUM SIMULATION WITH ULTRACOLD ATOMS IN OPTICAL LATTICES

2.1 INTRODUCTION

The solution of problems involving a large number of quantum particles interacting among each other is very hard from the theoretical point of view even for idealized simple systems such as the single-band Fermi Hubbard model where spin-1/2 fermions move in a lattice with an energy cost in two fermions with opposite spin are on the same lattice site. While the motivation to study these models comes mostly from solid-state systems with the notable example of the high-temperature superconductors [5], a direct quantitative connection between solid-state experiments and many-body models is always questionable, given the number of approximations and simplifications implicit in the model descriptions.

In this perspective, quantum simulation [7–9] is a powerful approach for examining quantum systems experimentally in a controlled and clean framework. By quantum simulation we refer to the experimental realization of one of these idealized models using a quantum platform. Ultracold atoms are among the most established platforms for quantum simulations of a variety of quantum systems, and they have nowadays obtained a long list of impressive results and successes.

In particular, optical lattices [9, 48] are a conceptually simple tool to simulate lattice models. In this chapter we present a very limited introduction to this huge field, focusing on some aspects which are instrumental to the new research reported in the present thesis. In particular we will give a very short introduction to optical lattices, which are the common thread of all the new results of this thesis, and two alkali atoms systems as a powerful tool for the quantum simulation of multicomponent fermionic lattice systems.

2.2 OPTICAL LATTICES AND ATOM ATOM INTERACTION

Optical lattices are artificial crystals generated by pairs of counterpropagating laser beams. When loaded with ultracold atoms, they provide a remarkable playground for realizing synthetic matter that allows to address the quantum simulation of solid state models and even to go beyond and simulate quantum systems which are not accessible in materials.
Since the optical lattices are composed of light, the injected atoms have to be neutral if we want the lattice to introduce a potential for the atoms. Cold atomic system involving neutral atoms in optical lattices are therefore conceptually equivalent to a neutral atom subject to a temporally oscillating electric field $\mathbf{E}(t)$ which can be described in terms of the AC-Stark effect. A varying electromagnetic field induces a time-dependent electric dipole moment $\mathbf{d} = \alpha(\omega)\mathbf{E}$ which in turn interact with each other resulting in a shift in the atomic energy level $\Delta E = -\frac{1}{2}\langle E^2(t)\rangle_t \alpha(\omega)$. The shift depends on the dynamic polarizability $\alpha(\omega)$ of the atom.

$$V_{dip} = -\frac{1}{2}\Re(\alpha(\omega))\langle \mathbf{E}^2(\mathbf{r},t)\rangle_t, \tag{2.1}$$

The laser beams constructing the optical lattice are typically produced by reflecting a focused and polarized laser on a mirror thus inducing a standing wave. The laser beam is characterized by the unit polarization vector $\hat{\mathbf{e}}$ and the electric field $\mathbf{E}(\mathbf{r},t) = E_0\hat{\mathbf{e}}\cos(\mathbf{kr}-\omega t)$, with the amplitude E_0.
.
In this case the potential felt by the atoms will be

$$V_{dip}(\mathbf{r},t) \propto \mathbf{E}^2(\mathbf{r},t) = 4E_0^2\cos^2(\omega t)\cos^2(\mathbf{kr}), \tag{2.2}$$

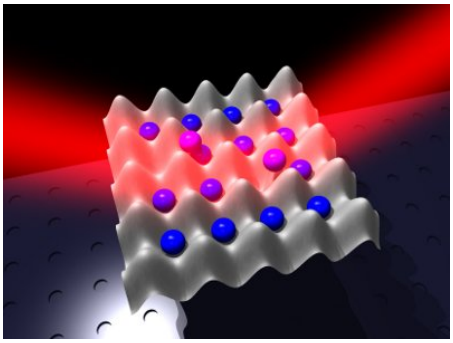

Figure 2.1: **Schematic representation of atoms in an optical lattice**

Generally, the time scales relevant for the dynamics of the atoms is much larger than the inverse of the laser frequency, therefore we can safely average the potential over time obtaining an effective periodic potential for atoms. Writing now the result in a general case where we consider d pairs of counterpropagating lasers forming a d-dimensional lattice, we obtain

$$V_{lattice}(\mathbf{r}) = \langle V_{dip}(\mathbf{r},t)\rangle_t = V_0 E_r \sum_{i=1}^{d}\cos^2(k_i x_i), \tag{2.3}$$

where V_0 is the parameter controlling the lattice depth, x_i is the coordinate in i-th spatial dimension and $k_i = 2\pi/\lambda$ is the quasi-momentum in the reciprocal space determined by the wavelength of the laser. Hence an optical lattice is basically defined by its geometrical form, which can reproduce a variety of lattice in different dimensions [11] (square, cubic, honeycomb, ...) [7, 21, 49–51] its depth and its wavelength controlling the spatial periodicity. in Fig 2.2 we show a few examples of already realized lattice structures on which lattice structures the corresponding band structure.

For example the realization of the honeycomb lattice [10, 49] lead to the observation of the famous topological Haldane model [20], which is extremely hard to observe in solid-state systems

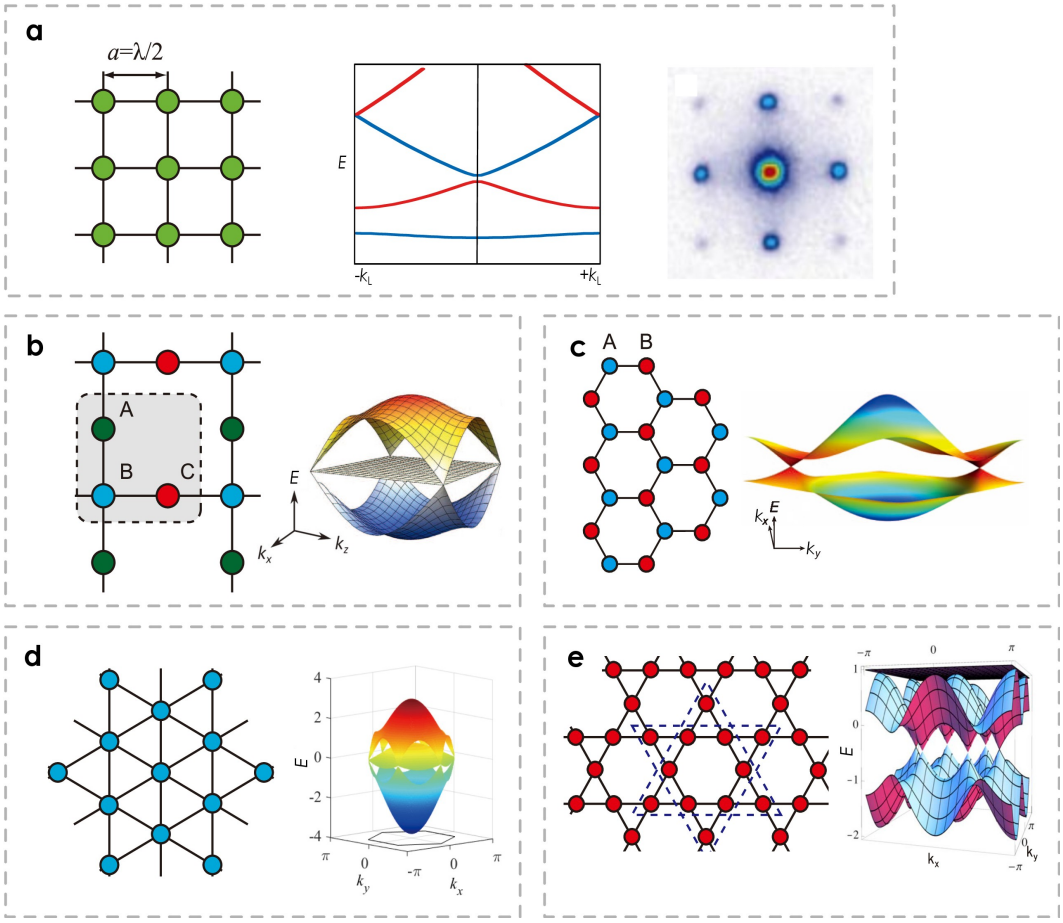

Figure 2.2: **Lattice geometries and corresponding Bloch bands. a** real space square lattice (left) with lattice spacing $a = \lambda/2$, where λ is the wavelength of the lase and Bloch bands with laser wavenumber $k_F = \pi/a$ (middle). The right image shows a Bose-Einstein condensate obtained from an free expansion initialized with a 3D cubic lattice. **b** Lieb optical lattice with three sublattice structure and band structure with a flat band in the first excited level. **c** honeycomb lattice with sublattice A and B and the famous Dirac bands. **d** triangular lattice with Dirac dispersion **e** Kagome lattice and with band structure exhibiting Dirac points and a flat band on top. The figure is taken from Ref. [7]

If the lattice is sufficiently deep, we can assume that the atoms spend all of their time in the minima of the potential, just like the electrons in a solid in which the wavefunctions are localized around the ionic potential (tight-binding approximation). Hence, they behave as particles in a lattice model. The values of V_0 and λ conjure to determine the tunneling integrals connecting different minima of the potential and the value of the effective inter-particle interation. Conventionally, the trapping potential is expressed in units of the recoil energy $E_R = \frac{\hbar^2 k^2}{2m}$, the energy gained by an atom absorbing a photon.

The success of cold atoms relies on the ability to a have unprecedented of control on the parameters of the models subject of the quantum simulation [8–10, 52]. Most interestingly the interaction among atoms is highly tunable in sharp contrast with solid-state systems. In dilute gases, such as those used in typical cold-atom experiments, the atoms interact via two-body scattering potentials and can be described by the conventional quantum scattering theory [53], three-body processes are usually negligible due the larger inter-particle distance. The inter-atomic interaction can be governed via Feshbach resonances [54–57], where the scattering properties can be arbitrarily modified from attractive to repulsive interactions by varying external magnetic fields. The two body collisions at low density and temperature determines a very short range interatomic potential, where the spatial range r_0 is significantly smaller than the thermal wavelength $\lambda_T = \sqrt{2\pi\hbar/mk_BT}$ and therefore only states with zero angular momentum ($l = 0$) ,so called $s-wave$ states, contribute. Moreover due to the anti-symmetric nature of the fermionic wave function s-wave scattering among spin polarized particles is excluded leading to interactions restricted to fermions with different spins. The s-wave scattering length a enters in the effective inter atomic potential as $U(\mathbf{r}) = (4\pi\hbar^2/m)\delta(\mathbf{r})$, where m is the mass of the components of the gas and $\delta(\mathbf{r})$ is local Dirac delta function representing the short-range nature of the interaction.

A key aspect of cold-atom systems is that the interaction can be controlled exploiting the so-called Fano-Feshbach [54] resonances. The resonance is created when the groundstate (closed channel) potential energy curve and an excited state (open channel) with different spin values can be tuned by a magnetic field in such a way that the bound state of the interparticle potential between the two atoms in the groundstate becomes degenerate with the large-distance asymptotic potential energy,value, where the spectrum becomes continuous, in the excited state. When the field B makes these two energies coincide, the scattering length between the atoms diverges.

The scattering length in the presence of coupling which connects the two channels follows indeed the following simple equation

$$a = a_{bg}\left(1 - \frac{\Delta_B}{B - B_0}\right), \tag{2.4}$$

where Δ_B denotes the width of the Feshbach resonance and a_{bg} is the scattering length coming from the background that is away from resonance and B_0 is the resonance magnetic field. From the formula it is obvious that we can tune the scattering length, and consequently the interparticle interaction, from negative to positive through a divergence.

Using these ingredients, one can realize in a laboratory models for fermions and bosons experiencing a short-range, essentially local interaction. In this thesis we focus on fermionic systems motivated more or less directly by solid-state systems. The simplest microscopic model describing interacting spinful Fermions on a lattice is the one band Fermi-Hubbard model. The interaction among the Fermions is modeled by a purely local repulsion, which is well motivated by the above discussion in the context of cold atoms, as opposed to solid-state, where the use of a local interaction involves a serious approximation. Initially, the Hubbard model was introduced in the solid state context motivated by materials with partially filled bands displaying fascinating correlation effects. However, because of the point interaction the model is an ideal candidate for

modern ultracold atoms in optical lattices experiments, where the interaction is indeed short-range as we have seen above. The basic model includes two terms and reads

$$\hat{\mathcal{H}} = \sum_{i,j,\sigma} t_{ij} \hat{c}^{\dagger}_{i\sigma} \hat{c}_{j\sigma} + U \sum_{i} \hat{n}_{i\uparrow} \hat{n}_{i\downarrow}, \tag{2.5}$$

where $\hat{c}^{\dagger}_{i\sigma}$ ($\hat{c}_{i\sigma}$) denotes the fermion creation (annihilation) operator of at site i with spin $\sigma = \uparrow, \downarrow$, and $\hat{n}_{i\sigma}$ is the corresponding number operator.
In this section we do not enter into the immense body of research devoted to the single-band Fermi-Hubbard model. In the chapter about the methods we will give some basic theoretical introduction to the model and its main results. In the rest of the chapter we focus instead on the main experimental ideas that the lead to the possibility to simulate multicomponent $SU(N)$ Hubbard models [50] using alkaline-earth like atoms. The simulation of the single-band Fermi Hubbard model on the honeycomb lattice can instead be realized with a variety of atoms, but we will not enter the details of this implementation.

2.3 ALKALINE-EARTH LIKE ATOMS

Ultracold Alkaline-earth like atom (AEA) [58] such as Strontium or Ytterbium, which have two electrons in their outer shell, are a precious tools for precision measurements and for the quantum simulation of quantum systems with an $SU(N)$ symmetry [17, 34, 59–61]. The realization of a cooling sufficient to reach the quantum degeneracy regime for the fermionic isotope of Ytterbium, ^{173}Yb opens the possibility to simulate novel quantum phases like a $SU(N)$ Fermionic Mott insulator [14–16, 52], of course loading these atoms in an optical lattice. Moreover within AEA the existence of Orbital Feshbach resonances [55–57] has been demonstrated, opening other opportunities to study multicomponent Fermi systems with tunable interactions. It must be however noted that due to the inherent simple structure of AEA the experimental observation of quantum magnetism is rather prohibited due to low entropy requirements determined by the effective spin-spin interaction.
The greatest advantage of AEA is that, since the electronic groundstate has spin $S = 0$, it is basically decoupled from the nuclear spin ($I > 0$). In the ground state $|g\rangle = |^1S_0\rangle$ the spin and angular momentum are completely zero ($J = 0$). Therefore all the scattering lengths are independent of the nuclear spin. This implies that the $N = 2I + 1$ components of the spin, where $I = 5/2$ for ytterbium, interact with each other with the same coupling, i.e., they display an $SU(N)$ symmetry.
Moreover the two electrons in the outer shell supply a great playground for two orbital quantum simulations, where the excited metastable state $|e\rangle = |^3P_0\rangle$ is coupled to $^1S_0$ via dipole transitions. This enriches the possible collisions between atoms which can take place in four channels labeled ee, gg, eg^+, eg^- according to the electronic states involved. For dilute gases, all the possible interactions are purely local and thereby in the spirit of the Hubbard model.
We give an example of measured values of the $s-$wave scattering lengths for various fermionic AEA which can be cooled down to quantum degeneracy. Interestingly, we find both positive and negative scattering lengths, which can be used to simulate different multicomponent strongly interacting models. For the case of ^{173}Yb, which is the main object of two chapters of this thesis, the scattering length is positive hence the

interactions are repulsive. This means that, loading this system in an optical lattice, we can simulate a $SU(N)$ repulsive Fermi-Hubbard model. The magnitude of the s-wave scattering length is also crucial in the evaporative cooling process [14]

Atom species	nuclear spin I	Symmetry group	scattering length
^{171}Yb	$\frac{1}{2}$	$SU(2)$	$-0.15(19)[^{171}Yb]$, $-30.6(3.2)[^{173}Yb]$ [62]
^{173}Yb	$\frac{5}{2}$	$SU(6)$	$10.55(11[^{173}Yb]$, $-30.6(3.2)[^{171}Yb]$ [62]
^{87}Sr	$\frac{9}{2}$	$SU(10)$	$5.09(10)[^{87}Sr]$ [63]

Table 2.1: Table of fermionic AEA, symmetry group of the and the scattering lengths. These species were cooled down to quantum degeneracy.

In the following we write down the many-body lattice Hamiltonian representing the physics of two-orbital electrons with $SU(N)$ symmetric interaction loaded in an optical lattice.

2.3.1 $SU(N)$ *symmetric Hubbard model*

We derive now based on the properties of AEA in the context of cold atoms in optical lattice the corresponding Hubbard model following [34, 64] and references therein. Our starting point is the Hamiltonian describing the two-body interactions between our ^{173}Yb atoms considering the possibility of populating both the ground state (g) and the excited state (e)

$$\begin{aligned}\hat{\mathcal{H}}_{AEA} = \sum_{\alpha,m}\int d\mathbf{r}\hat{\Psi}^{\dagger}_{m\alpha}(\mathbf{r})\Big(-\frac{\hbar^2}{2m}\nabla^2 + V_m(\mathbf{r})\hat{\Psi}_{m\alpha}(\mathbf{r}) \\ + \hbar\omega_0\int d\mathbf{r}\big(\hat{\rho}_e(\mathbf{r}) - \hat{\rho}_g(\mathbf{r})\big) + \frac{u_{eg^+}+u_{eg^-}}{2}\int d\mathbf{r}\hat{\rho}_e(\mathbf{r})\hat{\rho}_g(\mathbf{r}) \\ + \sum_{m,\alpha<\beta} u_{mm}\int d\mathbf{r}\int d\mathbf{r}\hat{\rho}_{m\alpha}(\mathbf{r})\hat{\rho}_{m\beta}(\mathbf{r}) \\ + \frac{u_{eg^-}-u_{eg^+}}{2}\sum_{\alpha\beta}\int d\mathbf{r}\hat{\Psi}^{\dagger}_{g\alpha}(\mathbf{r})\hat{\Psi}_{g\beta}(\mathbf{r})\hat{\Psi}^{\dagger}_{e\alpha}(\mathbf{r})\hat{\Psi}_{e\beta}(\mathbf{r})\end{aligned} \tag{2.6}$$

,

where the Fermi field operator $\hat{\Psi}^{\dagger}_{m\alpha}(\mathbf{r})$ creates a Fermion at position $\mathbf{r}$ and orbital $m = e, g$ with spin α and the corresponding density operator quantum number resolved is denoted with $\rho_{m\alpha}(\mathbf{r})$, where the sum over the indices gives the total density at $\mathbf{r}$. The fermionic field operators obey the conventional anti-commutation relations following the Fermi statistic and Pauli principle. The optical trap is labeled by $V_m(\mathbf{r})$ where each orbital o can feel a different contribution and the two orbitals g and e are energetically separated by $\hbar\omega_0$. The $2I+1$ Zeeman levels define the spin quantum number as $\alpha = -I, \cdots, I$. The interaction u_c is determined by the scattering length a_c of each collision channels $c = ee, gg, eg^+, eg^-$ as $u_c = (4\pi\hbar^2/m)a_c$.
In this model the atoms move freely in the three-dimensional space except for the

trapping potential. In order to arrive at an expression similar to Eq. (2.5) we express the Fermi fields in the Wannier basis defined by the optical lattice

$$\hat{\Psi}^{\dagger}_{m\alpha}(\mathbf{r}) \equiv \sum_{i} \sum_{\alpha} \sum_{n} w_{i\alpha n}(\mathbf{r}) \hat{c}_{im\alpha n}, \tag{2.7}$$

where $\hat{c}^{\dagger}_{im\alpha n}(\hat{c}_{im\alpha n})$ is the creation (annihilation) operator for a Fermion at lattice site $\mathbf{r}_i$ and orbital m with spin α and n denotes the lattice band index we introduced for completeness. Generally, in cold atomic experiments only the lowest band is occupied, thus we continue with the single-band description for each orbital and drop n and the Hamiltonian for AEA atoms in second quantization reads

$$\begin{aligned}\hat{\mathcal{H}}_{AEA} = &\sum_{\alpha,m} \sum_{i,j} t^{ij}_{o} \hat{c}^{\dagger}_{im\alpha} \hat{c}_{jm\alpha} + \sum_{i} \frac{U_{gg}}{2} \hat{n}_{ig}(\hat{n}_{ig} - 1) + \frac{U_{ee}}{2} \hat{n}_{ie}(\hat{n}_{ie} - 1) \\ &+ U_d \sum_{i} \hat{n}_{ie} \hat{n}_{ig} + U_{ex} \sum_{i} \hat{c}^{\dagger}_{ig\alpha} \hat{c}^{\dagger}_{ie\beta} \hat{c}_{ig\beta} \hat{c}_{ie\alpha},\end{aligned} \tag{2.8}$$

where the energy parameters are defined as follows

- Hopping integral: $t^{ij}_{m} = \int d\mathbf{r} w^{*}_{im}(\mathbf{r}) \big(-\frac{\hbar^2}{2m} \nabla^2 + V_m(\mathbf{r}) \big) w^{*}_{jm}(\mathbf{r})$
- Inter atomic interaction per orbital: $U_{mm} = u_{mm} \int d\mathbf{r} |w|^4_{im}(\mathbf{r})$
- Intra orbital interaction: $U_{eg^{\pm}} = u_{eg^{\pm}} \int d\mathbf{r} |w|^2_{e}(\mathbf{r}) w^2_{g}(\mathbf{r})$
- Direct orbital interaction: $U_d = \frac{U_{eg^+} + U_{eg^-}}{2}$
- Exchange interaction: $U_{ex} = \frac{U_{eg^+} - U_{eg^-}}{2}$

This is indeed a very rich model which contains and extends several solid-state models. If we force the number of spin components to $N = 2$ we have a two-band Hubbard model with an energy distance between the two orbitals which corresponds to a crystal-field splitting in a solid. The interorbital interactions can play an important role as discussed at length in the solid-state framework. In this thesis we will only consider fermions in the groundtate, but we will consider $N = 3$, which turns out to be the minimal model to study flavour-selective phenomena associated to fermionic interactions and the consequent many-body correlation effects.

2.3.2 *Raman transitions and coupling between spin states*

Raman transitions are a very versatile tool in in ^{173}Yb experiments, used to manipulate coherently the nuclear spin degree of freedom by inducing a coherent laser coupling between spin states using two-photon Raman transitions. We illustrate the basic concept on a three-level system in a Γ configuration [65, 66] with only two spin states, but the concept is easily extended to a larger nuclear-spin manifold. The simple Γ scheme depicted in Fig 2.7 involves two stable nuclear spin states of the ground state $^1S_0$, here we arbitrarily chose $|g,\searrow\rangle$ and $|g,\downarrow\rangle$ and the higher-energy state $|e\rangle$, which, due to the large single-photon detuning $\Delta_{1,2}$, is barely populated so that it can only play the role of an intermediate state in a Raman transition. The two ground states correspond to the atomic resonance frequencies labeled by ω_{01} and ω_{02} and are coupled by two laser fields, which induce two-photon processes. We would like to anticipate that with this simple scheme the effect of spin-orbit interaction (SOC)and external magnetic fields [67–69] can be simulated and in order to understand this remarkable connection we derive an effective Hamiltonian that displays a dispersion relation reminiscent of SOC starting for the Γ configuration.

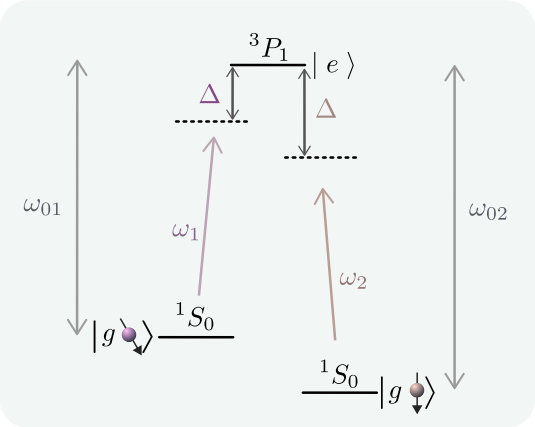

Figure 2.3: **Raman transitions for experimental set up** A schematic drawing of the SU(3) Raman coupling τ, where only two flavors are coupled

The total electric field interacting with the "Raman system" reads as follows

$$\mathbf{E}(\mathbf{r},t) = \hat{\epsilon}_1 E_{01}\cos(\mathbf{k}_1\cdot\mathbf{r}-\omega_1 t) + \hat{\epsilon}_2 E_{02}\cos(\mathbf{k}_2\cdot\mathbf{r}-\omega_2 t), \tag{2.9}$$

where ω_1 and ω_2 are the frequencies of the two light beams and $\epsilon_{1,2}$ are the corresponding polarization vectors. In the rotating frame of the laser fields we can write down a non-interacting Hamiltonian modeling the illustrated Gamma scheme as:

$$\hat{\mathcal{H}}_\Gamma = \hat{\mathcal{H}}_0 + \Delta_1 |g,\searrow\rangle\langle g,\searrow| + \Delta_2 |g,\downarrow\rangle\langle g,\downarrow|, \tag{2.10}$$

where $\Delta_i = \omega_i - \omega_{0i}$ $i = 1,2$ is the detuning of each transition and $\hat{\mathcal{H}}_0$ denotes the kinetic energy term. By using the rotating wave approximation (RWA) the Hamiltonian representing the interaction between the Γ system and the electric field $\mathbf{E}(\mathbf{r},t)$ reads

$$\hat{\mathcal{H}}_I = \frac{\hbar}{2}\left[\Omega_1 e^{i\mathbf{k}_1\cdot\mathbf{r}}|e\rangle\langle g,\searrow| + \Omega_2 e^{i\mathbf{k}_2\cdot\mathbf{r}}|e\rangle\langle g,\downarrow| + h.c\right], \tag{2.11}$$

where $\hbar\Omega_\alpha = -\langle e|\,\mathbf{d}\,|g,\alpha\rangle\cdot\mathbf{E}_{0\alpha}(\mathbf{r})$, $\alpha = \searrow,\downarrow$ defines the single-photon Rabi frequency. We now work out an effective Hamiltonian which describes spin-flip processes. We start from the time-dependent ansatz $|\Psi\rangle = c_1(t)|g\searrow\rangle + c_2(t)|g\downarrow\rangle + c_3(t)|e\rangle$, where $c_i(t)$ $i = 1,2,3$ are time dependent probability amplitudes. Inserting this wavefunction in the Schrödinger equation we obtain three coupled differential equations for the probability amplitudes $c_i(t)$. If we make an adiabatic approximation in which we

assume the detunings Δ_α to be large enough to make the state $|e\rangle$ barely populated and therefore $\langle \partial c_3(t)/\partial t \rangle \approx 0.$, we obtain an effective two-level system with the following Hamiltonian

$$\hat{\mathcal{H}}_{Raman} = \begin{pmatrix} \hat{\mathcal{H}}_0 + \frac{|\Omega_\searrow|^2}{4\Delta_R} & \frac{\hbar\Omega_\searrow\Omega_\downarrow^*}{4\Delta_R} e^{i\mathbf{q}_R\cdot\mathbf{r}} \\ \frac{\hbar\Omega_\searrow^*\Omega_\downarrow}{4\Delta_R} e^{-i\mathbf{q}_R\cdot\mathbf{r}} & \hat{\mathcal{H}}_0 + \frac{|\Omega_\downarrow|^2}{4\Delta_R} - \Delta_0 \end{pmatrix}, \tag{2.12}$$

where $\mathbf{q}_R = 2\mathbf{k}_R \equiv \mathbf{k}_1 - \mathbf{k}_2$ is the momentum transfer during a spin-flip from $|\searrow\rangle$ to $|\downarrow\rangle$, $\Delta_R = (\Delta_1 + \Delta_2)/2$ is the detuning under the assumption that $\Delta_0 \equiv |\Delta_1 - \Delta_2| << \Delta_R$. The Hamiltonian shows a direct coupling between the two spin states, which is a complex number with amplitude $\frac{\hbar\Omega_\searrow\Omega_\downarrow^*}{4\Delta_R}$ and a phase dependent on the transferred momentum $\mathbf{q}_R$. In the experiment discussed in Chapter 8 the transferred momentum during a Raman process is set to zero, which means that the two beams controlling the transition propagate along the same direction. In this case we can simply further the Hamiltonian introducing the real Raman frequency

$$\Omega_{Raman} \equiv \frac{\Omega_\searrow\Omega_\downarrow}{2\Delta_R} \tag{2.13}$$

and making use of the Pauli matrices we obtain the following effective Hamiltonian

$$\hat{\mathcal{H}}_{Raman} = \frac{\hbar\Omega_{Raman}}{2}\hat{\sigma}_x + \left(\hat{\mathcal{H}}_0 + \frac{\hbar\Omega_\searrow^2}{4\Delta_R}\right)\frac{\hat{\sigma}_0 + \hat{\sigma}_z}{2} + \left(\hat{\mathcal{H}}_0 + \frac{\hbar\Omega_\downarrow^2}{4\Delta_R}\right)\frac{\hat{\sigma}_0 - \hat{\sigma}_z}{2} \tag{2.14}$$

which describes exactly the physics we anticipated, in which the two spin states are directly coupled. The physics of this simple model is obviously dominated by the competition between the Raman term and the diagonal terms and by the breaking of the full $SU(N)$ symmetry. The investigation of a similar Hamiltonian for a $SU(3)$ system will be the main subjects of the experiments and theoretical calculations reported in Chapter 7 and Chapter 8

2.4 SYNTHETIC DIMENSIONS, ARTIFICIAL GAUGE FIELDS AND NON-TRIVIAL TOPOLOGY

As we have seen in the last section Raman transitions are a versatile tool to manipulate spin states inducing a coupling between the different spin states. We ended the section with a Hamiltonian that closely resembles a spin-orbit coupling term. In this section we discuss how this Raman-induced coupling can be used to engineer non-trivial topological properties which can be described in terms of artificial gauge fields [23–30]. Most of the cold-atom schemes designed to simulate artificial gauge fields on a lattice are based on treating the nuclear spin state as a synthetic dimension, as shown in Fig. 2.4.

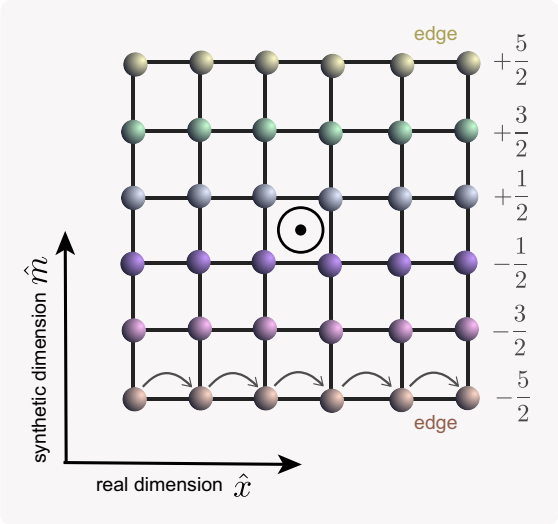

Figure 2.4: **Synthetic dimension** Schematic picture of a general protocol to use the internal spin state as a synthetic dimension and to introduce artificial magnetic fields by using Rama processes as hoppings in the synthetic dimension

Here we show schematically a one-dimensional optical lattice along the x direction, while the Raman processes are interpreted as tunneling states between sites in the internal spin state, which plays the role of an extra dimension with a limited number of sites given by the different spin states, from -5/2 to 5/2 in our example. Since the hopping in the synthetic dimension can be made complex and its phase can be controlled, one can engineer it in a way such that, if we move around a plaquette such as the one marked with a circle, the hoppings acquire an overall phase, in complete analogy with the Aharonov-Bohm phase resulting from the flux of a magnetic field if we interpret the system as a two-dimensional strip. This is precisely the artificial gauge field that we can now simulate in a cold-atom framework.
The advantage of realizing synthetic magnetic fields in optical lattice compared to real magnetic fields in solid state systems, lies in the possibility to achieve exceptionally large magnetic fluxes in comparison with the hopping amplitude, and on the unprecedented control which can be used also to design topological phases. We will now examine an experimentally accomplished topologically nontrivial state which uses the above discussed general strategy.
The experimental realization of topological insulators is an example of the kind of phenomena that we explore in Chapter 6, though we present a different version of a quantum Hall system that is a three-dimensional version with two spatial dimension and one synthetic dimension.

2.4.1 *Exploring the topology of a quantum Hall system at the microscopic level*

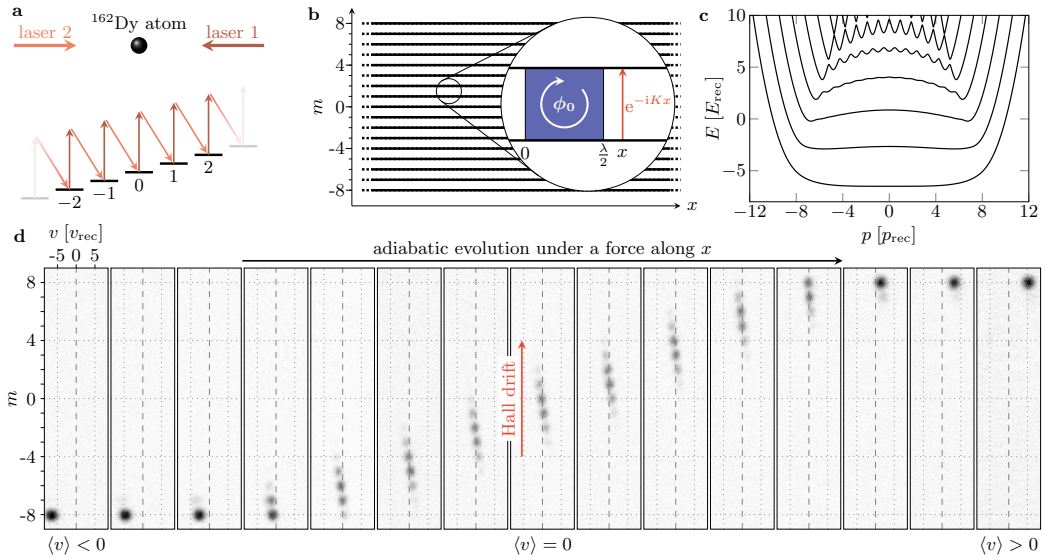

Figure 2.5: **Artificial quantum Hall system. a** Laser scheme exploited to couple the magnetic sublevels m of a ^{162}Dy atom **b** spin ladders as synthetic dimension forming together with the spatial dimension a finite two dimensional Hall Ribbon. The complex hopping between spin projections induces a complex phase reminiscent of the Aharonov Bohm phase. The blue square indicates a magnetic unit cell containing a quantum flux Phi_0. **c** Measured dispersion relation with quantum level structure. **d** Imaging of the atomic cloud exhibiting the adiabatic evolution of the spin projection m and the velocity $\hat{v}$ subject to an external. Figure taken from Ref. [22]

In this set up [22] a topological system was realized using ultracold ^{162}Dy atoms whose dynamics takes place on a synthetic two-dimensional quantum Hall ribbon with one spatial and one artificial dimension. The latter dimension is spanned by $2J+1 = 17$ magnetic sublevels coupled by coherent light thus inducing a magnetic field. The Aharonov-Bohm phase of a charged particle subject to a magnetic fields is simulated with a complex hopping amplitude between the spin ladders where the spin transition imparts a recoil photon $p_{rec} = \hbar K$ with coupling strength $K = 4\pi/\lambda$ and $\lambda = 626.1\mathrm{nm}$ (light wave length). The atom dynamics is governed by the dominant optical transition of the atom light interaction and is represented by the following Hamiltonian,

$$\hat{\mathcal{H}} = \frac{1}{2}M\hat{v}^2 - \frac{\hbar\Omega}{2}\left(e^{-iK\hat{x}}\hat{J}_+ + e^{iK\hat{x}}\hat{J}_-\right) + V(\hat{J}_z), \tag{2.15}$$

where M is the mass of the atoms, $\hat{v}$ their velocity, $\hat{J}_\pm, \hat{J}_z$ are the ladder and spin projection operators respectively. $V(\hat{J}_z) = -\hbar\Omega\hat{J}_z^2(2J+3)$ is a potential stemming from light shifts and is controlled by Ω, which is proportional to the laser electric fields. The canonical momentum $\hat{p} = M\hat{v} + p_rec$ is a conserved under a light-induced spin transition and its dynamics is described by

$$\hat{\mathcal{H}}_p = \frac{(p - p_{rec}\hat{J}_z)^2}{2M}M\hat{v}^2 - \hbar\Omega\hat{J}_x + V(\hat{J}_z), \tag{2.16}$$

reminiscent of the Landau momentum. The kinetic energy along the synthetic dimension is modeled by $\hat{J}_x$. This set up is similar to a Hall system with a ribbon geometry, where the edges are bounded by $m = \pm J$ as depicted in the schematic Fig 2.4 and 2.5 (b) . The analogy is demonstrated by the energy bands that display the structure of dispersionless Landau levels. The Landau level physics is explored by imaging the atomic cloud after a free flight subject to a magnetic field which allows measuring the velocity $\hat{v}$ and the spin projection m. The system displays three different behaviours determined by momentum p as demonstrated in Fig 2.5 (d). (i) **left-moving edge** spin-polarized gas ($m = -J$) the mean velocity $\langle\hat{v}\rangle$ of the atoms motion is negative and corresponds to a left-moving edge. (ii) **transverse Hall drift** resonant transitions along the spin-projection induced by the force F_x leading to vanishing velocity, i.e atoms motion is hindered along x. (iii) (i) **right-moving edge** the synthetic edge $m = J$ is reached with the positive mean velocity $\langle\hat{v}\rangle > 0$ signaling a right-moving edge. Overall these three regimes form the edge and bulk modes where the finite velocity modes represent metallic egde modes and the zero velocity in the center of the synthetic lattice is analogous to a insulating bulk mode.

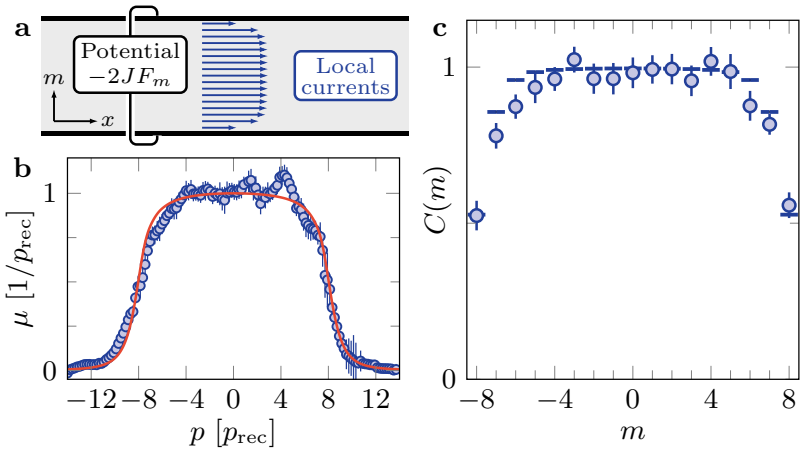

Figure 2.6: **Hall response a** application of a potential difference on the synthetic edges, inducing local currents used for measuring the Hall response. **b** Hall mobility $\mu(p)$ measured via the velocity due to a force along m. **c** Local Chern marker $C(m)$ resolved in the synthetic dimension corresponding to a integrated weighted mobility μ.

To further examine the Landau levels, the investigate their quantized Hall response which reveals the topological nature of the Hall ribbon. In this set up the Hall response is generated by applying a potential difference (Fig 2.6 (a)) across the edges equip the atoms with a transverse velocity. In their setup such a potential is modeled by a Zeeman term $-F_m\hat{J}_z$ and is added to Hamiltonian (2.16). Then the Hall mobility is defined as

$$\mu = \frac{1}{p_{\mathrm{rec}}}\frac{\partial}{\partial p}(p - M\langle\hat{v}\rangle) \tag{2.17}$$

and is shown in Fig 2.6b.μ vanishes in the edge mode sector, being undisturbed by the magnetic field while it is close to the classical value in the bulk. Since the system is finite it does not exhibit a gap in the energy spectrum thus the Hall response for the entire energy branch connected to the ground state is not fully physical. However, the

topological character in the finite-size ribbon can be characterized by the local Chern marker [70] C(m) (that we discuss in some details in Chapter 6), a coordinate-space analogue of the Chern number in conventional topological bulk systems, which is 1 in the bulk and fluctuates on the edges. The measurement is particularly interesting, for our theoretical proposal in Chapter 6 where we study a quantum spin Hall system on a finite honeycomb structure characterizing the topological state by the local Chern marker. The discussed experiment is one of the very first experiments detecting the local Chern marker and is a very remarkable realization of a Hall system paving the ways towards the experimental study of topological finite-size systems.

2.5 MOTT TRANSITION FOR SU(N) SYSTEMS IN OPTICAL LATTICE EXPERIMENTS

As discussed in the previous section optical lattices provide a versatile platform for studying interacting matter by confining the atoms in periodic arrays reminiscent of the ionic potentials in solid crystals. In contrast with solid-state materials and devices, optical lattices are clean and controlled frameworks where a broad range of parameters and lattice structures can be explored. For example interatomic interactions, density, dimensionality, artificial magnetic fields and other parameters can be tuned by confining the atoms under specific conditions. One of the most studied model in cold atoms is the conventional Hubbard model, where the interactions are typically manipulated via Feshbach resonance. Within AEA gases the interactions among atoms can be adjusted using magnetic Feshbach resonances (MFR), which unfortunately, do not allow the manipulation of the interaction in the ground state, however an alternative route is provided by Optical Feshbach resonance [55, 56]

This technique relies on Photoassociation processe [71] which are used to couple colliding atoms into an excited bound state which in turn induces a Feshbach resonance that modifies their scattering length. Having control of the interatomic interactions is particularly important in order to create a Mott insulating state [15–19] and moreover to observe an interaction-driven metal to Mott insulator transition [12–14]. In the following we discuss an example about the realization of a SU(6) Mott insulator using ^{173}Yb atoms following Ref. [14, 34] which represents the general experimental framework for the proposal and measurements that we present in Chapter 7 and Chapter 8, in which we discuss orbital selective Mott transitions within SU(3) Raman coupled Hubbard models. As we discussed above, AEA in an optical lattice provide a great playground for the SU(N) generalization of the Hubbard model, which is the subset to the model (2.8) in which we limit to the pure groundstate electronic state g:

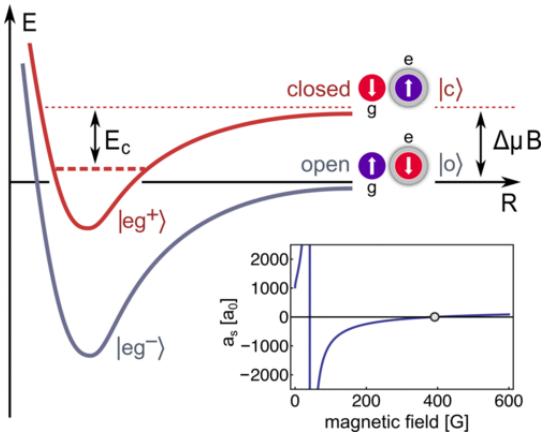

Figure 2.7: **Scheme of ^{173}Yb orbital Feshbach resonances** OFR affect the scattering among two atoms each residing in the $|^1S_0\rangle$ $|^3P_0\rangle$ respectively. Figure taken from Ref. [56]

$$\hat{\mathcal{H}} = -t_g \sum_{\langle i,j \rangle} \left(\hat{c}^{\dagger}_{\alpha,i} \hat{c}_{j\alpha} + h.c \right) + \frac{U_{gg}}{2} \sum_i \hat{n}_i (\hat{n}_i - 1), \tag{2.18}$$

$\langle i, j \rangle$ denotes next-neighbor lattice sites and $\hat{c}^{\dagger}_{\alpha,i}(\hat{c}_{i\alpha})$ creates (destroys) are particle with nuclear spin α at lattice site i and the corresponding density operator $\hat{n}_{i\alpha}$ where the sum over all spins measure the total fermion occupation per site. We assume that the lattice is sufficiently deep enough in order to apply the single band description. The model is characterized by two energy scales, the kinetic energy denoted by t_g and the inter atomic interaction U_{gg}, where g refers to the ground state. As already mention $U_g g$ is governed by Feshbach resonances and therefore U_{gg} is proportional to a_s the s-wave scattering length. Within these experiments U_{gg} and t_g can not be tuned independently, but their ratio U_{gg}/t_g can be modified by varying the lattice depth of the lattice potential adjusting the intensity of the laser beams creating the lattice. The conditions in order to induce a Mott insulator require the interaction energy to dominate the kinetic energy, i.e $U_{gg} >> t_g$, and the temperature $T << U_{gg}/k_B$. Moreover the lattice filling, n must assume an integer value smaller than the total number of available spin components α. A Fermi liquid is expexted to be realized when $t_g >> U_g, Tk_B$ as well when n deviates from an integer value. The temperature must also exceed the magnetic ordering temperature, in turn dependent on the chosen lattice and the dimensionality. Finally, a Band insulator can be realized when the system is completely filled with the nuclear spin states per lattice sites. Also in the latter case the atomic motion is blocked due to Pauli principle instead of the interaction. In Ref. [14] they realize a $SU(6)$ Hubbard model using ^{173}Yb atoms loaded adiabatically [14] in their ground state $|g = {}^1S_0\rangle$ in a 3D optical lattice generated by orthogonal counter propagating laser beams. In order to reach sufficiently cold temperatures a trapping potential is added that adds a site dependent onsite energy, i. e

$$\hat{V}_{trap} = \sum_i V_i \hat{n}_i, \tag{2.19}$$

where $V_i = 0.5 \sum_i m\omega_i^2 a^2 / 2 \left(\mathbf{R_i}/a \right)^2$ a harmonic potential depending on the trapping frequencies ω_i. The system was initialized by loading the gas in a 3D dipole trap followed by an adiabatic ramping of the lattice depth until a deep lattice was obtained with an initial temperature of $T_i/T_F \approx 0.2$. Importantly, the filling has been limited to two fermions per site at most, which is crucial in order to realize the Mott insulating phase. They can measure the Mott gap directly using photo-association (see Chapter 8 for some more details) after injecting energy into the gas that leads doublons and holons to evaporate from the trap and can be counted. The doublon production rate depends on the frequency of the modulation applied to the lattice in order to start the doublon/holon creation and reveals a peak at the frequency analogous to the Mott gap, i. e ($\approx U_g/\hbar$). Furthermore this procedure can be exploited to estimate the temperature of the gas. Interestingly comparing the temperatures taken from $SU(2)$ and $SU(6)$ Mott insulating gases, it turned out that the temperature of the $SU(6)$ gas was smaller by a factor of 2 or 3 than the $SU(2)$ temperature. This is attributed to the adiabatic loading which can cool down systems with higher nuclear spin state manifold more effectively and can be explained by the entropy stored in the spin degrees of freedoms.

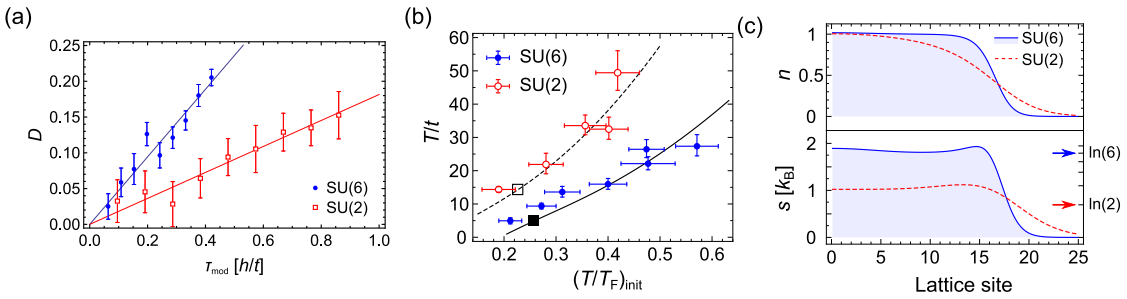

Figure 2.8: **SU(N) Mott insulators and doublon reproduction rate** (a) shows the measurement of the doublon production rate (b) the Temperatures for the SU(6) blue circles and SU(2) red circles Fermi gases obtained using the DPR. (c) density (upper panel) and entropy (lower panel) as a function of the lattice site. Figure is taken from Ref. [14]

Assuming the atomic limit and a Mott state, i. e tunneling between lattice sites is highly suppressed , the spin entropy per atom in a SUN) Fermi gas is bounded from above by ln(N). Adiabatically loading the gas into an optical lattice the clean Mott insulating state is expected to arise at $T_{int}/T_F \propto \ln(N)\pi^2$, where T_{int} is the initial temperature of the gas in the harmonic trap before the loading into the lattice. We can conclude that a gas with higher spin manifold reduces the required initial temperature and thereby the large spin cools down the systems effectively by absorbing entropy from the kinetic contribution. This mechanism reminds of the Pomeranchuk cooling [14].

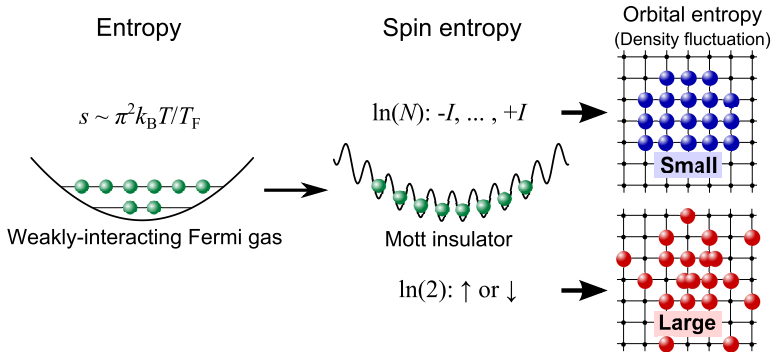

Figure 2.9: **Schematic entropy mechanism reminiscent of Pomeranschuk cooling in an** SU(N) **Fermi gas** Illustration of the entropy's role in the transition from weakly interacting degenerate Fermi gas to a Mott insulator. Larger spin degrees of freedom are able to absorb entropy and thereby reduce density fluctuations, which control the temperature.Figure is taken from Ref. [14]

3

HUBBARD MODEL AND DYNAMICAL MEAN FIELD THEORY

3.1 INTRODUCTION

In this chapter we present a short review of some of the basic properties of the fermionic Hubbard model, which is the main common building element of all the original material presented in this thesis. The literature on this model, and especially on its three-dimensional version, is immense and we do not attempt a review of the many results and on the large number of methodologies which have been introduced and developed to understand and solve this elusive model. Rather, we will limit ourselves to introduce a small number of main concept which are useful to understand our investigations on strongly correlated effective nanoflakes of honeycomb lattice (Chapter 5 and Chapter 6) and of cold-atom inspired three-component Hubbard model with Raman coupling between two nuclear-spin levels.

In particular, after an introduction about the Fermi-liquid [72–74] and Mott insulating [3] states and the transition connecting then, we will focus on the approach that we used to study these problems, namely the Dynamical Mean-Field Theory (DMFT) [42], a powerful non perturbative method which is often considered as the state-of-the-art method to study the Mott transition. We will briefly discuss the general ideas of the method, some specifical aspects of our implementation using an exact diagonalization solver [75–77], including the case where the spin is not conserved, and finally we devote some space to the real-space generalization of DMFT, which is necessary to study inhomogeneous systems.

3.2 THE FERMI-HUBBARD MODEL

The simplest microscopic model describing interacting spinful Fermions on a lattice is the one-band Fermi-Hubbard model. The interaction among the Fermions is modeled by a purely local repulsion, due to the assumption that the fermions are intensely screened. The model has a rather long history started in 1963 when the model was introduced to study itinerant magnetism in some transition-metal oxides. For many years the model has been used to study properties of materials with partially filled 3d -bands displaying fascinating correlation effects. However, because of the point interaction the model is an ideal candidate for modern experiments using ultracold atoms in optical lattices, where the interaction is indeed short-range, while in the framework of solid-state physics, the relevance of the Hubbard model for real materials depends on the validity of several approximations about the range of the potential and on the possibility to neglect the interaction with the lattice.

The basic model includes two terms and reads

$$\hat{\mathcal{H}} = \sum_{i,j,\sigma} t_{ij} \hat{c}^{\dagger}_{i\sigma} \hat{c}_{j\sigma} + U \sum_{i} \hat{n}_{i\uparrow} \hat{n}_{i\downarrow}, \tag{3.1}$$

where $\hat{c}^{\dagger}_{i\sigma}$ ($\hat{c}_{i\sigma}$) denotes the fermion creation (annihilation) operator of at site i with spin $\sigma = \uparrow, \downarrow$, and $\hat{n}_{i\sigma}$ is the corresponding number operator. Though model and its derivation is very standard and can be found in numerous publications, we present a brief derivation due to the central role of this model in all the calculations that we present. In the presence of a periodic potential given by the lattice, the kinetic energy term satisfies the eigenvalue equation according to Bloch theorem

$$\hat{\mathcal{H}}_0 \Psi_{\alpha\mathbf{k}}(\mathbf{x}) = \epsilon_{\alpha}(\mathbf{k}) \Psi_{\alpha\mathbf{k}}(\mathbf{x}), \tag{3.2}$$

where to each band α corresponds the energy dispersion $\epsilon_{\alpha}(\mathbf{k})$. In cold atomic experiment we can take a lattice sufficiently deep to make the band gap Δ_{12} between the first and second band much larger than the other energies involved. Under this condition it is sufficient we can treat the states of the fermions in a lowest-band only description

$$\hat{\mathcal{H}}_0 = \sum_{\alpha,\mathbf{k}} |\alpha, \mathbf{k}\rangle \, \epsilon_{\alpha}(\mathbf{k}) \, \langle \alpha, \mathbf{k}| \approx \sum_{\mathbf{k}} |\mathbf{k}\rangle \, \epsilon(\mathbf{k}) \, \langle \mathbf{k}| \,. \tag{3.3}$$

Under the same circumstances, it is very convenient to choose a local real space basis, called Wannier basis (for reasons we will understand soon) and perform a Fourier transformation on the eigenstates using

$$|\mathbf{k}\rangle = \frac{1}{L} \sum_{i} e^{i\mathbf{k}\mathbf{R}_i} |\mathbf{R}_i\rangle \,. \tag{3.4}$$

In terms of the above Wannier states [78], we obtain a real space site-dependent Hamiltonian

$$\hat{\mathcal{H}}_0 = \sum_{\mathbf{k}} |\mathbf{k}\rangle \, \epsilon(\mathbf{k}) \, \langle \mathbf{k}| = \sum_{i,j,\mathbf{k}} \frac{e^{i\mathbf{k}(\mathbf{R}_i - \mathbf{R}_j)} \epsilon(\mathbf{k})}{L^2} |i\rangle \, \langle j| \equiv \sum_{i,j} t_{ij} \, |i\rangle \, \langle j| \,, \tag{3.5}$$

with a hopping amplitude

$$t_{ij} = \int d\mathbf{r} w_i(\mathbf{r}) [-\hbar \frac{\nabla^2}{2m} + \hat{V}(\mathbf{r})] w_j(\mathbf{r}) \tag{3.6}$$

t_{ij} describing the hopping rate from site j to site i. Restricting the hopping only to adjacent site gives the simplest tight-binding model Hamiltonian

$$\hat{\mathcal{H}}_0 = \sum_{\langle i,j \rangle} t_{ij} \, |i\rangle \, \langle j| \,, \tag{3.7}$$

which is the conventional kinetic energy term of the Hubbard model.
Including the interaction among fermions which depends only on their distance in real space i.e $U(\mathbf{R}_i, \mathbf{R}_j) = U(\mathbf{r}_i - \mathbf{r}_j) \equiv U(\mathbf{d})$, the interaction is translation invariant and can be also expressed in the basis defined by the Wannier functions

$$U_{ijmn} = \int d\mathbf{r}_1 \, d\mathbf{r}_2 U(\mathbf{d}) w^*_i(\mathbf{r}_1) w^*_j(\mathbf{r}_2) w_l(\mathbf{r}_1) w_m(\mathbf{r}_2) \tag{3.8}$$

When the original interaction is short-ranged, as it happens in dilute cold-atom systems, or the long-range interaction is screened, the fermions feel their mutual interaction only when they occupy the same site i, which due to Pauli principle is only possible only if the fermions have a different spin $\sigma = \uparrow, \downarrow$, lead to the familiar interaction of the standard $SU(2)$ Fermi-Hubbard model

$$\hat{\mathcal{H}}_{int} = U \sum_i \hat{n}_{i\uparrow}\hat{n}_{i\downarrow}, \tag{3.9}$$

Though the model seems at first glance very simple, it is not exactly solvable except for the very specific one-dimensional case [79]. In order to gain first insights into the model we discuss two limits, the weakly interacting regime ($t \ll U$) in the following section and the strongly interacting regime ($t \gg U$) in the subsequent section. The most challenging and interesting part is intermediate regime where the two energy scales of the problem are comparable and simple and/or perturbative methods can not be applied safely. In order to approach this region a number of approaches, ranging from purely numerical to semi analytical have been devised. Here we use Dynamical Mean-Field Theory, which has proved particularly effective in describing the transition between the two opposite regimes.

3.2.1 *Fermi Liquid Theory and Quasiparticles*

Interacting many-body fermionic system represent a formidable challenge and to find a general and unified theoretical description is one of the most elusive undertakings since the birth of solid state theory. A first step towards this mission is to restrict the study to a specific limit, such as the weakly interacting regime. Landau established in 1956 a phenomenological theory in which the low-energy properties of the metal are reminiscent to the spectrum of the elementary excitations of the a free Fermi gas, hence the name of Fermi-liquid which defines the name of the theory as "Landu theory of normal Fermi liquids".
Within this theory the connection between non interacting and weakly interaction fermions emerges from adiabatically turning on the interaction so that the eigenstates of the interacting system evolve adiabatically from the eigenstates of the free fermions. That means there exist a one-to-one correspondence among the states of the free Fermion gas and the Fermi liquid. The new excitations of the interacting system are not associated to excitations of physical particle, but of effective object which behave as the original particles at low energy and temperature, called quasiparticles. Obviously this assumption is not generally valid, as in the case of phase transitions or formation of bound states.
On other words, Fermi liquid theory portrays adequately the physics of a complex many-particles systems by relying on the concept of quasi-particles, which have a finite lifetime contrary to the non interacting particles, but they become more and more stable when we consider excitations close to the Fermi surface.
Quasi-particles can be understood as dressed fermions where the cloud around an undress fermion is caused by the effective medium induced by the interacting particles. Indeed the dressed fermions are heavier than the non-interacting Fermions and carry an effective mass m^* larger than the bare mass m, which reflects the reduction of their mobility. The bare band mass originates from band theory as discussed above, describ-

ing the motion in a periodic potential. Therefore the effective mass is a consequence of the correlations induced by the interactions and it can be thereby used as a measure of the degree of correlation

In order to understand the relation between the non-interacting and the weakly interacting particles in the Fermi liquid regime we examine the main quantities involved and derive the effective mass. We start from the single-particle Green's function, which describes the propagation of a single-particle state

$$G_{\mathbf{k}\sigma}(\tau) \equiv -T_\tau \langle \hat{c}_{\mathbf{k}\sigma}(\tau)\hat{c}^\dagger_{\mathbf{k}\sigma}(0)\rangle, \tag{3.10}$$

where $\hat{c}_{\mathbf{k}\sigma}(\tau) = e^{\tau\mathcal{H}}\hat{c}_{\mathbf{k}\sigma}e^{-\tau\mathcal{H}}$ is the imaginary time evolution of the fermionic destruction operator with momentum $\mathbf{k}$ and spin σ. Transforming the Green's function to frequency space we can easily obtain the exact result for non-interacting fermions

$$\mathcal{G}_{\mathbf{k}\sigma}(\omega) = \frac{1}{\omega + \mu - \epsilon_{\mathbf{k}}} \tag{3.11}$$

and the interacting Green's function can be obtained via the Dyson equation

$$G_{\mathbf{k}\sigma}(\omega) = \frac{1}{\omega + \mu - \epsilon_{\mathbf{k}} - \Sigma_{\mathbf{k}\sigma}(\omega)}, \tag{3.12}$$

where $\Sigma_{\mathbf{k}\sigma}(\omega)$ is the self-energy, a function containing all the effects of the interaction on the single-particle properties. This equation is in general purely formal because the self-energy can not be computed exactly except for some specific limits. We elaborate on the calculation of $\Sigma_{\mathbf{k}\sigma}(\omega)$ in section 3.3. At this point however, we limit our analysis to the vicinity of the Fermi energy $\omega = 0$ and $\mathbf{k} = \mathbf{k}_F$ and we assume that the self-energy is regular and it can be expanded [72] in powers of the frequency as

$$\Sigma_{\mathbf{k}\sigma}(\omega) = \Sigma_{\mathbf{k}\sigma}(0) + \omega \cdot \frac{\partial \Sigma_{\mathbf{k}\sigma}(\omega)}{\partial \omega}\bigg|_{\omega=0} + \omega^2 \cdot \frac{\partial^2 \Sigma_{\mathbf{k}\sigma}(\omega)}{\partial \omega^2}\bigg|_{\omega=0} + \cdots \tag{3.13}$$

One can prove that in perturbation theory at zero temperature the first contribution to the imaginary part of the self-energy $\Im\Sigma_{\mathbf{k}\sigma}(\omega)$ comes at the second order in ω, so that, for very low-frequency we only have the two contributions

$$\begin{aligned} &\Sigma_{\mathbf{k}\sigma}(0) \in \mathbb{R} \\ &\frac{\partial \Sigma_{\mathbf{k}\sigma}(\omega)}{\partial \omega}\bigg|_{\omega=0} \in \mathbb{R} \leqslant 0 \end{aligned} \tag{3.14}$$

Then, in the same spirit of Landau phenomenological theory we find

$$\Im\Sigma_{\mathbf{k}\sigma}(\omega) = \Gamma \propto \left(\omega^2 + (\pi k_B T)^2\right). \tag{3.15}$$

This is a crucial results because $\Im\Sigma_{\mathbf{k}\sigma}(\omega)$ plays the role of a scattering rate and therefore as well proportional to the inverse life time of a single-particle state in an interacting fermion system. Eq. (3.15) implies that the lifetime of the quasiparticles tends to become infinite as we approach low-energy $\omega \to 0$ and low-temperature $T \to 0$,.

Before we insert the result of the self-energy in the Green's function let us define the quasiparticle weight

$$\begin{aligned} Z_{\mathbf{k}_F} &= \Big(1 - \frac{\partial \Sigma_{\mathbf{k}\sigma}(\omega)}{\partial \omega}\Big|_{\omega=0}\Big)^{-1} \\ \tilde{\epsilon}_{\mathbf{k}} &= Z_{\mathbf{k}_F}\epsilon_{\mathbf{k}} \\ \tilde{\mu} &= Z_{\mathbf{k}_F}\big(\mu - \Sigma_{\mathbf{k}\sigma}(0)\big). \end{aligned} \tag{3.16}$$

Then we obtain that the low-energy Green's function is

$$G_{\mathbf{k}\sigma}(\omega) = \frac{Z_{\mathbf{k}_F}}{\omega + \tilde{\mu} - \tilde{\epsilon}_{\mathbf{k}} - i\Gamma}, \tag{3.17}$$

which, if Γ can be neglected, which happens at small ω describes a non-interacting Green's function with a dispersion renormalized by the same factor $Z_{\mathbf{k}_F}$ which also plays the role of a weight. This gives a formal description of the quasi-particle picture, where the low-energy Green's function does not describe a real particle anymore, but a fraction of it, i.e it describes the quasi-particle excitations. If we neglect the correction coming from the momentum dependence of the self-energy, a choice which will be later justified in the context of Dynamical Mean-Field Theory, the quasi-particle mass enhancement is given by $m^*/m = 1/Z_{\mathbf{k}_F}$. This means that a very small quasi-particle weight corresponds to a very large effective mass, hence to almost localized quasiparticles.
From the Green's function we can compute the spectral function

$$A_{\mathbf{k}\sigma}(\omega) \equiv -\frac{1}{\pi}\Im G_{\mathbf{k}\sigma}(\omega + i0^+), \tag{3.18}$$

where we used the Fourier transformed Green's function from imaginary time τ to frequency space denoted by $omega$ and $i0^+$ is typically added for integration reasons. Summing the spectral function over the momenta $\mathbf{k}$ we obtain the density of states as

$$N_\sigma(\omega) = \frac{1}{V}\sum_{\mathbf{k}} A_{\mathbf{k}\sigma}(\omega). \tag{3.19}$$

Both of the quantities can be in principle accessed in experiments using photoemission measurements where both objects are weighted by the Fermi function $f(\omega)$. The spectral function $A_{\mathbf{k}\sigma}(\omega)f(\omega)$ can be obtained by exploiting angle resolved photoemission and the density of states can be measured by angle integrated photoemmission.
In this section we have learned that, under reasonably generic circumstances, one can expect that a weakly interacting system of particles behaves, at low-energy, like a collection of effective renormalized excitations, called quasiparticles. A crucial parameter is introduces, the quasiparticle weight, which measures the fraction of fermoin which still behaves like a free particle and, at the same time, the renormalization of the dispersion and the inverse of the interaction-driven effective mass renormalization.
It must be however noted that the Fermi-liquid picture is not necessarily limited to very small interactions. If no symmetry breaking takes place, we can envision a situation where the quasiparticle weight can become very small and even vanish continuously, leading to a divergent effective mass corresponding to a localization of the particles.

3.2.2 *Mott insulators and the Mott transition*

The band theory of solids was the first theory able to successfully describe electronic properties and predict the metallic or insulating state of the systems based on the filling of the bands. However, this theory is based on a single-particle picture, which means that it assumes that the electrons effectively do not interact with each other, but experience an effective potential. It is therefore reasonable to expect that the theory can fail in systems where the presence of strong interaction determines the physics.

An example of this failure has been reported already in the first half of the twentieth century, where several transition-metal oxides are clearly found to be insulators despite the count of electrons would give a partially filled band, i.e., a metal according to the bend theory.

Mott and Peierls [80] were the first who proposed that this sharp deviation from the prediction could be a consequence of a predominance of the Coulomb repulsion which localizes the electrons giving rise to a novel insulating state completely different from a band insulator, which has been called a Mott insulator [2].

They proposed an explanation which anticipated the physics of the Hubbard model several years before its introduction. In order to understand the Mott insulating state, it is convenient to first understand the system in the absence of interaction and then adiabatically introducing the repulsion among fermions. In the non-interacting case and at half-filling all the eigenstates are obviously completely delocalized and the system describes a metal. When the interation is "switched on", the kinetic energy has to compete against the repulsion, which imposes constraints to the fermionic motion. A fermion becomes indeed unlikely to move towards a site where another fermion with opposite spin is present. Therefore, the larger the repulsion, the less the fermions "like" to move.

The competition between the two energy scales present in the Hubbard model determines the overall state. Clearly, when U is still sufficiently weak the electrons prefer to remain mobile since Coulomb energy cost for creating a doubly occupied site (or doublon) is not very high and the delocalization energy prevails. However, when U is very large, the formation of doublons is energetically very costly which in turn prevents the electrons to move around the lattice because the hopping leads to a smaller energy gain.

Therefore the best configuration to minimize the energy is to localize exactly one fermion per site over the entire lattice and suppress density fluctuations. This is the simple cartoon of the Mott insulator.

The evolution from the metal to the Mott insulator [2], called Mott-Hubbard transition, is a phenomenon induced by the correlations between fermions generated by the interaction. Understanding the central role of correlations in the creation of the Mott state makes it clear why the band theory fails completely to describe Mott insulators and the Mott transition.

When the density deviates from an average filling corresponding to the number of lattice sites, density fluctuations are present even for very large U and the insulating nature breaks down. We stress that, for system where the local Hamiltonian can host more than two fermions, like multiorbital or $SU(N)$ systems, a Mott insulator can occur at any commensurate filling that is not a fully filled, i.e a band insulator. In this case we will have that every site hosts exactly the same integer number of fermions.

A final remark has to made about the tendency towards long-ordered phases. In general strongly correlated systems are susceptible to several instabilities where the spin and/or orbital degree of freedom order spatially leading to a spontaneous symmetry breaking. The most notable example is the antiferromagnetic state of the half-filled single-band Hubbard model, where the spins are staggered in space if the lattice is bipartite. We discuss this aspect in detail in Chapter 4 where we derive and effective strong coupling theory for an extended version of the Hubbard model, but, for the Hubbard model on a bipartite lattice, antiferromagnetism is present, at very low temperatures, also in weak coupling, somehow hiding the Mott-Hubbard transition that we described.
However, even in these situations where the low-temperature states break the symmetry, we expect that the physics of the Mott transition, namely the evolution between a Fermi liquid and a Mott insulator, will be observed at higher temperatures. In this thesis we will consider both situations where the system retains magnetic order (Chapter 5 and Chapter 6) and regimes where we expect the ordering to be washed out by temperature (Chapter 7 and Chapter 8).

3.3 DYNAMICAL MEAN-FIELD THEORY

In the previous section we discussed two limits of the Hubbard model: the weakly interacting regime described by Fermi liquid theory and the strongly interacting regime where hopping is strongly suppressed and the ground state is a Mott insulator. However, the complexity of the Hubbard model is not simply captured by the two limits and one can expect a rich phase diagram in between. As we discussed before, this question has been the object of countless investigations using a variety of methods, most of which have been designed specifically to solve the Hubbard model, in most cases in two dimensions.
In this work we focus on a strategy which followed an original path with respect to most previous methods. n order to tackle the difficulty to solve strongly correlated electron systems Walter Metzner and Dieter Vollhardt in 1989 introduced another limit in which the coordination number of the lattice (or the dimensionality) d is sent to infinity [81] thus each lattice site is connected to infinitely many neighbouring sites. In this regime one finds immense simplifications to the perturbation theory, for example the self-energy turns out to be momentum independent

$$\Sigma(\mathbf{k}, \omega) \longrightarrow \Sigma(\omega) \tag{3.20}$$

This idea allowed to develop a quantum extension of the mean-field approach in which the spatial degree of freedom is frozen, but the local quantum fluctuations are completely accounted for. To be more concrete, the Hubbard model in this limit can be mapped onto a self-consistent quantum impurity model, i.e. to a single interacting site hybridized with non-interacting bath. The interacting site is representative of any site of the original lattice model, in a mean-field spirit. Hence, the interaction of a site with the rest of the lattice is replaced by the embedding in an effective bath which is determined self-consistently in order to embody effectively the presence of the remaining of the lattice. This theory was established by Antoine George and Gabriel Kotliar et all and is called Dynamical mean-field theory (DMFT) [42].

We depict schematically the main idea of DMFT in Fig 3.1. The lattice problem is mapped to a single impurity atom embedded in a non-interacting medium of fermions, which results in dynamical fluctuations on the impurity site due to the hybridization with the bath. The local theory is interacting while the kinetic contribution is transmitted through a self-consistency scheme. As matter of fact, the solution of the impurity model, despite being much lighter and simpler than solving the original lattice model represents still an interacting quantum problem which on one hand requires some numerical treatment, but at the same time contains the full information about the local quantum dynamics.

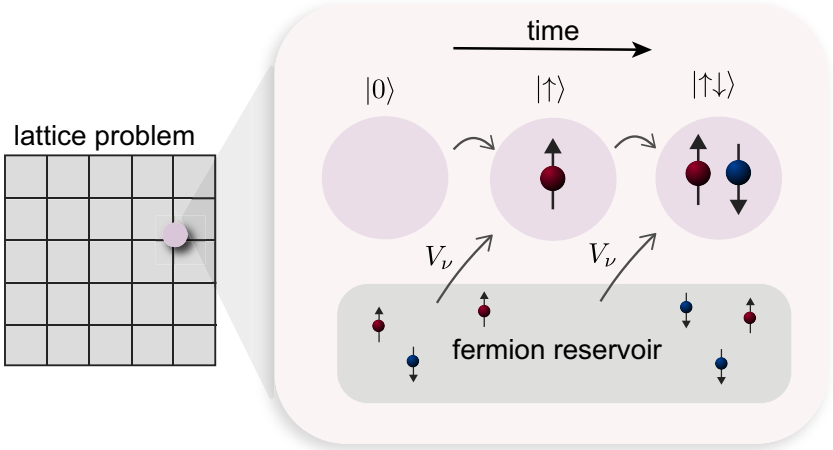

Figure 3.1: **Cartoon of Dynamical mean field theory** DMFT of strongly correlated lattice fermions. The full lattice (grey-green) is replaced with a single impurity atom coupled to a fermionic bath. Within this scheme the dynamics of fermions (red and blue) restricted to a central atom (in mauve) corresponds to fluctuation among different atomic states as a function of time. We illustrate the simplest case of an atom fluctuating between four states: empty atom $|0\rangle$, singly occupied atom $|\uparrow\rangle, |\downarrow\rangle$, doubly occupied $|\uparrow\downarrow\rangle$ where the sequence starts from an empty state followed by two transitions with transition probability V_ν in which the atom absorbs two fermions in total.

The natural observable to address this physics is the local single-particle Green's function, which describes the probability amplitude depending on time τ' to create a fremion with $\hat{c}^\dagger_{i\sigma}$ and destroy it at a later time τ with $\hat{c}_{i\sigma}$ on the same lattice site

$$G_{i\sigma}(\tau - \tau') \equiv -\langle \hat{c}_{i\sigma}(\tau)\hat{c}^\dagger_{i\sigma}(\tau')\rangle. \tag{3.21}$$

The self-consistency condition requires that the Green's function computed on the interacting site of the effective impurity model coincides with the local component of the lattice Green's function of the original lattice model computed with the local self-energy obtained by the impurity model.

$$G^{imp}(\omega) = G^{loc}(\omega) \equiv \sum_k \frac{1}{\omega - \epsilon_k + \mu - \Sigma^{imp}(\omega)} \tag{3.22}$$

in other words, the dynamics on the impurity model coincides with the local dynamics of a lattice model with a momentum-independent self-energy. This condition is exact in the limit of infinite coordination, and it can be used as an approximation in finite

dimension. The conditions for DMFT to be an accurate solution is the momentum-dependence of the self-energy. If a system has a self-energy which is weakly dependent on momentum, regardless of its dimensionality, DMFT will be an accurate approach.
In the next section we describe how the effective impurity model can be derived in the limit of infinite coordination [42]

3.3.1 *Cavity Method*

In this section we demonstrate that in the limit of infinite coordination one can obtain an effective local action involving the fermions only on a given site 0 which depends on a single function of time (or frequency) and we derive the above self-consistency condition.
The cavity method [42, 82] relies on the construction of a cavity that is singled out from the entire system, which in our case is a single lattice site $i = 0$.
We start the derivation by writing down the partition function Z of the Hubbard model using a functional integral formulation in terms of Grassmann variables. Note that Grassmann variables are not directly fermionic operators, though are very convenient for a fermionic functional formalism. The partition function reads

$$Z = \int \prod_{i,\sigma} \mathcal{D}[c^{\dagger}_{i\sigma}, c_{i\sigma}] e^{S}, \tag{3.23}$$

where we denote the Grassmann variables with c_σ and $c^{\dagger}_{\sigma}$ which trough out the thesis we usually use for fermionic annihilation and creation operator and the action S is

$$S = \int_0^\beta d\tau \Big(\sum_{ij,\sigma} c^{\dagger}_{i\sigma}(\partial_\tau - \mu) c_{j\sigma} + \sum_{ij,\sigma} t_{ij} c^{\dagger}_{i\sigma} c_{j\sigma} + U \sum_i n_{i\uparrow} n_{i\downarrow} \Big) \tag{3.24}$$

The goal is to obtain an effective theory for lattice site $i = 0$ therefore it is necessary to trace out the entire degrees of freedom of the system but the cavity, i.e

$$\frac{1}{Z_{\text{eff}}} e^{-S_{\text{eff}}[c^{\dagger}_{0\sigma} c_{0\sigma}]} = \frac{1}{Z} \int \prod_{i \neq 0,\sigma} \mathcal{D}[c^{\dagger}_{i\sigma}, c_{i\sigma}] e^{-S} \tag{3.25}$$

We can describe the system by dividing the contributions from the system in three terms. The selected cavity site is represented by an action $S_{i=0} \equiv S_0$, the rest of the lattice without the cavity site is denoted by $S^{(0)}$ and the coupling between the cavity and remaining lattice is ΔS. The three contributions are defined as follows

1. generic removed site $i = 0$

$$S_0 = \int_0^\beta d\tau S_0(\tau) = \int_0^\beta d\tau \sum_\sigma c^{\dagger}_{0\sigma}(\tau)(\partial_\tau - \mu) c_{0\sigma}(\tau) + U n_{0\uparrow}(\tau) n_{0\downarrow}(\tau), \tag{3.26}$$

2. cavity for site 0 (lattice without site 0)

$$S^{(0)} = \int_0^\beta d\tau \Big[\sum_{i\neq 0,\sigma} c^\dagger_{0\sigma}(\tau)(\partial_\tau - \mu)c_{0\sigma}(\tau) + U n_{i\uparrow}(\tau) n_{i\downarrow}(\tau) + \sum_{i,j\neq 0,\sigma} \Big(t_{ij} c^\dagger_{i\sigma}(\tau) c_{j\sigma}(\tau) + h.c \Big) \Big], \tag{3.27}$$

3. hybridization between site 0 and the cavity

$$\Delta S = \int_0^\beta d\tau \Delta S(\tau) = \int_0^\beta d\tau \sum_{i,\sigma} \Big(t_{i0} c^\dagger_{i\sigma}(\tau) c_{0\sigma}(\tau) + h.c \Big) \tag{3.28}$$

Inserting these in Eq. (3.25)we obtain

$$\frac{e^{-S_{eff}}}{Z_{eff}} = \frac{1}{Z} e^{-S_0} \int \prod_\sigma \mathcal{D}[c^\dagger_{i\sigma}, c_{i\sigma}] e^{-\Delta S} e^{-S^{(0)}} = \frac{Z^{(0)}}{Z} e^{S_0} \langle e^{-\Delta S} \rangle_{cavity} \tag{3.29}$$

where $Z^{(0)}$ is the partition function of the cavity and $\langle e^{-\Delta S} \rangle_{cavity}$ the expectation value of the hybridization action with respect to the cavity. We realize that $\frac{Z^{(0)}}{Z}$ is a renormalization since it doesn't contain any operators and we can write effective action as

$$S_{eff} = S_0 - \ln \left(\frac{Z^{(0)} Z_{eff}}{Z} \right) - \ln \left(\langle e^{-\Delta S} \rangle_{cavity} \right) \tag{3.30}$$

It remains to determine $\langle e^{-\Delta S} \rangle_{cavity}$ which we approximate by performing an expansion of the cavity degrees of freedom as

$$\exp\left(\int_0^\beta d\tau \Delta S(\tau) \right) \approx 1 + \int_0^\beta d\tau \Delta S(\tau) + \tfrac{1}{2!} \int_0^\beta d\tau_1 \int_0^\beta d\tau_2 [\mathcal{T}_\tau \Delta S(\tau_1) \Delta S(\tau_2)] + \dots$$

$$\begin{aligned} \langle e^{-\Delta S} \rangle_{cavity} &= \langle 1 - \int_0^\beta d\tau \Delta S(\tau) + \frac{1}{2!} \int_0^\beta d\tau_1 \int_0^\beta d\tau_2 [\mathcal{T}_\tau \Delta S(\tau_1) \Delta S(\tau_2)] \mp \dots \rangle_{cavity} \\ &= \left(\langle 1 \rangle_{cavity} - \int_0^\beta d\tau \langle \Delta S(\tau) \rangle_{cavity} + \frac{1}{2!} \int_0^\beta d\tau_1 \int_0^\beta d\tau_2 \langle \mathcal{T}_\tau \Delta S(\tau_1) \Delta S(\tau_2) \rangle_{cavity} \mp \dots \right) \\ &= \left(1 + \frac{1}{2!} \int_0^\beta d\tau_1 \int_0^\beta d\tau_2 \langle \mathcal{T}_\tau \Delta S(\tau_1) \Delta S(\tau_2) \rangle_{cavity} + \dots \right) \end{aligned} \tag{3.31}$$

where all odd order terms vanish because of the fermionic nature of Grassman variables. The effective action reads with this approximation

$$S_{eff} = S_0 - \ln \left(\frac{Z^{(0)} Z_{eff}}{Z} \right) - \ln \left(1 + \frac{1}{2!} \int_0^\beta d\tau_1 \int_0^\beta d\tau_2 \langle \mathcal{T}_\tau \Delta S(\tau_1) \Delta S(\tau_2) \rangle_{cavity} + \dots \right) \tag{3.32}$$

and we have to on the definition of $\Delta S(\tau_i)$ and express it an a more explicit form as follows

$$\begin{aligned}
\langle \mathcal{T}_\tau \Delta S(\tau_1)\Delta S(\tau_2)\rangle_{cavity} =& \left\langle \mathcal{T}_\tau \sum_{i,\sigma}\left(t_{i0}c^\dagger_{i\sigma}(\tau)c_{0\sigma}(\tau)+h.c\right)\times\sum_{j,\sigma}\left(t_{j0}c^\dagger_{j\sigma}(\tau)c_{0\sigma}(\tau)+h.c\right)\right\rangle_{cavity}\\
=& \left\langle \mathcal{T}_\tau \sum_{ij,\sigma}\Big(t_{i0}t_{0j}c^\dagger_{i\sigma}(\tau_1)c_{0\sigma}(\tau_1)c^\dagger_{0\sigma}(\tau_2)c_{j\sigma}(\tau_2)\right.\\
&\left.+\, t_{0i}t_{j0}c^\dagger_{0\sigma}(\tau_1)c_{i\sigma}(\tau_1)c^\dagger_{j\sigma}(\tau_2)c_{0\sigma}(\tau_2)\Big)\right\rangle_{cavity}\\
=& \sum_{ij,\sigma} t_{0i}t_{j0}c^\dagger_{0\sigma}(\tau_1)\langle c_{i\sigma}(\tau_1)c^\dagger_{j\sigma}(\tau_2)\rangle_{cavity}\, c_{0\sigma}(\tau_2)\\
=& \sum_{ij,\sigma} t_{0i}t_{j0}c^\dagger_{0\sigma}(\tau_1)G^{(0)}_{ij}(\tau_1-\tau_2)c_{0\sigma}(\tau_2).
\end{aligned} \tag{3.33}$$

where we introduced the cavity Greens function $G^{(0)}_{ij}(\tau_1-\tau_2)=\langle c_{i\sigma}(\tau_1)c^\dagger_{j\sigma}(\tau_2)\rangle_{cavity}$ and used $t_{i0}t_{0j}c^\dagger_{i\sigma}(\tau_1)c_{0\sigma}(\tau_1)c^\dagger_{0\sigma}(\tau_2)c_{j\sigma}(\tau_2)=t_{0i}t_{j0}c^\dagger_{0\sigma}(\tau_1)c_{i\sigma}(\tau_1)c^\dagger_{j\sigma}(\tau_2)c_{0\sigma}(\tau_2)$ which follows from relabeling.

It remains to take care of the higher order terms

$$\mathfrak{G}^{(0,n)}_C(\tau_1\dots\tau'_n)\equiv\sum_{i_1,\dots,j_n} G^{(0)}_{C,i_1,\dots,i_n,j_1,\dots j_n}(\tau_1,\dots\tau'_n)\prod_{l=1}^{n}t_{i_l,0}t_{0,j_l}. \tag{3.34}$$

$$S_{\text{eff}}=S_0+\sum_{n=1}^{\infty}\int d\tau_1\dots d\tau_n d\tau'_1\dots d\tau'_n c^\dagger_{0\sigma}(\tau_1)\dots c^\dagger_{0\sigma}(\tau_n)\mathfrak{G}^{(0,n)}_C(\tau_1\dots\tau'_n)c_{0\sigma}(\tau'_n)\dots c_{0\sigma}(\tau'_1) \tag{3.35}$$

This expression remains very complicated and its computation is tremendously expensive. However crucial simplifications take place in the limit fo large coordination. In particular the hopping amplitudes in the limit $d\to\infty$ need to scale as $t_{ij}\propto 1/\sqrt{d}^{|i-j|}$ in order to obtain a finite expectation value of the kinetic energy. Due to the scaling behavior of the hopping parameters the scaling of the single-particle Green's function is determined in large dimensions as $G_{ij\sigma}\propto d^{-\frac{1}{2}|\mathbf{r}_i-\mathbf{r}_j|}$, which is very important result, since it decides the behavior of the connected Green's function in the infinite d limit and moreover we anticipate it leads to the main result in DMFT on the self-energy which we postpone to a later point in this section. From the scaling behavior of the single particle Green's function follows

$$G^{(0)}_{C,i_1,\dots,i_n,j_1,\dots j_n}(\tau_1,\dots\tau'_n)\propto\prod_{l=1}^{n}\sqrt{d}^{|i_1-i_l|}\times\sqrt{d}^{|i_1-j_l|} \tag{3.36}$$

therefore the n-th order expansion scales as d^{n-2} [42] and therefore only the second order term survives in the infinite limit. We obtain for the effective action

$$S_{\text{eff}}=S_0+\int d\tau_1 d\tau_2\sum_\sigma c^\dagger_{0\sigma}(\tau_1)\sum_{ij}t_{i0}t_{0j}G^{(0)}_{ij}(\tau_1-\tau_2)c_{0\sigma}(\tau_2). \tag{3.37}$$

Inserting the definition of S_0 we obtain the so called *Weiss-field*:

$$\mathcal{G}_0^{-1}(\tau_1-\tau_2) = -(\frac{\partial}{\partial\tau_1}-\mu)\delta_{\tau_1\tau_2} - \sum_{ij} t_{i0}t_{0j}G_{ij}^{(0)}(\tau_1-\tau_2). \tag{3.38}$$

This is the first crucial simplification in the limit of large coordination. Among all the different correlators involving many particles, only the second-order contribution survives. All the effect of the rest of the lattice is described by a single function of imaginary time. Still, we have not yet concluded our task, because we still have no simple way to compute the Weiss field.
In order to simplify further the expression and to highlight the role of $\sum_{ij} t_{i0}t_{0j}G_{ij}^{(0)}(\tau_1-\tau_2)c_{0\sigma}(\tau_2)$ clearer we define the hybridization function

$$\Delta_\sigma(\tau_1-\tau_2) \equiv \sum_{ij} t_{i0}t_{0j}G_{ij}^{(0)}(\tau_1-\tau_2). \tag{3.39}$$

The hybridization function Δ_σ measures the coupling between the selected site and the rest of the lattice.
In the following it is more convenient to Fourier transform from imaginary time τ formulation to the fermionic Matsubara frequncy $i\omega_n$, where $\omega_n = (2n+1)\pi/\beta$. Applying a Fourier transformation $f(i\omega_n) = \int_0^\beta d\tau f(\tau)e^{+i\omega_n\tau}$, where f is a generic function, to the hybridization function $\Delta_\sigma(\tau)$ we obtain

$$\Delta_\sigma(i\omega_n) = \sum_{ij} t_{i0}t_{0j}G_{ij}^{(0)}(i\omega) = \sum_{ij} t_{i0}t_{0j}\left(G_{ij}(i\omega_n) - \frac{G_{i0}(i\omega_n)G_{0j}(i\omega_n)}{G_{00}(i\omega_n)}\right) \tag{3.40}$$

The last equality follows from an expansion of the Green's function with respect to the hopping parameter t and is valid for any lattice with an removed site. In order to evaluate the sum we express the lattice green's function using again a Fourier transformation, but now relating spatial dimension to the quasi-momentum $\mathbf{k}$ we obtain

$$G_{ij}(i\omega_n) = \frac{1}{L}\sum_{\mathbf{k}} e^{i\mathbf{k}(\mathbf{r}_i-\mathbf{r}_j)}G_{\mathbf{k}}(i\omega_n) = \frac{1}{L}\sum_{\mathbf{k}} e^{i\mathbf{k}(\mathbf{r}_i-\mathbf{r}_j)}\frac{1}{i\omega_n+\mu-\Sigma(i\omega_n)-\epsilon_{\mathbf{k}}}. \tag{3.41}$$

It is very important to note that the self-energy $\Sigma(i\omega_n)$ remains independent of $\mathbf{k}$ and the momentum dependence enters through the dispersion relation, which is simply the Fourier transform of the hopping parameter $\epsilon_{\mathbf{k}} = \sum_i t_{0i}e^{-i\mathbf{k}\mathbf{r}_i}$. The sum in the hybridization function has a very complicated structure thus we introduce a short notation to simplify the following steps. We define $\xi \equiv i\omega_n+\mu-\Sigma(i\omega_n)$ and establish recursively

$$g_0 = \frac{1}{L}\sum_{\mathbf{k}}\frac{1}{\xi-\epsilon_{\mathbf{k}}}, \tag{3.42}$$

$$g_1 = \frac{1}{L}\sum_{\mathbf{k}}\frac{\epsilon_{\mathbf{k}}}{\xi-\epsilon_{\mathbf{k}}} = \frac{1}{L}\sum_{\mathbf{k}}\left(\frac{\epsilon_{\mathbf{k}}-\xi}{\xi-\epsilon_{\mathbf{k}}}+\frac{\xi}{\xi-\epsilon_{\mathbf{k}}}\right) = -1+\xi g_0, \tag{3.43}$$

$$g_2 = \frac{1}{L}\sum_{\mathbf{k}} \frac{\epsilon_{\mathbf{k}}^2}{(\xi - \epsilon_{\mathbf{k}})} = \frac{1}{L}\sum_{\mathbf{k}} \left(\epsilon_{\mathbf{k}} \frac{\epsilon_{\mathbf{k}} - \xi}{\xi - \epsilon_{\mathbf{k}}} + \frac{\xi \epsilon_{\mathbf{k}}}{\xi - \epsilon_{\mathbf{k}}} \right) = -0 + \xi g_1, \tag{3.44}$$

where we used the completeness as $1/L\sum_{\mathbf{k}} = 1$ and $\sum_{\mathbf{k}} \epsilon_{\mathbf{k}} = 0$ Inserting the above relation in the hybridization function we obtain

$$\begin{aligned} \Delta_\sigma(i\omega_n) &= g_2 - \frac{g_1^2}{g_0} \\ &= \xi(-1 + \xi g_0) \\ &= i\omega_n + \mu - \Sigma_\sigma(i\omega_n) - G_{0\sigma}^{-1}(i\omega_n) \end{aligned} \tag{3.45}$$

giving us an equation for the Weiss field function $\mathcal{G}_{0\sigma}^{-1}(i\omega_n) = i\omega_n + \mu - \Delta_\sigma(i\omega_n)$, the expression

$$\mathcal{G}_{0\sigma}^{-1}(i\omega_n) = G_{0\sigma}^{-1}(i\omega_n) + \Sigma_\sigma(i\omega_n). \tag{3.46}$$

Therefore the Weiss field, which is the unknown quantity that defines the effective local theory can be written in terms of the local component of the lattice Green's function $G_{0\sigma}(i\omega_n)$ and of the local self-energy $\Sigma_\sigma(i\omega_n)$. In this sense, this is a self-consistency condition that connects the effective field to lattice properties computed within the DMFT approximation. If we observe that the Weiss field plays the role of the non-interacting Green's function of the effective theory, Eq. (3.46) coincides with Eq. (3.22)

3.4 SOLUTION OF THE EFFECTIVE LOCAL THEORY

In the previous section we derived the self-consistent DMFT equations which show that a self-consistent local theory can be defined. This effective problem corresponds to the Anderson impurity model (AIM), initially introduced to describe the Kondo-effect in solid state systems. The model Hamiltonian reads
The Hamiltonian expressing the impurity bath problem consists of three parts

$$\hat{\mathcal{H}}_{\text{AIM}} = \hat{\mathcal{H}}_{\text{loc}} + \hat{\mathcal{H}}_{\text{bath}} + \hat{\mathcal{H}}_{\text{hyb}} \tag{3.47}$$

where the local part $\hat{\mathcal{H}}_{\text{loc}}$ describes fermions on the site that we called so far o

$$\hat{\mathcal{H}}_{\text{loc}} = -\sum_{\sigma} \mu_\sigma \hat{n}_\sigma + U \hat{n}_\sigma \hat{n}_{\sigma'}, \tag{3.48}$$

while $\hat{\mathcal{H}}_{\text{bath}}$ describes a non-interacting bath

$$\hat{\mathcal{H}}_{\text{bath}} = \sum_{\nu\sigma} \epsilon_\nu^{\text{bath}} \hat{n}_{\nu\sigma}^{\text{bath}} \tag{3.49}$$

and the hybridizing Hamiltonian $\hat{\mathcal{H}}_{\text{hyb}}$ couples the impurity to the bath

$$\hat{\mathcal{H}}_{\text{hyb}} = \sum_{\nu\sigma} (V_\nu \hat{c}_\sigma^\dagger \hat{d}_{\nu,\sigma}^{\text{bath}} + \text{h.c.}), \tag{3.50}$$

where $\hat{c}^\dagger_\sigma$ is the fermionic creation operator of the impurity with the corresponding density $\hat{n}_\sigma = \hat{c}^\dagger_\sigma \hat{c}_\sigma$ and $\hat{d}^{bath}_{\nu,\sigma}$ is a destruction operator of fermion from the non-interacting bath where the bath levels are counted with ν. The fermions hybridize between bath and the impurity site via with the hybridization V_ν.
In the framework of impurity models, one usually defines the hybridization function

$$\Delta(i\omega_n) = \sum_\nu \frac{|V_\nu|^2}{i\omega_n - \epsilon^{bath}_\nu} \tag{3.51}$$

It is easy to see, integrating out the bath fermions, that the Hamiltonian (3.48) reproduces the local action we obtained within DMFT

$$\mathcal{G}_0^{-1}(i\omega_n) = i\omega_n + \mu - \Delta(i\omega_n). \tag{3.52}$$

If the above condition holds, the AIM is a Hamiltonian representation of the local action. Hence one can solve it to obtain the self-energy and the impurity Green's function, which are related by the Dyson equation of the impurity model

$$G^{-1}_{\sigma,imp}(i\omega_n) = \mathcal{G}_0^{-1}(i\omega_n) - \Sigma_{\sigma,imp}(i\omega_n) \tag{3.53}$$

So, the DMFT requires a calculation of the Green's function of the AIM subject to the self-consistency condition (3.22). The self-consistency can be imposed iteratively starting from a guess for the Weiss field, computing the Green's function and the self-energy. Then the self-consistency is used to generate a new Weiss field, hence a new AIM. The procedure is iterated until the Weiss field is unchanged in the iterations.
Various methods have been developed for solving the AIM. Among these, we can mention numerical approaches ranging from the Continuous Time Quantum Monte Carlo to Numerical Renormalization Group to seminalytical approaches like iterated perturbation theory and slave-particle methods.
In this thesis the AIM is solved with an exact diagonalization algorithm (ED) [75–77], a simple approach which works accurately in reasonable times. The idea is to truncate the sum over bath levels in the AIM to a finite number N_s which allows for a numerical diagonalization of the Hamiltonian in the finite Hilbert space. Using the Lanczos/Arnoldi diagonalization [75] one can solve the system for relatively large N_s obtaining the groundstate and, crucially in the DMFT context, the Green's function. In this thesis we limit ourselves to $T = 0$ calculations, which require only the knowledge of the groundstate of the AIM. The method can be extended to finite temperature, but this is extremely more expensive because it requires the calculation of a significant number of excited states. Given the complexity of the models treated in this thesis, we limit to $T = 0$.
In the exact diagonalization scheme, there is a further step in the iterative procedure. After a new Weiss field is obtained through the self-consistency, this has to be represented as a discrete Weiss field with N_s levels. This is achieved by minimizing a distance function between the target Weiss field and the discrete version
After the impurity quantities are computed at the iteration step l, the Weiss field $[\mathcal{G}^{-1}]^{l+1}$ through the self-consistency condition can be computed using the Anderson parameters by minimizing the function of the parameters defining the Anderson model [64]

$$\Gamma(\{V_{\nu\sigma}\},\{\epsilon_{\nu\sigma}\}) \equiv \left(\sum_n f(i\omega_n)|[\mathcal{G}(i\omega_n)] - i\omega_n + \mu - \Delta^{N_s}(i\omega_n)| \right), \tag{3.54}$$

where the function f can be chosen according to the problem at hand. This is the only numerical error made in the ED solution of the DMFT.

3.5 SPIN-MIXING FORMALISM

So far we restricted, as it happens in most derivations and discussione, the DMFT equations to the case where the Green's functions and the self-energies are diagonal in the spin index. In the presence of explicit spin-orbit coupling or in the case in which, for example, the S_x component of the spin is finite, we need a formalism which allows for non diagonal Green's functions in the spin state
The spin-mixing terms can be obtained considering an AIM that additionally contains the coupling of the impurity states to bath states with opposite spin. The AIM-Hamiltonian with spin-mixing takes the form

$$\hat{\mathcal{H}}^{\sigma\sigma'}_{\text{AIM}} = \hat{\mathcal{H}}_{\text{loc}} + \hat{\mathcal{H}}_{\text{bath}} + \hat{\mathcal{H}}^{\sigma\sigma'}_{\text{hyb}} \tag{3.55}$$

where again the local part $\hat{\mathcal{H}}_{\text{loc}}$ describes the fermions on the single site by the Hamiltonian

$$\hat{\mathcal{H}}_{\text{loc}} = -\sum_\sigma \mu_\sigma \hat{n}_\sigma + U\hat{n}_\sigma\hat{n}_{\sigma'}, \tag{3.56}$$

decoupled from the bath Hamiltonian $\hat{\mathcal{H}}_{\text{bath}}$ for the non-interacting bath splitted in spin-resolved Hamiltonians

$$\hat{\mathcal{H}}_{\text{bath}} = \sum_\sigma \hat{\mathcal{H}}^\sigma_{\text{bath}} = \sum_{\nu\sigma} \epsilon^{\text{bath}}_{\nu\sigma}\hat{n}^{\text{bath}}_{\nu\sigma} \tag{3.57}$$

and the hybridizing Hamiltonian $\hat{\mathcal{H}}^{\sigma\sigma'}_{\text{hyb}}$ couples the impurity with spin σ to the bath, also including the coupling to the other spin components σ' as follows

$$\hat{\mathcal{H}}^{\sigma\sigma'}_{\text{hyb}} = \sum_{\nu\sigma} (V^\sigma_\nu \hat{c}^\dagger_{0,\sigma}\hat{d}^{\text{bath}}_{\nu,\sigma} + W^{\sigma'}_\nu \hat{c}^\dagger_{0,\sigma}\hat{d}^{\text{bath}}_{\nu,\sigma'}), \tag{3.58}$$

where V^σ_ν is the conventional hybridization function, that is used in the traditional DMFT and the extension is due to he anomalous hybridization function $W^{\sigma'}_\nu$ which couples the impurity spin σ to bath states corresponding to other spin components σ'. Then the impurity action reads

$$S_{\text{eff}} = \int d\tau d\tau' \left(\hat{c}^\dagger_\uparrow(\tau), \cdots, \hat{c}^\dagger_\downarrow(\tau) \right) \hat{\mathcal{G}}^{-1}(\tau-\tau') \begin{pmatrix} \hat{c}_\uparrow(\tau') \\ \vdots \\ c_\downarrow(\tau') \end{pmatrix} + U \int d\tau \sum_{\sigma<\sigma'} \hat{n}_\sigma(\tau)\hat{n}_{\sigma'}(\tau), \tag{3.59}$$

containing the Weiss field matrix that extends to

$$\langle\sigma|\,\hat{\mathcal{G}}^{-1}(\tau)\,|\sigma'\rangle = \langle\sigma|\left[\delta(\tau)(\partial_\tau - \mu_\sigma) + \Delta_{\sigma\sigma}(\tau)\right]\delta_{\sigma\sigma'} + \Delta_{\sigma\sigma'}(\tau)\,|\sigma'\rangle\,. \tag{3.60}$$

The main extension lies in the hybridization functions which are not only spin-conserving anymore and they are defined as

$$\Delta_{\sigma\sigma}(i\omega_n) = \sum_{\mathbf{k}} \frac{|V_{\mathbf{k}}^{\sigma}|^2 + |W_{\mathbf{k}}^{\sigma'}|^2}{i\omega_n - \epsilon_{\mathbf{k}}^{\sigma}} \tag{3.61}$$

$$\Delta_{\sigma\sigma'}(i\omega_n) = \sum_{\mathbf{k}} \frac{V_{\mathbf{k}}^{\sigma}(W_{\mathbf{k}}^{\sigma})^*}{i\omega_n - \epsilon_{\mathbf{k}}^{\sigma}} + \frac{W_{\mathbf{k}}^{\sigma'}(V_{\mathbf{k}}^{\sigma'})^*}{i\omega_n - \epsilon_{\mathbf{k}}^{\sigma'}} \tag{3.62}$$

which satisfy the relation $(\Delta_{\sigma\sigma'}(i\omega_n))^* = \Delta_{\sigma'\sigma}(-i\omega_n)$.
The spin mixing introduces spin coupled Weiss-field, Green's function and self-energy, which means they are not diagonal in spin space anymore. Having a Green's function coupling different spin components gives the opportunity to compute quantities based on spin-flip operators. This is particularly useful in the case of computing the magnetic state with local in-plane magnetic ordering by $\langle \hat{S}_i^x \rangle = \langle \frac{1}{2}(\hat{S}^+ + \hat{S}^-) \rangle = \langle \frac{1}{2}(\hat{c}_\uparrow^\dagger \hat{c}_\downarrow + \hat{c}_\downarrow^\dagger \hat{c}_\uparrow) \rangle$ and $\langle \hat{S}_i^y \rangle = \langle \frac{1}{2i}(\hat{S}^+ - \hat{S}^-) \rangle = \langle \frac{1}{2i}(\hat{c}_\uparrow^\dagger \hat{c}_\downarrow - \hat{c}_\downarrow^\dagger \hat{c}_\uparrow) \rangle$. For computing the local out-of-plane magnetization $\langle \hat{S}_i^z \rangle = \frac{1}{2}(\hat{n}_{i\uparrow} - \hat{n}_{i\downarrow})$, where $\hat{n}_{i\sigma}$ is the local occupation at site i and spin $\sigma = \uparrow, \downarrow$ the spin mixing extension is not necessary. We use this part in Chapter 6. It is also possible to avoid this step, by computing all the quantities in the basis that diagonalized the spin-mixing term exploiting the fact that the rest of the Hamiltonian is invariant. We explain this part in Chapter 7 and Chapter 8

3.6 REAL-SPACE DMFT (RDMFT)

The derivation of DMFT that we presented assumes that every site is equivalent. However DMFT can be extended to inhomegeneous and/or finite size systems [43–46] generalizing the idea behind the method. In this section we briefly review how to implement real-space DMFT (RDMFT), which can be applied to the inhomogeneous finite systems we use in this thesis. For the extension to inhomogeneous systems we consider the Fermi Hubbard model with an arbitrary additional site-dependent local pontential ϵ_i and the Hamiltonian reads

$$\hat{\mathcal{H}} = \sum_{i,j,\sigma} t_{ij} \hat{c}_{i\sigma}^\dagger \hat{c}_{j\sigma} + U \sum_i \hat{n}_{i\uparrow}\hat{n}_{i\downarrow} + \sum_{i\sigma} (\mu - \epsilon_i)\hat{n}_{i\sigma} \tag{3.63}$$

The idea is to map every lattice site onto a different AIM (while in standard DMFT all the sites are considered equivalent). We recall that the AIM for the i-th site is described by the dynamical Weiss field $\mathcal{G}_{0i\sigma}(i\omega_n)$, where σ denotes the spin and $i\omega_n$ the frequency. In order to arrive at this point we start with the real space Dyson equation for a lattice system

$$(\hat{G}_\sigma^0)^{-1}(i\omega_n) - \hat{\Sigma}_\sigma(i\omega_n) = (\mu + i\omega_n)\hat{1} - \hat{t} - \hat{\epsilon} - \hat{\Sigma}_\sigma(i\omega_n) \tag{3.64}$$

with the unit operator $\hat{1}$, the hopping operator $\langle i|\,\hat{t}\,|j\rangle = -t_{ij}$ and the on-site energy operator $\langle i|\,\hat{\epsilon}\,|j\rangle = \delta_{ij}\epsilon_{ij}$, the self-energy operator $\langle i|\,\hat{\Sigma}_\sigma(i\omega_n\,|j\rangle = \Sigma_{ij\sigma}(i\omega_n)$. Following the derivation of the previous section the local Green's function for lattice site i

$$G_{ii\sigma}(\tau) = \frac{1}{Z_{\mathrm{eff}}^{(i)}} \int \prod_{\sigma'} Dc_{i\sigma'}^\dagger Dc_{i\sigma'} c_{i\sigma}(\tau) c_{i\sigma}^\dagger(0) e^{-S_{\mathrm{eff}}^{(i)}}. \tag{3.65}$$

Fortunately, the extension to real-space is straightforward since the derivation of the single-site DMFT equation did not rely on translation invariance and the arguments about the scaling of the connected Green's function and hopping amplitudes remain valid, hence the effective action for every lattice site reads

$$S_{\mathrm{eff}}^{(i)} = -\int d\tau d\tau' \sum_{\sigma} c_{i\sigma}^{\dagger}(\tau)\mathcal{G}_{\sigma}^{-1}(\tau-\tau')c_{i\sigma}(\tau') + U\int d\tau n_{i\uparrow}(\tau)n_{i\downarrow}(\tau), \tag{3.66}$$

with the site dependent Weiss field $\mathcal{G}_{\sigma}^{-1}(\tau-\tau')$:

$$\mathcal{G}_{i\sigma}^{-1}(\tau) = \delta(\tau)(-\partial_{\tau}+\mu-\epsilon_i) - \Delta_{i\sigma}(\tau), \tag{3.67}$$

where the hybridization function in Matsubara frequency follows the definition of the last section, but instead of a fixed lattice site $i = 0$, a site dependence is added and we obtain

$$\Delta_{i\sigma}(i\omega_n) = \sum_{mn} t_{im}t_{ni}G_{mn}^{(i)}(i\omega) = \sum_{mn} t_{mi}t_{in}\left(G_{mn}(i\omega_n) - \frac{G_{mi}(i\omega_n)G_{in}(i\omega_n)}{G_{ii}(i\omega_n)}\right), \tag{3.68}$$

the hopping amplitudes t_{mi}, t_{in} are in principle the same as before, but in order to highlight the extension to real-space we added the site dependent index, where $G_{mn}^{(i)}(i\omega)$ denotes the cavity Green's function without site i. The crucial assumption in DMFT is the restriction of the self-energy being purely local, which remains valid in the real-space extension though a site dependence is added, i. e

$$\Sigma_{ij\sigma}(i\omega_n) = \delta_{ij}\Sigma_{ii\sigma}(i\omega_n) \tag{3.69}$$

For closing the reals space self-consistency loop, the impurity self-energy of each AIM $\Sigma_{i\sigma}^{imp}(i\omega_n) = \mathcal{G}_{i\sigma}^{-1}(i\omega_n) - G_{ii\sigma}^{-1}(i\omega_n)$ has to be related to the lattice self-energy $\Sigma_{ii\sigma}(i\omega_n) = \Sigma_{i\sigma}(i\omega_n)$. For simplicity we capture all the purely local operators in one operator as

$$\hat{\xi}(i\omega_n) = (i\omega_n+\mu)\hat{1} - \hat{\epsilon} - \hat{\Sigma}(i\omega_n), \tag{3.70}$$

where $\hat{\xi}(i\omega_n) = \langle i|\,\hat{\xi}(i\omega_n)\,|j\rangle = \delta_{ij}\xi_{ij}(i\omega_n)$ is a diagonal matrix in real space. Then we obtain the matrix equation for the Green's function

$$\hat{G}_{\sigma}^{-1}(i\omega_n) = \hat{\xi}(i\omega_n) - \hat{t}. \tag{3.71}$$

The, rewriting the equation for the hybridization function (Eq. 3.68) as $\Delta_{i\sigma}(i\omega_n)G_{ii\sigma}(i\omega_n)$ we obtain

$$
\begin{aligned}
&G_{ii\sigma}(i\omega_n)\langle i|\hat{t}\hat{G}_\sigma(i\omega_n)\hat{t}|i\rangle - \langle i|\hat{t}\hat{G}_\sigma(i\omega_n)|i\rangle\langle i|\hat{G}_\sigma(i\omega_n)\hat{t}|i\rangle \\
&= G_{ii\sigma}(i\omega_n)\langle i|\left(\hat{\xi}(i\omega_n)-\hat{G}_\sigma^{-1}(i\omega_n)\right)\hat{G}_\sigma(i\omega_n)\left(\hat{\xi}(i\omega_n)-\hat{G}_\sigma^{-1}(i\omega_n)\right)|i\rangle \\
&-\langle i|\left(\hat{\xi}(i\omega_n)-\hat{G}_\sigma^{-1}(i\omega_n)\right)\hat{G}_\sigma(i\omega_n)|i\rangle\langle i|\hat{G}_\sigma(i\omega_n)\left(\hat{\xi}(i\omega_n)-\hat{G}_\sigma^{-1}(i\omega_n)\right)|i\rangle \\
&= G_{ii\sigma}(i\omega_n)\langle i|\left(\hat{\xi}(i\omega_n)\hat{G}_\sigma(i\omega_n)\hat{\xi}(i\omega_n)+\hat{G}_\sigma^{-1}(i\omega_n)\right)|i\rangle \\
&-\langle i|\left(\hat{\xi}(i\omega_n)\hat{G}_\sigma(i\omega_n)-\hat{1}\right)|i\rangle\langle i|\left(\hat{G}(i\omega_n)\hat{\xi}_\sigma(i\omega_n)-\hat{1}\right)|i\rangle \\
&= G_{ii\sigma}^2(i\omega_n)\xi_{ii\sigma}^2(i\omega_n) - G_{ii\sigma}(i\omega_n)\xi_{ii\sigma}(i\omega_n) \\
&- G_{ii\sigma}^2(i\omega_n)\xi_{ii\sigma}^2(i\omega_n) + 2G_{ii\sigma}(i\omega_n)\xi_{ii\sigma}(i\omega_n) - 1 \\
&= G_{ii\sigma}(i\omega_n)\xi_{ii\sigma}(i\omega_n) - 1
\end{aligned}
\tag{3.72}
$$

from which follows

$$
G_{ii\sigma}^{-1}(i\omega_n) = (i\omega_n+\mu)+\epsilon_i-\Delta_{i\sigma}(i\omega_n)-\Sigma_{i\sigma}(i\omega_n) \tag{3.73}
$$

the relation between the lattice Green's function $G_{ii\sigma}(i\omega_n)$ and the lattice self-energy $\Sigma_{i\sigma}(i\omega_n)$ to the Weiss-field of the AIM on the ith site $\mathcal{G}_{i\sigma}(i\omega_n) = i\omega_n+\mu-\epsilon_i-\Delta_{i\sigma}$ and we obtain that the Weiss fields are then coupled by the self-consistency condition which involves the real-space Green's function $G_{ij\sigma}(i\omega_n)$ as

$$
\mathcal{G}_{0i\sigma}^{-1}(i\omega_n) = G_{ii\sigma}^{-1}(i\omega_n)+\Sigma_{i\sigma}(i\omega_n), \tag{3.74}
$$

As a matter of fact RDMFT requires to solve as many independent AIM's as the number of sites in the original system. The various impurities are coupled by the self-consistency condition. The scaling of the approach with the number of sites is therefore very good, as it is basically linear except for the cost of inverting the Green's function of the finite system to construct the new Weiss fields.
In general the computational effort can be reduced using the lattice symmetry to reduce to the minimum the number of independent sites and introducing an AIM for each independent site. It is important to stress that a great advantage in using RDMFT for inhomogeneous systems is the ability to capture long-range correlation, such as magnetic long-range correlation (see Chapter 6) trough the self-consistency equations as well as accurate spatial spectral properties (see section 3.7.1.). It must be noted that, while DMFT is naturally formulated in the thermodynamic limit, RDMFT is limited to finite systems, even if the scaling with the number of sites is not prohibitive.

3.7 METAL TO INSULATOR TRANSITION AT HALF-FILLING

After establishing the DMFT approach we can discuss one of its most successful applications which is the study of the Mott transition in the Hubbard model. Within DMFT the full spectral function $A(\omega)$ is accessible and reveals information about the emergence of a Mott transition for example upon increasing the interaction U starting from a metallic solution. It is established that DMFT hosts two independent solutions, one metallic and the other insulating. The Mott insulating state exist for any $U > U_{c_1}$ and the metallic solution for $U < U_{c_2}$ depending from which site the transition is approached. From theoretical predictions based on numerical simulations and analytical calculations the relation $U_{c1} < U_{c2}$ [83] has been firmly established therefore a coexisting region including both phases can be found when $U_{c_1} < U < U_{c2}$. This indicates a first-order transition at $U = U_c$ that appears when free energies of each solution cross. However, the phase transition can be also of second order, when $U_c = U_{c2}$ as it was shown to happen for $T = 0$ in [83].

. We discuss the evolution of the density of states (DOS) (which is directly related to the spectral function) upon increasing U starting from the non-interacting solution $U = 0$ following the well known studies from Ref. [42, 84–86] . In the absence of interaction, i. e $U = 0$, the system displays a free fermion DOS characterized by the bare bandwidth W as shown in Fig 3.2 first panel. In this regime the fermions are completely delocalized and their spectral function mirrors the DOS of a band metal, with the chemical potential in the middle of the band. Adding interaction induces the formation of a coherent quasiparticle peak at the Fermi level accompanied by two particle-hole symmetric broad peaks which are a precursor of the Hubbard bands [1] best visible in the third panel highlighted in green of Fig 3.2 . The Hubbard bands reflect the incoherent excitations of the spectral function and are the analog of high-energy excitations induced by the Hubbard repulsion. The three-peak structure illustrates exactly the remarkable dual nature of fermions, which can be captured within DMFT. On the one hand the low energy properties reveal the formation of itinerant quasiparticles, on the other hand the high-energy excitations display the tendency to localize. Increasing U the quasi-

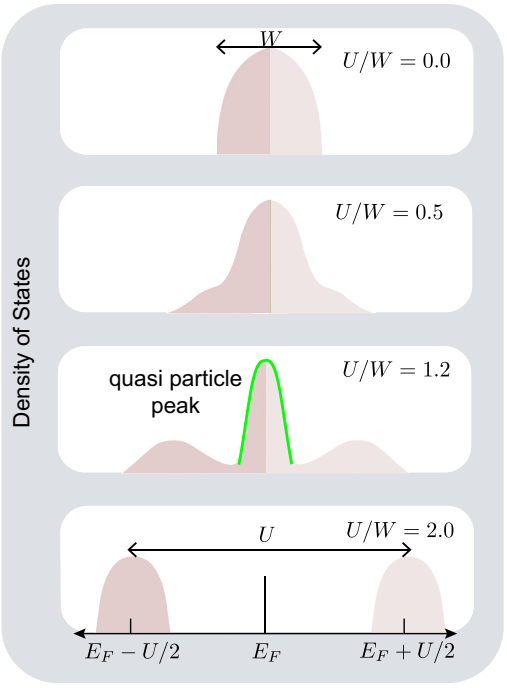

Figure 3.2: **Density of states DOS** of fermions upon increasing interaction. The spectral features across the metal to Mott insulator transition (top to bottom) for the half-filled Hubbard model suppressing magnetic solutions. The first three plots display a metallic peak while the last plot exhibits only the Hubbard bands revealing a Mott insulating state

particle peak becomes narrower and the dual character get more and more suppressed until a fully Mott localized state is reached at U_{c2} demonstrated by a large Mott gap of order U between the two Hubbard bands and no spectral weight.
When the quasi-particle peak is pronounced and the low energy physics is dominating the system is in a Fermi liquid regime in which the theory is valid. Sine within DMFT the self-energy is momentum independent, the width of the quasi-particle peak which is related to the quasi-particle weight $Z = (1 - \partial\Sigma/\partial\omega)^{-1}$ is nothing else but the effective mass enhancement $m/m* = Z^{-1}$, which diverges when the quasi-particle weight and therefore the peak vanishes. Thus in a Mott localized state the particles masses are infinitely heavy.

3.7.1 *Mott transition of Fermions in a three dimensional optical trap - a RDMFT example*

So far we discussed the basic Mott transition obtained within single-site DMFT in a rather general context focusing on the elementary feature how a MIT can be unveiled. In the following we discuss an example in the framework of cold atomic systems that was studied by means of RDFMT discussed in section 3.6. In the presence of a harmonic trap, which in cold atomic experiments can not be avoided, RDMFT comes in particularly handy to study the MIT under these conditions. In the presence of a harmonic trap the Hubbard model reads

$$\hat{\mathcal{H}} = -t \sum_{i,j,\sigma} \hat{c}^{\dagger}_{i\sigma}\hat{c}_{j\sigma} + U \sum_{i} \hat{n}_{i\uparrow}\hat{n}_{i\downarrow} + V_0 \sum_{i\sigma} \mathbf{r}_i^2 \hat{n}_{i\sigma} \tag{3.75}$$

where $\hat{c}^{\dagger}_{i\sigma}(\hat{c}_{i\sigma})$ denote the fermionic creation (annihilation) operator and $\hat{n}_{i\sigma} = \hat{c}^{\dagger}_{i\sigma}\hat{c}_{i\sigma}$ measures the density of a fermion with spin $\sigma =\uparrow,\downarrow$ at site i. t is the next-neighbour hopping amplitude and U is the effective on-site interaction. The presence of a harmonic trap breaks the translational invariance and the system becomes inhomogeneous, though rotational invariance remains, thus within RDMFT a reduced set of inequivalent sites see Eq. (3.64).
Generally, the harmonic potential allows for the existence of the metallic phase, the Mott insulating phase, and the band insulating phase next to each other due to the inhomogenous density distribution. The phase stable in each region is determined according to the density in the region of the trap, thereby also only one of these phases can be present. In the following discussion the authors of the presented work [13] used the NRG [87] to solve the AIM. They show a transition from a band insulator at $U/D = 0.0$, 1.0 and 2.0 with a large pleateau of density 2 to metal at $U/D = 3.0$ with an inhomogeneous distribution in the center of the trap to a Mott insulator at $U/D = 4.5$ with a density pleateau at 1. Here the reference energy is half-of the bandwidth $D = 6t$. Before the full Mott insulator is reached, the center of the trap exhibits a metallic region at $U/D = 4.0$ and a Mott pleateau at a larger radius. This set is supposed to simulate a realistic cold-atom experiment with a fixed number of particles $N = 2869$. The advantage of using RDMFT in this set up compared to using a local density approximation (Chapter 8) is the ability to study spatial dependence of the spectral function more accurately as demonstrated in Fig 3.4 since the lattice sites are coupled trough the self-consistency equations.

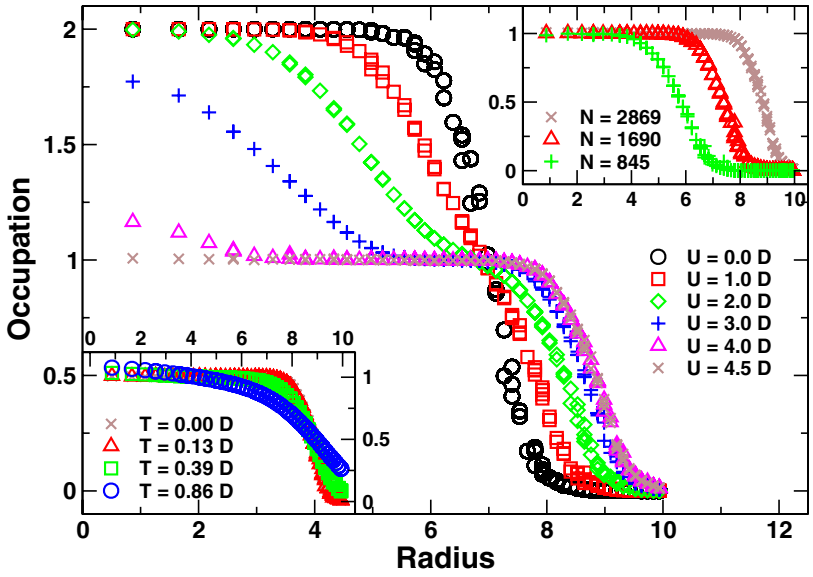

Figure 3.3: **Occupation distribution determined by harmonic potential** Main panel: The density distribution across the Band insulator to Metal to Mott insulator is shown upon increasing the interaction U Upper inset: dependence of the particle number in the system at $U/D = 4.5$ and $N = 2869$. Lower panel : temperature effect on $U/D = 4.5$ The figure is taken from Ref. [13]

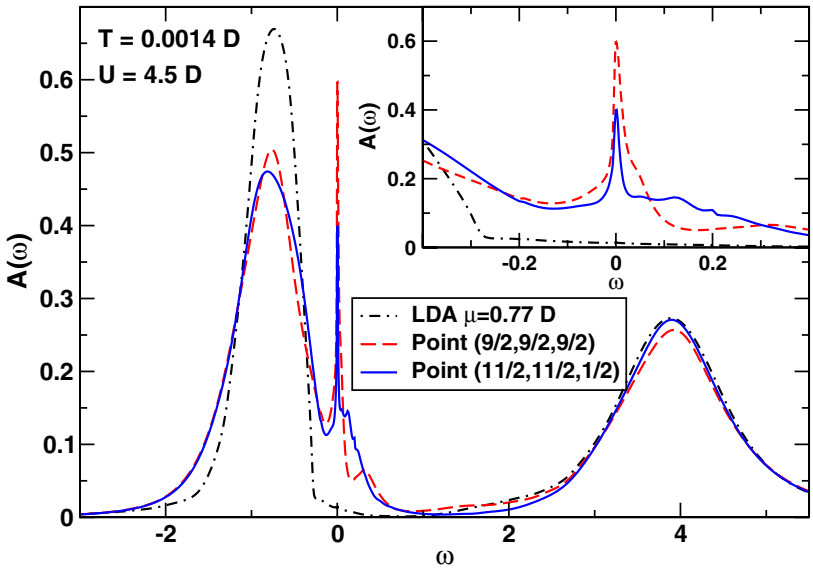

Figure 3.4: **Local spectral function at different positions in the trap** The spectral functions located a the boundary of the Mott pleateau is shown for two different points in trap computed within RDFMT. The grey dashed line shows the spectral function at a comparable point computed within LDA which does not display the same spectral features, though it reproduces the occupation accurately. The figure is taken from Ref. [13]

4

HUBBARD MODEL IN THE STRONG COUPLING LIMIT

4.1 INTRODUCTION

In the previous chapter we discussed a powerful method to treat strongly correlated system, which is able to capture the entire range of parameters, from weakly to strongly interacting regime. Remarkably, DMFT is able to capture local quantum fluctuations in a non-perturbative way and can give access to many intermediate phenomena. It can be very beneficial though, to estimate the physics in the strongly interacting by isolating the role of quantum fluctuation and determine to what extend they govern the physics. In this chapter we derive on the basis of strong coupling expansion [4, 47] an effective Hamiltonian for the Kane-Mele Hubbard model examined in Chapter 6. The Kane-Mele Hubbard model contains three terms, that are next-neighbor hopping, the Hubbard repulsion and an additional term, that acts as a spin-selective next-nearest neighbor hopping with a complex phase. This chapter is very technical and should just prepare for the next two chapters. We will discuss the model itself in Chapter 6, and focus here simply on a technical aspects of how to obtain an effective Hamiltonian.

4.2 STRONG COUPLING EXPANSION FOR THE KANE-MELE-HALDANE-HUBBARD MODEL

One of the simplest limits we can take is the strongly interacting regime, where U is very large compared to the other energy scales, i.e $|t_1/U| << 1$ and $|t_2/U| << 1$. The Hilbert space is restricted to a given energy manifold of the Hubbard-Kane-Mele model, where tunneling process are only happening virtually resulting in effectively interacting spins. We can start by defining projected fermion operators, so called Hubbard operators [4], which are projected creation and annihilation operators, where the diagonal operators are nothing but the projection operators $\hat{P}_{i\alpha}$ and the off-diagonal operators can viewed was transition operators from one state $|\alpha\rangle_i$ to state $|\beta\rangle_i$:

$$\hat{X}_i^{\beta\leftarrow\alpha} = |\beta\rangle_i \langle\alpha|_i , \quad \hat{X}_i^{\alpha\leftarrow\alpha} = |\alpha\rangle_i \langle\alpha|_i = \hat{P}_{i\alpha} \tag{4.1}$$

To give a concrete example the transition from an empty site i ($|0\rangle_i$)to a singly occupied site i with a spin ($|\sigma\rangle_i$) can be expressed by means of the Hubbard operators and the conventional annihilation and creation operators as

$$\hat{X}_i^{\sigma\leftarrow 0} = \hat{c}_{i\sigma}^{\dagger}(1 - \hat{n}_{i\bar{\sigma}}) \tag{4.2}$$

We also need to know the inverse expression, i. e how can we express the creation and annihilation operators in terms of the Hubbard operators. For this purpose we have

to realize the effect of applying either the creation operator to an unknown state. Let's take for example the creation operator for a spin-up fermion $\hat{c}^{\dagger}_{i\uparrow}$. The two states to which it is applicable is an empty site $|0\rangle_i$ and a site occupied by a spin-down fermion $|\downarrow\rangle_i$. Therefore this creation operator is a superposition of both Hubbard operators that express a transition to each of the two states:

$$\hat{c}^{\dagger}_{i\uparrow} = \hat{X}_i^{\uparrow\leftarrow 0} + \hat{X}_i^{\uparrow\downarrow\leftarrow\downarrow} \tag{4.3}$$

$$\hat{c}^{\dagger}_{i\downarrow} = \hat{X}_i^{\downarrow\leftarrow 0} - \hat{X}_i^{\downarrow\uparrow\leftarrow\uparrow} \tag{4.4}$$

due to the convention $\hat{c}^{\dagger}_{i\uparrow}\hat{c}^{\dagger}_{i\downarrow}|0\rangle_i = -\hat{c}^{\dagger}_{i\downarrow}\hat{c}^{\dagger}_{i\uparrow}|0\rangle_i = |\uparrow\downarrow\rangle_i$.
then the general formula is

$$\begin{aligned}\hat{c}^{\dagger}_{i\sigma} &= \hat{X}_i^{\sigma\leftarrow 0} + \mathrm{sgn}(\sigma)\hat{X}_i^{\sigma\bar{\sigma}\leftarrow\bar{\sigma}} \\ \hat{c}_{i\sigma} &= \hat{X}_i^{0\leftarrow\sigma} + \mathrm{sgn}(\sigma)\hat{X}_i^{\bar{\sigma}\leftarrow\sigma\bar{\sigma}}\end{aligned} \tag{4.5}$$

where $\mathrm{sgn}(\uparrow) = +1$ and $\mathrm{sgn}(\downarrow) = -1$. Moreover the product of two Hubbard operators is

$$\hat{X}_i^{\gamma\leftarrow\delta}\hat{X}_i^{\beta\leftarrow\alpha} = \delta_{\delta\beta}\hat{X}_i^{\gamma\leftarrow\beta}\hat{X}_i^{\beta\leftarrow\alpha} = \delta_{\delta\beta}\hat{X}_i^{\gamma\leftarrow\alpha} \tag{4.6}$$

and the commutation relation is

$$\begin{aligned}[\hat{X}_i^{\gamma\leftarrow\delta}, \hat{X}_j^{\beta\leftarrow\alpha}] &= \delta_{ij}\left(\hat{X}_i^{\gamma\leftarrow\delta}\hat{X}_j^{\beta\leftarrow\alpha} - \hat{X}_j^{\beta\leftarrow\alpha}\hat{X}_i^{\gamma\leftarrow\delta}\right) \\ &= \delta_{ij}\left(\delta_{\delta\beta}\hat{X}_i^{\gamma\leftarrow\alpha} - \delta_{\alpha\gamma}\hat{X}_i^{\beta\leftarrow\delta}\right).\end{aligned} \tag{4.7}$$

Now having established these relations we can express the Hamiltonians in terms of the new operators.

$$\begin{aligned}\hat{\mathcal{H}}_t^{+} = -\sum_i\sum_\sigma \mathrm{sgn}(\sigma)\Bigg(&t_1\sum_\delta\left(\hat{X}_i^{\sigma\bar{\sigma}\leftarrow\bar{\sigma}}\hat{X}_{i+\delta}^{0\leftarrow\sigma} + \hat{X}_{i+\delta}^{\sigma\bar{\sigma}\leftarrow\bar{\sigma}}\hat{X}_i^{0\leftarrow\sigma}\right) \\ &+ t_2\sum_\eta\left(\alpha_\sigma e^{if(\eta)}\hat{X}_i^{\sigma\bar{\sigma}\leftarrow\bar{\sigma}}\hat{X}_{i+\eta}^{0\leftarrow\sigma} + \alpha_\sigma e^{-if(\eta)}\hat{X}_{i+\eta}^{\sigma\bar{\sigma}\leftarrow\bar{\sigma}}\hat{X}_i^{0\leftarrow\sigma}\right)\Bigg)\end{aligned} \tag{4.8}$$

$$\begin{aligned}\hat{\mathcal{H}}_t^{-} = -\sum_i\sum_\sigma \mathrm{sgn}(\sigma)\Bigg(&t_1\sum_\delta\left(\hat{X}_i^{\sigma\leftarrow 0}\hat{X}_{i+\delta}^{\bar{\sigma}\leftarrow\sigma\bar{\sigma}} + \hat{X}_{i+\delta}^{\sigma\leftarrow 0}\hat{X}_i^{\bar{\sigma}\leftarrow\sigma\bar{\sigma}}\right) \\ &+ t_2\sum_\eta\left(\alpha_\sigma e^{if(\eta)}\hat{X}_i^{\sigma\leftarrow 0}\hat{X}_{i+\eta}^{\bar{\sigma}\leftarrow\sigma\bar{\sigma}} + \alpha_\sigma e^{-if(\eta)}\hat{X}_{i+\eta}^{\sigma\leftarrow 0}\hat{X}_i^{\bar{\sigma}\leftarrow\sigma\bar{\sigma}}\right)\Bigg)\end{aligned} \tag{4.9}$$

$$\begin{aligned}\hat{\mathcal{H}}_t^{0} = &-\sum_i\sum_\sigma\left(t_1\sum_\delta\hat{X}_i^{\sigma\leftarrow 0}\hat{X}_{i+\delta}^{0\leftarrow\sigma} + t_2\sum_\eta\alpha_\sigma e^{if(\eta)}\hat{X}_i^{\sigma\leftarrow 0}\hat{X}_{i+\eta}^{0\leftarrow\sigma} + h.c\right) \\ &-\sum_i\sum_\sigma\left(t_1\sum_\delta\hat{X}_i^{\sigma\bar{\sigma}\leftarrow\bar{\sigma}}\hat{X}_{i+\delta}^{\bar{\sigma}\leftarrow\sigma\bar{\sigma}} + t_2\sum_\eta\alpha_\sigma e^{if(\eta)}\hat{X}_i^{\sigma\bar{\sigma}\leftarrow\bar{\sigma}}\hat{X}_{i+\delta}^{\bar{\sigma}\leftarrow\sigma\bar{\sigma}} + h.c\right)\end{aligned} \tag{4.10}$$

Now we can write the full Hamiltonian in terms of the above sub-Hamiltonians

$$\hat{\mathcal{H}} = \hat{\mathcal{H}}_U + \hat{\mathcal{H}}_t^+ + \hat{\mathcal{H}}_t^- + \hat{\mathcal{H}}_t^0 \tag{4.11}$$

Performing a canonical transformation [47] that should achieve to disconnect different subbands

$$\hat{\mathcal{H}}^{\star_1} = e^{i\hat{S}^{(1)}} \hat{\mathcal{H}} e^{-i\hat{S}^{(1)}} \tag{4.12}$$

up to second order processes involving two sites we have the conventional generator, where double occupied state is used as an intermediate step

$$\hat{S}^{(1)} = \frac{i}{U}(\hat{\mathcal{H}}_t^+ - \hat{\mathcal{H}}_t^-) \tag{4.13}$$

the commutators from the expansion we have to evaluate are

$$i[\hat{S}^{(1)}, \mathcal{H}_t^+ + \hat{\mathcal{H}}_t^-] = \frac{2}{U}[\hat{\mathcal{H}}_t^+, \hat{\mathcal{H}}_t^-] \tag{4.14}$$

$$i[\hat{S}^{(1)}, \hat{\mathcal{H}}_t^0] = \frac{1}{U}\left([\hat{\mathcal{H}}_t^+, \hat{\mathcal{H}}_t^0] + [\hat{\mathcal{H}}_t^0, \hat{\mathcal{H}}_t^-]\right) \tag{4.15}$$

$$\frac{i^2}{2}[\hat{S}^{(1)}, [\hat{S}^{(1)}, \hat{\mathcal{H}}_U]] = -\frac{1}{U}[\hat{\mathcal{H}}_t^+, \hat{\mathcal{H}}_t^-] \tag{4.16}$$

We have to evaluate these commutators.

4.2.1 *Homogeneous system at half-filling*

The only term that can contribute is $(\hat{\mathcal{H}}_t^-, \hat{\mathcal{H}}_t^+)$, since we can not decrease the number of double occupied sites any further under projection. With this we can write the commutator for pair contributions as

$$
\begin{aligned}
&[\hat{\mathcal{H}}^+_t, \hat{\mathcal{H}}^-_t]_2 = [\hat{\mathcal{H}}^+_{t_1}, \hat{\mathcal{H}}^-_{t_1}]_2 + [\hat{\mathcal{H}}^+_{t_2}, \hat{\mathcal{H}}^-_{t_2}]_2 \\
=& -2t_1^2 \sum_i \sum_\delta \sum_{\sigma\sigma'} \mathrm{sgn}(\sigma)\mathrm{sgn}(\sigma') \left(\hat{X}_i^{\sigma'\leftarrow 0} \hat{X}_{i+\delta}^{\bar{\sigma}'\leftarrow\sigma'\bar{\sigma}'} \hat{X}_{i+\delta}^{\sigma\bar{\sigma}\leftarrow\bar{\sigma}} \hat{X}_i^{0\leftarrow\sigma} \right) \\
& -2t_2^2 \sum_i \sum_\eta \sum_{\sigma\sigma'} \mathrm{sgn}(\sigma)\mathrm{sgn}(\sigma') \left(\alpha_\sigma \alpha_{\sigma'} \hat{X}_i^{\sigma'\leftarrow 0} \hat{X}_{i+\eta}^{\bar{\sigma}'\leftarrow\sigma'\bar{\sigma}'} \hat{X}_{i+\eta}^{\sigma\bar{\sigma}\leftarrow\bar{\sigma}} \hat{X}_i^{0\leftarrow\sigma} \right) \\
=& -2t_1^2 \sum_i \sum_\delta \sum_{\sigma\sigma'} \mathrm{sgn}(\sigma)\mathrm{sgn}(\sigma') \left(\delta_{\sigma\sigma'} \hat{X}_i^{\sigma'\leftarrow\sigma} \hat{X}_{i+\delta}^{\bar{\sigma}'\leftarrow\bar{\sigma}} + \delta_{\sigma\bar{\sigma}'} \hat{X}_i^{\sigma'\leftarrow\sigma} \hat{X}_{i+\delta}^{\bar{\sigma}'\leftarrow\bar{\sigma}} \right) \\
& -2t_2^2 \sum_i \sum_\eta \sum_{\sigma\sigma'} \mathrm{sgn}(\sigma)\mathrm{sgn}(\sigma') \alpha_\sigma \alpha_{\sigma'} \left(\delta_{\sigma\sigma'} \hat{X}_i^{\sigma'\leftarrow\sigma} \hat{X}_{i+\eta}^{\bar{\sigma}'\leftarrow\bar{\sigma}} + \delta_{\sigma\bar{\sigma}'} \hat{X}_i^{\sigma'\leftarrow\sigma} \hat{X}_{i+\eta}^{\bar{\sigma}'\leftarrow\bar{\sigma}} \right) \\
=& -2 \sum_i \sum_\sigma \left(t_1^2 \sum_\delta \hat{X}_i^{\sigma\leftarrow\sigma} \hat{X}_{i+\delta}^{\bar{\sigma}\leftarrow\bar{\sigma}} + t_2^2 \sum_\eta \hat{X}_i^{\sigma\leftarrow\sigma} \hat{X}_{i+\eta}^{\bar{\sigma}\leftarrow\bar{\sigma}} \right) \\
& +2 \sum_i \sum_\sigma \left(t_1^2 \sum_\delta \hat{X}_i^{\bar{\sigma}\leftarrow\sigma} \hat{X}_{i+\delta}^{\sigma\leftarrow\bar{\sigma}} - t_2^2 \sum_\eta \hat{X}_i^{\bar{\sigma}\leftarrow\sigma} \hat{X}_{i+\eta}^{\sigma\leftarrow\bar{\sigma}} \right) \\
=& +2t_1^2 \sum_i \sum_\delta \left(\hat{S}_i^+ \hat{S}_{i+\delta}^- + \hat{S}_i^- \hat{S}_{i+\delta}^+ + 2\hat{S}_i^z \hat{S}_{i+\delta}^z + \frac{\hat{n}_i \hat{n}_{i+\delta}}{2} \right) \\
& -2t_2^2 \sum_i \sum_\eta \left(\hat{S}_i^+ \hat{S}_{i+\eta}^- + \hat{S}_i^- \hat{S}_{i+\eta}^+ - 2\hat{S}_i^z \hat{S}_{i+\eta}^z - \frac{\hat{n}_i \hat{n}_{i+\eta}}{2} \right) \\
&= +4t_1^2 \sum_i \sum_\delta \left(\mathbf{S}_i \mathbf{S}_{i+\delta} + \frac{\hat{n}_i \hat{n}_{i+\delta}}{2} \right) - 4t_2^2 \sum_i \sum_\eta \left(\hat{S}_i^x \hat{S}_{i+\eta}^x + \hat{S}_i^y \hat{S}_{i+\eta}^y - 2\hat{S}_i^z \hat{S}_{i+\eta}^z - \frac{\hat{n}_i \hat{n}_{i+\eta}}{2} \right)
\end{aligned}
\tag{4.17}
$$

where we used the definitions

- $\sum_\sigma \hat{X}_i^{\sigma\leftarrow\sigma} \hat{X}_j^{\bar{\sigma}\leftarrow\bar{\sigma}} = -2\left(\hat{S}_i^z \hat{S}_j^z - \frac{\hat{n}_i \hat{n}_j}{4}\right)$ (diagonal)
- $\sum_\sigma \hat{X}_i^{\bar{\sigma}\leftarrow\sigma} \hat{X}_j^{\sigma\leftarrow\bar{\sigma}} = \hat{S}_i^+ \hat{S}_j^- + \hat{S}_i^- \hat{S}_j^+$ (off-diagonal)

Note that here in the next-nearest neighbor contribution the phase $e^{if(\eta)}$ from $\hat{\mathcal{H}}^-_{t_2}$ cancels with the phase $e^{-if(\eta)}$ from $\hat{\mathcal{H}}^+_{t_2}$.
Now we want to include three-site terms at half-filling for which we need to go in higher order in the expansion

$$
\hat{\mathcal{H}}^\star = e^{i\hat{S}^\star} \hat{\mathcal{H}} e^{-i\hat{S}^\star}, \tag{4.18}
$$

where

$$
\begin{aligned}
i\hat{S}^\star &= i\hat{S}^{(1)} + i\hat{S}^{(2)} \\
&= \frac{1}{U}(\hat{\mathcal{H}}^+_t - \hat{\mathcal{H}}^-_t) + \frac{1}{U^2}\left([\hat{\mathcal{H}}^+_t, \hat{\mathcal{H}}^0_t] + [\hat{\mathcal{H}}^-_t, \hat{\mathcal{H}}^0_t] \right)
\end{aligned}
\tag{4.19}
$$

inserting in the Hamiltonian we get

$$
\hat{\mathcal{H}}^{\star 2} = \hat{\mathcal{H}} + i[\hat{S}^\star, \hat{\mathcal{H}}] + \frac{i^2}{2}[\hat{S}^\star, [\hat{S}^\star, \hat{\mathcal{H}}]] + \dots \tag{4.20}
$$

$$i[\hat{S}^{(2)}, \hat{\mathcal{H}}_U] = -\frac{1}{U}[(\hat{\mathcal{H}}_t^+ - \hat{\mathcal{H}}_t^-), \hat{\mathcal{H}}_t^0] \tag{4.21}$$

$$i[\hat{S}^{(2)}, \mathcal{H}_t^+ + \mathcal{H}_t^-] = \frac{2}{U^2}\hat{\mathcal{H}}_t^-\hat{\mathcal{H}}_t^0\hat{\mathcal{H}}_t^+ \pm \dots \tag{4.22}$$

with $\dots$ we denote other terms which do not contribute at half-filling involving three-sites, as well as this term $i[\hat{S}^{(2)}, \hat{\mathcal{H}}_t^0]$ which is why we don't compute it. The following term $\frac{i^2}{2}[\hat{S}^{(2)}, [\hat{S}^{(2)}, \hat{\mathcal{H}}_U]]$ is of order $1/U^3$ and we neglect it. However mixed terms are of order $1/U^2$ and we need to compute these

$$\begin{aligned}&\frac{i^2}{2}\Big([\hat{S}^{(1)}, [\hat{S}^{(2)}, \hat{\mathcal{H}}_U]] + [\hat{S}^{(2)}, [\hat{S}^{(1)}, \hat{\mathcal{H}}_U]]\Big)\\ &= \frac{1}{2U^2}(-3\hat{\mathcal{H}}_t^-\hat{\mathcal{H}}_t^0\hat{\mathcal{H}}_t^+ \pm \dots)\end{aligned} \tag{4.23}$$

summing the relevant terms up, we obtain for three site terms at half-filling

$$\frac{1}{2U^2}\hat{\mathcal{H}}_t^-\hat{\mathcal{H}}_t^0\hat{\mathcal{H}}_t^+ \tag{4.24}$$

We can express $\hat{\mathcal{H}}_t^-\hat{\mathcal{H}}_t^0\hat{\mathcal{H}}_t^+$ in terms of clock-wise and anti-clockwise hopping processes. This is necessary because during a clock-wise and an anti-clockwise process a phase is picked up, which is different with respect to the process.

$$\hat{\mathcal{H}}_t^-\hat{\mathcal{H}}_t^0\hat{\mathcal{H}}_t^+ = \hat{\mathcal{P}}^{\circlearrowleft} + (\hat{\mathcal{P}}^{\circlearrowleft})^\dagger \tag{4.25}$$

$$\begin{aligned}\hat{\mathcal{P}}_1^{\circlearrowleft} =& \sum_{ijk}\sum_{\sigma_1,\sigma_2,\sigma_3}\Big(\mathrm{sgn}(\sigma_3)\mathrm{sgn}(\sigma_1)t_{kj}t_{ik}t_{ji}\hat{X}_k^{\sigma_3\leftarrow 0}\hat{X}_j^{\bar{\sigma}_3\leftarrow\sigma_3\bar{\sigma}_3}\hat{X}_i^{\sigma_2\leftarrow 0}\hat{X}_k^{0\leftarrow\sigma_2}\hat{X}_j^{\sigma_1\bar{\sigma}_1\leftarrow\bar{\sigma}_1}\hat{X}_i^{0\leftarrow\sigma_1}\Big)\\ =& -t_1^2t_2\sum_{ijk}\sum_{\sigma_1,\sigma_2,\sigma_3}\alpha_{\sigma_2}e^{i\Phi_{ik}}\mathrm{sgn}(\sigma_3)\mathrm{sgn}(\sigma_1)\hat{X}_i^{\sigma_2\leftarrow\sigma_1}\hat{X}_j^{\bar{\sigma}_3\leftarrow\bar{\sigma}_1}\hat{X}_k^{\sigma_3\leftarrow\sigma_2}\\ &- t_2^3\sum_{ijk}\sum_{\sigma_1,\sigma_2,\sigma_3}\alpha_{\sigma_2}e^{i\Phi_{kj}}e^{i\Phi_{ik}}e^{i\Phi_{ji}}\hat{X}_i^{\sigma_2\leftarrow\sigma_1}\hat{X}_j^{\bar{\sigma}_3\leftarrow\bar{\sigma}_1}\hat{X}_k^{\sigma_3\leftarrow\sigma_2}\end{aligned} \tag{4.26}$$

$$\begin{aligned}\hat{\mathcal{P}}_2^{\circlearrowleft} =& \sum_{ijk}\sum_{\sigma_1,\sigma_2,\sigma_3}\Big(\mathrm{sgn}(\sigma_3)\mathrm{sgn}(\sigma_1)t_{ik}t_{kj}t_{ji}\hat{X}_i^{\sigma_3\leftarrow 0}\hat{X}_k^{\bar{\sigma}_3\leftarrow\sigma_3\bar{\sigma}_3}\hat{X}_k^{\sigma_2\bar{\sigma}_2\leftarrow\bar{\sigma}_2}\hat{X}_j^{\bar{\sigma}_2\leftarrow\sigma_2\bar{\sigma}_2}\hat{X}_j^{\sigma_1\bar{\sigma}_1\leftarrow\bar{\sigma}_1}\hat{X}_i^{0\leftarrow\sigma_1}\Big)\\ =& -t_1^2t_2\sum_{ijk}\sum_{\sigma_1,\sigma_2,\sigma_3}e^{i\Phi_{ik}}\mathrm{sgn}(\sigma_1)\hat{X}_i^{\sigma_3\leftarrow\sigma_1}\hat{X}_j^{\bar{\sigma}_2\leftarrow\bar{\sigma}_1}\hat{X}_k^{\bar{\sigma}_3\leftarrow\bar{\sigma}_2}\\ &- t_2^3\sum_{ijk}\sum_{\sigma_1,\sigma_2,\sigma_3}e^{i\Phi_{ik}}e^{i\Phi_{kj}}e^{i\Phi_{ji}}\hat{X}_i^{\sigma_3\leftarrow\sigma_1}\hat{X}_j^{\bar{\sigma}_2\leftarrow\bar{\sigma}_1}\hat{X}_k^{\bar{\sigma}_3\leftarrow\bar{\sigma}_2}\end{aligned} \tag{4.27}$$

note that here $\mathrm{sgn}(\sigma_n)\cdot\alpha_{\sigma_n} = 1$, coming from the spin-orbit hopping.
Then we obtain

$$
\begin{aligned}
\hat{\mathcal{H}}_3^\star = & \frac{t_1^2 t_2}{U^2} \sum_{\langle ijk \rangle} \sin(\Phi_\triangle) \Big[2(\hat{S}_i^z + \hat{S}_j^z + \hat{S}_k^z) - 24 \hat{S}_i^z \hat{S}_j^z \hat{S}_k^z \\
& - 24 \Big(\hat{S}_i^z (\hat{S}_j^x \hat{S}_k^x + \hat{S}_j^y \hat{S}_k^y) + \hat{S}_k^z (\hat{S}_i^x \hat{S}_j^x + \hat{S}_i^y \hat{S}_j^y) - \hat{S}_j^z (\hat{S}_i^x \hat{S}_k^x + \hat{S}_i^y \hat{S}_k^y) \Big) \Big] \\
& \frac{t_2^3}{U^2} \sum_{\langle\langle ijk \rangle\rangle} \sin(\Phi_{\triangle_2}) \Big[2(\hat{S}_i^z + \hat{S}_j^z + \hat{S}_k^z) - 24 \hat{S}_i^z \hat{S}_j^z \hat{S}_k^z \\
& - 24 \Big(\hat{S}_i^z (\hat{S}_j^x \hat{S}_k^x + \hat{S}_j^y \hat{S}_k^y) + \hat{S}_k^z (\hat{S}_i^x \hat{S}_j^x + \hat{S}_i^y \hat{S}_j^y) - \hat{S}_j^z (\hat{S}_i^x \hat{S}_k^x + \hat{S}_i^y \hat{S}_k^y) \Big) \Big]
\end{aligned}
\tag{4.28}
$$

This effective spin-coupling term emerges from third-order processes, which at half-filling are significantly smaller than the second order terms in Eq. (4.2.1), yet in a challenging competition between next-neighbor and next-nearest neighbor as well as in-plane and out-of plane magnetic ordering state this term can determine the final magnetic state. For example the magnetic ordering discussed in Chapter 6 can be attributed to this term.

5

CONTROLLING AND INDUCING MAGNETISM IN THE HONEYCOMB LATTICE

5.1 INTRODUCTION

In this chapter and the following we discuss the first of the two main concepts we explored in the present thesis, namely the possibility to induce novel physics in honeycomb lattice system by tuning the trapping potential in order to confine the fermions in a finite region of space. The choice of the honeycomb lattice is mainly motivated by its relevance in solid-state physics, where it has been realized in a very clean way thanks to the discovery of graphene. Furthermore, the same lattice is a prototype for a nunber of important theoretical concepts.

Graphene [88, 89] is indeed nothing but a two-dimensional sheet of carbon atoms arranged on a honeycomb lattice which has attracted an unprecedented interest as it represents on one hand the realization of an almost ideal nontrivial quantum system, and at the same time it is characterized also by extraordinary mechanical, electronic, thermal, and transport properties [89, 90].

From a more theoretical perspective, the rise of graphene has increased the interest in the properties of quantum particles on the honeycomb lattice. One of the most elusive properties of solid-state graphene systems is magnetism. Infinite, or very large, graphene sheets do not show magnetic ordering [91], which is instead proposed and realized in *nanoscopic* structures composed by a small number of carbon atoms when the termination have a so-called zigzag pattern [92, 93]. However, the instability of zigzag edges severely limits the realization of magnetic graphene nanostructures and the first solid experimental evidence is very recent [94] Besides the synthesis of a variety of graphene-based systems, this has also pushed the community to devise quantum simulators of the honeycomb lattice using ultracold atoms [10, 49, 50, 95],which can access regimes which are not easily reached in solid-state systems. Graphene nanoflakes are promising candidates for magnetism [96, 97]. Their theoretical phase diagram is quite rich, and it is characterized by a strong competition between short-range antiferromagnetic (AF) and long-range ferromagnetic (FM) correlations. The former are particularly strong in insulating half-filled flakes with one fermion per site, while the latter emerge when the density is reduced and the carriers become more mobile. In principle this competition might be exploited to manipulate the magnetic ground state by, e.g., electrostatic [96, 98, 99] or chemical doping [100–102] and to engineer different kinds of spin filters [100, 101, 103–106]. This rich scenario is however so far largely unexplored owing to the technical difficulties to control the edges of solid-state graphene nanosystems.

5.2 MAGNETIC NANOFLAKES

In this chapter we model the system in terms of a finite two-dimensional honeycomb lattice

$$\hat{\mathcal{H}} = -t \sum_{\langle i,j\rangle,\sigma} (\hat{c}^{\dagger}_{i\sigma}\hat{c}_{j\sigma} + h.c) + U \sum_{i} \hat{n}_{i\uparrow}\hat{n}_{i\downarrow} \tag{5.1}$$

where $\hat{c}^{\dagger}_{i\sigma}$ ($\hat{c}_{i\sigma}$) denotes the creation (annihilation) operator for spin-1/2 fermions and $\hat{n}_{i\sigma}$ is the density operator at site i for the two spin states, labeled by $\sigma \in \{\uparrow,\downarrow\}$. $\hat{n}_i = \sum_\sigma \hat{n}_{i\sigma}$ is the total density on site i. t denotes the nearest-neighbor tunneling amplitude and$U$ the on-site repulsion.
The honeycomb lattice is generated by the vectors

$$\mathbf{a}_1 = \frac{a}{2}(1,\sqrt{3}), \quad \mathbf{a}_2 = \frac{a}{2}(3,-\sqrt{3}), \tag{5.2}$$

with length $\sqrt{3}a$ that is determined by the lattice spacing a. Further more we introduce the nearest neighbor vectors

$$\delta_1 = \frac{a}{2}(1,\sqrt{3}), \quad \delta_2 = \frac{a}{2}(1,-\sqrt{3}), \quad \delta_3 = a(-1,0), \tag{5.3}$$

from which we can construct the six next-nearest neighbour vectors

$$\eta_{1,2} = \pm\mathbf{a}_1, \quad \eta_{3,4} = \pm\mathbf{a}_2, \quad \eta_{5,6} = \pm(\mathbf{a}_2 - \mathbf{a}_1) \tag{5.4}$$

The reciprocal lattice vectors are

$$\mathbf{b}_1 = b(1,\sqrt{3}), \quad \mathbf{b}_2 = b(1,-\sqrt{3}), \tag{5.5}$$

where $b = 2\pi/3$.
On an infinite honeycomb lattice and at half-filling (one fermion per site) the model displays a quantum phase transition as a function of U/t from a Dirac semimetal to an antiferromagnetic insulator [107]. For large lattices, the onset of magnetism has been estimated at the critical interaction strength $U_c \simeq 3.87t$ [108] by means of numerically exact quantum Monte Carlo simulations. When the average density deviates from one fermion per site the system is typically metallic and it can show tendency towards ferromagnetism.
In this work we focus on small systems in which the translational invariance is broken and finite-size effects are relevant. In particular, the density will not be uniform throughout the system. In a picture where the local density influences the short-range magnetic ordering, one can have regions close to half-filling where AF ordering is favored, and regions with a different density where ferromagnetism can take over, leading to a potentially rich phase diagram.
In the solid state context it has been proposed that in small systems, AF spin ordering establishes at the boundaries, especially for zig-zag edges [93, 96, 98]. Ramarkably, theoretical [96] and experimental [109] studies suggest that the edges retain their magnetic moments up to room temperature.
In the following section we examine the magnetic state of a small graphene structure with zigzag edges in a symmetric shape that we call "nanoflake", at half-filling. The

hexagonal nanostructure we are going to investigate (see Fig 5.2) has a bipartite honeycomb lattice structure and consists of $L = 54$ lattice sites. The flake is C_3 rotationally symmetric which allows us to identify 6 inequivalent sites belonging to each of the two triangular sublattices, hence a total of $N_{ineq} = 12$ inequivalent sites. Treating the two sublattices as fully independent is crucial to allow a complete freedom to obtain either an AF or FM state, or a mixture of the two, depending on the competition of magnetic correlations.
We classify this nanoflake as 3N hexagonal nanoflake from the fact that we have 3 hexagons on the border in each C_6 rotational sector. Increasing the size of the flake and thereby the number of hexagons on the boundary would lead to the label $4N, 5N, \ldots$. In this section we focus on the 3N flake, but discuss in the following section also larger structures.

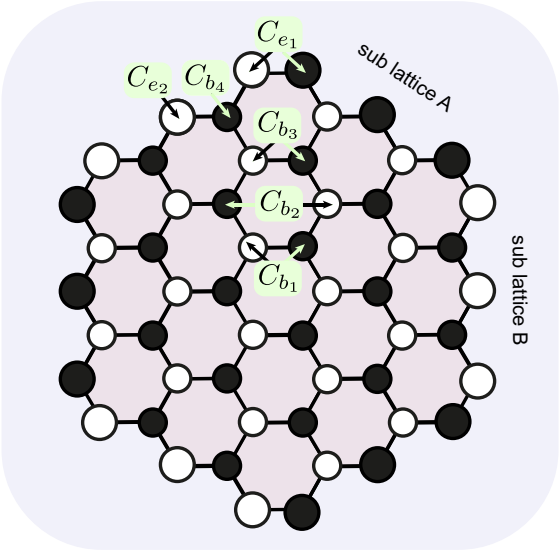

Figure 5.1: **Schematic illustration of a** 3N **nanoflake**. The picture dispalys a hexagonal graphene nanoflake with zigzag edges.The black (sub lattice A) and white (sub lattice B) sites highlight the bipartite lattice structure and the green labels distinguishes the inequivalent atoms per sublattice with C_{b_i} $i = 1, 4$ denoting bulk atoms and C_{e_j} $j = 1, 2$ identifies edge atoms. The actual number of inequivalent sites is completed by the rotational $\mathbf{C_3}$ symmetry.

Magnetic transition of a 3N *nanoflake*

In the following section we examine the properties of the zigzag nanoflake at half-filling (average density $\langle n \rangle = 1$) and focus on the onset of a magnetic state, in particular the AF ground state, including a comparison between the non magnetic solution and the magnetic solution.
In order to characterize the appearance of magnetic ordering in the flake, we plot the evolution as a function of U of the local z-axis magnetization $\langle \hat{S}^z_i \rangle = \hat{n}_{i\uparrow} - \hat{n}_{i\downarrow}$ for representative sites in the flake taken as the most "extreme" representative of different regions, namely C_{b_1} - the inner bulk site and C_{e_2} the zigzag edge site. The main difference between bulk and edge sites is their connectivity: While the bulk sites always have three neighbors the edge sites are only connected to two other sites. This makes

the edge sites more sensitive to the interaction effects than the bulk ones. In general terms, one expects the electronic correlations and their magnetic fingerprints to be stronger at the edges.

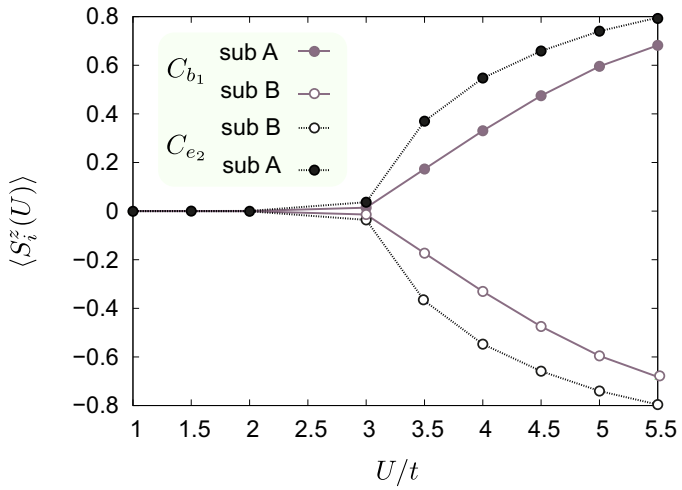

Figure 5.2: We plot the local magnetic moment $\langle S_i^z\rangle = \langle n_{i\uparrow} - n_{i\downarrow}\rangle$ for representative bulk C_{b_1} and edge C_{e_2} atoms and for each sublattice. With respect to bulk and edge the magnetic moment shows a clear dichotomy

The results are shown in Fig. 5.2, where we report the magnetization of the two mentioned sites on both sublattices. The other inequivalent sites are not shown, but they follow an AF pattern. Interestingly the onset of antiferromagnetism happens at a finite value of $U/t \approx 3.0$ at which all inequivalent sites simultaneously form magnetic moments, yet with different strength due to the connectivity we mentioned above. Therefore we observe a quantitative difference between bulk and edge atoms upon increasing the interaction until a fully compensated AF state is reached.
Since this thesis evolves around Mott transition and magnetism, we also examine the weak to strong coupling transition when suppressing the magnetic state. A good quantity to characterize this transition it the quasi-particle weight $Z = (1 - \Im\Sigma(i\omega_n)/\omega_n)^{-1}$, introduced in Chapter 3 which displays the quasiparticle bandwidth reduction by a factor Z. Therefore, when Z drops to zero the quasi particle picture breaks down and the particle localize. In the present case, Z actually depends on the site index as a consequence of the inhomogeneity.
In Fig. 5.2 we compare the local version of this quantity for the nonmagnetic and magnetic solution in the regime where the AF transition takes place for representative edge site, i.e C_{b_1} - the inner bulk site and C_{e_2} the zigzag edge site.
It is evident that the Z of the edge sites is significantly smaller than the bulk one, in agreement with our expectations. They also appear to vanish at different interaction strengths. While the PM solution shows, as expected, monotonically decreasing Z's, at the onset of AF, the Z of the magnetic solutions starts instead to grow, leading to a minimum. In the limit of very large U, the Z approaches 1. This is a well known results for bulk systems which we recover in our small cluster. In this specific case this also implies that for large U also the difference between bulk and edge tends to reduce.
These results also imply that Z is not a particularly helpful quantity to explore the onset of magnetism, what we wanted to demonstrate with the plot. The following analysis

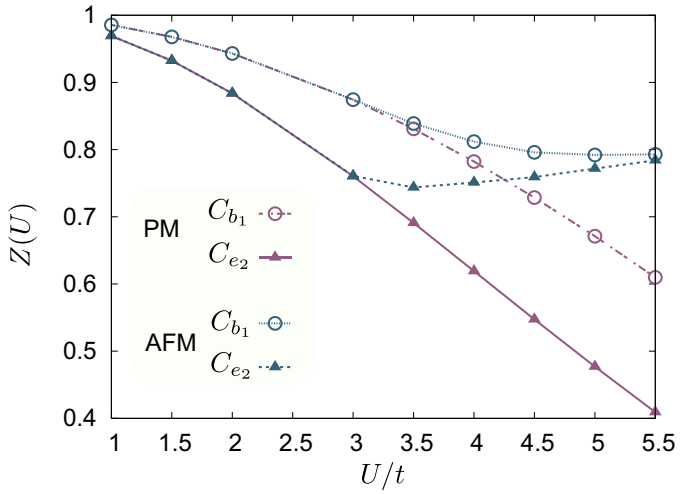

Figure 5.3: **Quasi particle weight $Z(U)$ for the bulk and edge atoms** for nonmagnetic (PM) and magnetic (AF) solutions. In the paramagnetic regime for increasing U the quasi-particle weight Z trends towards zero, signaling an insulating state. On the other hand the AF solution has always a finite Z which has a minimum at intermediate interactions.

about the nanostructures will not use Z anymore. For the sake of completeness, we also biefly discuss the behavior of the imaginary part of the self-energy $\Im\Sigma(i\omega_n)$ as function of Matsubara frequencies shown in Fig 5.2.

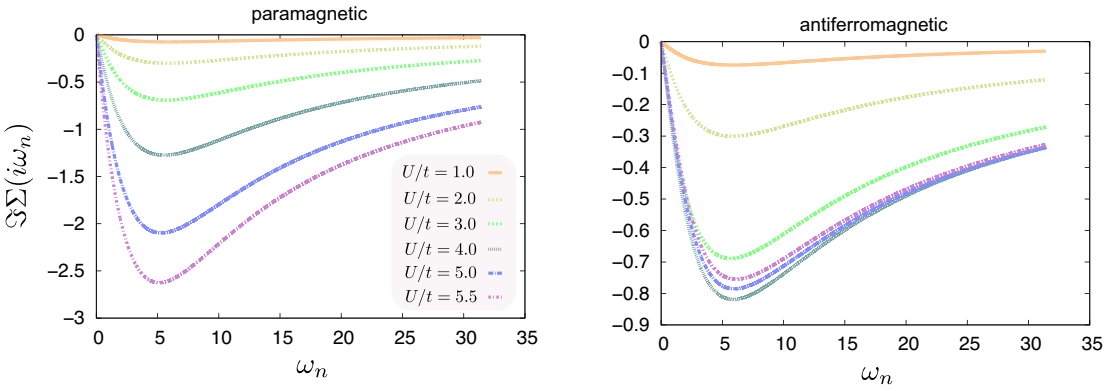

Figure 5.4: **Imaginary part of the self-energy as a function of Matsubara frequency** $\Im\Sigma(i\omega_n)$ is the imaginary part of the self-energy as a function of Matsubara frequency and corresponds to the quasi-particle weight in Fig 5.2 and 5.2. Left shows the PM solution and right the AF solution for selected interaction strength.

For weak interaction $U/t = 2.0$ Z is basically a constant line that doesn't change increasing the frequency, obviously the same for the AF and PM case. Across the PM Mott transition $\Im\Sigma(i\omega_n)$ decreases strongly followed by an increase that results in a tail. The pronounced change in this quantity leads to a large derivative which in turn causes Z to drop to zero. In the AF case the tendency is similar as in the PM case, for obvious reason, but after the transition point $\Im\Sigma(i\omega_n)$ shrinks again.
In order to identify the edge and bulk states of the flake we make use of the local and spin-resolved spectral function $A_{i\sigma}(\omega) = -\frac{1}{\pi}\Im G_{i\sigma}(\omega)$. Not only can it reveal the metallic or insulating nature of the system, but also shows us the imbalance between

spin-up and down-particles per site. In the PM case the spin-resolved spectral function is on top for each sub lattice and spin component and is different for the bulk and edge site. Allowing the magnetic solution we find very small spin-dependent effect at the interaction when the magnetic transition occurs (i.e at U/t=3.0), and the AF spectral function and the PM spectral function mainly coincide, up to some fluctuations as shown in Fig 5.2. The establishment of AF ordering can be directly witness at the spectral function, where the imbalance of the spin-components is clearly visible and opposite on the other sublattice. Moreover a large Mott gap is visible. Notice that despite both the edge and the bulk are both AF, their spectral properties are somewhat different.

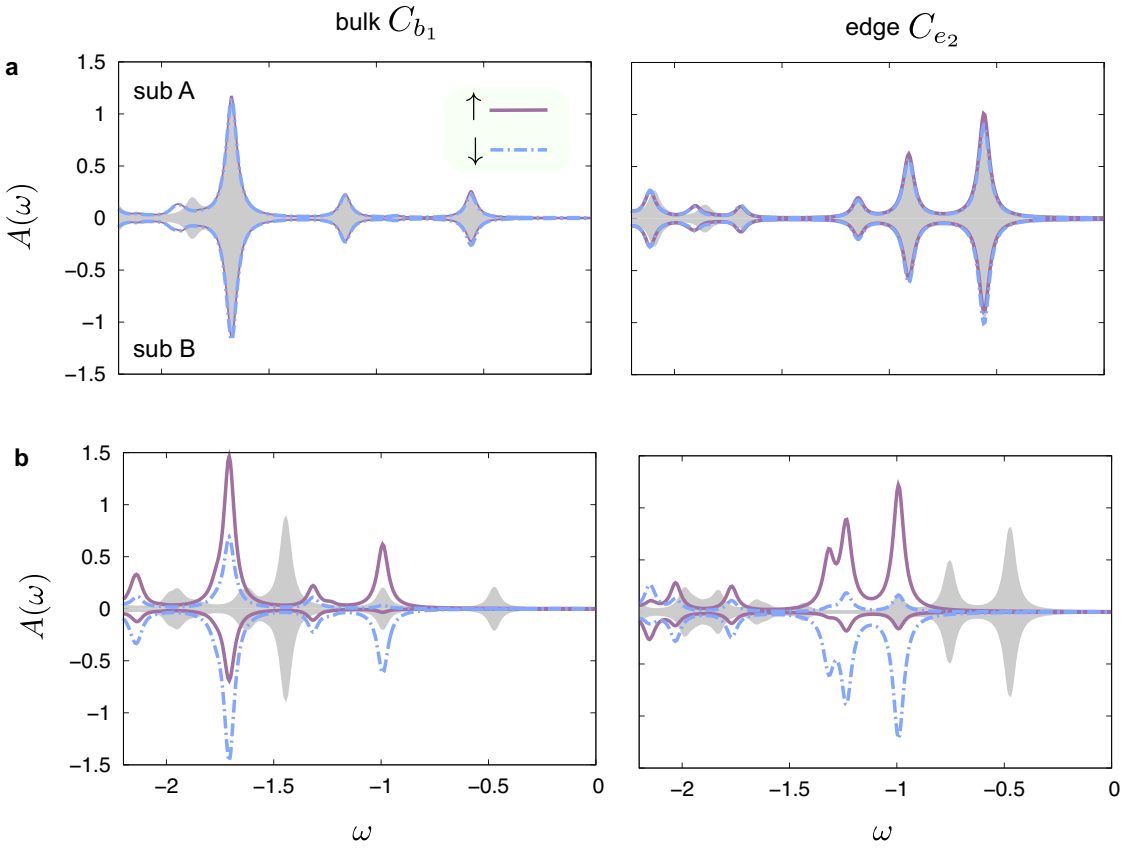

Figure 5.5: **Spin-resolved local spectral function** We show the local spin-resolved DMFT spectral function $A(\omega)$ in the low energy regime for the bulk atoms and edge atoms. Sub lattice A is plotted in the upper panel (above zero) and sublattice B in the lower panel (below zero) within each plot. In the magnetic (purple & blue) calculation we yield a fully compensated AF insulator, while in the nonmagnetic calculation (grey shaded area) the nanoflake is a semiconductor. Parameters are fixed to $U/t = 3.0$ (upper pannel) and $U/t = 4.0$ (lower panel), $\langle \hat{n} \rangle = 1$, and $T = 0$, were U slightly before and after the transition point where magnetism emerges respectively.

We conclude the introduction to uniform nanoflakes by investigating formation and strength of magnetic moments for different flake sizes.

5.3 SIZE EFFECTS IN UNIFORM NANO FLAKES

We complete the introduction to uniform nanoflakes by examining the effect of size on magnetic state of the flake. In Fig 5.6, for the three different size where 5N is the largest structure and 3N the smallest flake, we plot the evolution of themagnetic moment increasing U. While the 4N and 3N display mainly the same behavior across the transition with small modifications in the strength of the magnetic moment, the 5N flake stands out and undergoes a AF transition already around $U/t \approx 2.5$, which is particularly strong on the edges, while the bulk remains similar with respect to the smaller structures.
These results may appear at glance contradictory with the expectation that in the limit of very large lattices the system becomes homogeneous and the critical U becomes *larger* than the one we find in our nanoflakes. However, we can build a physical intuition about this result. In Fig. 5.7 we plot the evolution of the magnetic moments with the size of the flake for a fixed value of $U/t = 3.75$. It is clear that the edge magnetization is going up, while the bulk one is decreasing. For very small systems, the flake is so little that it is is basically impossible to distinguish between a bulk and an edge and magnetism is favored by the reduced kinetic energy of the edges, hence the critical U is smaller than that of the infinite system. When we increase the flake, the edge is better defined, and it becomes more and more magnetic and somehow decoupled from the bulk. Further increasing the size, the edge becomes less and less important and it basically disappears in the thermodynamic limit.

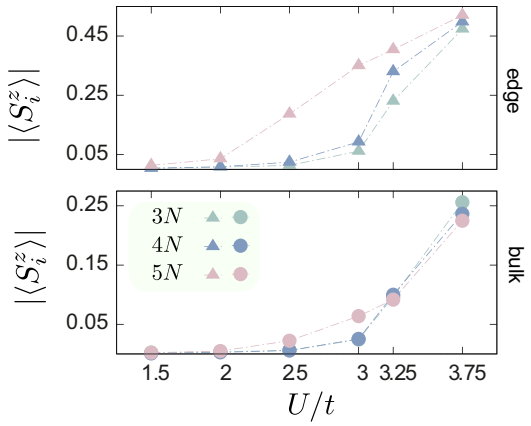

Figure 5.6: **Magnetic transition and size effects**: The magnetic moments at edge and bulk sites are shown as a function of U/t in regions where the AF takes place.

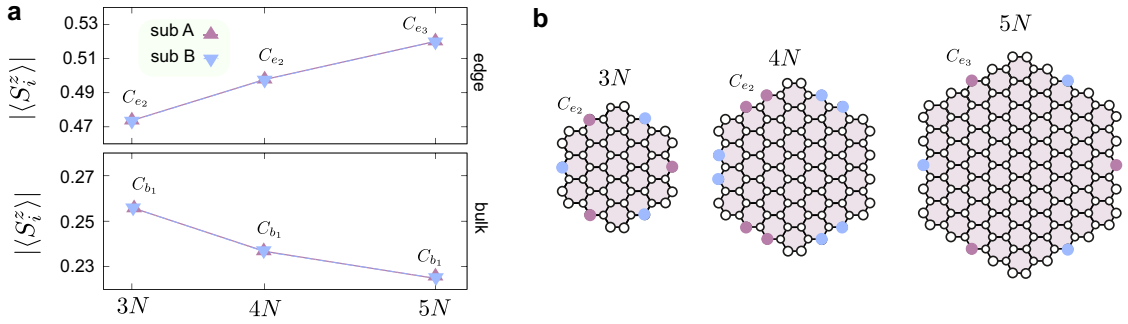

Figure 5.7: **Local magnetic moments as a function of flake size. a** The evolution of the magnetic moments at edge and bulk sites are shown as a function of the flake size from 3N to 5N for fixed interaction strength $U/t = 3.75$. **b** illustration of flakes with different size.

5.4 ARTIFICIAL NANOFLAKES IN A COLD-ATOM SYSTEM

In this section we propose an alternative route to realize artificial honeycomb-lattice nano structures in the framework of ultracold atom systems trapped in optical lattices, following a popular strategy to design quantum simulators of systems which are only approximately realized in solid state.

The idea is to induce magnetism in effective nanoflakes formed by cold atoms moving in optical lattices [9, 110]. By engineering an optical lattice with the graphene honeycomb structure [10, 49, 50, 95, 111, 112] , confined by a strong harmonic trapping potential, leads to a region of fermions forming a cluster reminiscent of *nanoflakes*. We depict the idea in a schematic illustration in Fig. 5.8.

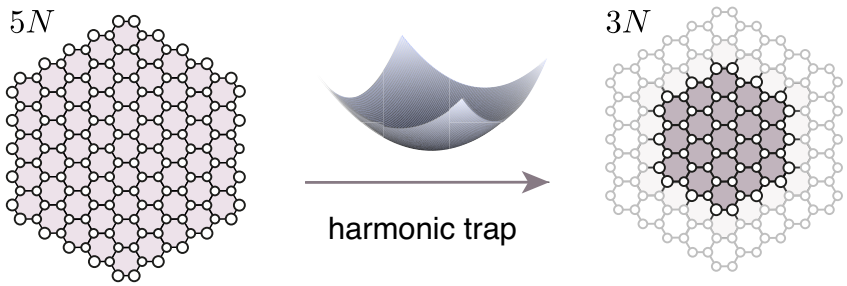

Figure 5.8: (Color online) Protocol for the realization of artificial nanoflakes by spatial confinement using an optical trapping potential. Solid and shaded lines denote the 5N and 3N hexagonal flakes, respectively.

As we shall see in the following, this new set-up actually adds an important feature. The presence of the trap can induce significant density modulations in the system. Given the rich theoretical phase diagram once we also include the density as a variable and the strong competition between antiferromagnetic (AF) and ferromagnetic (FM) correlations, we can expect new results to extend those obtained for uniform nanoflakes.

Again, we model our artificial structure by a Fermi-Hubbard model and add a harmonic potential:

$$\begin{aligned}\hat{\mathcal{H}} = &- t \sum_{\langle i,j\rangle,\sigma} (\hat{c}^{\dagger}_{i\sigma}\hat{c}_{j\sigma} + h.c) + U \sum_{i} \hat{n}_{i\uparrow}\hat{n}_{i\downarrow} \\ &+ \sum_{i} (V_i - \mu)(\hat{n}_{i\uparrow} + \hat{n}_{i\downarrow}),\end{aligned} \tag{5.6}$$

where $\hat{c}^{\dagger}_{i\sigma}$ ($\hat{c}_{i\sigma}$) denotes the creation (annihilation) operator for spin-1/2 fermions and $\hat{n}_{i\sigma}$ is the density operator at site i for the two spin states, labeled by $\sigma \in \{\uparrow,\downarrow\}$. $\hat{n}_i = \sum_\sigma \hat{n}_{i\sigma}$ is the total density on site i. t denotes the nearest-neighbor tunneling amplitude, U the on-site repulsion while the chemical potential μ controls the number of fermions. $V_i = V_0 r_i^2$ is a harmonic trapping potential, with $\mathbf{r}_i = (x_i, y_i)$ the lattice coordinate and $r_i = |\mathbf{r}_i|$. In our calculations we consider a $L = 150$ sites lattice with hexagonal shape and zigzag edges the geometric center of which, $\mathbf{r} = (0,0)$, coincides with the minimum of the parabolic potential, as shown in the left panel of Fig. 5.8. Also in the presence of the trap, we solve the model using a real-space (DMFT) approach, which has been previously used to study inhomogeneous systems, such as cold atoms [45, 113, 114], and nanostructures [115–117], including isolated graphene nanoflakes [96]. As in the case without parabolic potential, yet intrinsically inhomogeneous system we treat the confinement effects by acquiring a dependence on the specific lattice site of the self-energy, i.e., $\Sigma_{ij\sigma} = \delta_{ij}\Sigma_{i\sigma}$, and we obtain for the real-space Dyson equation

$$G^{-1}_{ij\sigma}(i\omega_n) = (i\omega_n + \mu)\delta_{ij} + V_i\delta_{ij} - t_{ij} - \Sigma_{i\sigma}(i\omega_n)\delta_{ij}, \tag{5.7}$$

where $V_i = V_0 r_i^2$, the on-site energy due to the potential, enters and modifies the lattice problem. Therefore, we can describe the different behavior of bulk and edge sites and moreover the emergence of magnetic exchange correlations controlled by the density distribution due to the trap and the Coulomb repulsion. We focus on the results examined in the previous sections 5.2, 5.3,5.2, as well as following previous calculations in a solid-state set-up [96, 105] We start from the 150-site cluster that we label as 5N (we recall this notation where N is the number of sites on an edge). This structure contains smaller graphene clusters with size (4N, 3N, ...) with the same symmetry, yet the edge termination can vary(bearded), an example is shown in Fig. 5.9 (f). Ideally, all of these artificial nanostructures can be stabilized by the trapping potential. In the following we show that this protocol induces sufficiently well defined artificial edges which reproduce the different edges of their solid state counter part.
This allows us to prove whether our protocol to confine atoms in effective nanostructures actually works in configurations which have already been tested. In this light we refrain from a detailed comparison with potential concrete realizations with specific cold-atom experiments, which we postpone to future research. We notice that a similar scheme, where the optical trapping is used to induce quantum states in an optical lattice loaded with ultracold fermions, has been realized in Ref. [118]. As discussed in the following, the electronic distribution and the magnetic ordering of the fermions in the trapping potential depend on the value of the local repulsion, which in cold-atom experiments can easily be controlled via tuning the strength of the optical lattice and the scattering length, when Feshbach resonances are available. We consider two

case: $U/t = 3.75$ and 11.25. The first value corresponds to a realistic choice for actual graphene, and it falls in the range where the semimetal to AF insulator transition takes place for the infinite honeycomb lattice [107, 108]. The latter is sufficient to put any graphene structure deeply in the Mott state, where the fermions are described as localized spins interacting via a Heisenberg exchange. In all our calculations we consider $N_f = 54$, which coincides with the number of sites composing the 3N nanoflake with zigzag edges. Thus, if the fermions can be trapped in the portion of space corresponding to the 3N flake we would have one fermion per site (half filling), which is the ideal situation for the onset of AF ordering, at least for a homogeneous system. On the other hand, for our system of 150 sites, the average filling is $n = N_f/L = 0.36$, i.e. a small density which makes interactions marginally effective. Therefore, in the absence of the trapping potential we have no magnetic effects and the fermions are spread over the whole system also for large interaction strength.
This nonmagnetic state is the starting point to introduce the harmonic potential. Increasing the strength V_0, we progressively localize the fermions in the central region. This is demonstrated in Figs. 5.9 (a-c), where we show the map of the local density $\langle \hat{n}_i \rangle$ on the whole system for calculations with $N_\uparrow = N_\downarrow$[1]. In the absence of the trap we recover a nearly homogeneous system (the small deviation is due to boundary effects) with $\langle \hat{n}_i \rangle \approx 0.36$ for every site i. Conversely for trapping potential strength $V_0/t = 0.4$ the fermions are spatially localized within a reduced region around the center of the trap. The sharpness of the confinement depends on the value of the Coulomb repulsion. We will first consider a system with the same number of fermions per each spin species $N_\uparrow = N_\downarrow = N_f/2$, where N_f is the total number of fermions, which is fixed. This is the standard situation for a cold-atom experiment, where the number of fermions in each species is conserved. As a second step we will also release this constraint, allowing the system to relax in a state with a finite global magnetization (i.e., with $N_\uparrow \neq N_\downarrow$). This situation would be realized in systems in which spin-flip processes are possible as a consequence of the coupling to an external environment or the inclusion of a small artificial spin-orbit coupling. From a theoretical perspective, this will be useful to clarify the tendency towards ferromagnetic ordering with a finite magnetization for some values of the interaction and of the trapping potential.

Artificial nanostructures

This section evolves around the artificial structure and how effective edges can be defined. For this purpose we illustrate how using an estimators can help to define an artificial edge regulated by the confinement of the trapping potential. The main quantity that determines an effective boundary is the density n_i and we analyzed it in two different ways.
First we investigate this aspect, purely on the density distribution in Figs. 5.9 (d,e) which shows the radial profile of the local density as a function of the radius from the trap center $r = |\mathbf{r}|$ for selected values of the trapping potential. For shallow potentials (e.g., $V_0/t = 0.1$ and 0.25) the average local density is low and thereby the fermions are weakly affected by the coulomb repulsion. Increasing the depth of the potential the fermions move towards the center of the trap and the real boundaries of the system

1 When we release the equal-population constraint the changes in the density profile are very small and they are basically invisible in the plots

become empty. This is a crucial point for our proposal, and we observe the important effect of the repulsion among fermions, which competes with the spatial charge accumulation. At $V_0/t = 0.4$ we witness the role of U in defining sharp boundaries. For relatively weak repulsion $U/t = 3.75$, as in Figs. 5.9 (a,d), the fermions pack in the center of the trap and approach the maximum density possible allowed by the Pauli principle. Though the fermions only occupy a region $r \geqslant 5$, the effective structure is highly non-uniform within the confinement region. However, at $U/t = 11.25$, as in Figs. 5.9 (c,e), occupied regions constitute only of half-filled fermions which are Mott localized, and energetically costly double occupancies $\langle \hat{n}_{i\uparrow}\hat{n}_{i\downarrow}\rangle$ are strongly suppressed throughout the lattice.

The reduction of doublons is opposed to the packing of fermions towars the center of harmonic potential where single occupation $\langle \hat{n}_i\rangle = 1$ is favored. In the strongly interacting regime, corresponding to a Mott state, the half-filled effective nanoflake is formed by fermions confined within a region $r \leqslant 4.5$. This structure is characterized by a local density of $n_i \simeq 1$, up to the effective edge radius, where the density drops sharply to zero. In terms of density, within the larger flake a smaller structure was induced by the interplay between the trapping potential and the repulsion and appears as a promising candidate for artificial nanoflake. We demonstrate this in Figs. 5.9 (d,e) where the vertical lines denote the radii corresponding to effective hexagonal nanoflakes (5N, 4N, and 3N) with different edge termination as labeled in Fig. 5.9(f). We stress once more in the strong coupling regime we observe sharp edges at $V_0/t = 0.4$ which match the 3N zigzag nanoflake, discussed in section 5.2, 5.3,5.2 which are identified as a promising candidate for the emergence of magnetism. However, not all effective flakes exhibit sharp boundaries as in this ideal case. For the definition of effective edges use two main indicators that are based on the density. In Fig. 5.4 we show the evolution of each possible edge site upon increasing the potential depth V_0. starting from a uniform lattice structure. This can be used as a first estimator to identify empty sites, which sharpness can be ambiguous. As a first measure we define a site empty if $\langle \hat{n}_i\rangle < 0.25$ which in turn defines the sites lying on the smaller next-nearest neighbor radius with respect to the center of the trap as possible candidate effective boundary. The arbitrary threshold $\langle \hat{n}_i\rangle < 0.25$ might not be accurate enough to define artificial boundaries and moreover, it is not clear if small densities can affect magnetic correlations, particularly in case of smooth inhomogeneous density distributions.

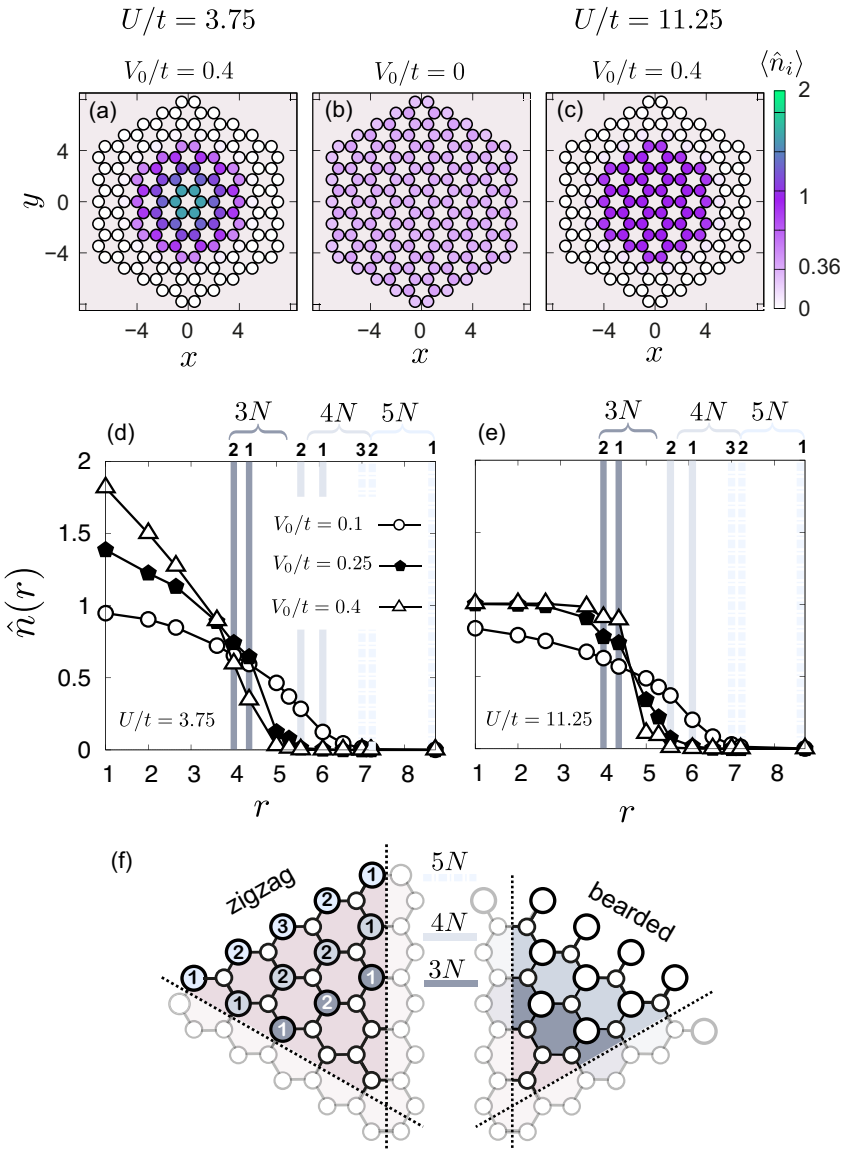

Figure 5.9: (Color online) Spatial confinement into artificial nanoflakes. (a-c) Map of the local density $\hat{n}(\mathbf{r}_i) = \langle \hat{n}_i \rangle$ in the absence of the trap, and for trapping potential strengths $V_0/t = 0.4$ at repulsion $U/t = 3.75$ and 11.25. (e-d) Radial density distribution for selected potential strengths $V_0/t = 0.1, 0.25, 0.4$, at $U/t = 3.75$ and 11.25. Average fermion density: $\langle \hat{n} \rangle = 0.36$. The vertical solid lines in panels (d-e) mark the positions of the edge sites, as labeled in panel (f), where only one-sixth of the flake is shown.

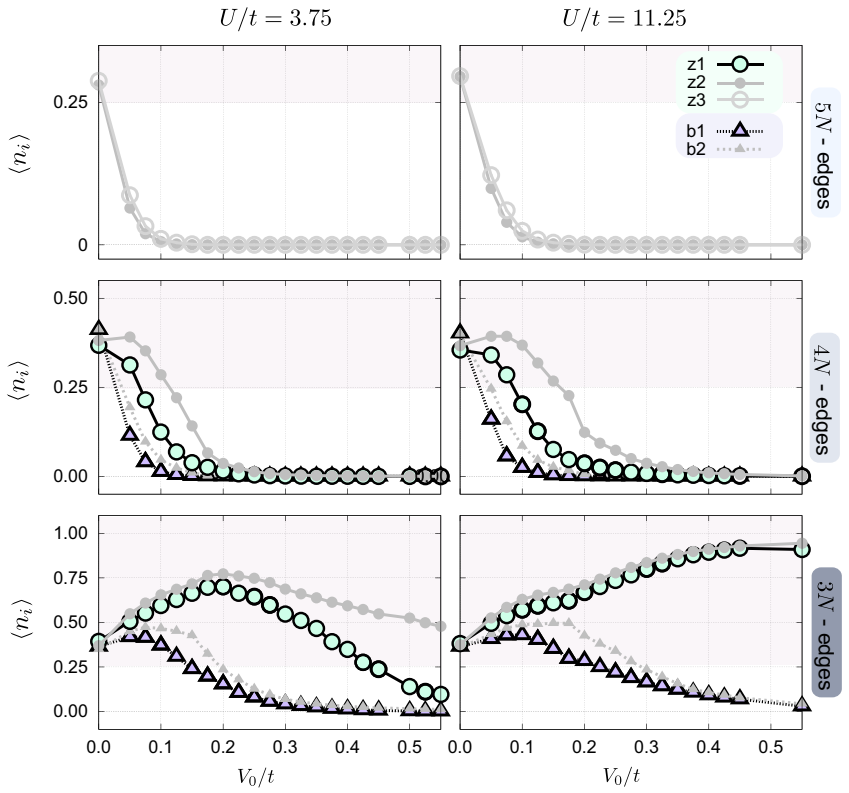

Figure 5.10: Densities $\langle n_i \rangle$ of potential edge sites i_{edge} of 5N, 4N, 3N flakes as a function of the trapping potentials amplitude V_0. From top to bottom we show larger to smaller structures. The structures can have different type of edges such zigzag denoted with z (green) and bearded labeled with b (purple). The numeration $1, 2, \ldots$ means that they belong to the same class of edges, but are at different radial distance from the center and are therefore not equivalent. The white (shaded grey) areasin the plot mark the threshold for considering a site empty (occupied). The left and right panels shows the weakly-correlated regime at $U/t = 3.75$ and the strongly-correlated regime at $U/t = 11.25$.

In addition we introduce a second definition of the effective edge r^*_{edge} as shown In Fig. 5.4 where the derivative of the density with respect to the position $\partial n/\partial r$ is maximal. Undeniably, these definitions have a degree of arbitrariness, but we verified that different criteria provide the same result. For large interactions the effective edges can be distinctively defined, while weak interactions leave room for interpretation and the boundary can smooth out into the dead layers. To be more concrete we compare the position of the effective edge obtained with a second estimators with which we access the sharp boundary by computing the derivative of the radial distribution for a fixed potential and identify the location of the maximum as the new edge, defined by

$$r^*_{edge} = \max_r \left| \frac{\partial n(r, V_0)}{\partial r} \right|_{V_0 = const.} . \tag{5.8}$$

The incompressible nature of the Mott insulator, is directly reflected in our results, where the density profile is robust upon the packing effect of the trapping potential. This is in contrast to the weak- and intermediate-coupling regimes, with a finite compressibility exhibiting the quantum fluid nature of the effective flakes.

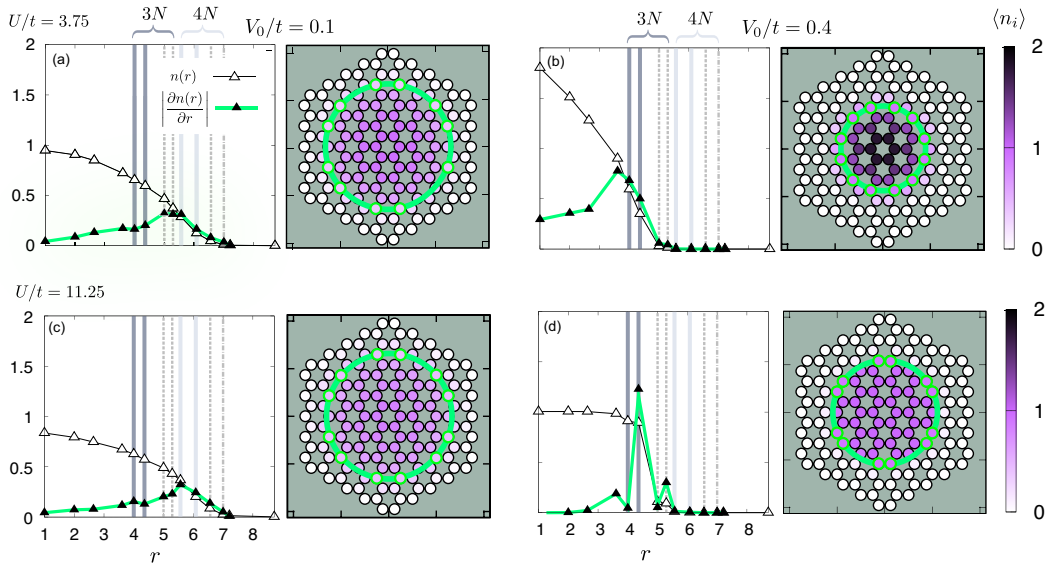

Figure 5.11: We show the absolute value of the derivative $|\partial n(r)/\partial r|$ of the radial density distribution $n(r)$ together with the density distribution as well as real-space plot of the density for selected values of trapping potential $V_0/t = 0.1,\ 0.4$ (left and right respectively). The upper panel shows the weaker-coupling regime at $U/t = 3.75$ ((a) and (b)) and the lower panel the strong-coupling regime at $U/t = 11.25$ ((c) and (d)) The vertical lines indicate the radius corresponding to the position of the different sites. Full lines from bright to dark denote larger to smaller nanoflake structures. Bold lines denote zigzag edges and dashed lines denote bearded edges. The neon-green boundaries in the real-space plot indicate the artificial edge obtained by the sharpest peak of the derivative of the radial density distribution.

we plot as a function of V_0/t the estimate of r^*_{edge} given by the position
In Figs. 5.4, we compare a case with clear artificial edges to cases with ambiguous boundaries. In the strong-coupling regime, the boundary obtained within the second approach is clear for many values of the trapping potential as depicted in (d) In the weak-coupling regime, the maxima are instead not pronounced and the radial distribution $n(r)$ tent to be smoother.
We identify an effective edge by averaging the position we estimated with the two quantities. However, there are cases (especially in the weak-coupling regime) where an edge can not clearly be defined. We summarize these results in Fig. 5.9. The horizontal lines mark the positions of the edge sites. Upon increasing V_0/t the fermionic cloud prefers to redistribute towards the center of the trap and the real boundaries turn into dead layers. Thereby the effective size is reduced. The contraction is faster in the weakly interaction regime compared to the strongly interacting regime due to the Hubbard repulsion acting as an internal pressure.
Interestingly, in both interaction regimes the system displays various effective flakes of different sizes upon the evolution of trapping potentials, where the 3N zigzag-edged flake is the most stable artificial structure. This is obviously not a coincident, since we choose the initial N_f to match a 3N half-filled nanoflake.

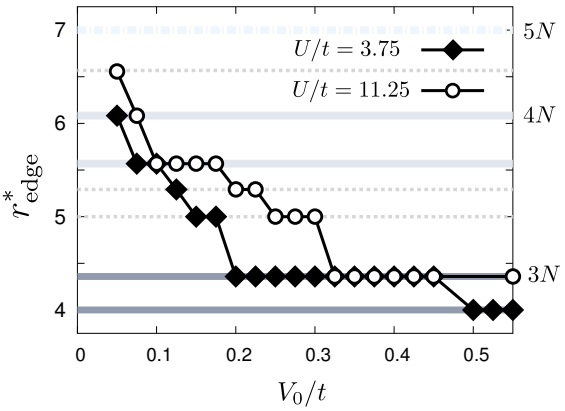

Figure 5.12: (Color online) Effective edge r^*_{edge} of the artificial flake induced by the trapping potential as a function of V_0/t. Horizontal lines correspond to the positions of the edge sites as labeled in Fig. 2(b). In this setup, the 3N flake is stable for a wide range of V_0/t.

Magnetism

After defining artificial nano structures, we are now in the position to examine if they actually support magnetic ordering. We report on the magnetic states in Fig. 5.13 showing real space color maps of the local magnetization along the z-direction. The local magnetic moment is determined by $\langle \hat{S}^z_i \rangle = \langle \hat{n}_{i\uparrow} - \hat{n}_{i\downarrow} \rangle$ and shown for two values of interaction and three values of trapping potential used in Fig. 5.8. Red (blue) indicates a positive (negative) magnetization. The bipartite nature of the honeycomb lattice allows us to establish magnetic states, by relating the magnetic moments of sub-lattices A and B to eachother, where a perfect AF state is formed when the magnetization of sublattice A is the opposite of that of sublattice B $\langle \hat{S}^z_{i_A} \rangle = -\langle \hat{S}^z_{i_B} \rangle$, while a FM state has the same magnetization on the two sublattices. In the presence of both, staggered and a uniform magnetization, the state is characterized as ferrimagnetic and in the absence of both, i. e vanishing local magnetic moments $\langle \hat{S}^z_{i_{A,B}} \rangle \approx 0$, we declare it In a nonmagnetic state. The results in Fig. 5.13 display a rich landscape of magnetic solutions on effective flakes, that have been established by the density as discussed in the previous section. The magnetic solution of the overall system should be zero in accordance to cold atomic experiments, since we start inducing magnetism from a paramagnetic state, which remains satisfied when fully compensated antiferromagnetic patterns emerge. We begin our analysis with the spin conserving, i. e $N_\uparrow = N_\downarrow = N_f/2$, or $\langle \hat{S}^z \rangle = 0$, where $\hat{S}^z = \sum_i \hat{S}^z_i$ results and consider the strong-coupling regime, with sharply defined effective 3N half-filled flakes as shown by our data for $U/t = 11.25$.
By design the fermion density is far below half-filling in the absence of or very shallow trapping potential (we recall that $\langle \hat{n}_i \rangle \approx 0.36$ at $V_0 = 0$). As expected the flake is not magnetic (not shown). Upon increasing V_0 the fermions are attracted towards the center of the trap, as depicted in Fig. 5.13(a,b), and clear AF pattern emerge in the center of the system. The inner rings displaying AF ordering have a density $\langle \hat{n}_i \rangle \approx 1$. The outer regions with finite density, around quarter filling $\langle \hat{n}_i \rangle \approx 0.5$, show weakly FM islands. In Fig.5.13(c) we show that increasing V_0/t leads to a dramatic enhancement of the magnetic moments, until a fully compensated Néel AF state is reached that covers the entire occupied central region. The evolution of the magnetic ordering in the

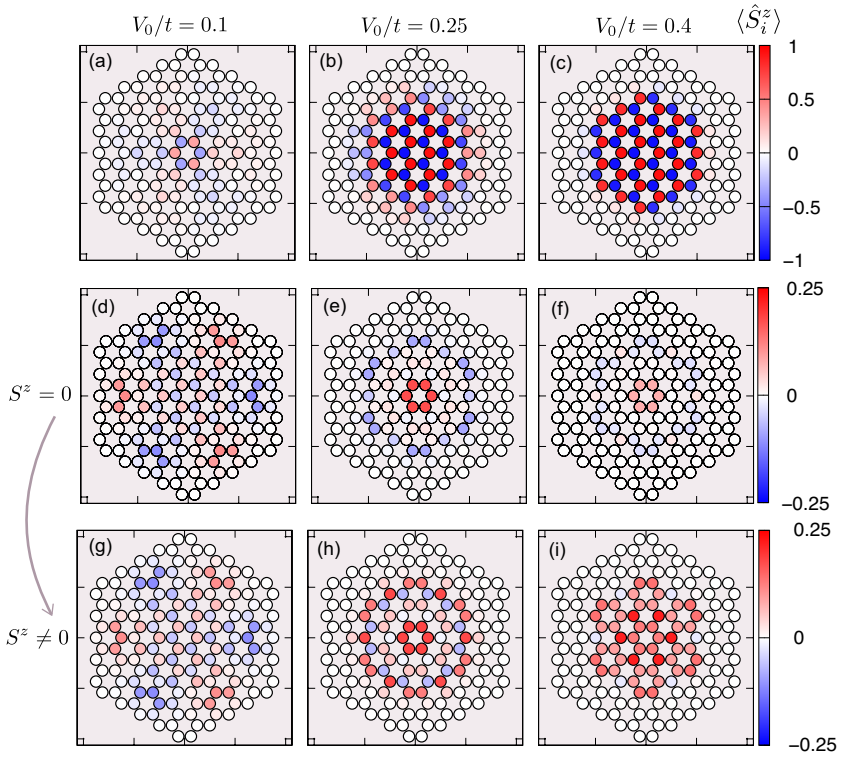

Figure 5.13: (Color online) Map of the local magnetization $\langle S_i^z \rangle$. The first row (a-c) presents results for $U/t = 11.25$, while the second row (d-f) shows data for $U/t = 3.75$ with $\langle S_z \rangle = 0$ and the third row (g-i)shows data for $U/t = 11.25$ with $\langle S_z \rangle \neq 0$. In all cases we show results for three different values of V_0/t. The competition of emergent AF and FM magnetic exchanges gives rise to different magnetic states, depending on the electronic density distribution determined by V_0/t and U/t.

strong coupling regime is not surprising and can be easily understood in terms of the strong-coupling limit ($U/t \gg 1$). In this limit the Hubbard model maps to an effective Heisenberg model with a next-neighbor AF exchange coupling $J = 4t^2/U$. The formation of well-defined magnetic effective flakes in the strong coupling regime is confirmed by the magnetic responses and proves that manipulating the systems with a trapping potential can induce a magnetic state. We probed the strong coupling set up under the spin conserving constrain $\langle \hat{S}_z \rangle = 0$ and then relaxed the condition, which didn't change the magentic solution, Therefore the AF solution is the actual ground-state of the system. While the strong coupling regime is quite clear and straightforward with a direct comparison to the solid-state counterpart the intermediate interaction regime (e.g., for $U/t = 3.75$) is more diffusive and peculiar. The evolution of the magnetic properties in Fig 5.13 (d-f) involves many different magnetic patterns due to less pronounced tendency towards the formation of magnetic moments in addition to the ambiguous definition of effective edges. The rich landscape of magnetic states can be explained by previous work on graphene nanoflakes [96], investigating the effect on the magnetic state when the densities are different from one fermion per site. Upon doping the uniform nanoflake FM correlations are favored which are more compatible with metallic behavior. The formation of FM correlation leads to a nontrivial evolution of artificial nanoflakes as a function of V_0/t, where the overall state is controlled by the competition between AF and FM correlations. For shallow traps and therefore low density, AF ordering establishes in the center of the system, though the magnetic moments are weaker compared to the strong coupling case. The outer region form small FM islands which change sign in each C_6 sector as shown in Fig. 5.13 (d), hinting towards long-range AF edge-edge correlations between FM domains. The domains are at distances $d_{AF} \approx 5r$ and are mediated by the short-range (i.e., $d_{AF} = r$) Heisenberg exchange. Deeper trapping potentials produce strongly inhomogeneous density distributions, where the interplay between interaction and harmonic potential is clearly dominated by the latter. The variety of occupations within the system leads to metallic FM regions surrounded by a nonmagnetic layers and and an external ring where the fermions have the opposite spin with respect to the center. Approaching the density 2 the inner regions favor FM correlations, which are rather suppressed by the $\langle \hat{S}_z \rangle = 0$ constraint, as visible in (Fig. 5.13 (f) for $V_0/t = 0.4$) We conclude that our results demonstrate a protocol for inducing and tuning the magnetism in the honeycomb lattice by using a trapping potential and adjusting the interaction strength. To underline this we pick an example at a fixed potential strength $V_0/t = 0.4$ where we observe a clear transition between FM and AF states (panels (b) and (e) or (c) and (f) of Fig. 5.13) changing the interaction strength. Finally,we want to give an idea how to strengthen FM correlations by relaxing the $\langle \hat{S}_z \rangle = 0$ constraint. This protocol, is from an experimental point of view, more challenging since it would require to include some mechanism able to flip the spins of the atoms. We accentuate the tendency towards the FM state in the weakly interacting regime, where polarization of spins minimizes the energy of the system contrary to the strongly interacting regime. The third row of Fig. 5.13 shows the enhancement of FM ordering by relaxing spin conservation.

5.5 CONCLUSIONS

In this chapter we have shown that a trapping potential can induce a variety of magnetic phases in an otherwise nonmagnetic honeycomb lattice. In particular, a parabolic potential can be used to trap the fermions in artificial nanoflakes, which inherits the properties that have been widely studied in a solid-state framework. The trapping is most effective for strong fermion-fermion repulsion, underlining the important effect of interactions in the realization of well-defined artificial edges. Our proposal shows a route to induce magnetism in artificial graphene nanostructures, and it is expected to be robust with respect to details of the system, i.e., actual size and number of fermions as long as the interactions can be made sufficiently strong to reach the Mott regime.
Also, when it is difficult to establish a direct correspondence with solid-state systems, because the trapping leads to strongly inhomogeneous density distributions, we find a competition between FM and AF tendencies. This leads to a tunable system evolving from a weak antiferromagnet to a ferromagnet. The magnetic ordering is also expected to be reflected in the transport properties, leading to highly nontrivial spin transport. The possibility to induce different magnetic states could be exploited to investigate spin-filter [105] and spin-valve effects within transport experiment in optical lattices [119, 120].

6

GOVERNING TOPOLOGICAL AND MAGNETIC ORDER IN ARTIFICIAL HONEYCOMB NANOFLAKES

6.1 INTRODUCTION

Interacting quantum many-body systems are often dominated by the competition between different phases, emerging from the rivalry of various degrees of freedom. The ability to control such competition, with the aim of creating novel states of matter, is of crucial importance in different contexts of condensed matter physics. Thanks to the tremendous progress achieved in the last few years, ultracold atoms have revealed as a promising platform to experimentally simulate different interacting systems, with an unprecedented level of control.

Recently, we have witnessed the realization of non-trivial topological states of matter within cold-atom platforms, such as Chern-insulators or bosonic Hofstadter systems [10, 20, 21, 51]. This enables to explore the interplay between symmetry protected topological states and the effects of interaction in a clean and controlled system, which is the main topic of the present chapter.

The presence of strong interactions typically leads to spontaneous symmetry breaking and formation of long-range ordered states. A paradigmatic example for symmetry broken phases caused by strong correlations is the antiferromagnetic ground state of the fermionic Hubbard model that breaks time-reversal symmetry (TRS). The first experimental realization of this state in Fermi-Hubbard system using quantum state engineering technique has been reported [110], but the quantum simulation of generic magnetic states remains still experimentally challenging [16, 119, 121, 122].

In topological insulators (TIs) the protecting symmetries are essential for the topology of the phase. In quantum spin-Hall insulators (QSHIs) [31, 32, 123] the protecting symmetry is the time-reversal symmetry and therefore one would expect the nontrivial topological character of these systems to be obliterated by the formation of magnetic ordering. Fortunately, in some situations topological properties can be preserved when the TI has more than one protecting symmetries and of them survives to the breaking of another. This leads to the possibility to engineer quantum states where magnetism and non-trivial topology coexist [33, 124–130].

Here we propose an experimentally feasible protocol to engineer correlated topological and magnetic states in cold fermion systems, following the ideas put forward in the previous chapter. In particular, we show that a confining harmonic potential can be used as a knob to govern the magnetic exchanges and to tune artificial topological states in an optical lattice. Using the Kane-Mele-Hubbard model [33, 124–130] as a paradigmatic model for 2D time-reversal symmetric topological insulators in presence of strong local interaction [33, 126, 131, 132], we characterize the formation of

correlated topological states and the emergence of complex magnetic ordering in a geometrically confined system.

The phase diagram of the Kane-Mele-Hubbard model, computed with quantum Monte-Carlo techniques, has been discussed in [126]. At half-filling and for finite Hubbard interaction the topological insulator is adiabatically connected to the ground-state of the Kane-Mele model. For very weak spin-orbit coupling the and intermediate Hubbard repulsion the model displays a trivial band-insulator solution. At strong interaction in-plane Néel Antiferromagnetic ordering is preferred, which can be easily understood from strong coupling expansions [47], while the antiferromagnetic Mott insulators with out-of plane magnetization is only for very weak spin-orbit interaction energetically favorable.
In finite size system the interplay between topology and correlation acquires deeper investigation. The effect of the Hubbard repulsion is effectively enhanced on the boundaries while TIs host peculiar edge states. The metallic edge states given by the Kane-Mele model are spin-filtered with spin-↑ and spin-↓ counter propagating along the edges and are out-of plane. In this work we examine the interplay between topology and magnetism a how complex coexisting states can be realized in cold atomic experiments. The first analysis evolves around the question how out-of plane magnetic moments on the edges of the nano flake exchange with the kinetic edge fermions. We address this questions by suppressing the in-plane magnetic solution, which in the bulk Kane-Mele Hubbard model is favored, for most of the parameter regime. This analysis is studied for the ideal case, i.e half filled nano flake without harmonic trap and then extended to the cold atomic context, including a trapping potential and applying the idea of the previous chapter. Specifically, because we are interested in parameter regimes, that are unlikely to reach in real condensed matter system, cold-atomic systems provide a perfect platform to explore the interplay of parameters due to their highly controllable setups. Enormous progress has been made in realizing topological phases, but magnetism in cold-atoms due to temperature effects still needs more improvement. In cold atomic systems, contrary to solid-state materials, the presence of a a confining potential can not be avoided and therefore a local description of the order parameters is necessary. By means of inhomogeneous dynamical mean-field theory (RDMFT), we solve the Kane-Mele-Hubbard model on a nanoflake. For measuring the topological order we use the notion of the local Chern-marker [70, 133, 134] which is real-space version of the conventional Chern number.

6.2 KANE-MELE MODEL

Kane and Mele introduced a model to study the effects of spin orbit interaction (SOC) in a single layer graphene at low energies. The presence of SOC converts graphene from an ideal and topologically trivial semi-metal to a topologically nontrivial quantum spin Hall insulator, that is insulating in the bulk yet hosts metallic edge states that can support transport of spin and charge. The model Hamiltonian reads

$$\hat{\mathcal{H}} = -t_1 \sum_{\langle i,j\rangle} \hat{\Psi}^\dagger_{i\sigma} \hat{\Psi}_{j\sigma} + it_2 \sum_{\langle\langle i,j\rangle\rangle} \nu_{ij} \hat{\Psi}^\dagger_i \sigma^z \hat{\Psi}_j \tag{6.1}$$

where $\hat{\Psi}_i^\dagger = (\hat{c}_{i\uparrow}^\dagger, \hat{c}_{i\downarrow}^\dagger)\big(\hat{\Psi}_i = (\hat{c}_{i\uparrow}, \hat{c}_{i\downarrow})\big) =$ is a spinor of creating (destructing) an electron on site i on the honeycomb lattice and $\langle i,j\rangle$ $\langle\langle i,j\rangle\rangle$ is the next-neighbor and next-nearest neighbor pair of lattice sites i and j respectively. The complex hopping term $it_2\nu_{ij}$ describes spin-orbit interaction in graphene and it is equivalent to a spin-selective staggered magnetic flux. As we already discussed, the lattice is bipartite, so it naturally allows for two-sublattice magnetic ordering.
Introducing a four-component spinor $\hat{\Psi}_{\mathbf{k}}^\dagger = (\hat{a}_{\mathbf{k}\uparrow}^\dagger, \hat{b}_{\mathbf{k}\uparrow}^\dagger, \hat{a}_{\mathbf{k}\downarrow}^\dagger, \hat{b}_{\mathbf{k}\downarrow}^\dagger)$, where $\hat{a}_{\mathbf{k}\sigma}^\dagger$ and $\hat{b}_{\mathbf{k}\sigma}^\dagger$ are associated to the creation of momentum-space Fourier transforms of the operators for spin-σ fermions on sublattice A and B, one can write the Hamiltonian as

$$\hat{\mathcal{H}} = \sum_{\mathbf{k}} \hat{\Psi}_{\mathbf{k}}^\dagger \hat{\mathcal{H}}_{\mathbf{k}} \hat{\psi}_{\mathbf{k}} \tag{6.2}$$

$$\hat{\mathcal{H}}_{\mathbf{k}} = \begin{pmatrix} \hat{\mathcal{H}}_{\mathbf{k}}^{\uparrow} & 0 \\ 0 & \hat{\mathcal{H}}_{\mathbf{k}}^{\downarrow} \end{pmatrix}, \tag{6.3}$$

with the spin-resolved sub Hamiltonians

$$\hat{\mathcal{H}}_{\mathbf{k}}^{\uparrow,\downarrow} = h_0\hat{\sigma}_0 + h_x\hat{\sigma}_x \pm h_y\hat{\sigma}_y \pm h_z\hat{\sigma}_z, \tag{6.4}$$

where $\hat{\sigma}_i$, $i = 0, x, y, z$ are the Pauli matrices and the coefficients h_i are defined as

$$\begin{aligned} h_0 &= 0 \\ h_x &= -t_1 \sum_{i=1}^{3} \cos(\mathbf{k}\cdot\delta_i) \\ h_y &= -t_1 \sum_{i=1}^{3} \sin(\mathbf{k}\cdot\delta_i) \\ h_z &= 2t_2 \sum_{i=1}^{6} \sin(\mathbf{k}\cdot\eta_i) \end{aligned} \tag{6.5}$$

The spectrum can obviously be obtained diagonalizing the 4×4 Hamiltonian for every lattice momentum.
This model obeys time reversal symmetry (TRS) as it can easily be understood noting that $\hat{\mathcal{H}}_{\mathbf{k}}^{\downarrow} = (\hat{\mathcal{H}}_{-\mathbf{k}}^{\uparrow})^\dagger$. Indeed the Kane-Mele model can be seen as a time-reversal invariant version of the celebrated Haldane model (which instead breaks TRS) which features integer quantum Hall effect.
$\mathbb{Z}_2$ topological insulator, also known as quantum spin Hall insulator (QSHI). It is characterized by a $\mathbb{Z}_2$ invariant $\nu = (\mathcal{C}_\uparrow - \mathcal{C}_\downarrow)/2$
The Kane-Mele model is basically constituted by two copies of the Haldane model in which the two spin component have opposite chirality. The topologically non-trivial state obtained for finite t_2 is called quantum spin Hall insulator (QSHI). This state is characterized by a $\mathbb{Z}_2$ topological invariant $\nu = (\mathcal{C}_\uparrow - \mathcal{C}_\downarrow)/2$ ($\mathcal{C}_\sigma$ being the Chern number of the σ fermions). which can only acquire values 0 or 1 (in the QSHI), in contrast with the Chern number characterizing the integer Quantum Hall effect that can take any integer values. The need for this new index is because the Hall conductance of the QSHI is bound to vanish because of TRS. The QSHI is characterized by

a new type of conducting edge states propagating in both directions, at both edges, without reflecting. That is again due to TRS which forbids backscattering between pairs of counterpropagating edge states, since electrons cannot flip their spin. These states are defined as helical edge states, because spin is correlated with the direction of propagation.
Without the spin-orbit term the well known tight binding model of honeycomb lattice is recovered and displays particle-hole symmetry bands with band touching at the six corners of the Brillouin zone, that reduce to the famous two inequivalent Dirac points:

$$\mathbf{K} = \left(\frac{2\pi}{3}, \frac{2\pi}{3\sqrt{3}}\right), \quad \mathbf{K}' = \left(\frac{2\pi}{3}, -\frac{2\pi}{3\sqrt{3}}\right). \tag{6.6}$$

In an infinite system the single particle spectrum is two-fold degenerate, i.e each spin has the same energy dispersion (upper panel corresponds to spin $\uparrow$ and lower panel tospin $\downarrow$) in Fig 6.1 , which reflect the Kramers degeneracy. Expanding the dispersion around K and K' one finds a linear dispersion reminiscent of the Dirac equation [], from which it becomes clear why these points are called Dirac points. The spin orbit term $\nu_{ij}\lambda$, opens a gap at these points and the sub lattice orbitals mix as depicted in Fig 6.1

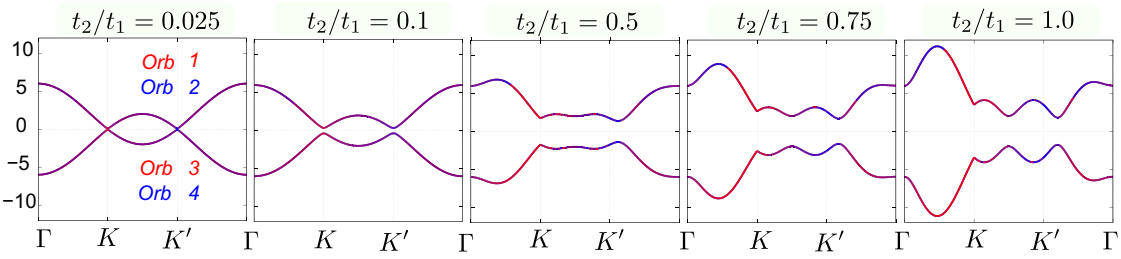

Figure 6.1: **Band structure of the Kane Mele model** Energy bands of the Kane-Mele model for selected values of the spin orbit term t_2. Along the path Γ, K, K', Γ. The four orbitals are equivalent to combinations of the sub-lattices and spin component.

The aim of this chapter is to investigate interacting Kane-Mele nanostructures, analyzing the destiny of the interplay between topology and strong correlations in small systems, in analogy to what we have done in the previous chapter for the honeycomb lattice in the absence of the spin-orbit coupling term. While the original proposal by Kane-Mele cannot be realized in graphene because of the basically negligible spin-orbit coupling, it can be realized in cold-atom systems.
Before presenting our results on nanoflakes, we review some important results on the interacting Kane-Mele model.

6.3 INTERACTING KANE-MELE MODEL

In this section we consider a Kane-Mele-Hubbard model which consists of the Hamiltonian in 6.2 and and additional on-site interaction term

$$\hat{\mathcal{H}}_U = U \sum_i \hat{n}_{i\uparrow}\hat{n}_{i\downarrow} \tag{6.7}$$

In this work we focus on the interplay between magnetism and topology, hence we briefly discuss the magnetic properties of the model. We start from the strong-coupling limit, where we can easily obtain an effective spin model for the localized electrons. In the standard Hubbard model ($t_2 = 0$), as we discussed in the previous chapter, the Hubbard model maps onto an SU(3) invariant antiferromagnetic Heisenberg model[47], hence the groundstate is expected to be antiferromagnetically ordered due to the bipartite nature of the lattice and all spin directions are completely degenerate.
The SOC term frustrates the two-sublattice AFM ordering, as it can be understood from the effective Heisenberg model with the two different super-exchange couplings between next-neighbor and next-nearest neighbor sites $\hat{\mathcal{H}}_{NN} = \frac{+4t_1^2}{U} \sum_i \sum_\delta \mathbf{S}_i \mathbf{S}_{i+\delta} + \frac{\hat{n}_i \hat{n}_{i+\delta}}{2}$ and $\hat{\mathcal{H}}_{NNN} = -\frac{4t_2^2}{U} \sum_i \sum_\eta \hat{S}_i^x \hat{S}_{i+\eta}^x + \hat{S}_i^y \hat{S}_{i+\eta}^y - 2\hat{S}_i^z \hat{S}_{i+\eta}^z - \frac{\hat{n}_i \hat{n}_{i+\eta}}{2}$. The NNN exchange couples the z components of the spins antiferromagnetically within the same sublattice, whereas the xy terms are coupled ferromagnetically. This clearly shows that the ordering along the z direction is frustrated by the presence of the t_2 term, while the x and y components do not compete, as the NNN term favors same spin alignment within each sublattice, which is fully compatible with global AFM ordering. Thus we can easily conclude that, as soon as t_2 is switched on the SU(3) spin symmetry is broken and the AFM ordering takes place in the plane.
However these results are stricly speaking limited to the large-U limit and only an explicit calculation can give reliable information on the intermediate U regime. We compare two phase diagrams that were obtained with two different techniques, one by means of quantum Monte Carlo simulations by Hohenadler et al [125] and the other one via variational cluster approach (VCA) Yu et al [135]. The phase diagrams are reported in the two panels of Fig. 6.2. The SOC coupling is here denoted as λ (notice that the axes are interchanged in the two plots).

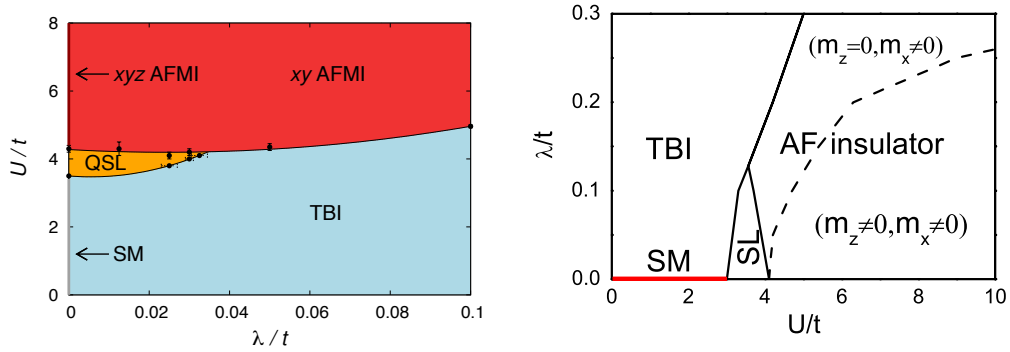

(a) QMC (b) VCA

Figure 6.2: **Ground state phase diagram of the Kane-Mele Hubbard model** (a) The phase diagram was obtained by means of QMC simulations and is taken from Ref. [125] . The parameters λ/t and U/t span a diagram with four phases, that are a Z_2 topological band insulator (TBI), a semimetal (SM) at $\lambda = 0$ and a quantum spin-liquid (QSL) and an antiferromagnetic insulator with out-of plane ordering at $\lambda/t = 0$ and in-plane ordering for $\lambda/t \geqslant 0.002$ (b) is taken from Ref. [135].

Both phase diagrams reproduce the semi-metal to QSHI transition in the weakly interacting regime upon increasing the SOC term (here λ). Increasing U in both cases

we enter in a magnetic Mott insulator through a tiny slice occupied by a Quantum Spin-Liquid Solution without spin ordering, limited to intermediate interactions and moderate SOC. For $U \gtrsim 4t$ the system enters in the Mott insulator regime. The main discrepancy is that the VCA calculations show an extended region of an antiferromagnetically ordered Mott insulator with magnetic order both transverse (xy) and longitudinal order z as depicted in Fig. 6.2 (b), while the more accurate QMC finds a planar AFM for any non vanishing λ in agreement with the strong-coupling result er discussed above.

Even if the QMC result is numerically more reliable, this comparison suggests that the competition between a planar AFM and a solution with also a z component can be non-trivial. Especially when the system under investigation is finite like our nanoflakes, we can expect a revival of a three-dimensional magnetism.

As we mentioned above, both studies predict also a quantum spin liquid phase, which can be only demonstrated computing non-local parameters. On the othe hand, this phase can not be defined on our finite system and we will not discuss it and rather focus on the topological insulator to antiferromagnet transition particularly on the finite size scaling of the magnetic ordering.

Before moving to our new results, we present some data about the finite-size scaling of the planar and longitudinal structure factors, which are computed using QMC in Ref. [125]

$$S^{x}_{AF} \equiv \sum_{\alpha} \frac{1}{L^2} \sum_{\mathbf{r}\mathbf{r}'} (-1)^{\alpha}(-1)^{\beta} \langle \Psi_0 | \hat{S}^{+}_{\mathbf{r}\alpha} \hat{S}^{-}_{\mathbf{r}'\beta} + \hat{S}^{-}_{\mathbf{r}\alpha} \hat{S}^{+}_{\mathbf{r}'\beta} | \Psi_0 \rangle , \tag{6.8}$$

$$S^{z}_{AF} \equiv \sum_{\alpha} \frac{1}{L^2} \sum_{\mathbf{r}\mathbf{r}'} (-1)^{\alpha}(-1)^{\beta} \langle \Psi_0 | \hat{S}^{z}_{\mathbf{r}\alpha} \hat{S}^{z}_{\mathbf{r}'\beta} | \Psi_0 \rangle , \tag{6.9}$$

where $\mathbf{r}, \mathbf{r}'$ are the unit cell labels and α, β denote the sublattice indices. On sublattice A the prefactor $(-1)^{\alpha} = 1$, while on sublattice B it is -1. These are directly related to the magnetization as $m^2_{\alpha} = S^{\alpha}/2L^2$.

The finite size scaling of the magnetic structure factor, shown in Fig. 6.3, show that the longitudinal ordering for spin-orbit coupled system is absent in the thermodynamic limit, i.e in real bulk systems, in the whole region of interaction between $U/t = 4$ and 8, while the planar component has a finite value for $U > 4.3$. Interestingly when the system size decreases and for the smaller values of the interaction reported the two structure factors are comparable and it becomes at least conceivable to have a finite z-axis magnetization.

In the following we focus on rather small nanoflakes in order to verify how the magnetic ordering shows up in this small systems, where we have an important role of the edges. In view of cold-atom experiments it should be noted that, based on our results of the previous chapter, we expect that the trapping potential gives rise to a well-defined effective nanoflake only when the interaction U is quite large.

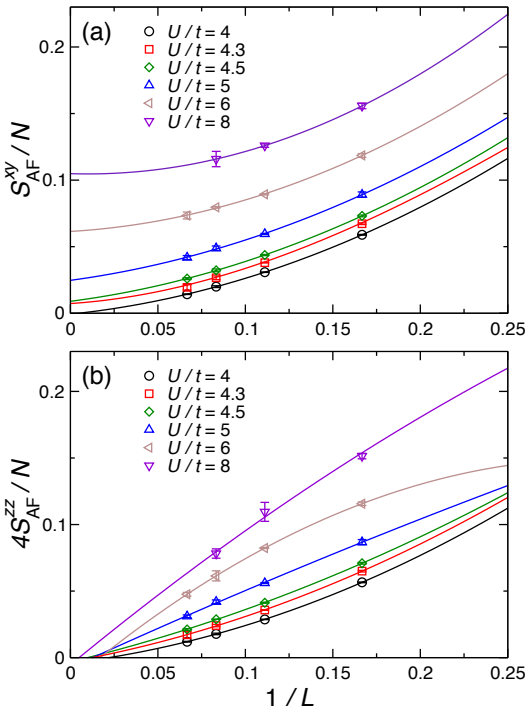

Figure 6.3: **Finite size scaling of the rescaled magnetic structure factor** (a) shows the in-plane magnetic structure factor S^{xy}_{AF}/N at λ/t across the AFMMI transtions for corresponding U/t (b) reveals the longitudinal structure factor S^{zz}_{AF} that indicates no long-ranger order upon increasing U/t. Figure taken from Ref. [125]

6.4 KANE-MELE HUBBARD MODEL ON THE NANOFLAKE

We consider a Hubbard-Kane-Mele model defined on the hexagonal nanoflakes with zigzag (ZZ) edges defined in the previous chapter described by the Hamiltonian formed by the tight-binding Kane-Mele model and the local Hubbard interaction

$$\begin{aligned}\hat{\mathcal{H}} = &- t_1 \sum_{\langle i,j\rangle,\sigma} \hat{c}^\dagger_{i\sigma}\hat{c}_{j\sigma} + U\sum_i \hat{n}_{i\uparrow}\hat{n}_{i\downarrow} \\ &- t_2 \sum_{\langle\langle i,j\rangle\rangle\sigma} \alpha_\sigma e^{i\phi_{ij}}\hat{c}^\dagger_{i\sigma}\hat{c}_{j\sigma},\end{aligned} \tag{6.10}$$

where $\hat{c}^\dagger_{i\sigma}$ ($\hat{c}_{i\sigma}$) denotes the creation (annihilation) operator of an electron at site i with spin σ, and $\hat{n}_{i\sigma}$ is the corresponding number operator. Here, t_1 is nearest-neighbors hopping amplitude, $\alpha_\sigma t_2 e^{i\phi_{ij}}$ is the the spin-selective next-nearest-neighbor hopping amplitude with a complex phase, where $\alpha_\uparrow = +1$ and $\alpha_\downarrow = -1$. The strength of local Coulomb-like repulsion is tuned by U.

We focus on the $3N$ isolated nanoflake without trapping potential, just like we did in the previous chapter, and we focus on the interplay between magnetism, which is not enriched by the presence of the frustration effects due to the t_2 term, and the topological properties of the electronic states. In the bulk system the competition originates a phase transition between the topological insulator and the magnetic Mott insulator. In a small inhomogeneous system, we can indeed find states where only a portion of the system (the edge) is magnetically ordered, and a non-trivial topology

can survive in the rest of the system, giving rise to a solution which symultaneously features non-trivial topology and magnetism. Therefore, before entering the details of our results, we discuss how we can characterize the topological properties of an inhomogeneous system.

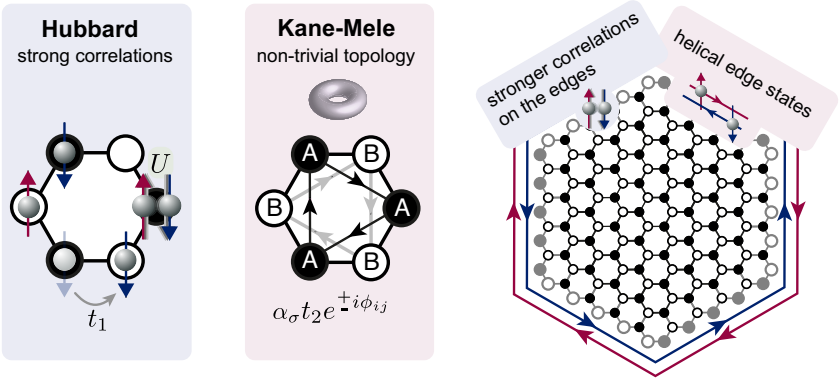

Figure 6.4: An illustration of the model where the left hexagon displays Hubbard model physics and the right hexagon shows a Kane-Mele term, where for each sublattice a different phase is picked up and each spin-component has a different sign.

6.4.1 *Topological Invariant*

In the presence of intrinsic spin-orbit interactions graphene is transformed from an ideal two-dimensional semi-metallic state to a quantum spin-hall insulator (QSHI) or $\mathbb{Z}_2$ topological band insulator (TBI) [31, 32, 123] The novel topological state makes graphene gapped in the bulk and supports transport of spin and charge along the edges. The topological nature of a large translationally-invariant systems can be measured by the Chern number [136, 137] from which we can build the $\mathbb{Z}_2$ topological index.
When translational invariance is broken, as in the case of the nanoflake, we have to resort to local topological invariants such as the local Chern marker [70, 133, 134] In order to define a local Chern marker, one needs to describe topological order in coordinates space, as opposed to momentum space. Indeed the Chern number is expressed through real-space operators as

$$\mathcal{C}_\sigma = \lim_{V\to\infty} \frac{1}{V} \int d\mathbf{r} 2\pi i \, \langle \mathbf{r}| \, x_P^\sigma y_Q^\sigma - y_P^\sigma x_Q^\sigma \, |\mathbf{r}\rangle \,, \tag{6.11}$$

where $x_P^\sigma = \hat{P}^\sigma \hat{x} \hat{Q}^\sigma$ and $y_Q^\sigma = \hat{Q}^\sigma \hat{y} \hat{P}^\sigma$ are the projected position operators in real-space. The operator $\hat{P}^\sigma$ projects onto occupied states and the projector $\hat{Q}^\sigma$ onto the unoccupied. The local chern marker that gives locally information about the topological state is defined as the integrand in Eq. (6.11), i.e

$$\mathcal{C}_\sigma(\mathbf{r}) = 2\pi i \, \langle \mathbf{r}| \, x_P^\sigma y_Q^\sigma - y_P^\sigma x_Q^\sigma \, |\mathbf{r}\rangle \,. \tag{6.12}$$

The right-hand side of Eq. (6.11) vanishes if open boundary conditions are taken, even for system which display a non-trivial topological character in periodic boundary conditions. This means that the integral of the Chern marker over the whole system must be zero.

On the other hand, for sufficiently large systems with open ends, the local Chern marker in the bulk has to coincide with the Chern number of an infinite periodic system, which is guaranteed by the properties of the wave function. The only way to reconcile these results is that at the boundaries of the open system the local Chern marker varies and reaches values opposite to the bulk result in order to ensure the vanishing of the integral in Eq.(6.11).
In view of our application, the local Chern marker allows us to define the topoloogical character on a local basis.
Another aspect to be stressed here is that usually topologically invariants such as the Chern number (or its local version) are defined for non-interacting electrons in terms of their dispersion. In this work, we have to deal with interacting systems, whose solution is not simply given by single-particle states with a well defined dispersion. Without entering the details, we use here the so-called topological Hamiltonian approach[138, 139], in which all the effects of the interactions at low-energy, can be described in terms of the zero-frequency limit of the self-energy. The latter quantity can be easily computed within DMFT and real-space DMFT, as we discussed before. Thus we obtain the topological Hamiltonian

$$\begin{aligned}\hat{\mathcal{H}}_{\sigma}^{top} = &- t_1 \sum_{\langle i,j\rangle} \hat{c}_{i\sigma}^{\dagger}\hat{c}_{j\sigma} - t_2 \sum_{\langle\langle i,j\rangle\rangle} \alpha_{\sigma} e^{i\phi_{ij}} \hat{c}_{i\sigma}^{\dagger}\hat{c}_{j\sigma} \\ &+ \sum_{i} \Re[\Sigma_{i\sigma}(\omega_0)]\hat{n}_{i\sigma},\end{aligned} \tag{6.13}$$

where $\hat{n}_{i\sigma}$ is the density operator and $\Re[\Sigma_{i\sigma}(\omega_0)]$ is the real-part of the local self-energy computed within the real-space scheme, which enters as a site-dependent single-particle potential. We can then simply solve the effective single-particle Hamiltonian $\mathcal{H}_{\sigma}^{top}|n,\sigma\rangle = \epsilon_n^{\sigma}|n,\sigma\rangle$ obtaining the eigenstates which allow us to compute the projectors $\hat{P}^{\sigma} = \sum_{\epsilon_n^{\sigma}<0} |n,\sigma\rangle\langle n,\sigma|$ and $\hat{Q}^{\sigma} = \sum_{\epsilon_n^{\sigma}\geqslant 0} |n,\sigma\rangle\langle n,\sigma|$.
In this way we can define the topological invariants and their local markers for our interacting inhomogeneous system.

6.4.2 *Antiferromagnetic ordering on the 3N nanoflake*

In the following we examine the magnetic ordering of the nanoflake keeping in mind the phase diagram of the bulk version. We remind about the role of the edges on the magnetic state discussed in the previous chapter. The main point is that, for a system which requires a critical value of U to become magnetic, such as the honeycomb lattice in the thermodynamic limit, we find AF ordering to establish for weaker interactions at the edges [96]. This general result is attributed to the fact the at the edges, strong electronic interactions are effectively stronger and therefore localizing electrons comes at a cheaper price. Thus, if we increase U we expect to develop magnetism at the edges at some value of U smaller than U_c while the bulk remains nonmagnetic until U is strong enough to magnetize the entire nanoflake.
When the SOC is included, this picture becomes even richer and the role of the edges is particularly intriguing. Without interaction the Kane-Mele model describes a QSHI with helical edge states and an insulating bulk. When the metallic edge state due to

SOC compete with the edge magnetism we can expect peculiar states different from the bulk system.

As we also discussed before, while the pure Hubbard model has full spin rotational invariance, the presence of the SOC term favors planar magnetism for large systems, while a more involved competition takes place for small systems.

To characterize the competition we compute the local out-of-plane magnetization $\langle \hat{S}^z_i \rangle = \frac{1}{2}(\hat{n}_{i\uparrow} - \hat{n}_{i\downarrow})$, where $\hat{n}_{i\sigma}$ is the local occupation at site i and spin $\sigma = \uparrow, \downarrow$ and the in-plane magnetic ordering by $\langle \hat{S}^x_i \rangle = \langle \frac{1}{2}(\hat{S}^+ + \hat{S}^-) \rangle = \langle \frac{1}{2}(\hat{c}^\dagger_\uparrow \hat{c}_\downarrow + \hat{c}^\dagger_\downarrow \hat{c}_\uparrow) \rangle$. Since the rotational invariance in the plane is not broken, we limit ourselves to the x component.

Furthermore to characterize the overall magnetic state of the flake we compute the staggered magnetization $m^{x,z}_{st} = \frac{1}{L}\sum_i (-1)^i \langle \hat{S}^{x,z}_i \rangle$, where L is the number of sites in the flake. We define a Néel-like AF state when the magnetization of sublattice A is the opposite of that of sublattice B $\langle \hat{S}^{x,z}_{i_A} \rangle = -\langle \hat{S}^{x,z}_{i_B} \rangle$, whereas a FM has the same magnetization on both sublattices. The state is ferrimagnetic when both a staggered and a uniform magnetization are present and nonmagnetic for vanishing local magnetic moments $\langle \hat{S}^{x,z}_{i_{A,B}} \rangle \approx 0$.

In Fig. 6.5 we show the global staggered magnetization of the nanoflake for different interaction regimes as a function of the SOC term t_2. The weakest presented interaction value $U/t_1 = 5.0$ is a value studied in the references about the bulk system, where an AFM Mott insulator to QSHI transition takes place upon increasing t_2/t_1. However, this value is relatively small and, according to the analysis of the previous chapter, is not promising in light of the cold-atom realization of an effective nanoflake, which requires larger interaction strengths.

We therefore consider also the interaction regimes $U/t_1 = 9.0,\ 10.5,$ and 11.25. The latter value is a candidate interaction strength to create artificial nanoflakes in the presence of a harmonic trapping potential.

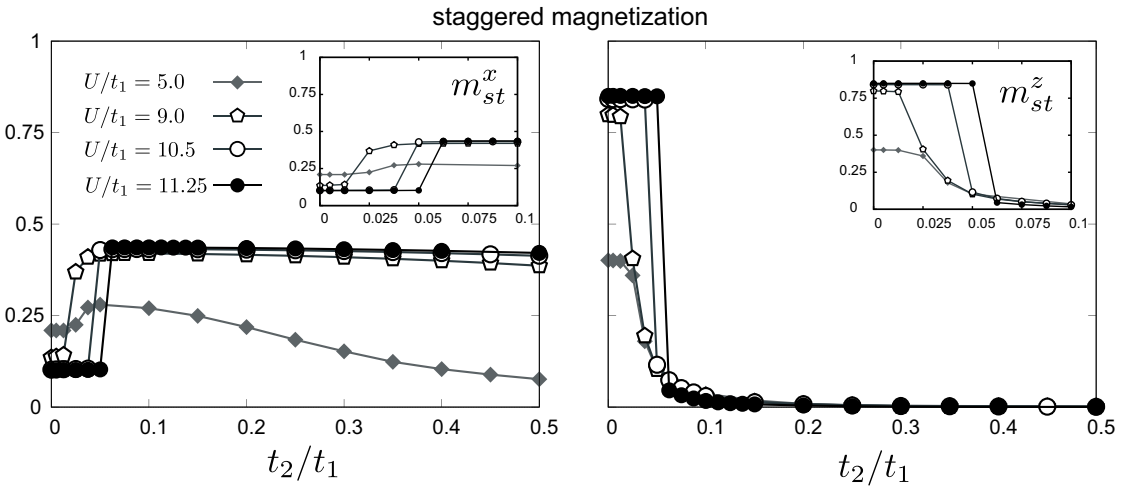

Figure 6.5: **Staggered magnetization as a function of spin orbit interaction** The staggered magnetization is shown for selected values of interaction U/t. The left figure shows the average of the transverse magnetic ordering m^x_{st} and the right figure the longitudinal m^z_{st}

For all the values of U we considered, without the SOC term, i.e $t_2 = 0$ the nanoflakes exhibits both longitudinal and transverse magnetic ordering for all the selected interaction values. This is compatible with the result of the infinite system, for which any

direction of the spin is equivalent. In our calculations on the finite flake we find that for small values of $U/t_1 = 5.0$ they strength of the magnetic moments in- and out-of plane do not differ dramatically, while in for stronger interaction values the m^z_{st} is considerably larger than the m^x_{st}. We are not able to assess whether this trend is a genuine feature of the finite-size system, or it simply depends on the direction that the iterative DMFT procedure took to achieve convergence.
The results remain close to this solution for small t_2/t_1 for the largest values of U and then they suddenly jump to a solution where the magnetization lies in the plane and the z-component completely vanishes. For smaller U we still find an evolution towards a planar AFM as t_2/t_1 grows, but the evolution becomes smoother and smoother as U decreases.
In Fig. 6.6 **a** we provide a real-space image of the magnetization along the x direction $\langle S^x(x,y)\rangle$ in the different sites of the nanoflake for $U/t_1 = 3.75$ and $t_2/t_1 = 0.55$. The value of the interaction is the same we used in the case of the nanoflake without SOC. The plot clearly shows that, as expected, an antiferromagnetic ordering forms at the edges of the flake, with a magnetization that rapidly falls when we approach the center. For larger values of U (not shown), the AF order invades instead the full flake.
In Fig. 6.6 **b** we show instead the local Chern marker $C_\uparrow(x,y)$ which demonstrates a very interesting result. The Chern number is indeed 1 in the whole bulk, where magnetism is absent, and it acquires non integer values in the boundary. Therefore we have that the nanoflake as a whole displays simultaneous AF ordering and non-trivial topology, associated with the spatial inhomogeneity of the electronic properties. This result is reminiscent of that obtained for a ribbon of the Bernevig-Hughes-Zhang model supplemented by a Hubbard repulsion [131, 133], where simultaneous edge magnetism and topologically non-trivial character has been reported.
We can rationalize this result noting that, despite the magnetic ordering breaks TRS, we have a remaining symmetry which can protect a topologically non-trivial state. In our example, the Kane-Mele model preserves axial spin-symmetry (ASS) also in the magnetic state, since the system is still invariant under rotations around the direction of the spin ordering. The topological phase where TRS is broken, but ASS is still present is called spin-Chern insulator (SCI) [124, 140]. Thanks to spin conservation in SCI's the Chern numbers for each spin-channel $\uparrow$ and $\downarrow$ can be computed independently, with an invariant $\mathcal{C}^S = \mathcal{C}_\uparrow - \mathcal{C}_\downarrow$. In our system the SCI is stabilized also by the inhomogeneity of the system, which allows to arrange the topological and the magnetic properties in different regions.
We also show the spatially resolved spectral function $A_i(\omega)$ for two sites,representative respectively of edge and bulk. The bulk is clearly insulating and that expands throughout the entire flake except for the edge, where spectral weight fills substantially the Mott gap.

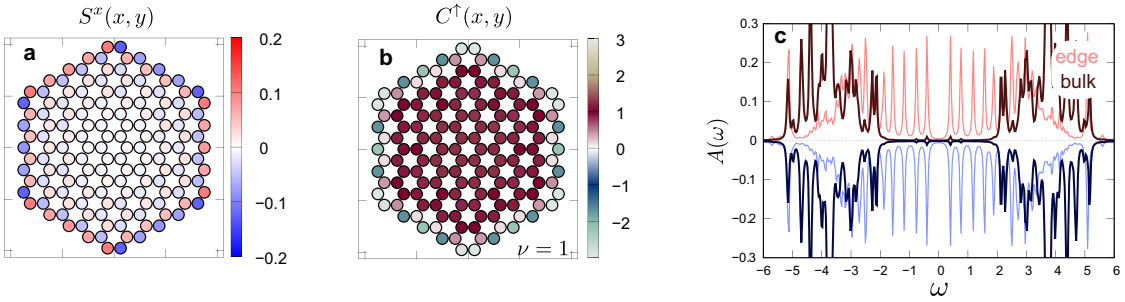

Figure 6.6: **Real space profile of magnetic and topological nanoflake** The spatially resolved magnetic moments $\langle S^x(x,y)\rangle$ (**a**) next to the local Chern marker $C_{\uparrow}(x,y)$ /(**b**) demonstrate the existance of magnetic and topological nanoflake, where magnetic order coexist with a QSHI. (**c**) The spatially and spin resolved spectral function $A_{i\sigma}(\omega)$ exhibits the existences of metallic edge states alongside with AFM ordering on the edges.

These results can not unfortunately be directly applied to real physical systems. On one hand, graphene does not show large enough SOC to make graphene nanoflakes a possible candidate to observe this new state. On the other hand, it is rather difficult to simulate them also in cold atomic experiments because the state is only found for moderate U/t_1. We have seen in the previous chapter that the idea to engineer an effective nanoflake manipulating the trapping potential is realistic only when the repulsive interaction is large enough to partially counteract the effect of the trapping potential, while in the regime of weak interactions the fermions tend to collapse (of couse respecting Pauli principle) in the center of the trap, leading to a band insulator as opposed to a Mott insulator.

While the S^x ordering is consistently the most stable magnetic state for $t_2 \neq 0$, we can still find an AF solution with magnetization along the z direction, especially for finite systems, where the competition between the two kind of ordering is closer, as we discussed above. On the other hand, being the tendency towards this ordering weaker, we expect that a larger U will be needed to give rise to the ordering. In particular, we expect that the intermediate region where magnetism is stable at the edges while the bulk is still non magnetic will be pushed to larger values of U/t_1 with respect to the in-plane solution. If this is realized, this scenario will be pushed to a range of U where we can at least hope to find an effective nanoflake in the presence of the trapping potential, making our proposal attainable within a cold-atom platform. This kind of state presents another useful feature, as the physical spin components $\uparrow$ and $\downarrow$ are associated with the ordered quantity, as opposed to the inplane magnetism, where the local magnetic moments are given by linear combinations of the physical species.

For this reason we also performed calculations inhibiting the in-plane magnetic ordering focusing purely on the out-of plane $spin-\uparrow$ and $spin-\downarrow$ interplay with the corresponding edge states.

In Fig. 6.7 we show the staggered magnetization in this solution using the same paramers as in Fig. 6.5. As expected, the z-axis magnetization is larger than in the unrestricted solution, In particular, for the three larger values of U, the magnetic cordering survives up to a significantly larger value of t_2/t_1. However, while for the largest value of U the magnetization presists in essentially the same value of the system at $t_2 = 0$ up to a very large value of t_2/t_1 and suddenly jumps into a nonmagnetic state,

for $U/t_1 = 9$ and 10.5, we find an intermediate window of t_2/t_1 in which the system has an intermediate staggered magnetization before losing any magnetism. This region is the intermediate regime that we found at small values of U for the unrestricted solution and here shifts to significantly larger interactions, as we anticipated above.

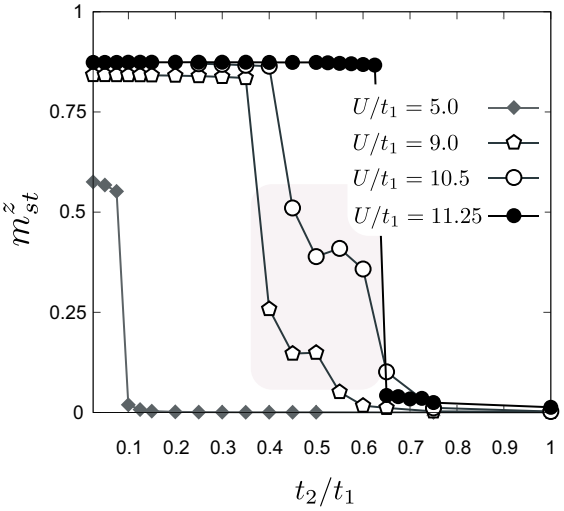

Figure 6.7: **Longitudinal staggered magnetization as a function of spin orbit interaction** The longitudinal staggered magnetization m^z_{st} upon increasing t_2 under the constraint of excluding transverse magnetic ordering for selected values of U/t_1. Coexisting regions of magnetic and topological order are illustrated by shaded areas.

We now examine in more details the real-space patterns of magnetization which give rise to the above average staggered magnetization. In Figs 6.8(a_1) - 6.8(a_3) we plot the real-space profile of the magnetic moments $\langle \hat{S}^z_i \rangle$. In this example we fix the intrinsic spin-orbit coupling amplitude to $t_2/t_1 = 0.5$ and increase the interaction strength.
Upon increasing U, the initially nonmagnetic nanoflake which we would find for small U/t_1 is progressively driven into a magnetically ordered state.
For the chose value of t_2, magnetism appears around $U/t = 9.0$. For this value a weak antiferromagnetic ordering establishes on boundary in the first and second layer, the 5N-layer - as depicted in Fig. 6.8 (a_1). For $U/t = 10.5$ the magnetic moments in the 5N- layer are much stronger compared to $U/t = 9.0$ and moreover also a magnetic ordering developed, though weaker, in the 4N-layer. The bulk only shows a small contribution to the staggered magnetization. In these regimes, the external magnetic layer coexist with an essentially nonmagnetic bulk. The radius of the layers depend on the interplay of two parameters, that is U and t_2. In agreement with the results for the overall staggered magnetization, we have also observed, though we do not not show it in an explicitly real-space profile, that for $t_2/t_1 = 0.4$ the same magnetic pattern emerges, but with stronger magnetic moments.
It is noteworthy, that we not only observe antiferromagnetic ordering in the magnetic ring, but also next-neighbor ferromagnetic correlations between the 4N- and the 5N-ring, if one looks very closely at Fig 6.8 (a_2). For $t_2/t_1 = 0.4$ this pattern is very strongly visible. This can be understood from the strong-coupling expansion we have already discussed. Due to the intrinsic spin-orbit coupling, the next-nearest-neighbor exchange is antiferromagnetic in z-direction, but ferromagnetic in the x and y direction. Clearly the z-axis ordering that we are addressing in this section is strongly frustrated.

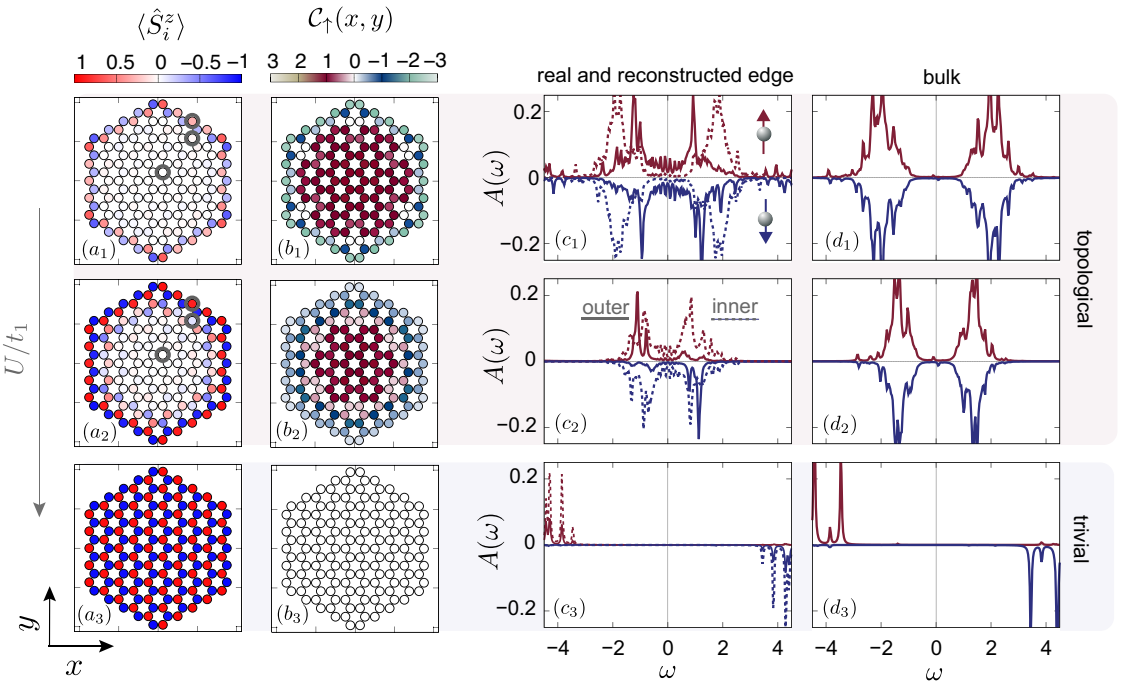

Figure 6.8: Spatially resolved local magnetic moments $\langle \hat{S}_i^z \rangle$ (a_i) , local Chern-marker $\mathcal{C}_\uparrow(x,y)$ for spin-↑-component (b_i) and local spectral function for edge (c_i) sites and bulk sites (d_i) $i = 1,2,3$ for both spin-components for increasing interaction strength across the AFM transition, $U/t_1 = 9.0$ ($i = 1$), $U/t_1 = 10.5$ ($i = 2$), and $U/t_1 = 11.25$ ($i = 3$).

One also should third-order terms into account, which are ferromagnetic in the z-direction see Chapter 4 For $U/t = 11.25$ the nanoflake is completely AFM ordered with an almost saturated magnetic moment as shown in Fig 6.8 (a_3). This state must be topologically trivial in two-dimensions.

The main question is whether, similarly to what we found for the planar ordering, we can find topologically non-trivial states when the magnetization is non-uniform. As we already discussed, topology is a non-local feature and once the protecting symmetry is broken, we might expect a sharp quantum phase transition from a topological to a trivial state breaking TRS. However, as mentioned before, the $U(1)$-symmetry around the z-axis is still conserved and topological order could coexist with the TRS-broken antiferromagnetic ordering

We can determine weather the nanoflake is in a topological state by computing the local Chern-marker (LCM) $\mathcal{C}_\sigma(\mathbf{r})$, with bulk averages of $\mathcal{C}_\sigma(\mathbf{r})$ giving the $\mathbb{Z}_2$ invariant characterizing the (QSHI). In order to avoid excessively busy figures we show in Figs 6.8 (b_1) - 6.8 (b_3) only the $\mathcal{C}_\uparrow(\mathbf{r})$ -component, since $\mathcal{C}_\downarrow(\mathbf{r}) = -\mathcal{C}_\uparrow(\mathbf{r})$, just like in a standard QSHI state.

In Fig 6.8(b_1) we report on the evolution of the LCM distribution across the magnetic transition. We observe when magnetic ordering starts to develop on the edges, $\mathcal{C}_\uparrow(\mathbf{r}) = 1$ in the bulk and undergoes positive and negative fluctuations when the edges are approached.

At $U/t = 9.0$ combining the result from magnetic profile shown in Fig 6.8 (a_1) and the LCM Fig 6.8 (b_1) we can conclude that indeed in the nanoflake the symmetry broken AFM state coexist with the topologically non-trivial state.

Upon increasing U we observe in Fig 6.8 (b_2) that the bulk area with a LCM corresponding to the $\mathbb{Z}_2$- invariant reduced. As the TI moves towards the center of the flake, the edges follow, moving towards the internal rings showing an interaction driven edge reconstruction and a preservation of the nontrivial topological character in the interior part of the bulk of the nanoflake.
To understand this result more deeply we also compute the spatially resolved spectral function. We plot the real space spectral function in Figs 6.8 (c_1)- 6.8 (c_3) on the boundary and in Figs 6.8 (d_1)- 6.8 (d_3) in the bulk. The upper panel in each figure displays the spectral properties of the spin-up component and the lower panel the spin-down component on a given site. In Fig 6.8 (c_1) the spectral function on the edge of the nanoflake displays metallic character (dark-red and dark-blue), while the spectral function on the 4N-layer already is exhibits a gap, as well as the other bulk sites as shown in Fig 6.8 (d_1). Also in the bulk we clearly see that the two spin component do not have the same spectral functions and none of them is symmetric around zero, a clear signature of the TRS breaking. In particular we see that the hole excitation of spin down fermions map to the particle excitation of spin up fermions and vice-versa. This is a crucial evidence that the topologically non-trivial state is not the conventional QSHI state, but it is the Spin-Chern Insulator which manifestly breaks TRS.
For larger interaction, with a larger magnetic ring, we observe, that real edges are now also insulating because of the large magnetic moment, but the sites of the 4N-layer are metallic as demonstrated in Fig 6.8 (c_2) supporting the behavior of the LCM in Fig 6.8 (b_2).
Therefore, the helical edge states are reconstructed in a smaller layer and separate the SCI in the spatially shrunken bulk from the magnetic external layers. The homogeneous Néel-like antiferromagnetic state is also reflected in the spectral function as plotted in Fig 6.8 (c_3) and Fig 6.8 (d_3) as well as in the lack of non-trivial topological signatures in the LCM.

6.4.3 *Dependence of the results on* t_2/t_1

We complement the analysis by showing the evolution of the local Chern marker and of the spectral functions as a function of the ratio t_2/t_1 for a moderate value of interaction $U/t_1 = 3.75$, which is a reasonable estimate for actual graphene, where some estimates give $t_2/t_1 = 0.025$
This is the interaction regime for the onset of magnetism. In large lattice, the critical interaction strength has been estimated to be $U_c/t \approx 3.87$ [108] by means of numerically exact Quantum Monte Carlo simulations. On finite size system with zigzag edges antiferromagnetic spin ordering establishes on its boundaries [93, 96, 98].

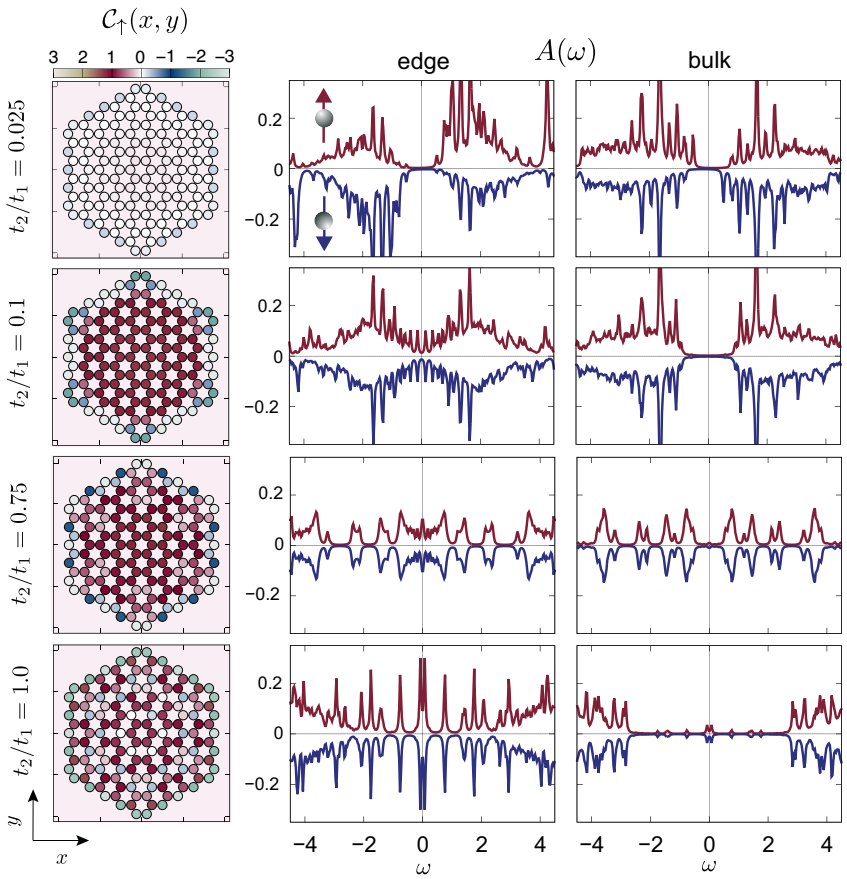

Figure 6.9: Evolution of the local Chern-marker $\mathcal{C}_\uparrow(x,y)$ for spin-↑-component (a_i) and spatially resolved spectral function for edge (b_i) sites and bulk sites (c_i) $i = 1,2,3,4$ for both spin-components of a 5N-nanoflake for increasing intrinsic spin-orbit coupling t_2 (from top to bottom) and $U/t_1 = 3.75$. The dark-red (blue) indicates the quantity for the spin-↑ (↓). Sketch (d) shows the lattice structure for two regimes of t_2 referenced to t_1.

In Fig 6.10(b_1) $A_{ii\sigma}(i\omega_n)$ and Fig 6.10(c_1) we clearly see that the system is AFM at the edge and in the bulk, while the LCM is essentially zero everywhere. Moreover we see a gap around the Fermi level ($\omega = 0$) indicating an insulator. On the edge sites these features are more pronounced while in the bulk it only hints towards a trivial antiferromagnetic insulator.
For the larger values of the spin-orbit coupling ($t_2/t_1 = 0.1, 0.75, 1.0$) Figs 6.10 (a_i)-6.10 (c_i), $i = 1, 2, 3$ the LCM is nonzero and the spectral function becomes nearly identical for the spin-up and spin-down component. We computed these quantities for the non-interacting case ($U/t_1 = 0.0$) and now they display the same behavior (we do not show this plot in order to avoid excessive plotting). Remarkably, even though $t_2/t_1 \ll U/t_1$ the system acts as if no interactions are present, describing a topologicaly non trivial insulator with metallic edges. For $t_2/t_1 = 0.1$ the LCM $\mathcal{C}_\uparrow(x, y)$ is one in the entire bulk and undergoes negative and positive fluctuations on the boundaries. The spectral function displays a metallic peak at the Fermi-level on the edge sites and an insulating gap in the bulk sites of the flake, demonstrating the existence of helical edge states. Increasing t_2/t_1 we noticedthat the LCM and the spectral function change their behavior. Though both quantities point towards a a topologically nontrivial state, i.e non vanishing LCM and metallic peak on the edges and insulting gap in the bulk, the indications are not as clean as in the $t_2/t_1 = 0.1$ example.
We can understand the effect from the limit of large t_2/t_1. When t_2 is approaching and exceeding t_1, effectively the honeycomb lattice divides into two weakly coupled copies of triangular lattices as depicted in Fig 6.10(d). Not only does the lattice structure and therefore the model change effectively, but also the system size of the triangular lattice flake is decreased and rotational symmetries are also broken. In the examples we show, the value of t_2 never exceeds the other parameters (U and t_1), but its effect is quite strong.

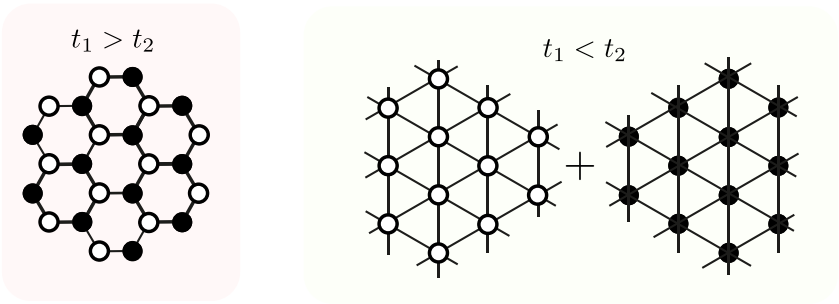

Figure 6.10: Sketch shows the lattice structure for two regimes of t_2 referenced to t_1.

6.5 EFFECTIVE NANOFLAKES IN A COLD-ATOM SETUP

In the previous sections we have highlighted that open nanoflakes of honeycomb lattice can host a very rich physics, especially if they feature a finite spin-orbit coupling t_2. While this is not the case of graphene, which has a very small SOC and moderate repulsive interaction, this regimes can be reached using cold-atoms loaded in optical lattices. In this systems we have a remarkable degree of control on the interaction, especially if a Feshbach resonance is available and on the value of the tunneling terms t_1 and t_2.

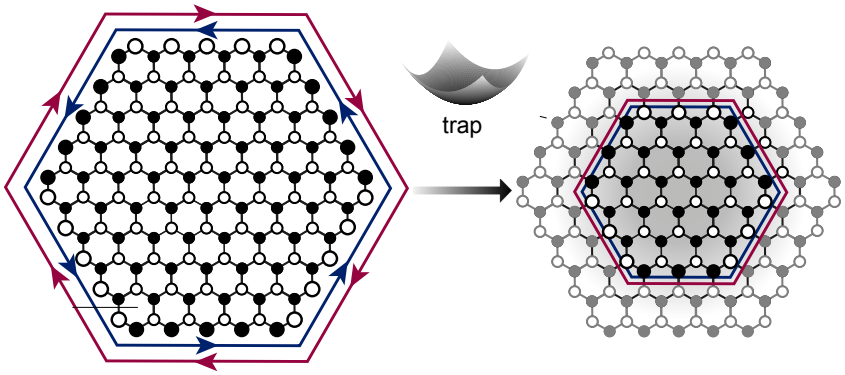

Figure 6.11: (Color online) Schematic illustration of the actual realization of a synthetic nanoflake using harmonic confinement in optical lattice electrons. Left: the desired effective flake with gapless edge states. Right: its realization via application of a trap on electrons in a graphene-like optical lattice.

In this section we use the same ideas described in Ref. [141] and in the previous chapter to confine the fermions in a limited portion of space which represents an effective synthetic nanoflake, as pictorially reproduced in Fig. 6.11. We demonstrate that the magnetic properties of a topologically non-trivial effective nanoflake can be manipulated by tuning the confining potential and the SOC t_2/t_1.

In complete analogy with the previous chapter, we consider a harmonic trapping potential superimposed to a hexagonal lattice with C_3-rotational symmetry $H_V = \sum_i (V_i - \mu)(\hat{n}_{i\uparrow} + \hat{n}_{i\downarrow})$. where $V_i = V_0 r_i^2$ is a harmonic trapping potential, $\mathbf{r}_i = (x_i, y_i)$ is the lattice vector to site i and $r_i = |\mathbf{r}_i|$. Finally, we introduced the chemical potential μ to control the number of particles in the system. In the following we fix the global atom number $N_f = 54$, which coincide with the number of sites in the 3N nanoflake. Tuning the potential amplitude V_0 we can confine the fermions in an essentially half-filled 3N flake (see Fig. 6.11), which realizes the closest situation with respect to our isolated nanoflake.

In Fig. 6.12 we show the results for a fixed optical trap with $V_0/t = 0.4$, a large value of the interaction $U/t_1 = 11.25$ and two values of the SOC term t_2/t_1 . We monitor the local density on every lattice site, the magnetization and the Local Chern marker/ For a large interaction strength and $t_2/t_1 = 0.4$ the fermions are trapped in a region which basically coincides with the 3N nanoflake. Accordingly we find a nearly perfect Néel AFM order and a topologically trivial state reflected by the vanishing LCM $C_{i\sigma} = 0$.

This configuration changes dramatically upon slightly increasing the SOC. For $t_2/t_1 = 0.5$ the density distribution within the trap becomes inhomogeneous. Half-filling is reached only in a reduced annulus of the flake, whereas regions of larger (smaller) occupation appears in the center (boundary) of the 3N flake, see Fig. 6.12 (d).

Magnetic order in this regime is largely frustrated by both the increased SOC and occupation redistribution, which reduces the tendency to local moment formation. However, a residual AFM ordering survives in the annulus region (see Fig. 6.12 (e)), where the nearly half-filled occupation favors NN-AFM magnetic exchanges. The suppression of the magnetic order unveils a non-trivial topological phase. In Fig. 6.12 (f) we show the distribution of the LCM in the nano-flake. This quantity assumes a quantized value $\mathcal{C}_\uparrow = 1$ in the bulk region of the artificial ZNGF.

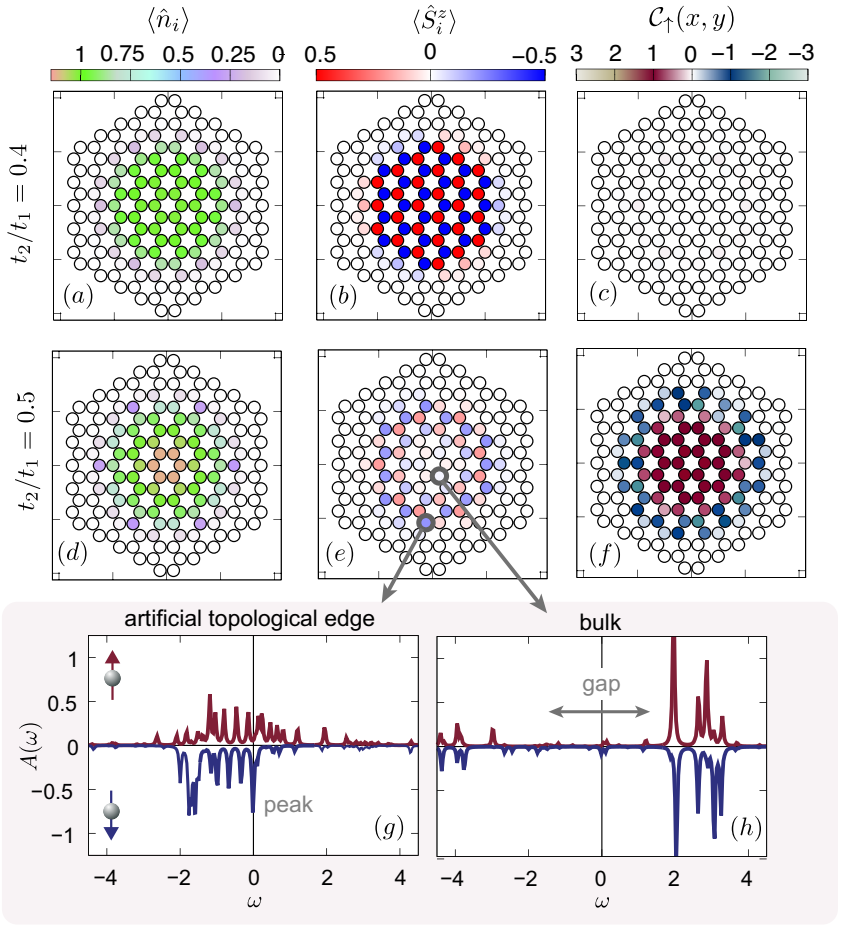

Figure 6.12: Map of the local magnetization $\langle \hat{S}_i^z \rangle$ (a_i), the local density $\langle \hat{n}_i \rangle$ (b_i), and the local Chern-marker $\mathcal{C}_\uparrow(x,y)$ (c_i) $i = 1, 2$ in the presence of a harmonic trap $V_0/t = 0.4$ and strong fermionic interaction $U/t_1 = 11.25$. Also in the presence of trap the transition from a trivial magnetically ordered state to a topologically nontrivial yet magnetically ordered state takes place upon increasing t_2.

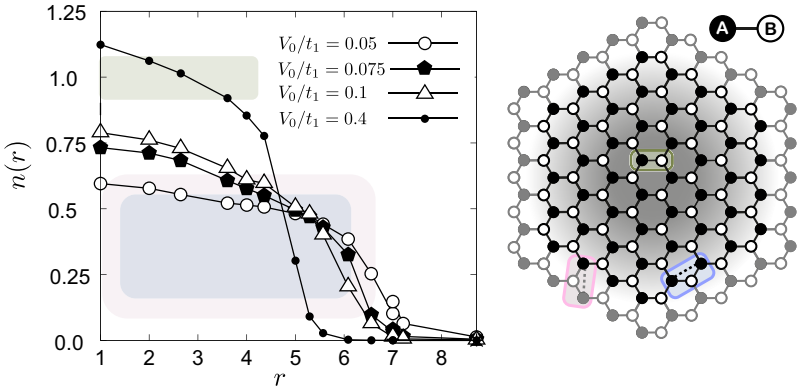

Figure 6.13: (a) Radial density distribution $n(r)$ for different potential strengths V_0. (b) shows the flake in the presence of the trap with highlighted areas corresponding to leading virtual processes shown in **Ring exchange I (II)**: Third order process leading to effective next(-nearest) neighbor ferromagnetic exchange. The green area in (a) and (b) shows the conventional AF super exchange at half-filling (see Chapter 4)

The topological nature of the system is further confirmed by the gapless edge modes localized at the system artificial 3N boundary. In panels (g) and (h) of Fig. 6.12 we present the spectral functions $A_i(\omega)$ for two sites located, respectively, on the artificial edge and in the bulk. The metallic character of the edge state is evident by the finite spectral weight at the Fermi level (panel (g)), whereas the spectral gap distributed over the entire bulk confirms the presence of a bulk insulator. The detection of true itinerant edge states is particularly important because it gives a further validation of our approach, demonstrating that the artificial nanostructure where the fermions are localized has the same properties of an actual isolated system with a well defined edge.

The modulation of the optical potential introduces new aspects in the magnetic properties of the flake, offering an example of an optical potential used to induce and control spin exchange[142, 143].

As we have already seen in the previous chapter, in the presence of a confining potential the density profile of the artificial flake is not homogeneous and, with a shape which depends on the model parameter and on the strength of the potential (See Fig. 6.12 (d) and Fig. 6.13 (a)). Assuming that the local magnetic properties are largely controlled by the density, we highlight in green the region of near half-filling, where we expect the properties of the isolated flake, and a region of near quarter-filling (pink and blue regions, see below). In the following we discuss the magnetic properties fo these regions.

In the next section we present a strong-coupling expansion, where we also assume that $\Delta\epsilon$, the difference in local energy between two sites is large. This is a situation that we expect to find for steep potentials, which is expected to be relevant close to the edges of the effective flake where the density is far from half-filling. We show below that, while the half-filled region is dominated by the standard second-order processes, in the outer region only third-order processes become relevant.

Such contributions can be constructed considering ring-exchange processes in a triangular plaquette with two spin-1/2 fermions based on the methods in the references [4, 144], see Fig. 6.14 Two sites of the plaquette belong to the sublattice A and have zero

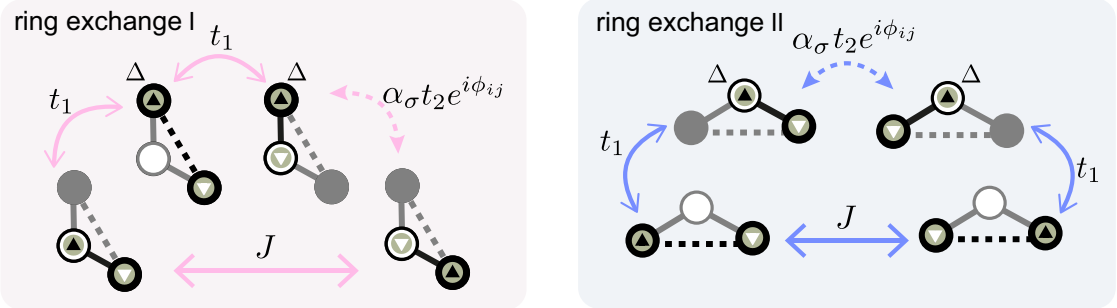

Figure 6.14: **Leading magnetic exchange in the nanoflake for shallow traps** The illustrated exchange corresponds to the regions highlighted in Fig 6.13 The virtual processes include **Ring exchange I (II)**: Third order process leading to effective Dzyaloshinskii-Moriya anisotropic exchange

on-site energy ($\epsilon_A = 0$) whereas the remaining site belongs to sublattice B and has $\epsilon_B \gg 0$.

6.5.1 *Strong coupling expansion at quater-filling*

As mentioned above, in the presence of a deep trap in a region not too close to the center we can treat also $1/\Delta\epsilon_i$, the difference of on-site energies, as a small parameter. We focus on a region where the system is around quarter filling (one fermion every two sites), a situation which can be approximately realized in the outer region of the trap as emphasized in Fig. 6.13. In the limit $U \to \infty$ double occupancy is fully excluded and magnetic exchange can only be mediated by a hole. The mechanism which leads to magnetism contains triangles with on-site energies [4, 144]. In order to obtain the effective Hamiltonian , i. e decoupling the upper and lower subbands, we treat $t_1 \ll \Delta\epsilon_i$ and $t_2 \ll \Delta\epsilon_i$ as perturbations. As a first step we consider $t_1 \ll \Delta\epsilon_i$ as perturbation and consider second order processes to eliminate contributions from $\tilde{\mathcal{H}}^0_{t_1}$ (see chapter 4). We define the Hamiltonian with the remaining terms $\tilde{\mathcal{H}}'$. Furthermore we denote with $\tilde{\mathcal{H}}_t$ the projected Hamiltonian without the effect of trap, i.e only the hopping Hamiltonian in the limit $U \to \infty$. Then in second order expansion gives

$$\begin{aligned}\hat{\mathcal{H}}^\star = \tilde{\mathcal{H}}' - \frac{1}{\Delta_1}\tilde{\mathcal{H}}^0_{t_1}\tilde{\mathcal{H}}^0_{t_1} \\ + \frac{1}{2}\left(\frac{\tilde{\mathcal{H}}^0_{t_1}\tilde{\mathcal{H}}^0_{t_2}\tilde{\mathcal{H}}^0_{t_1}}{\Delta_1\Delta_2} - \frac{\tilde{\mathcal{H}}^0_{t_1}\tilde{\mathcal{H}}^0_{t_1}\tilde{\mathcal{H}}^0_{t_2}}{\Delta_1\Delta_2} + \frac{\tilde{\mathcal{H}}^0_{t_1}\tilde{\mathcal{H}}^0_{t_2}\tilde{\mathcal{H}}^0_{t_1}}{\Delta_1\Delta_2} - \frac{\tilde{\mathcal{H}}^0_{t_2}\tilde{\mathcal{H}}^0_{t_1}\tilde{\mathcal{H}}^0_{t_1}}{\Delta_1\Delta_2}\right) + \dots,\end{aligned} \tag{6.14}$$

where Δ_1 is the energy difference due to the first Hamiltonian acting on the state and Δ_2 is the excitation energy that has to be paid due to second Hamiltonian.

For simplicity, we define clock-wise permutation operators

$$\begin{aligned}\hat{\mathcal{P}}_1^{\circlearrowleft} &= \sum_{ijk}\sum_{\sigma_1,\sigma_2,\sigma_3} t_{kj}t_{ik}t_{ji} \\ &\times \hat{X}_k^{\sigma_3\leftarrow 0}\hat{X}_j^{0\leftarrow\sigma_3}\hat{X}_i^{\sigma_2\leftarrow 0}\hat{X}_k^{0\leftarrow\sigma_2}\hat{X}_j^{\sigma_1\leftarrow 0}\hat{X}_i^{0\leftarrow\sigma_1} \\ &= -t_1^2 t_2 \sum_{ijk}\sum_{\sigma_1,\sigma_2,\sigma_3} \alpha_{\sigma_2} e^{i\Phi_{ik}}\hat{X}_i^{\sigma_2\leftarrow\sigma_1}\delta_{\sigma_1\sigma_3}\hat{X}_j^{0\leftarrow\sigma_3}\hat{X}_j^{\sigma_1\leftarrow 0}\hat{X}_k^{\sigma_3\leftarrow\sigma_2} \\ &- t^3 \sum_{ijk}\sum_{\sigma_1,\sigma_2,\sigma_3} \alpha_{\sigma_2} e^{i\Phi_{kj}}e^{i\Phi_{ik}}e^{i\Phi_{ji}}\hat{X}_i^{\sigma_2\leftarrow\sigma_1}\delta_{\sigma_1\sigma_3}\hat{X}_j^{0\leftarrow\sigma_3}\hat{X}_j^{\sigma_1\leftarrow 0}\hat{X}_k^{\sigma_3\leftarrow\sigma_2} \\ &= -t_1^2 t_2 \sum_{ijk}\sum_{\sigma} e^{i\Phi_{ik}}\left(\alpha_{\bar{\sigma}}\hat{X}_i^{\bar{\sigma}\leftarrow\sigma}\hat{X}_j^{0\leftarrow 0}\hat{X}_k^{\sigma\leftarrow\bar{\sigma}} + \alpha_\sigma e^{i\Phi_{ik}}\hat{X}_i^{\sigma\leftarrow\sigma}\hat{X}_j^{0\leftarrow 0}\hat{X}_k^{\sigma\leftarrow\sigma}\right)\end{aligned} \tag{6.15}$$

$$\hat{\mathcal{P}}_2^{\circlearrowleft} = -t_1^2 t_2 \sum_{ijk}\sum_{\sigma} e^{i\Phi_{ik}}\left(\alpha_{\bar{\sigma}}\hat{X}_i^{\bar{\sigma}\leftarrow\sigma}\hat{X}_j^{\sigma\leftarrow\bar{\sigma}}\hat{X}_k^{0\leftarrow 0} + \alpha_\sigma \hat{X}_i^{\sigma\leftarrow\sigma}\hat{X}_j^{\sigma\leftarrow\sigma}\hat{X}_k^{0\leftarrow 0}\right) \tag{6.16}$$

where we used the definitions

- (diagonal)
  $\sum_\sigma \alpha_\sigma \hat{X}_i^{\sigma\leftarrow\sigma}\hat{X}_l^{\sigma\leftarrow\sigma} = \frac{1}{2}\left(\hat{n}_i\hat{S}_l^z + \hat{S}_i^z\hat{n}_l\right)$
- (off-diagonal)
  $\sum_\sigma \alpha_{\bar{\sigma}}\hat{X}_i^{\bar{\sigma}\leftarrow\sigma}\hat{X}_l^{\sigma\leftarrow\bar{\sigma}} = \left(\hat{S}_i^+\hat{S}_l^- - \hat{S}_i^-\hat{S}_l^+\right)$

Then,

$$\tilde{\mathcal{H}}_{t_1}^0\tilde{\mathcal{H}}_{t_2}^0\tilde{\mathcal{H}}_{t_1}^0 = \hat{\mathcal{P}}_1^{\circlearrowleft} + (\hat{\mathcal{P}}_1^{\circlearrowleft})^\dagger = 4t_1^2 t_2 \sin(\phi_{ik})\hat{\mathbf{z}}\cdot\left(\mathbf{S}_i\times\mathbf{S}_k\right) \tag{6.17}$$

$$\tilde{\mathcal{H}}_{t_2}^0\tilde{\mathcal{H}}_{t_1}^0\tilde{\mathcal{H}}_{t_1}^0 = \mathcal{P}_2^{\circlearrowleft} + (\mathcal{P}_2^{\circlearrowleft})^\dagger = 4t_1^2 t_2 \sin(\phi_{ik})\hat{\mathbf{z}}\cdot\left(\mathbf{S}_i\times\mathbf{S}_j\right) \tag{6.18}$$

since $(\tilde{\mathcal{H}}_{t_2}^0\tilde{\mathcal{H}}_{t_1}^0\tilde{\mathcal{H}}_{t_1}^0)^\dagger = \tilde{\mathcal{H}}_{t_1}^0\tilde{\mathcal{H}}_{t_1}^0\tilde{\mathcal{H}}_{t_2}^0$, we evaluated all the relevant terms
there is also another term which is equivalent to $\mathcal{P}_1^{\circlearrowleft}$ but involving only next-nearest neighbor hopping processes, that is

$$\hat{\mathcal{P}}_3^{\circlearrowleft} - t^3 \sum_{ijk}\sum_{\sigma} e^{i\Phi_{kj}}e^{i\Phi_{ik}}e^{i\Phi_{ji}}\left(\alpha_{\bar{\sigma}}\hat{X}_i^{\bar{\sigma}\leftarrow\sigma}\hat{X}_j^{0\leftarrow 0}\hat{X}_k^{\sigma\leftarrow\bar{\sigma}} + \alpha_\sigma\hat{X}_i^{\sigma\leftarrow\sigma}\hat{X}_j^{0\leftarrow 0}\hat{X}_k^{\sigma\leftarrow\sigma}\right) \tag{6.19}$$

$$\tilde{\mathcal{H}}_{t_2}^0\tilde{\mathcal{H}}_{t_2}^0\tilde{\mathcal{H}}_{t_2}^0 = \hat{\mathcal{P}}_3^{\circlearrowleft} + (\hat{\mathcal{P}}_3^{\circlearrowleft})^\dagger = 4t_2^3 \sin(\Phi_\triangle)\hat{\mathbf{z}}\cdot\left(\mathbf{S}_i\times\mathbf{S}_k\right), \tag{6.20}$$

where $\Phi_\triangle = \Phi_{kj} + \Phi_{ik} + \Phi_{ji}$.

The terms with $\frac{1}{2}\left(\hat{n}_i\hat{S}_l^z + \hat{S}_i^z\hat{n}_l\right)$ come with a $\cos(\Phi)$, where in our case it is always $n\pi/2$ where $n = -3, -1, 1, 3$ and therefore zero.
Therefore the two dominant ring-exchanges, i.e. dubbed of type I and II in Fig. 6.14, carry respectively a NN and NNN ferromagnetic exchange. The resulting strong-coupling effective Hamiltonian 6.5.1 has a Dzyaloshinskii-Moriya [145, 146] (DM) form with anisotropic exchange terms induced by SOC:

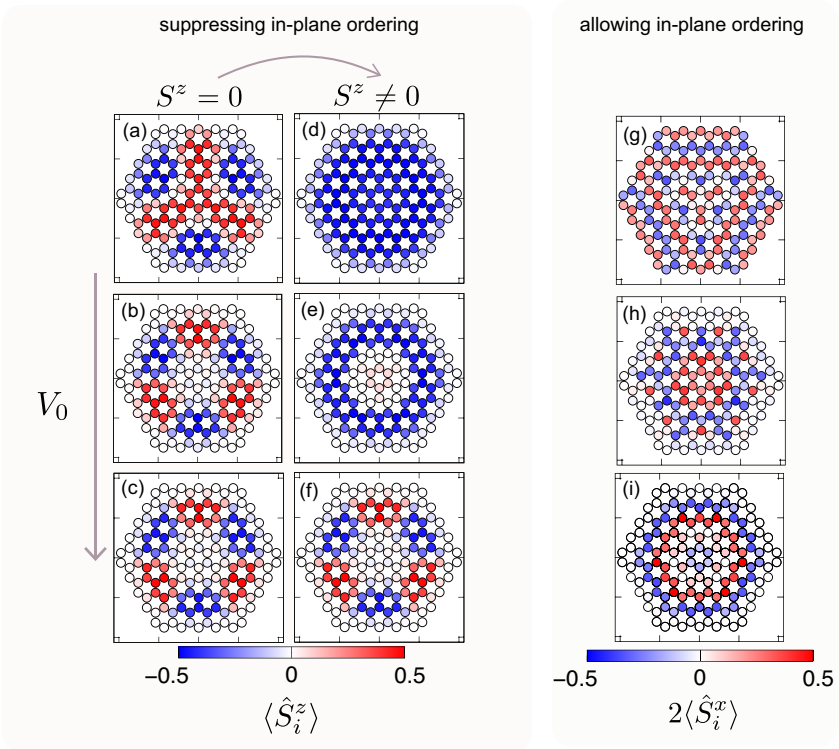

Figure 6.15: **Magnetic profile for honeycomb structure with large regions of quarter filling** The real-space resolved magnetic profile is shown upon increasing the potential strength V_0 remain a very shallow trap. first and second column only allow out-of plane ordering, while the third column includes in-plane magnetic solutions. The tendency is towards an in-plane configuration, though once stabilized the out-of plane ordering it is energetically favorable to remain in this configuration. The first column has an additional constrain on the entire system, namely S^z of the entire system has to be zero, while the second column allows for a finite average magnetization in favor of FM ordering. The last column was computed without constrains on the magnetic ordering. (a),(d) (g) show a nanoflake with $\langle n_i \rangle = 0.36$ with large FM regions. (b), (e),display the ordering at a shallow trap $V_0/t = 0.075$ and (h) $V_0/t = 0.05$ and (c), (f), (i) $V_0/t = 0.125$ displaying a clear magnetic ring in the quarter filling region, while the region close to half-filling is non-magnetic.

$$\hat{\mathcal{H}}^{\triangle} \approx \sum_{i,\delta,\eta} D_\delta \, \hat{\mathbf{z}} \cdot \mathbf{S}_i \times \mathbf{S}_{i+\delta} + D_\eta \, \hat{\mathbf{z}} \cdot \mathbf{S}_i \times \mathbf{S}_{i+\eta} \tag{6.21}$$

, where the couplings are $D_\delta = D_1$, $D_\eta = D_2 + D_3$, with $D_{1,2} \propto t_1^2 t_2 \sin(\phi_{i+\eta,i})/\epsilon_{1,2}$, $D_3 \propto t_2^3 \sin(\Phi_{\triangle})/\epsilon_3$ and $\epsilon_1 = \Delta_{i+\eta,i+\delta}(\Delta_{i+\eta,i+\delta} + \Delta_{i+\delta,i})$, $\epsilon_2 = \Delta_{i+\delta,i}(\Delta_{i+\delta,i} + \Delta_{i+\eta,i})$, $\epsilon_3 = \Delta_{i+\eta_0,i} + \Delta_{i+\eta,i}$, $\Delta_{ij} = V_i - V_j = V_0(\mathbf{r}_i^2 - \mathbf{r}_j^2)$. Finally $\Phi_{\triangle}$ is the phase of a triangle with three hopping events performed with t_2 and η_0 denotes the NNN vector to a hole. The effective DM, directly determined by the harmonic potential, is the source of FM ordering which compete with the tendency of the strongly interacting system to create AFM order.

We now compare the RDMFT results with these strong-coupling expectations. We first discuss the solution suppressing in-plane magnetic ordering. The system is initially prepared in a nearly homogeneously quarter filled flake using a shallow poten-

tial ($V_0 = 0.05$). This configuration displays homogenous ferromagnetic ordering as predicted by the perturbative argument, due to sufficiently large on-site energy differences. Slightly increasing the potential to $V_0 = 0.075$ induces a redistribution of the fermions in the flake. The occupation in the central region increases, creating a small paramagnetic region where no ordering tendency prevails. The effective boundary of the system is moved towards the 4N layer. Near the edge an annulus composed of 2 layers is at quarter filling and shows a stable FM ordering. Upon further increasing V_0 pushes the central region towards the half-filling. AFM correlations start to develop at both short (NN and NNN) and longer range, i.e. beyond NNN [96]. Because the half-filling regime is only approximately attained near the center, such correlations are not enough to create an AFM bulk. Yet, the edges of the 2N region dictate antiferromagnetic ordering on the all the armchair defect edges. This induces a ferromagnetic state in each in C_6-rotational sector in the quarter-filled region where the sign of the magnetic moment alternates on the armchair defect edge. These magnetic domain walls are a particular feature of the honeycomb structure with open boundaries and C_3-rotational symmetry. We can describe such magnetic regions as a collective spin of each ferromagnetic sector within the effective spin-model description. For larger confining potential strength an Néel AFM order establishes near the boundary which have occupation close to one. A homogenous AFM order in the 3N nanoflake can be created by tuning the SOC, as discussed above.

Allowing for in-plane magnetic ordering the solution of the first and second column obtained by forcing out-of plane ordering, remains stable and is energetically close to the solution in the last column. However, when the system is not stabilized in any specific configuration the honeycomb structure prefers in-plane ordering. The last column displays a clear chiral magnetic ordering which can be attributed to the dominating Dzyaloshinskii-Moriya anisotropic exchange which prefer spin spiral ordering with rotational character.

6.6 CONCLUSIONS

In conclusion, we studied the interplay of magnetic order and band topology in a graphene-like system of correlated fermions, realizable in cold-atom experiments. We addressed the interplay between topological properties and magnetic ordering triggered by the interactions in an isolated flake, showing the possible coexistence of magnetism and non trivial topology.

We demonstrated that a confining potential can actually be used to simulate an effective topological nanoflake, but also to manipulate the magnetic order in the system, tuning it into the desired state. In particular, using a strong-coupling expansion, we pointed out the direct relation between the leading spin-exchange mechanisms governing the magnetic properties in our system and the amplitude of the confining potential. We benchmarked these prediction with real-space DMFT calculations, showing the evolution of the magnetic ordering in presence of an optical trap. Our analysis adapts to the challenge of combining strongly interacting fermions and artificial gauge fields in cold-atomic experiments. Theoretical understanding of the influence of harmonic potential in the determination of the magnetic state paves the way to the design and realization of artificial correlated topological states. Although more realistic setup can

be envisaged to better compare with experiments, the qualitative scheme presented here offers a solid starting point to achieve this goal.

7

MULTIORBITAL SELECTIVE MOTT TRANSITION

7.1 INTRODUCTION

Multicomponent quantum systems in the presence of strong correlations emerge as a new paradigm from particle physics to material science [35–38, 40, 41, 147–149]. Especially in solid state, the expression 'multicomponent' usually refers to systems having more than two components. A two-component system is indeed a kind of minimal model in solid state, where we have in mind a single band of spin-1/2 fermions. As we shall discuss in the following, one can realize a multicomponent fermi system in solids where $M > 1$ atomic orbitals with spin 1/2 are relevant, or in cold-atom systems [14, 28, 58, 59, 61], where we can have fermions labeled by the nuclear spin, which can be, for example $S = 5/2$, which leads to 6 spin components.
The main reason for the interest in these systems is that the increased number of components is not a mere complication, but it can lead to novel physics which [14] is out of the reach of standard two-component Fermi system. Indeed when the system under consideration retains full rotational invariance in the multicomponent manifold, the physics of strong correlations is not qualitatively changed, and the Mott transition essentially follows the picture we described in Chapter 3.
The picture becomes much richer when the symmetry between the orbitals is broken, either in the form of the interaction and/or in the single-particle properties (for example if the different orbitals have different hopping amplitudes) [39]. Under these circumstances, novel phenomena can be realized. In this chapter and in the following we focus on selective phases, with the orbital selective Mott [35, 37, 149, 150] transition as the paradigm, a transition after which some components are Mott localized while others are still mobile. In the solid state context this phenomenon occurs in different situations, and it is typically favoured by the exchange coupling between orbitals, which favours high-spin configurations [38].
This so called "orbital selectivity" is the key concept for understanding various materials such as the popular iron-based superconductors [40, 148, 151–154] and other compounds with multiorbital low-energy electronic states. In order to identify the basic mechanism leading to orbital-selective physics, one can start from a simple model in which the symmetry between two otherwise degenerate orbitals is broken by their different hopping amplitudes. Indeed it has been found, that orbital selective insulators can be obtained for sufficiently large ratio between the hopping amplitudes as well as energy splittings that lead to strong density polarization among the orbitals with distinct degrees of correlation. The key role for stabilizing orbital-selective phases is played by the Hund's exchange coupling [151, 155] which breaks the orbital degeneracy of the interaction favoring high-spin state. This implies also an effective decoupling

between the orbitals, measured by vanishing interorbital charge correlations. However, solid-state platforms don't allow direct realization of these simple models which in turn precludes a direct verification of the elementary mechanisms triggering orbital selectivity. A clean and highly controllable framework can be provided by ultracold gases in optical lattices, in which a prototypical experimental system can be engineered in order to access directly orbital selective physics and its microscopic mechanism. In these atom-based quantum simulators the the selective behavior, namely, a splitting between the energy levels, can be realized via Raman processes (section 2.3.2). The presence of a tunable coupling between flavours, explicitly breaks the global symmetry of the many-body system and thereby enhances localization and flavor-selective behavior reminiscent of the physics dominating multi-orbital materials. In this thesis we analyze the fundamental physics behind the orbital selectivity combining theory and numerical simulation in collaboration with cold atomic experiments. This chapter addresses the origin and context of selectivity as well as a basic theoretical understanding of the orbital decoupling mechanism behind the selective Mott transition.

7.2 ORBITAL-SELECTIVE MOTT TRANSITION IN MULTIBAND SYSTEMS - SOLID STATE EXAMPLES

The physics of strongly correlated materials is governed by the metal to Mott insulator (MIT) transition. The basic mechanism for the localization of electrons can be explained by the Coulomb repulsion U dominating the kinetic energy gain t, which is typically given by the bare bandwidth $W = 2D$. This straightforward picture works for simple models, such as the single band Hubbard model, however real materials have more degrees of freedom and typically several orbital components are involved in these transition, as in the case for transition-metal oxides . In the orbitally degenerate case the on-site atomic states depend only on the total local charge, but the degeneracy might be lifted by crystal-fields, the Coulomb exchange energy J, and orbital dependent hopping amplitudes. These effects can dramatically revise the conventional MIT. One of the most spectacular examples is the iron-based superconductor in which the selective Mottness is induced by the Hund's coupling which decouples the charge excitations in different orbitals. It can be understood as a collection of single-band doped Mott insulators, where the degree of correlation in each orbital is determined by doping.
We can write down a general minimal model representing the basic physics occurring in iron-based super conductors [152]:

$$\hat{\mathcal{H}}_{Fe} = \hat{\mathcal{H}}_0 + \hat{\mathcal{H}}_{int} \tag{7.1}$$

compared to simple single band Hubbard model also here we have a term $\hat{\mathcal{H}}_0$ modeling the kinetic energy on a tight binding level, but with a more complex structure including intra-orbital and inter-orbital hopping and reads

$$\hat{\mathcal{H}}_0 = \sum_{i\neq j}\sum_{m,m'}\sum_{\sigma} t^{ij}_{mm'}\hat{c}^{\dagger}_{im\sigma}\hat{c}^{\dagger}_{jm'\sigma} + \sum_{i,m,\sigma}(\epsilon_m - \mu)\hat{n}_{im\sigma}, \tag{7.2}$$

where $\hat{c}^{\dagger}_{im\sigma}$ ($\hat{c}_{im\sigma}$) denotes the fermionic creation (annihilation) operator with index lattice site i orbital m and with spin $\sigma = \uparrow, \downarrow$, and $\hat{n}_{im\sigma}$ is the corresponding number operator. $t^{ij}_{mm'}$ is the multi-orbital extension of the conventional hopping amplitude

(Eq. (2.8)), ϵ_m is the orbital dependent on-site energy, and μ the chemical potential controlling the density. The external electronic structure of iron is composed of 5 d orbitals as depicted in Fig 7.2 upper panel which are the dominating contribution in the iron based materials. The interaction in these materials is modeled by the Kanamori Hamiltonian

$$\begin{aligned}\hat{\mathcal{H}}_{int} =& U \sum_{i,m} \hat{n}_{im\uparrow}\hat{n}_{im\downarrow} + U' \sum_{i,\sigma} \sum_{m>m'} \hat{n}^{d}_{im\sigma}\hat{n}_{im'\bar{\sigma}} \\ &+ (U' - J_H) \sum_{i,\sigma} \sum_{m>m'} \hat{n}_{im\sigma}\hat{n}_{im'\sigma} \\ &,\end{aligned} \tag{7.3}$$

where $\hat{n}_{im\sigma}$ is the electron occupation operators at site i and orbital m with spin σ. The interactions involve the conventional Coulomb repulsion U, is the strength controlling $U' = U - 2J_H$) the intra-orbital repulsion and inter-orbital Coulomb repulsions and J_H is the Hund's coupling. In Ref. [40] they discuss the orbital decoupling mechanism on doped $BaFe_2As_2$ and stoichiometric KFe_2As_2 and show that each orbital is basically a doped single-band Mott insulator, responsive to its own filling. The orbital resolved quasi-particle weight as a function of doping and orbital filling provides a clear understanding of multi orbital materials as shown in Fig. 7.1. The orbital selective Z displays behavior reminiscent of the typical single band transition, where Z is proportional to the doping and goes to zero at half-filling.

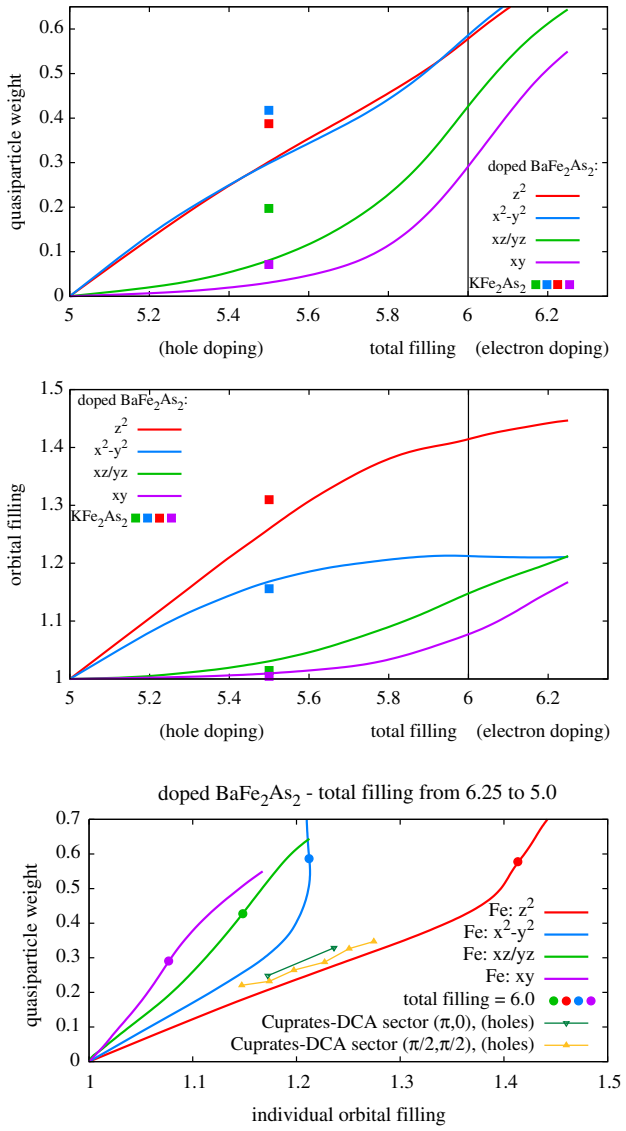

Figure 7.1: Orbitally resolved quasi-particle weight Z_α and orbital filling for doped $BaFe_2As_2$ and stoichiometric KFe_2As_2 (squares) taken from reference [40]. These were computed within slave-spin mean field.

The elementary mechanism leading to orbital selectivity in the iron bases materials can be studied in the framework of cold atoms. We illustrate a simple comparison between iron orbitals and Raman coupled ^{173}Yb atoms used in cold atomic experiments for simulating orbital selective physics. In the following section we build a a theoretical basis for a Raman coupled SU(3) symmetric version of the Hubbard that later in Chapter 8 is studied ^{173}Yb cold atomic experiments.

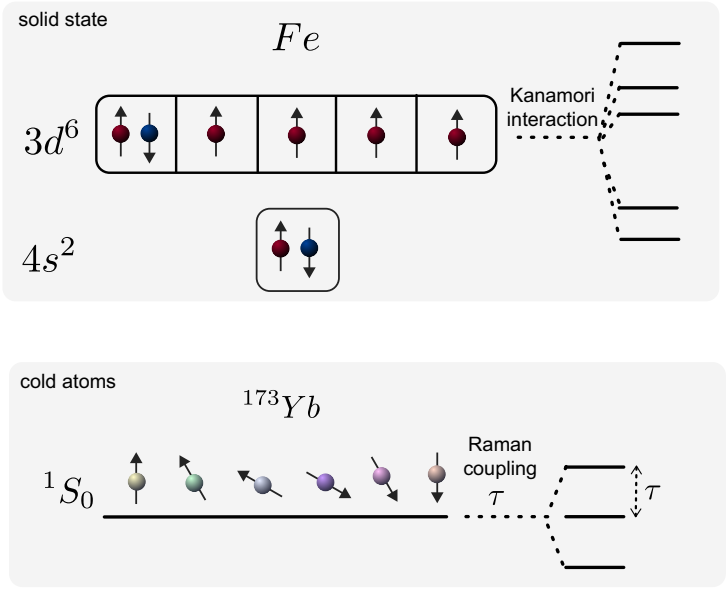

Figure 7.2: **Sketch of orbital selective system in different context**The upper figure illustrates the hybdidization of d orbitals in Iron atoms where the splitting of the levels is induced by the Kanamori interaction which contains the Hund's coupling. The lower figure displays the nuclear spin mixing due to Raman coupling of a SU(N) symmetric ^{173}Yb gas.

7.3 SELECTIVE INSULATORS WITHIN THREE-COMPONENT FERMIONIC GASES WITH BROKEN SU(3) SYMMETRY AND SYMMETRIC COUPLING

One of the simplest setups for studying selective phases is given by three-component gas with couplings among the flavors that have a real amplitude. In this section we review the results of Ref. [156], where the general formalism and a specific realization of the Raman-induced breaking of SU(N) symmetry have been introduced.

In this work it has been introduced a coupling between different spin states which can also be understood as hopping in a synthetic dimension with spin ladders as depicted in Fig. 7.3 [156–158]. In the language of gauge fields and cold atoms, this choice corresponds to zero magnetic flux and therefore this model addresses purely selective physics coming from the interplay for an external field and Mott localization. The general model Hamiltonian is given by

$$\begin{aligned}\hat{\mathcal{H}} = &- t \sum_{\langle i,j\rangle,\alpha} (\hat{c}^{\dagger}_{i\alpha}\hat{c}_{j\alpha} + h.c) + \sum_{i,\alpha,\beta} (\hat{c}^{\dagger}_{i\alpha}\tau_{\alpha\beta}\hat{c}_{i\beta} + h.c) \\ &+ U \sum_{i,\alpha<\beta} (\hat{n}_{i\alpha} - \frac{1}{2})(\hat{n}_{i\beta} - \frac{1}{2}) - \mu \sum_{i,\alpha} \hat{n}_{i\alpha},\end{aligned} \tag{7.4}$$

where $\hat{c}^{\dagger}_{i\alpha}(\hat{c}_{j\alpha})$ is the creation (annihilation) operator of a fermion with flavor α at site i and $\hat{n}_{i\alpha} = \hat{c}^{\dagger}_{i\alpha}\hat{c}_{i\alpha}$ is the corresponding number operator. amplitude t is the strength of the nearest-neighbor hopping, U is the local repulsion among the fermions and μ is the chemical potential, which controls the particle number of the system. Note that here the formalism is not restricted to $SU(3)$, but to N spin components. The so called "Raman" matrix $\tau_{\alpha\beta}$ is a $N \times N$ matrix and couples the internal degrees of freedom locally. Considering only real amplitudes, the matrix is real and symmetric with zero diagonal elements.

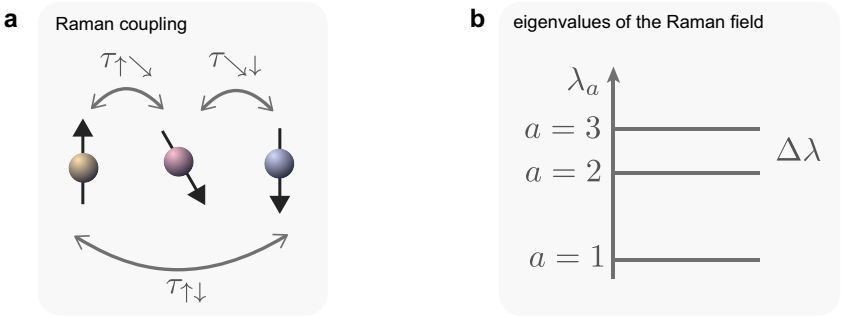

Figure 7.3: **Raman coupling - hopping processes along synthetic dimensions** Schematic illustration of the $SU(3)$-Raman matrix emphasizing the interpretation of hopping processes along synthetic dimension (**left**) and its corresponding eigenvalues (**right**).

In ^{173}Yb cold atomic experiments the hopping processes along synthetic dimensions can be realized by means of Raman transitions between the hyperfine states [157, 158]. In these setups set ups nearest-neighbor processes ($\tau_{\uparrow\downarrow=0}, N \geqslant 3$) have been implement so far, though the coupling of next-nearest spin species and higher order can be realized. In the following we will consider only the $SU(3)$ case. Diagonalizing a general $SU(3)$ Raman matrix we obtain complicated eigenvalues [156], that display the breaking of the $SU(3)$ symmetry . For this theses we only consider $\tau_{\uparrow\downarrow} = 0$ where the structure of the eigenvalues simplifies dramatically to $\lambda_1 = -\sqrt{\tau^2_{\uparrow\searrow} + \tau^2_{\searrow\downarrow}}$, $\lambda_2 = 0$, and $\lambda_3 = +\sqrt{\tau^2_{\uparrow\searrow} + \tau^2_{\searrow\downarrow}}$, where the order $1, 2, 3$ corresponds to the ordering from lowest to highest eigenvalue and they are equally spaced. For sake of convenience and clarity we are going to work in the basis which diagonalizes the Raman matrix. A canonical transformation in spin space is possible since the interaction remains invariant. For $\tau_{\uparrow\searrow} \neq \tau_{\searrow\downarrow}$ and $\tau_{\uparrow\downarrow} = 0$ the normalized eigenvectors remain a little complicate and moreover depend on the value of the couplings. However for $\tau_{\uparrow\searrow}, \tau_{\searrow\downarrow} \equiv \tau$, the eigenvectors are independent of the couplings

$$\begin{aligned}
\nu_1 &= \frac{1}{2}(1,-\sqrt{2},1) \quad (\lambda_1 = -\sqrt{2}\tau) \\
\nu_2 &= \frac{1}{\sqrt{2}}(-1,0,1) \quad (\lambda_2 = 0) \\
\nu_3 &= \frac{1}{2}(1,\sqrt{2},1) \quad (\lambda_3 = +\sqrt{2}\tau) \\
&.
\end{aligned} \tag{7.5}$$

and the fermionic operators transform as

$$\begin{aligned}
\hat{\Psi}_p = \begin{pmatrix} \hat{c}_\uparrow \\ \hat{c}_\searrow \\ \hat{c}_\downarrow \end{pmatrix} = \hat{U}\hat{\Psi}_R = \begin{pmatrix} 1/2 & -1/\sqrt{2} & 1/2 \\ -1/\sqrt{2} & 0 & +1/\sqrt{2} \\ 1/2 & +1/\sqrt{2} & 1/2 \end{pmatrix} \begin{pmatrix} \hat{c}_1 \\ \hat{c}_2 \\ \hat{c}_3 \end{pmatrix} \\
= \frac{1}{2} \begin{pmatrix} \hat{c}_1 - \sqrt{2}\hat{c}_2 + \hat{c}_3 \\ \sqrt{2}(\hat{c}_1 + \hat{c}_3) \\ \hat{c}_1 + \sqrt{2}\hat{c}_2 + \hat{c}_3 \end{pmatrix}
\end{aligned} \tag{7.6}$$

All the calculations are performed in the Raman basis with flavors $\alpha = 1,2,3$. In addition of being formally simple it is also a good basis for characterizing the orbital selective behavior since the Green functions and self-energies are diagonal in this basis and therefore also the quasi-particle weight, that is a good quantity to describe a Metal insulator transition.

7.3.1 *Density-driven Mott transition within non-degenerate Raman levels*

In this section we review some results about the Mott transition in the $SU(3)$ system as discussed in Ref. [156]. We recall the most conventional example in the $SU(2)$ Hubbard models. As it is well known, a Mott transition can be driven by the interaction U if the occupation is fixed to an integer number, or by a change of the density which drives the system towards an integer filling, as long as the interaction is large enough. For weak interactions the model displays a Fermi-liquid behavior and for increasing interaction undergoes a transition to a correlation driven Mott-insulator. In order to stabilize a Mott phase the density per site has to be exactly integer, hence in the $SU(2)$ case the only possibility is one particle per site, which is the half-filling condition.
For $SU(N > 2)$ a Mott state is possible for more integer fillings as long as they are smaller then the total number of flavors, i.e generally for $SU(N)$ $\langle \hat{n} \rangle = m$, $m \in 1,..,N-1$. A direct way to study the density-driven Mott transition is to follow the evolution of the density as a function of the chemical pontential. This also entails the evaluation of the charge compressibility $\kappa = \partial n/\partial \mu$, which is the derivative of the density with respect to the chemical potential. When the latter quantity vanishes, a gapped stated is reached, while a diverging compressibility signals the occurance of a phase separation. Further information about the type of transition can be taken from the effective masses m^*, which diverge in a Mott localized state.
The $SU(3)$ Hubbard model in the absence of τ has three degenerate levels and undergoes a Mott transition when the density corresponds to 1 or 2 fermions per site. Notice

that in this case, and for every odd number of components, the Mott transition can not happen at half-filling, which corresponds to 1.5 fermions per site. In the absence of any symmetry breaking, the two Mott transitions occur at the same critical $U_c \simeq 3.5D$. For finite τ/D the transition from a Metal to an insulator occurs for a smaller critical interaction value $U_c(\tau) < U_c(0)$ and it acquires a flavour-selective character which is particularly evident in the the Raman basis We discuss the example of $U/D = 2.5$. In

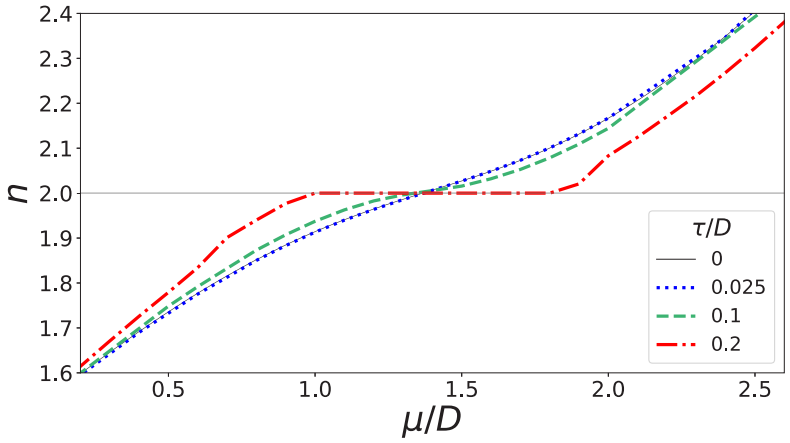

Figure 7.4: **Density driven Mott transition for raman coupled interacting** $SU(3)$ **fermions** The total density n as a function of the chemical potential μ/D is shown for four selected values of τ/D. The interaction strength is $U/D = 2.5$. Figure is taken from Ref. [156].

the absence of the external field the interaction value is too low for a Mott state and the curve grows smoothly for increasing μ as shown in Fig. 7.4. The behavior does not change until a critical value of τ is reached. Fig. 7.4 shows $\tau/D = 0.20$ for which the density displays a dramatically different behavior as for lower and zero τ values. The smooth increasing behavior is interrupted by a clear plateau at $\langle \hat{n} \rangle = 2$ in a range of chemical potential $1 < \mu \lesssim 1.9$. This plateau marks the existence of an incompressible state and the opening of Mott gap.

These result demonstrate that, if we fix the interaction to $U = 2.5D$, we observe a transition from a metal to a correlation-driven insulator by switching a sufficiently large τ. This result may appear very counterintuitive especially if we use the language of the synthetic dimension, where τ acts as a hopping in the finite extra dimension defined by the internal-spin state.

Intuitively, one might expect the opposite effect, that the critical interaction value U_c is pushed to a larger value by τ because an extra hopping channel is expected to favour delocalized metallic states over the localized Mott insulator.

The reason for this intriguing opposite behavior is due to the correlation-induced redistribution of fermionic density between the itinerant states corresponding eigenstates of the local Raman matrix. In other words the main effect of τ is to build linear combinations of the original spin components which turn out to localize more easily than the original fermions. In order to understand this effect it is necessary to analyze flavour-selected properties.

The left panel of Fig. 7.5 shows the orbital-resolved densities in the Raman basis as function of μ/D for three selected values of τ. It is clear that due to broken $SU(3)$

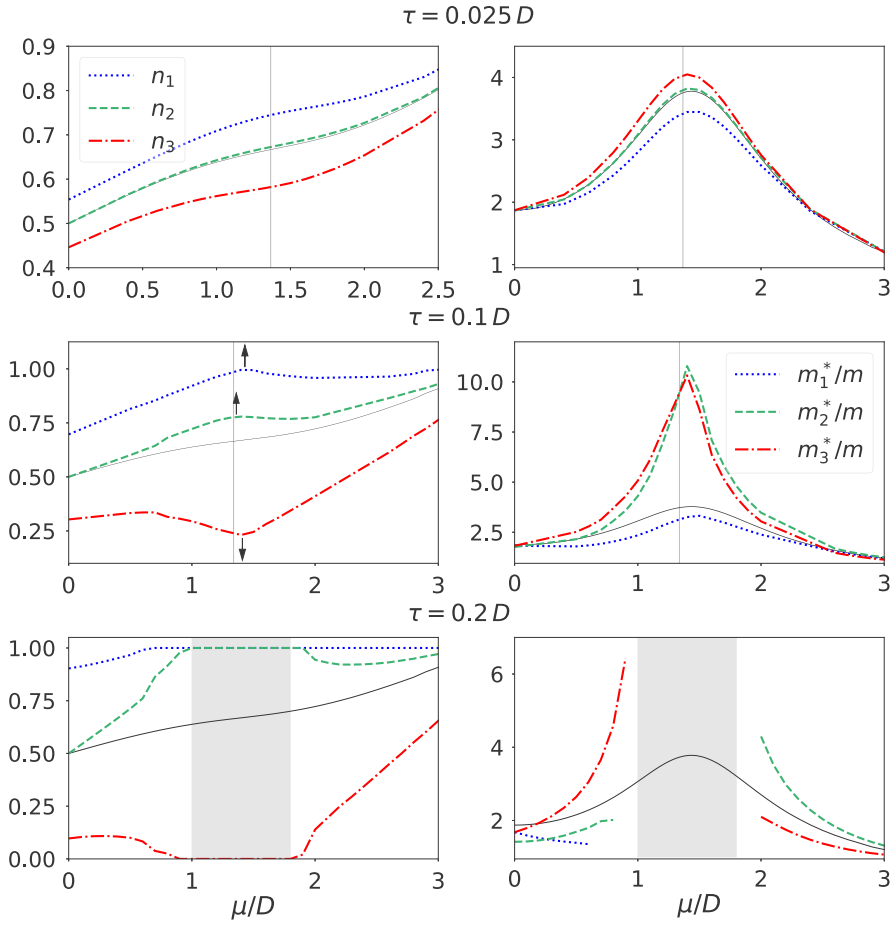

Figure 7.5: Flavor resolved densites (left) and effective masses (right) as a function of the chemical potential μ/D is shown for four selected values of τ/D. The interaction strength is $U/D = 2.5$

symmetry one expects already in the non-interacting case that the different states of the Raman basis have different occupations because they have different energy. The main point is that the interactions emphasize this effect, leading to a further differentiation in the occupations of the various levels, which becomes particularly strong in the Mott insulating state.

In the interacting regime with $U/D = 2.5$ and $\tau/D = 0.025$ the values of the orbital-resolved densities deviate from each other, but remain with the same metallic behavior as in the absence of the external field (first panel of Fig. 7.5). Further increasing τ the effective splitting between the Raman states gets enhanced until $\tau a u$ is strong enough to polarize the densities to integer filling $\langle \hat{n}_1 \rangle = \langle \hat{n}_2 \rangle = 1$ and empty occupation $\langle \hat{n}_3 \rangle = 0$ with total density $\langle \hat{n} \rangle = 2$ as shown in the last panel of Fig. 7.5. This effect is attributed to the large orbital polarizability due to strong correlations, a result which is connected with the large spin susceptibility of a standard $SU(2)$ Hubbard model.

Though the interaction strength $U/D = 2.5$ would be too weak to induce a Mott localized state, the Raman coupling indeed, pushes the degree of correlation to sufficient strong level and triggers a strongly orbital selective system.

In order to understand the flavor resolved transition and the "Mottness" of the fermionic mixture, we analyze the corresponding effective mass renormalization m^*_α/m (where m is the bare mass of the lattice fermions in the absence of the interactions) which are presented in the right column of Fig. 7.5. Generally, this quantity is a good indicator for a Mott transition by measuring the reduction of the components coherent motion. In the eigenstate basis of the Raman field this quantity is diagonal and from a theoretical point of view easily analyzed, however the direct comparison with experiment is not straightforward, because this quantity is not easily or directly accessible. A thorough comparison between theory and experiment will be carried out in the the next chapter, where we will also address the observables which are more easily compared with experimental measurements. Here we focus on a purely theoretical study which highlights the basics of our understanding of orbital selectivity in three-component Fermi systems.

In the metallic case ($\tau = 0.025$ and 0.10) the effective masses m^*_α/m have maxima around $\langle \hat{n} \rangle = 2$, but do not diverge as they suppose to in the conventional Mott transition. The lifted degeneracy of the flavor levels is reflected in the values of the effective masses, but the behaviors as a function of the chemical potential are similar, with a maximum around the chemical potential where the total density approaches $\langle \hat{n} \rangle = 2$ Note that the largest effective mass corresponds to the least occupied orbital (i.e., the one which is highest in energy).

Increasing τ we find that the effective masses of the two least populated species grow substantially suggesting that the system is entered in a highly-correlated "heavy-fermion" regime with $m^*_\alpha/m \simeq 10$, while the most populated species has a much smaller effective mass. Finally, where the Mott insulator is reached (lowest panels), we find a tendency towards a divergence of the effective mass of the lowest populated species when the chemical potential approaches the region where the Mott insulator is stable. The effective mass in not defined in this latter region, where there are no mobile quasiparticles.

Hence, the work of Ref. [156] has shown that a Raman coupling τ makes Mott localization easier, and induces strongly orbital-selective effective mass renormalization effects.

We refer to that manuscript for more examples of this physics using slightly different Raman-coupling matrices.

8

MOTT TRANSITION OF THREE-COMPONENT ^{173}Yb GASES IN AN OPTICAL LATTICE

8.1 INTRODUCTION

The previous chapter introduced "orbital selectivity" as the key concept for understanding various orbital materials and established a theoretical basis on the most elementary orbital decoupling mechanism. In order to narrow down the notion of orbital selective Mott transition, a simple SU(3) -symmetric Hubbard model designed to be realized in cold-atom experiments was analyzed in the previous chapter. The main interest of this part of the present thesis is to unveil the microscopic mechanism and build a direct connection with the experimental framework of ultracold gases in optical lattices. Generally, quantum simulations with cold atoms are highly controllable and a broad range of parameter regimes can be studied [9, 52, 120]. Though this statement is true, each cold atomic experiment has specific restrictions, while being flexible in other aspect.
The following study on the orbital selective Mott transition was performed in collaboration with the experimental group led by Leonardo Fallani at LENS and University of Florence and it was directly inspired by the work explained in the previous chapter. For this SU(N) experiment it was more convenient to implement an asymmetric tunable coupling between the flavors, more specifically, out of three flavors only two have been coupled. This novel set up, which is slightly different than the model explained in the previous chapter, needs a new basic theoretical study, that is provided in this chapter. After the purely theoretical study, a realistic and direct connection with experiment is built by including the effects of a harmonic potential by means of a local density approximation and the real experimental parameters are used. This allows us to compare the results of the experiment with our theoretical study. The elusive microscopic mechanism leading to orbital selectivity in multi-orbital materials can be verified by the cold atomic experiment and is in good agreement with our theoretical study.

8.2 EXPERIMENTAL PROCEDURE TOWARDS MICROSCOPIC MECHANISM OF ORBITAL SELECTIVITY

Before we simulate the experimental scenario within our theoretical framework, we present in some detail the experimental procedure and measurements used to detect the orbital selectivity of the electronic correlations. The experiment is based on ^{173}Yb, the fermionic isotope we have discussed before in section 2.3. In order to realize a situation close to the proposal of Ref. [156] only three of the six components are selected as depicted in Fig 8.1.

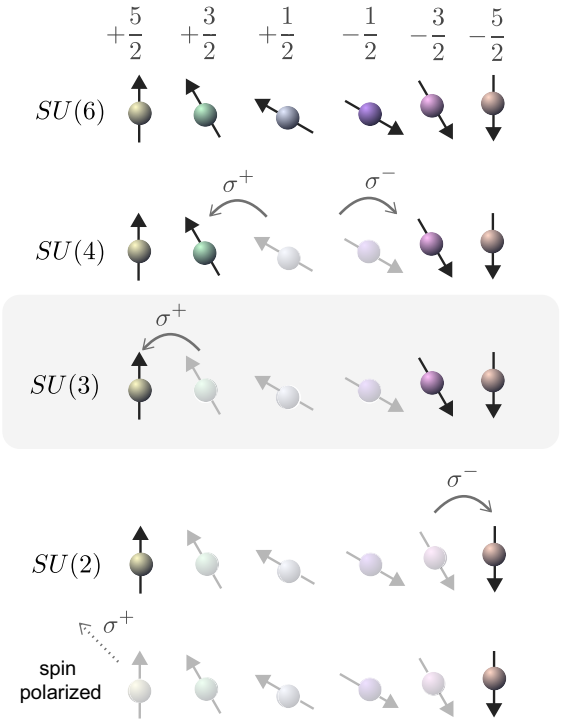

Figure 8.1: **Spin manipulation exploiting $^1S_0 \rightarrow {}^3P_1$ transition within sequential optical pumping** Schematic representation of spin preparation defining the $SU(N \leqslant 6)$ spin mixture. Via optical pumping the number of components can be manipulated through σ^+ and σ^- polarized beams

These $SU(3)$ symmetric nuclear spin states $\pm\frac{5}{2} \cap -\frac{1}{2}$ are realized by means of optical pumping schemes [66]. The main goal is to select and manipulate the nuclear spin states selectively which can be achieved by exploiting magnetic fields. Coupling two states by means of two-photon Raman coupling, breaks the $SU(3)$ symmetry thus creates dressed eigenstates states. As we discuss below, it is convenient from the experimental point of view to consider a system where only two flavors are coupled and the mixture of the three flavours has the same population.

8.2.1 *Experimental procedure towards the Raman ground-state*

In this subsection we discuss some general aspects of the present experiment and in particular of the interactions and densities which are realized experimentally and that define the theoretical model that we will address in the following.

The ground state of the Raman coupled Fermi-Hubbard model is achieved by initializing an unbalanced $SU(2)$ sample composed of optimized $|\pm 5/2\rangle = |\uparrow,\downarrow\rangle$ nuclear spin states. That means the population of each spin state was carefully adjusted by modifying the frequencies involved in the optical pumping scheme in order to obtain a $\downarrow$ sample that is $2/3$ of the entire atomic population. Then the $SU(2)$ sample including the $\uparrow$ and $\downarrow$ with $N_\uparrow/2 = N_\downarrow/2 = N_{at}/3$ is loaded in the deep 3D lattice by performing two step intensity lattice spline ramps [66]. This seemingly peculiar initial configuration, allows the experimental group to create a balanced sample composed of an equal steady population including all the three flavors $\uparrow, \searrow, \downarrow$ coherently coupled. At this stage the spin states can be coupled and the $SU(3)$ is explicitly broken. The coupling is implemented using $556nm$ Raman beams that are detuned by $1758MHz$ compared to the single-photon transition $g \rightarrow {}^3P_1$. The $\sigma^+\sigma^-$ transitions get excited by choosing the polarization of the beams orthogonal to the quantization axis, i. e in the horizontal plane, followed by a linear spin-level splitting due to the external magnetic field mentioned earlier. Since the level splitting is linear several spin-state combinations are separated by the same energy shift and undesired states are also obtained. This issue is solved by Raman processes involving spin-resolved light shifts [65]. The following point is crucial in order to understand why only two spin states are coupled instead of three as in the proposal by Ref. [156]. For each external magnetic field and light power of the Raman beams an energy shift is created for which the precise resonance condition has to be found that matches the two photon processes. This experimental procedure is quite challenging thus coupling only two levels is more convenient and sufficient enough to study selectivity. After this procedure, the experimental group prepared an equal mixture of atoms in the three nuclear spin states (orbitals) $+5/2 \equiv \uparrow$, $-1/2 \equiv \searrow$, $-5/2 \equiv \downarrow$ under the constrain $N_{5/2} = N_{-1/2} = N_{-5/2}$.

The coupling strength τ is directly measured from the Rabi oscillations [66] with frequency $\Omega_R = 6t/\tau$. After the adiabatic ramp the experimentalists obtain dressed states which are equally populated by the three flavors. This feature is very important and it forces us to focus on the equal flavour density distribution also in our theoretical calculations. When the dressed state is prepared they measure the number of atoms in double occupied sites without resolving the spin nature of the pairs $(-5/2, -1/2)$ or $(-5/2, -5/2)$.

Finally, the strength of the on-site repulsion is controlled via a modulation of t the lattice depth s. The sample is loaded in 3D optical lattices with lattice depth $s[E_R]$, which corresponds to the values of the on-site Hubbard repulsion given in the following table. Within one experimental cycle all parameters remain unchanged and only N_{at} is

lattice depth $s[E_R]$	$U[Hz]$	U/D
4	473	0.46
8	960	2.61
12	1414	9.6
15	1800	22.21

tuned.

8.2.2 *Measurements to detect Mott transitions and selective correlations*

In this section we present some details of the experimental strategy used to study orbital-selective correlations and Mott physics. In general a Mott transition is characterized by several quantities and observables, such as the behavior of the density, the compressibility and the double occupation as well as the quasi-particle weight. From a theory point of view several methods exist in order to compute the desired quantities rather easily. However, in cold atomic set ups due to experimental procedures, not all these observables can be directly measured. Fortunately, the number of doubly occupied lattice sites, often called doublons, can be measured in different ways and it provides a direct information about Mott localization and lack thereof [66, 159]
The derivative of the number of doublons D with respect to the total particle number N $\partial D/\partial N$ provides a direct information about the rigidity of the Mott state, somehow similar to the compressibility. If the system is a metal, adding new particles, naturally leads to new doublons, while in a Mott insulator, the energetic cost of double occupancy is reduced.
In general terms, the number of doubly occupied sites can be measured experimentally by photoassociation spectroscopy [71], a process involving two atoms form a bound state by absorbing a photon. It is a versatile tool and can be applied to a broad range of problems such as measuring pair correlations in strongly correlated matter. This technique is very complicated and we advise the reader to study reference [66, 71] for more details. In this experiment photoassociation is used to determine the atom-loss spectrum by applying a photoassociation pulse in order to remove multiply-occupied lattice sites. The atom-loss spectrum is determined by taking the difference of the probe when the photoassociation transition is excited due to shining resonant light (red light) and afterwards with off-resonant light (blue light).

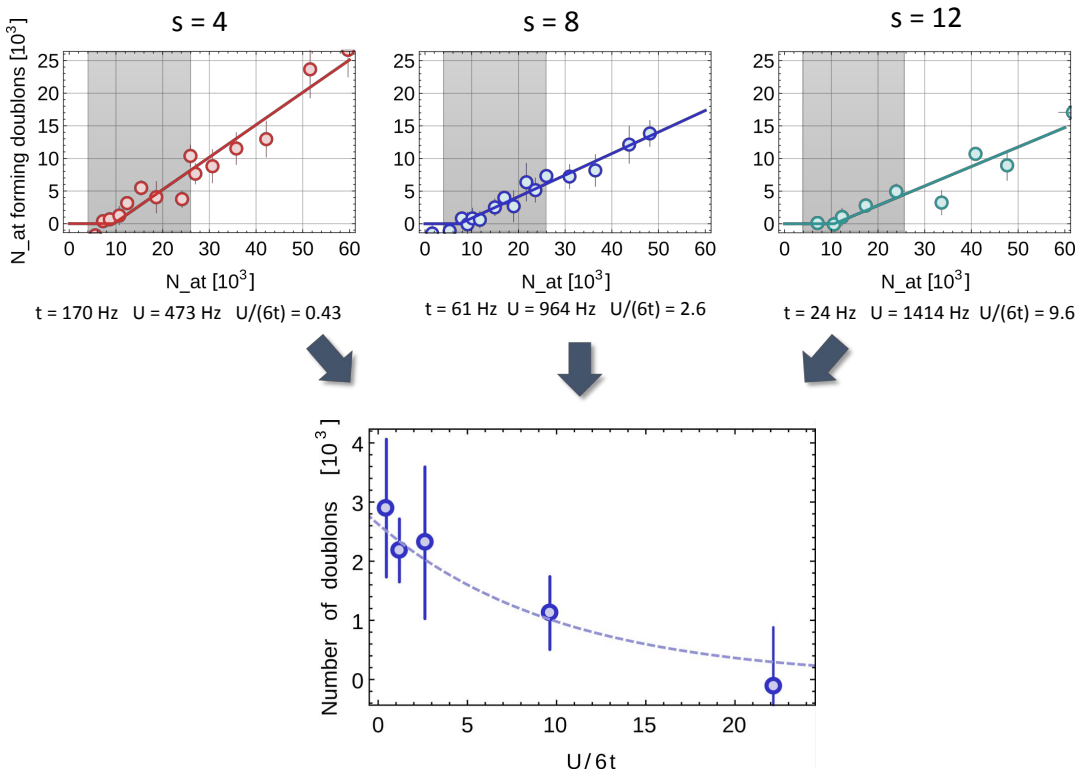

Figure 8.2: **Experimental doubly- and triply-occupied sites as a function of the number of atoms** The number of doubly occupied sites as a function of the number of atoms is shown for three different values of the trapping potential, which correspond to increasing U/D going from left to right. the bottom panel shows the average over the grey area as a global measure of the double occupation plotted as a function of U/D. The reduction of doublons as a function of the interaction strength is apparent.

The only problem of this approach is that, for a three-component system, the probe is sensitive both to double occupations and to triple occupations (triplons), and the measured signals is the sum of the two. However, if we focus on the Mott transition around $\langle n \rangle = 1$, the number of triplons is expected to be much smaller than that of doublons $\langle T \rangle \ll \langle D \rangle$, as we will show explicitly in the following.
In Fig. 8.2 we show the evolution of doublons (including triplons) as a function of the number of atoms in the absence of τ for three values of the lattice depth $s = 4E_R$ which correspond to increasing values of U/D moving from the left to the right.
The physical picture is quite simple. If the interaction is not sufficient to drive a Mott transition in the absence of Raman coupling, the number of doubly occupied sites grows smoothly and steadily by increasing the number of sites, as expected in a metallic state, where the creation of doublons is not inhibited by the Hubbard interaction.
Upon increasing the Hubbard repulsion U in the absence of τ one naturally observes a pronounced decrease in the multiple-occupied lattice sites which is a first signature towards a localized phase. The dependence on the number of atoms also highlight the onset of a Mott state. If the number of particles is relatively small, adding more particles does not increase the double occupancies, because many empty lattice sites are available. When the number of particles reaches the number of available sites (determined in turn by the strength of the trapping potential), double occupancy becomes energetically costly, hence it is unfavoured. This leads to a global decrease of D which grows slowly as the number of particles in enhanced.
In order to provide a global estimate of the degree of correlation and to improve the statistics, an average over the region marked in grey has been performed and used as the experimental estimate of the number of doublons (plus triplons) in the system. This is the marker of the degree of correlation that will be used in this chapter.
More concretely, the numbers we will present in comparison between experiment and theory in this thesis are obtained averaging between 5 thousand and 35 thousand particles

$$\frac{D}{N}(\tau) = \left[\left(\sum_{n=5k}^{35k} 1 \right)^{-1} \sum_{n=5k}^{35k} \frac{D_{at}(n)}{N_{at}(n)} \right](\tau) \tag{8.1}$$

$$\frac{D_{\alpha\beta}}{D_{at}}(\tau) = \left[\left(\sum_{n=5k}^{35k} 1 \right)^{-1} \sum_{n=5k}^{35k} \frac{D_{\alpha\beta}(n)}{D_{at}(n)} \right](\tau) \tag{8.2}$$

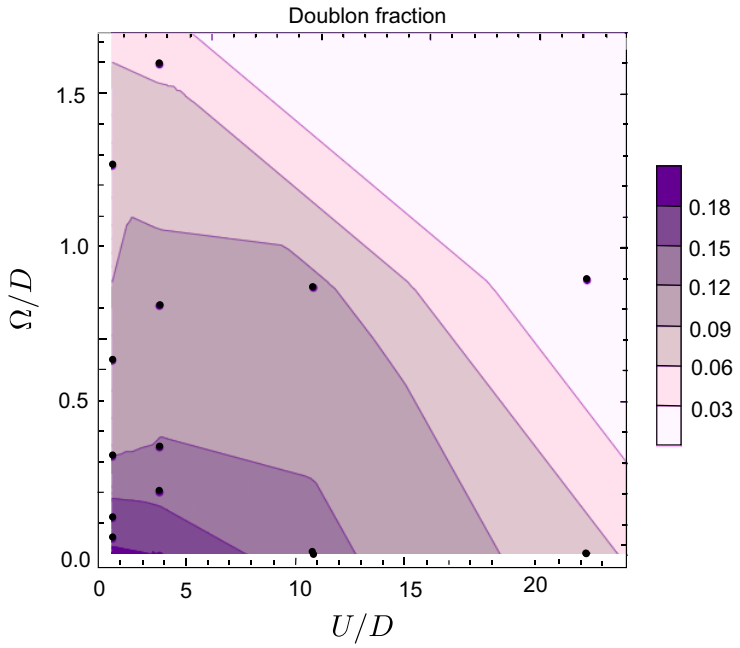

Figure 8.3: **Experimental phase diagram** The experimentally obtained phase diagram shows the doublon fraction as a function of U and τ and shows a clear reduction of doublons upon increasing the given parameters. The main points were measured and optically completed by interpolation. The figure is taken from Ref. [66]

Using this quantity we can draw a kind of exprimental phase diagram which is constructed as an intensity plot of the doublon fraction D/N. The results, summarized in Fig 8.3, exhibit a clear tendency towards reduction of doubly occupied sites upon increasing the interaction, but also by increasing the Raman coupling. This confirms already one of the two qualitative results we discussed in the previous chapter, namely the increased tendency towards Mott localization induced by increasing the Raman coupling, at odds with its interpretation in terms of hopping in the synthetic dimension.

In this section we do not show experimentally obtained results on the flavor resolved measurements since we include them in the theory discussion, which follows in the next sections. However, while a measure of the total number of doubly occupied sites is sufficient to detect a standard Mott transition, the investigation of an orbital-selective behavior requires to resolve the different kinds of doublons $\langle \hat{n}_\alpha \hat{n}_\beta \rangle$, where α and β span the different spin components, as we wil discuss in the following. Fortunately, the photoassociation spectroscopy can be adapted to achieve this goal. In particular orbital-resolved doublons can be detected applying a magnetic field which splits the photoassociation transition into three different transitions centered at different frequency, each corresponding to one of the three combination of the three spin flavors [71], as shown in Fig. 8.4. To be more precise, the number of each kind of doublon can be addressed by performing three different high-magnetic field (60G) spectroscopy runs starting from a SU(2) mixture of each flavor combination. The singular addressable resonances are reported in Fig 8.4 and allow to identify the frequency and thereby the flavor combination.

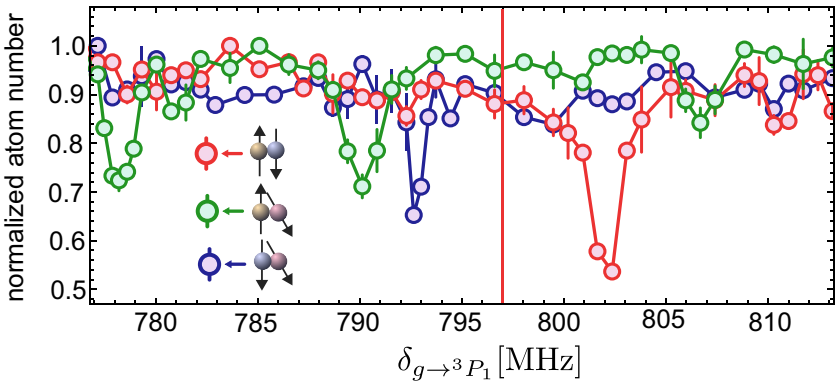

Figure 8.4: **Spectroscopies near the photoassociation resonance frequencies** The photoassociation transition at the frequency marked with a red line, splits by applying a magnetic field of 60G into three peaks corresponding to each flavor resolved doublon pair. This technique is used to selectively address different spin mixtures and thereby the detection of doubly occupied sites can be distinguished among the flavors. The figure is taken from Ref. [66] and a little modified

8.3 ORBITAL SELECTIVE MOTT TRANSITION WITHIN NON-DEGENERATE RAMAN LEVELS AND ASYMMETRIC COUPLING

In the previous section we discussed the experimental procedure for realizing and detecting an orbital selective Mott insulator inspired by the proposal of Ref. [156]. The model for the corresponding theoretical study that follows reads

$$\begin{aligned}\hat{\mathcal{H}} = &-t\sum_{\langle i,j\rangle,\alpha}(\hat{c}^{\dagger}_{i\alpha}\hat{c}_{j\alpha}+h.c)+\sum_{i,\alpha,\beta}(\hat{c}^{\dagger}_{i\alpha}\tau_{\alpha\beta}\hat{c}_{i\beta}+h.c)\\ &+U\sum_{i,\alpha<\beta}\left(\hat{n}_{i\alpha}-\frac{1}{2}\right)\left(\hat{n}_{i\beta}-\frac{1}{2}\right)-\mu\sum_{i,\alpha}\hat{n}_{i\alpha},\end{aligned} \tag{8.3}$$

where again $\hat{c}^{\dagger}_{i\alpha}(\hat{c}_{j\alpha})$ is the creation (annihilation) operator of a fermion with flavor α at site i and $\hat{n}_{i\alpha}=\hat{c}^{\dagger}_{i\alpha}\hat{c}_{i\alpha}$ is the corresponding number operator. The next-neighbor hopping is tuned by t, U is the Hubbard repulsion among the flavors and μ controls the total particle number per site i. The crucial and peculiar constituent of the model is the Raman matrix defined as

$$\hat{\tau}=\begin{pmatrix}-h & 0 & 0\\ 0 & h/2 & -\tau\\ 0 & -\tau & h/2\end{pmatrix}. \tag{8.4}$$

Note that compared to the model in the previous chapter, the matrix has diagonal terms, yet it remains traceless and hermitian. The off-diagonal term connecting components $\searrow$ and $\downarrow$ is the Raman coupling which, as we discussed in section 7.2 here couples only two species, leaving the third uncoupled. The diagonal term is instead introduced in order to impose that the population of the three flavours are the same, as in the experiment. As it will become explicit in the following, for $h=0$ and total densities in the range we are interested in, τ favors the population of the two coupled

spins $\searrow$ and $\downarrow$ (which remain identical) with respect to the uncoupled spin $\uparrow$, namely $n_{\searrow} = n_{\downarrow} > n_{\uparrow}$. Therefore the terms proportional to h are introduced to counteract this unbalance and reproduce the experimental condition $n_{\searrow} = n_{\downarrow} = n_{\uparrow}$.
This implies that, in our calculation, we do not simply need to adjust the chemical potential to obtain the desired total density, but we also have to adjust the value of h to obtain equal populations. Fig. 8.5 gives a cartoon of the effect of the field h where the position of the various spins is meant to represent the densities of the spin species. This field is necessary for achieving that all the flavour densities are equal in accordance to the experimental procedure. The interpretation of a hopping in a synthetic dimension seems here less authentic, since the hopping is only among two synthetic sites, while one synthetic site is uncoupled.

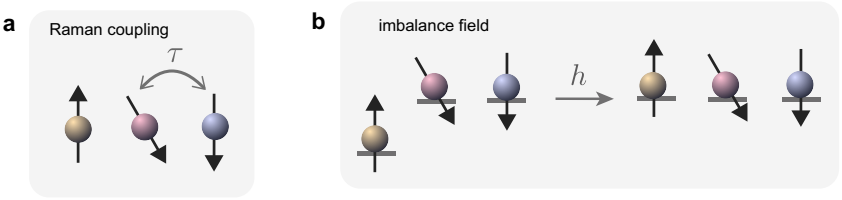

Figure 8.5: **Raman coupling and population imbalance field for experimental set up** A schematic drawing of the SU(3) Raman coupling τ, where only two flavors are coupled (**left** and the imbalance field h for controlling the flavor resolved density population $\langle n_\alpha \rangle$

8.3.1 *Eigenstates and basis transformation from Raman basis to physical basis*

For convenience reasons the computation within DMFT of the occupation numbers and other relevant quantities was performed in the Raman basis - the basis, where $\hat{\tau}$ is diagonal. Diagonalizing $\hat{\tau}$ gives the eigenvalues

$$\begin{aligned} \lambda_1 &= -h \quad \text{(uncoupled flavor)} \\ \lambda_2 &= \frac{1}{2}(h - 2\tau) \quad \text{(Raman coupled flavor)} \\ \lambda_3 &= \frac{1}{2}(h + 2\tau) \quad \text{(Raman coupled flavor)} \end{aligned} \tag{8.5}$$

with corresponding eigenvectors $v_1 = (1,0,0)$, $v_2 = 1/\sqrt{2}(0,1,1)$, and $v_3 = 1/\sqrt{2}(0,-1,1)$
Note that for adjusting the equal density distribution, the inequality $\lambda_3 > \lambda_1 > \lambda_2$ is always satisfied. Moreover the unitary matrices to transform from the Raman to the physical basis and vice versa does not depend on the parameters, τ and h. With this information we can write down the relation between the flavor resolved density and flavor resolved double occupancy in the physical basis by expressing the creation and annihilation in each basis.

$$\hat{\Psi}_p = \begin{pmatrix} \hat{c}_\uparrow \\ \hat{c}_\searrow \\ \hat{c}_\downarrow \end{pmatrix} = \hat{U}\hat{\Psi}_R = \begin{pmatrix} 1 & 0 & 0 \\ 0 & 1/\sqrt{2} & -1/\sqrt{2} \\ 0 & 1/\sqrt{2} & 1/\sqrt{2} \end{pmatrix} \begin{pmatrix} \hat{c}_1 \\ \hat{c}_2 \\ \hat{c}_3 \end{pmatrix} = \begin{pmatrix} \hat{c}_1 \\ \frac{1}{\sqrt{2}}(\hat{c}_2 - \hat{c}_3) \\ \frac{1}{\sqrt{2}}(\hat{c}_2 + \hat{c}_3) \end{pmatrix} \tag{8.6}$$

Then the densities and double occupancies read

$$\begin{aligned}\hat{n}_\uparrow &= \hat{c}_\uparrow^\dagger \hat{c}_\uparrow = \hat{c}_1^\dagger \hat{c}_1 = \hat{n}_1 \\ \hat{n}_\searrow &= \hat{c}_\searrow^\dagger \hat{c}_\searrow = \frac{1}{2}(\hat{n}_2 + \hat{n}_2 - \hat{c}_2^\dagger \hat{c}_3 - \hat{c}_3^\dagger \hat{c}_2) \\ \hat{n}_\downarrow &= \hat{c}_\downarrow^\dagger \hat{c}_\downarrow = \frac{1}{2}(\hat{n}_2 + \hat{n}_3 + \hat{c}_2^\dagger \hat{c}_3 + \hat{c}_3^\dagger \hat{c}_2)\end{aligned} \tag{8.7}$$

since in the physical basis we need all densities to be equal, we must have $\langle c_2^\dagger c_3 + c_3^\dagger c_2 \rangle = 0$. The flavor resolved double occupancies read

$$\begin{aligned}\hat{n}_\uparrow \hat{n}_\searrow &= \frac{1}{2}(\hat{n}_1 \hat{n}_2 + \hat{n}_1 \hat{n}_3 - \hat{n}_1 \hat{c}_2^\dagger \hat{c}_3 - \hat{n}_1 \hat{c}_3^\dagger \hat{c}_2) \\ \hat{n}_\uparrow \hat{n}_\downarrow &= \frac{1}{2}(\hat{n}_1 \hat{n}_2 + \hat{n}_1 \hat{n}_3 + \hat{n}_1 \hat{c}_2^\dagger \hat{c}_3 + \hat{n}_1 \hat{c}_3^\dagger \hat{c}_2) \\ \hat{n}_\searrow \hat{n}_\downarrow &= \hat{n}_2 \hat{n}_3\end{aligned} \tag{8.8}$$

In the physical basis we expect $\langle \hat{n}_\uparrow \hat{n}_\searrow \rangle = \langle \hat{n}_\uparrow \hat{n}_\downarrow \rangle$ and therefore $\langle \hat{n}_1 \hat{c}_2^\dagger \hat{c}_3 + \hat{n}_1 \hat{c}_3^\dagger \hat{c}_2 \rangle = 0$ We also need quantities in the the physical basis such as the self-energy and the quasi-particle weight, which is obtained from the self-energy. The post processing procedure can not be directly applied to the quasi-particle weight with the same transformation use for the densities, but first the constituents for the Dyson equation have to be independently transformed. The Dyson equation for obtaining the self-energy

$$\Sigma_\alpha(i\omega_n) = \mathcal{G}_{0,\alpha}^{-1}(i\omega_n) - G_\alpha^{-1}(i\omega_n) \tag{8.9}$$

Since we don't have off-diagonal terms with respect to the Raman index, we obtain for the Weiss-fields $\mathcal{G}_{0,\alpha}(i\omega_n)$ and the Greens functions $G_\alpha(i\omega_n$ the following relations

$$\begin{aligned}\mathcal{G}_{0,\uparrow}(i\omega_n) &= \mathcal{G}_{0,1}(i\omega_n) \\ \mathcal{G}_{0,\searrow}(i\omega_n) &= \frac{1}{2}\big(\mathcal{G}_{0,2}(i\omega_n) + \mathcal{G}_{0,3}(i\omega_n)\big) \\ \mathcal{G}_{0,\downarrow}(i\omega_n) &= \frac{1}{2}\big(\mathcal{G}_{0,2}(i\omega_n) + \mathcal{G}_{0,3}(i\omega_n)\big)\end{aligned} \tag{8.10}$$

$$\begin{aligned}G_\uparrow(i\omega_n) &= G_1(i\omega_n) \\ G_\searrow(i\omega_n) &= \frac{1}{2}\big(G_2(i\omega_n) + G_3(i\omega_n)\big) \\ G_\downarrow(i\omega_n) &= \frac{1}{2}\big(G_2(i\omega_n) + G_3(i\omega_n)\big)\end{aligned} \tag{8.11}$$

their inverse are simply

$$(\mathbf{G}^{\mathrm{phys}})^{-1}(i\omega_n) = \mathrm{diag}\left(\frac{1}{G_\uparrow(i\omega_n)}, \frac{1}{G_\searrow(i\omega_n)}, \frac{1}{G_\downarrow(i\omega_n)}\right) \tag{8.12}$$

$$(\mathcal{G}_0^{\mathrm{phys}})^{-1}(i\omega_n) = \mathrm{diag}\left(\frac{1}{\mathcal{G}_{0,\uparrow}(i\omega_n)}, \frac{1}{\mathcal{G}_{0,\searrow}(i\omega_n)}, \frac{1}{\mathcal{G}_{0,\downarrow}(i\omega_n)}\right) \tag{8.13}$$

$$\begin{aligned}\Sigma_{\uparrow}(i\omega_n) &= \frac{1}{\mathcal{G}_{0,1}(i\omega_n)} - \frac{1}{G_1(i\omega_n)} \\ \Sigma_{\searrow}(i\omega_n) &= \frac{2}{\mathcal{G}_{0,2}(i\omega_n) + \mathcal{G}_{0,3}(i\omega_n)} - \frac{2}{G_2(i\omega_n) + G_3(i\omega_n)} \\ \Sigma_{\downarrow}(i\omega_n) &= \Sigma_{\searrow}(i\omega_n)\end{aligned} \tag{8.14}$$

Then, we can evaluate the quasi-particle weight in the physical basis from the self-energies using the conventional formula

$$Z_\alpha = \left(1 - \frac{\partial \Re \Sigma_\alpha(\omega)}{\partial \omega}\right)^{-1} \tag{8.15}$$

8.4 OCCUPATION DISTRIBUTION

After having established how the important observable can be computed, we can finally move to the DMFT calculations for our experimentally-driven set-up for an orbital-selective three-component Mott transition.
Before discussing the Mott transition and its orbital-selective character, we discuss in some details the evolution of the observables as a function of the chemical potential μ and the results for the field h necessary to obtain democratic occupation of the physical orbitals.
This study, besides helping us to characterize the Mott transition in a similar way as what has been done in Ref. [156], is also important in view of the comparison with experiments, where we have to consider an inhomogeneous system in the presence of a harmonic trap. This will be handled by means of a local-density approximation, where the density in a given position of the trap is obtained solving for a homogenous system with the chemical potential fixed by the local value of the trapping potential.
All the calculations that we present are performed using an exact diagonalization solver (see section 3.4) at zero temperature using a Lanczos/Arnoldi diagonalization. This choice does not allow in principle a direct comparison with the experiments, which are performed at a finite temperature, which is typically a non-negligible fraction of the Fermi energy.
However, we prefer to start from T=0 for several reasons

- The $T = 0$ study highlight the intrinsic groundstate physics of the system. Temperature effects are expected to partially wash out these features. On the other hand, it is well known that the fingerprints of the Mott transition can be observed at fairly high temperatures
- The experimental temperature is not directly accessible and a rather involved comparison with theory is necessary. This is particularly true when the atoms are loaded in an optical lattice. This means that we can not just simulate the system at a given experimental temperature
- Using our ED solver, finite temperature calculations are particularly demanding, especially when the trapping potential has to be taken into account. Considering also the above points, we preferred to complete a systematic study at zero temperature instead of just a few selected finite-temperature calculations.

All the calculations are performed on a Bethe lattice and with $N_s = 6$ bath sites in the exact-diagonalization discretization of the bath. The convergence of the results for static observables as a function of N_s has been verified.

In Fig. 8.6 we plot the evolution of the field h and the corresponding eigenvalues of the Raman matrix that we obtain for a fixed value of $U/D = 2.61$ and varying the chemical potential requiring that $n_\uparrow = n_\searrow = n_\downarrow$. It turns out that for every value of the physical parameters, the order of the eigenvalues remains the same as in the absence of h with the uncoupled flavor always being the intermediate-energy state, while the odd combination of the coupled spins always has lower energy and the even combination higher energy. In the right panel we also highlight the fact that the evolution of the h-field as a function of the chemical potential μ follows the same behavior for a wide range of values of τ.

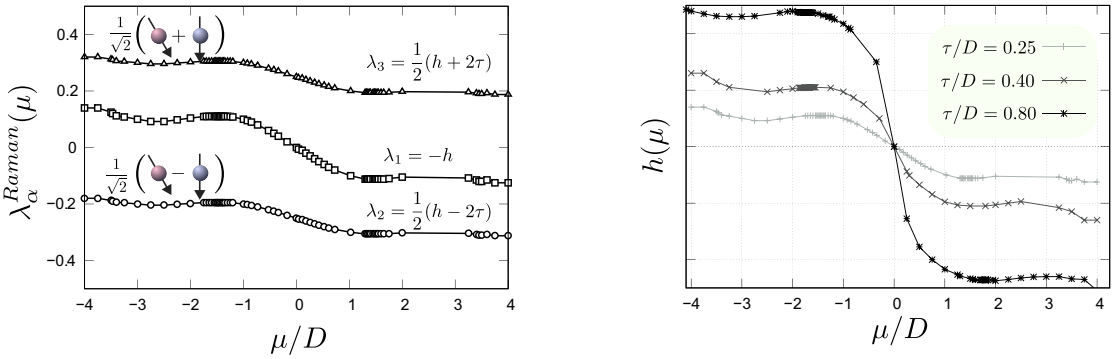

Figure 8.6: **Left:** the eigenvalues of the Raman matrix are shown for $\tau/D = 0.25$ as a function of mu/D. The eigenvalues are determined specifically to adjust the flavor densities to be equal in the physical basis for each chemical potential, i. e $\langle n_\uparrow \rangle = \langle n_\searrow \rangle = \langle n_\downarrow \rangle$. The order of the eigenvalues remains the same for each μ and each τ value. **Right:** for selected values of τ the field h for controlling the flavor imbalance is shown as a function of the chemical potential μ.

We can then move to the evaluation of the observable as a function of the chemical potential. In the left panel of 8.7 we plot the total density as a function of the chemical potential for $U/D = 2.61$, one of the values which are used in the experiment. This analysis follows directly what we reproduced from Ref. [156] in Chapter 7.

In the absence of τ we find that $n(\mu)$ grows with μ without any plateau or anomaly. This testifies that the system is in a metallic state for every density, as expected as $U < U_c \simeq 3.5D$.

When we switch on τ the curves tend to flatten horizontally around total densities $\langle \hat{n} \rangle = 1$ and 2 and plateaux are find for $\tau = 0.40$ which correspond to a vanishing compressibility $\kappa = \partial n/\partial \mu$ signalling the onset of a Mott insulating regime induced by the Raman field which closely reminds the result of Ref. [156] .

In the second and third panels, we show the evolution of double occupation $\langle \hat{d} \rangle = \langle \hat{n}_\uparrow \hat{n}_\searrow + \hat{n}_\uparrow \hat{n}_\downarrow + \hat{n}_\searrow \hat{n}_\downarrow \rangle$ and triple occupation $\langle \hat{t} \rangle = \langle \hat{n}_\uparrow \hat{n}_\searrow \hat{n}_\downarrow \rangle$. Clearly both quantities grow as the chemical potential increases thereby increasing the density. The Mott plateau are however associated with a slower growth which correspond to the higher energy cost of multiple occupation determined, in this specific case, by the Raman field.

Precisely this information will be used in the experiment to point out the selective nature of correlations.
This plot also shows clearly that in the region of chemical potential corresponding to $\langle n \rangle = 1$ the number of triply occupied sites is negligible with respect to doubly occupied sites. Hence, we can interpret the experimentally measured quantity as basically coincident with the actual number of doublons.

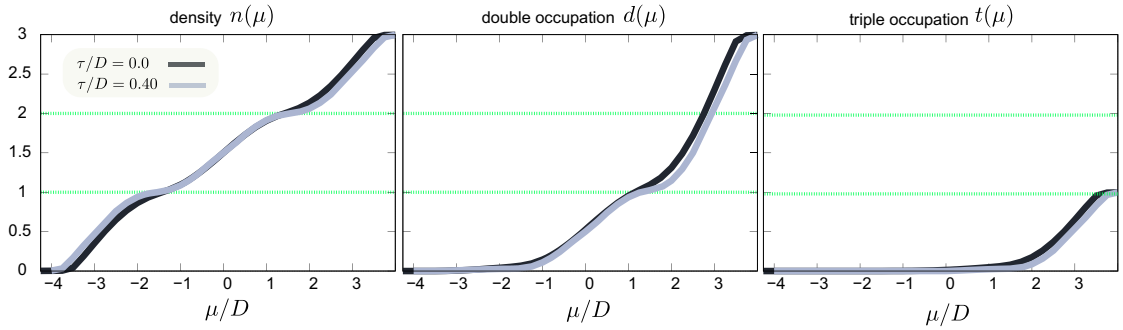

Figure 8.7: The occupation distribution as a function of the chemical potential μ/D is shown for $\tau/D = 0$ and 0.4. The first panel shows the total density $\langle n \rangle = \langle n_\uparrow + n_\searrow + n_\downarrow \rangle$, the second panel the total double occupation $\langle d \rangle = \langle n_\uparrow n_\searrow + n_\uparrow n_\downarrow + n_\searrow n_\downarrow \rangle$ and the last panel the triple occupation $\langle t \rangle = \langle n_\uparrow n_\searrow n_\downarrow \rangle$

8.4.0.1 *Mott transition at $n_\alpha = 1/3$ for a homogeneous system*

We are now in the position to study the model which describes the system realized in the ^{173}Yb-experiments. Before entering a more direct comparison with the experimental results, we first characterize the Mott transition and its orbital-selective properties in a hypothetical homogeneous infinite systems, which represents the idealized version of the experimental set-up. We consider a homogeneous system at a density of one fermion per site and we study the evolution as a function of U/D tracking the standard correlation-induced Mott transition and the possibility of an orbital-selective degree of correlation. In the Mott state with density $\langle \hat{n} \rangle = 1$ in the physical basis the occupation is distributed with $\langle \hat{n}_\alpha \rangle = 1/3$, $\alpha = \uparrow, \searrow, \downarrow$, while in the Raman basis the population is ordered according to $\langle \hat{n}_1 \rangle = 1/3, \langle \hat{n}_2 \rangle = 2/3$ and $\langle \hat{n}_3 \rangle = 0$. Therefore we have performed single-site DMFT calculations and optimized the flavour-resolved controlling parameter h and the density controlling parameter μ in order to fix $\langle \hat{n} \rangle = 1$ and $\langle \hat{n}_\alpha \rangle \equiv 1/3$ for $\alpha = \uparrow, \searrow, \downarrow$ following the evolution as a function of the two control parameters, the interaction U and the Raman coupling τ. Each pair of U and τ requires a new set of μ and h, which makes the present calculations significantly more demanding than those of Ref. [156], where the densities of the different species where left free to adapt to the value of τ and the field h was not present.
We focus on the typical observables which allow to track a Mott transition, namely the quasiparticle weight Z_α and the double occupancy $d_{\alpha\beta}$, which in the present case obviously depend on the orbital indices.

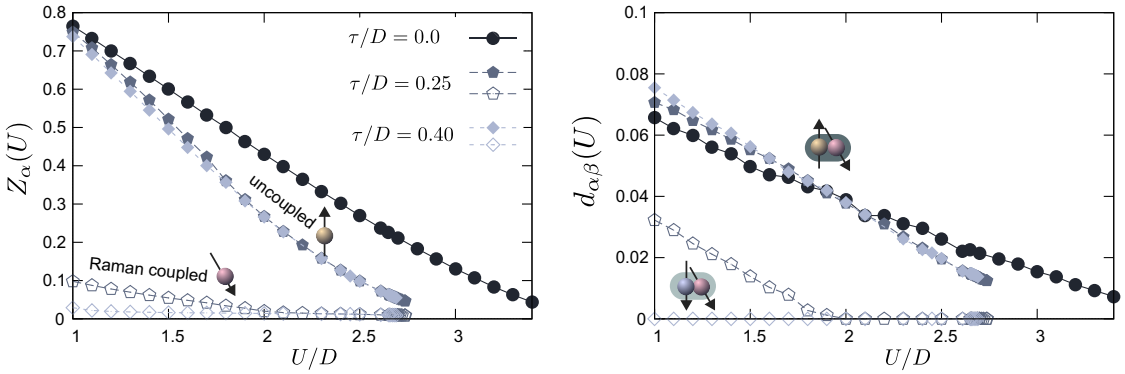

Figure 8.8: **Interaction driven Mott transition with Raman coupling** The flavor resolved quasi-particle weight Z (**left**) and the flavor resolved double occupations $d_{\alpha\beta}$ (**right**) are shown as a function of interaction strength U/D for selected values of Raman coupling $\tau/D = 0.0, 0.40$ (dark to bright). The total density $\langle \hat{n} \rangle = \langle \hat{n}_\uparrow + \hat{n}_\searrow + \hat{n}_\downarrow \rangle = 1$ is always fixed where each flavor contributes a third of the total density.

The main outcome of the analysis is that the field τ favors Mott localization, similarly to what we discussed in Chapter 7, and its orbital-selective nature. The two coupled flavours indeed become localized much more easily (for a much smaller U) than the uncoupled flavour.

Notice that this result is not a trivial generalization of [156]. While the choice of a Raman field coupling only two species is not expected to change the picture, since in the Raman basis the structure of eigenvalues is the same as for the nearest-neighbour coupling including all three flavors, the constraint $\langle \hat{n}_\uparrow \rangle = \langle \hat{n}_\searrow \rangle = \langle \hat{n}_\downarrow \rangle = 1/3$ could in principle change the picture, as it reduces the tendency towards orbital polarization in the Raman basis, which can be very strong when the interaction is large. However, the results that we report in the following demonstrate that the suppression of the polarization does not spoil the two main results, namely the reduction of the critical U for a Mott transition and the emergence of orbital-selective correlations.

In Fig. 8.8 (a) we show the flavour-resolved quasi particle weight Z_α (left) for the uncoupled species $\uparrow$ and for the two coupled species $\downarrow$ and $\searrow$. Since the Raman term couples the two latter components symmetrically, they have the same value for the quasi-particle weight and other observables. It is evident that, as soon as τ is switched on, the coupled species acquire a significantly smaller Z and a much stronger dependence on τ with respect to the $\uparrow$ spin. This is the most direct, at least theoretically, signature of orbital selectivity.

Moreover one finds that the two coupled orbitals undergo a Mott transition for a critical value $U_{OSMT}(\tau) < U_c(\tau = 0)$. Specifically for quite large $\tau = 0.40$ and $\tau = 0.80$ the $\searrow$ and $\downarrow$ components are freezing their motion already around $U/D = 2.0$ and $U/D = 1.0$ respectively, which is a very weak interaction compared to $U_c(\tau = 0)/D \approx 3.5$. On the other hand, the uncoupled component remains metallic also above $U_{OSMT}(\tau > 0)$. Still we find that $Z_\uparrow(U)$ approaches zero at $U_c(\tau > 0) < U_c(\tau = 0)$, where the full system becomes Mott insulating.

To summarize these first results, τ generally increases the overall degree of correlations, even if in a substantially orbital-selective way, and induces a collective Mott insulating state at an earlier $U_c(\tau > 0)$.

In Fig. 8.8 (b) we show the flavour-resolved double occupation $d_{\alpha\beta}(U)$ corresponding to $Z_\alpha(U)$. As we already discussed, these quantities are particularly important because they are directly measured in the experiments that accompany our theoretical work. As we shall see, these observables complete the infomation obtained by the quasiparticle weight which, despite being a theoretically useful concept, cannot be measured in an equally direct way.
As a matter of fact, also in this case, we have only two independent quantities, namely $d_{\alpha\beta}(U)$ where one of the two indices is the uncoupled species $\uparrow$ and the case where both indices belong to the coupled subset $d_{\downarrow\searrow}(U)$. We clearly see that the first quantity is only weakly affected by τ, similarly to $Z_\uparrow$, signaling that the uncoupled species dominates in this correlator. On the other hand, the double occupancy involving the two coupled species reflect the localization of both components and tracks the vanishing of the corresponding quasi-particle weight. The strong sensitivity of these orbital-selective double occupancy is a first important indication in light of the comparison with the experiments.
In order to better highlight how the Raman coupling τ favours orbital-selective Mott transitions, in Fig. 8.9 we show the evolution of the quasiparticle weights Z_α and of the double occupancies $d_{\alpha\beta}$ as a function of τ for selected interaction values $U/D = 2.30$ and 2.61.

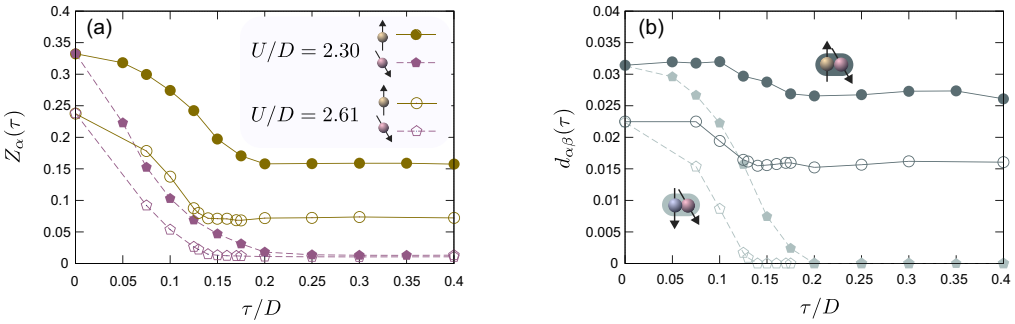

Figure 8.9: **Raman coupling driven Mott transition of interacting** $SU(3)$ **fermions** The flavor resolved quasi-particle weight Z (**a**) and the flavor resolved double occupations $d_{\alpha\beta}$ (**b**) are shown as a function of the Raman coupling $\tau aU/D$ for $U/D = 2.61$ is shown. The total density $\langle \hat{n} \rangle = \langle \hat{n}_\uparrow + \hat{n}_\searrow + \hat{n}_\downarrow \rangle = 1$ is always fixed where each flavor contributes a third of the total density.

The plots clearly show that the coupled species become Mott insulating rather rapidly as a function of U while, for these two values of the interaction, the uncoupled species remain metallic even for quite large τ.
The most interesting aspect that this plot highlights is that $Z_\uparrow$ and $d_{\uparrow\downarrow}$ not only remain finite, but they are essentially constant as a function of τ up to values of the order of 0.8 (we show in the plot only up to 0.4), twice as much as the critical τ for orbital-selective localization. This region suggests that, as soon as the coupled species Mott localize, they are essentially out of the game. Further increasing τ has not a huge effect on the uncoupled species, even if one has to keep in mind that the three flavours are always coupled by the $SU(3)$-symmetric Hubbard interaction, which makes this effective decoupling an interesting and non-trivial phenomenon.

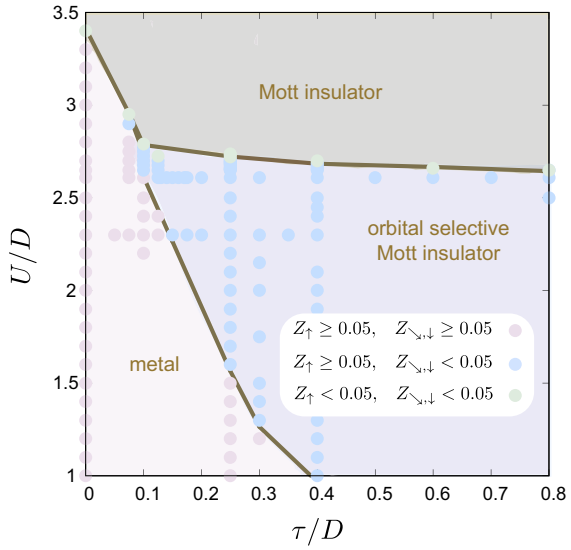

Figure 8.10: **Theoretical phase diagram on orbital selective phases** The phase diagram was obtained with single site DMFT calculations under the constrain $\langle \hat{n} \rangle = 1$, $\langle \hat{n}_\alpha \rangle = 1/3$. Flavor resolved quasi-particle weight is the main indicator in the determination of the phase regions. Computed values are denoted with dots: pink (metallic), blue (osmit), green (MIT)

We summarize the results presented in Fig. 8.8 and Fig. 8.9 and complete them by more values of τ and U (which are not shown in these figures for the sake of readability) in a phase diagram Fig 8.10. The determination of the phase boundaries are determined the behavior of the quasi particle weight as follows. In principle the Mott transition and its orbital-selective version are associated with a vanishing quasiparticle weight. Operatively, in drawing the diagram we consider a state metallic when the Z_α of all the flavors is larger or equal than 0.05 and a Mott state when they are smaller than 0.05. The orbital selective phase is characterized by the mixture of these conditions, i.e $Z_\uparrow(\tau, U) >= 0.05$ and $Z_{\searrow,\downarrow}(\tau, U) < 0.05$. Therefore, the phase boundaries can be a little blurry but the overall trend is sharp. The choice of this cutoff has been motivated by the discreteness of the bath. In a future work, we will clean this result, at least for specific values of the interaction, performing a systematic study as a function of N_s and of the fictitious inverse temperature β used to define a Matsubara frequency grid even if the calculation is performed at $T = 0$. We underline that this extrapolation is particularly demanding in this specific case because of the need to adjust the field h.

8.5 THE EXPERIMENTAL SET-UP: LOCAL DENSITY APPROXIMATION

As we mentioned above, the experimental realization of our system requires the presence of a harmonic trapping potential which constraints the atoms in a portion of space. Therefore the quantum fluid experiences, besides the optical lattice, also an inhomogeneous potential whose effect must be taken into account. The effect of the potential can be indeed also qualitative, as phases with a larger density can be hosted by the central region of the trap, leaving the external region to lower-density states. This can in-

deed favour phase separation and inhomogeneities, in particular in strongly correlated systems, where intrinsic tendency towards phase separation has been reported.
The effect of the trap can be easily described theoretically in terms of a site-dependent single-particle potential, which one can also treat as a site-dependent chemical potential $\mu(\rho)$, where ρ identifies a lattice site in terms of its distance from the center of the trap, where the trapping potential is conventionally taken as zero. The two contributions to the single-particle potential are the standard site-independent chemical potential μ_0 that controls the total particle number and a local potential strength $V(\rho)$, i.e.,

$$\mu(\rho) = \mu_0 - V(\rho), \tag{8.16}$$

where rho is a dimensionless distance (measured in lattice spacing) and the potential is given by

$$V(\rho)/E_R = \left(\frac{\pi}{2}\alpha\rho\right)^2, \tag{8.17}$$

with $\alpha = h\langle f_{trap}\rangle/E_R$, f_{trap} is the trap frequency and E_R is the recoil energy.
For comparing to the experimental data it is convenient to express all energies in units of the recoil energy E_R instead of half of the bandwidth $D = 6t$. For example we can compute the chemical potential in units of E_R as

$$\mu/E_R = \frac{\mu}{D} \times \frac{D}{E_R} \tag{8.18}$$

Furthermore, typically one measures the energies in terms of the corresponding frequencies with a natural unit in Hz. In the specific experimental setup the recoil energy was given by $E_R = 2000$Hz and the hopping amplitude $t = 61$Hz.
With this information we can compute the total particle number N_{at} and total doublon and triplon number D_{at} and T_{at}. In a Local-Density Approximation (LDA) these quantities are given by

$$N_{at} = 4\pi \int_0^\infty d\rho \rho^2 n[\rho, \mu(\rho)] \tag{8.19}$$

$$D_{at} = 4\pi \int_0^\infty d\rho \rho^2 d[\rho, \mu(\rho)] \tag{8.20}$$

$$T_{at} = 4\pi \int_0^\infty d\rho \rho^2 t[\rho, \mu(\rho)] \tag{8.21}$$

where $o[\rho, \mu(\rho)]$ is a local operator computed in a homogeneous system with $\mu = \mu(\rho)$ and o spans over density, double occupation and triple occupation operators.
We notice that in principle we could compute the local contributions to N, D and T using a real-space DMFT for a finite system. However, a realistic modeling would require a very large number of sites which coupled with the three spin components and the need to tune the field h to fix the equal-density condition, would make the calculations extremely demanding, as opposed to those of Chapter 5 and Chapter 6. Therefore we resorted, as usual in the field, to a Local-Density Approximation, where we simply assume that the local properties of our inhomogeneous system are given by the local observables computed in a homogeneous system with the local chemical potential $\mu(\rho)$. Thus in Eqs. (8.19,8.20,8.21) we use the LDA estimates defined above.

These formulas can obviously also be applied to their flavor resolved constituents. Notice that, in this specific experimental set up the measurement can not distinguish between doublons and triplons which are bot measured.
A possible experimental probe of a Mott transition and its potentially selective behavior is the measurement of double occupancies as a function of the total particle number. For our theoretical calculations, this means to compute N and D as a function of the global chemical potential and then to eliminate the chemical potential plotting D as a function of N.
As a first step we can construct the observable profile and simulate the distribution of the density and double occupied sites as well as triply occupied sites. We select $\mu_0 = 0.0,\ 0.2,\ 0.3$ which corresponds to examples in the window over which the experimental measurements are averaged. All of the profiles display signatures of Mott plateaus at $\langle n \rangle = 1$ and 2 hinting towards incompressible states.

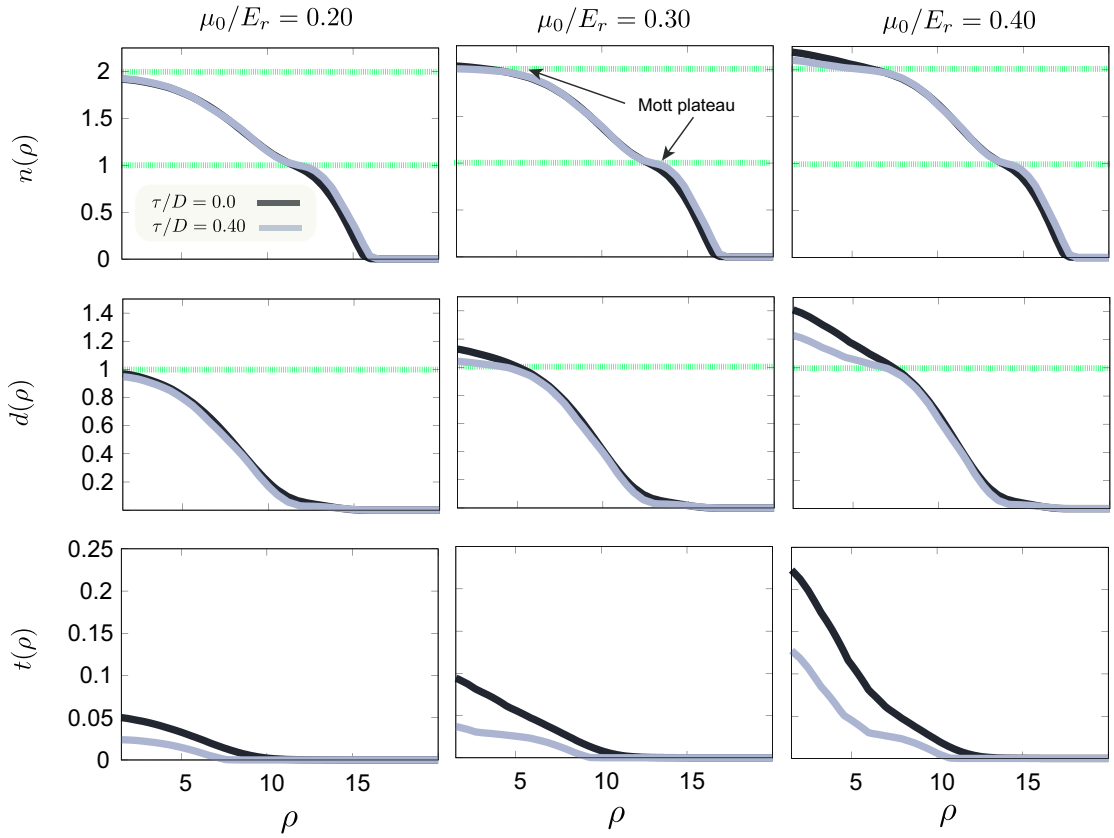

Figure 8.11: The distribution of the three different relevant observables: density (n), double occupancy (d) and triple occupancy (t) is shown as a function of the radius from the trap center. The distribution was constructed with the local density approximation and is shown for three different chemical potentials $\mu_0 = 0.2,\ 0.3,\ 0.4$ that corresponds to realistic particle number used in the experiment.

We then analyze the behavior of the total number of particles and doublons as a a function of the chemical potential μ_0. The number of particles monotonously increase upon increasing μ_0 in a way which only weakly depends on the Raman coupling τ as depicted in Fig. 8.12 (**left**). However, the total number of doublons per total atom number D_{at}/N_{at} shows some dependence on τ (Fig. 8.12 **right**) reflecting again the stronger tendency towards Mott localization in the presence of a finite Raman coupling.

Also, while N_{at} grows rather rapidly with μ_0 in the whole range that we consider, the groth of D_{at} is first very slow, then it has a rather sharp upturn around $\mu_0 \simeq 1.0$ and then bends down.

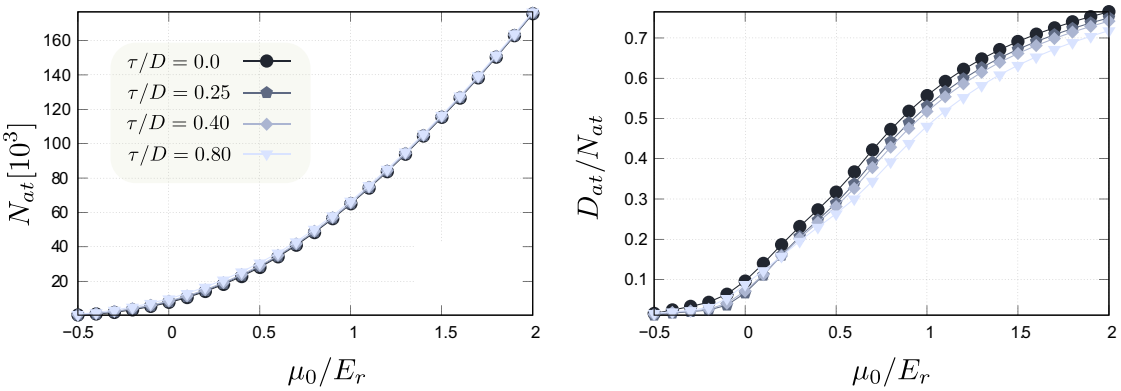

Figure 8.12: **Left:** The total atom number N_{at} is shown as a function of the chemical potential μ_0 for four selected values of the Raman coupling τ. **Right:** shows the percentage of the total number of doublons with respect to the total atom number as a function of the chemical potential μ_0 for selected values of τ/D.

These results can be easily rationalized by plotting the total number of doublons D_{at} as a function of N_{at}, as in the experiment. We first have a rather well defined region where increasing the number of particles does not lead to an equal enhancement of double occupation. This is easily understood considering that, due to the trapping potential, the particles are almost localized in a finite region of space in the center of the trap. When we add more and more fermions, they will first occupy this region. Until the number of fermions is smaller than the number of sites available in this region and if U (and τ) is such that the system wants to be in a Mott state, we can indeed add particles without creating double occupancies. When the number of particles exceed an occupation of one fermion/site, if we try to add more particle, we are bound to create doubly occupied sites and D_{at} starts to grow rapidly.

Therefore, while in a metallic state we expect a smooth growth of double occupancy as a function of the number of particles, in a Mott state we expect a rather sharp crossover. If the system is deep in the Mott state, we expect the growth of D_{at} to be slower because of the higher energetic cost of double occupancies. It must be noted that, in the presence of the trap, the change in behavior between the two regimes will be less sharp than in a lattice with a finite number of sites. Furthermore, the experiments are performed at finite temperature, which can make the crossover less sharp. Fig. 8.13 shows this information for our experimental set up. The qualitative trend of D_{at} completely confirms our expectations. In particular we find that increasing τ leads to a decrease of double occupancy and to a sharper crossover, confirming the increased localization that we predicted.

In Fig. 8.14 we present the experimentally accessible estimate of orbital selectivity. We plot indeed the fraction of double occupancy involving the two coupled species, which we have shown to be a very helpful indicator of an orbital-selective localization. We plot the combination $D_{\searrow\downarrow}/(D_{\searrow\downarrow} + D_{\uparrow\downarrow})$, which is 1 in an SU(3) Mott insulator, as shown by the data for $\tau = 0$. For finite τ we find instead this quantity starts very slow for small N_{at} and it reaches the value of 1 only asymptotically for very large number

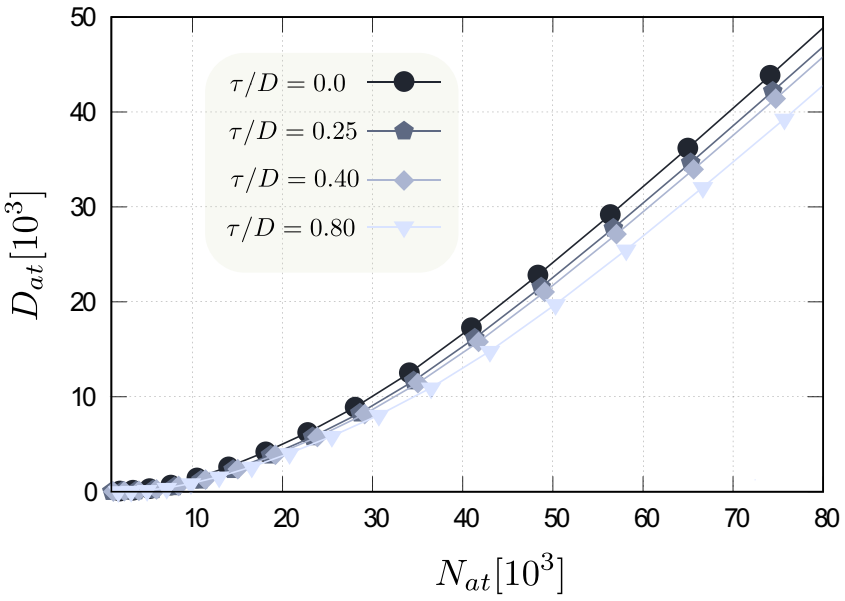

Figure 8.13: **Total doublon D_{at} number shown as a function of the total atom number N_{at}** For four selected values of the Raman coupling τ the total number of doublons in the system is shown upon increasing the total atom number. The figure demonstrates the suppression of doublons induced by the Raman coupling.

of particles, where the effect of interactions disappear because a band insulator is approached.
This confirms that, in the whole Mott insulator and in the neighbouring strongly correlated metallic solution, the correlations are strongly orbital selective and that this observable is a good probe of this physics.

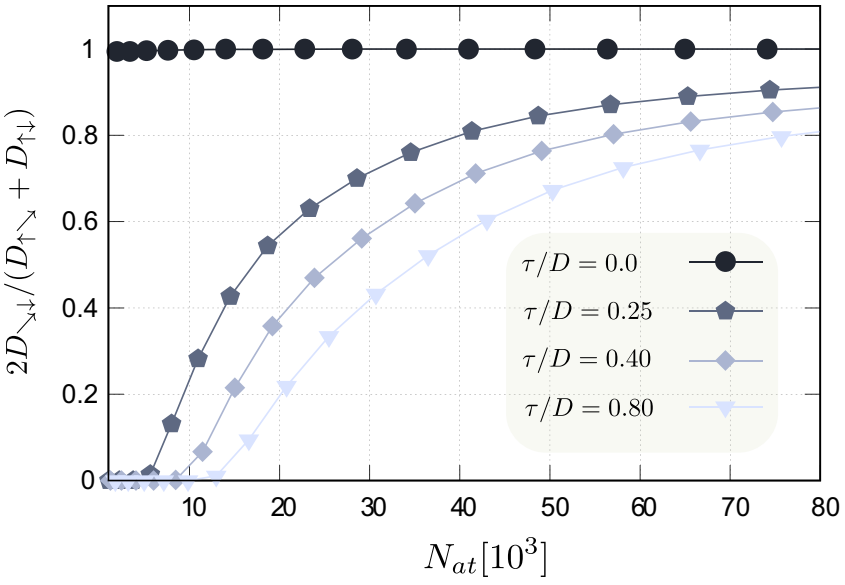

Figure 8.14: **Flavor resolved doublon fraction as a function the total particle number** The doublon fraction $D_{\searrow\downarrow}/(D_{\searrow\downarrow} + D_{\uparrow\downarrow})$, the ratio between the doublons of the two coupled spins with the doublons with the uncoupled spin as a function of the total particle number for selected τ/D is shown

8.6 DIRECT COMPARISON BETWEEN EXPERIMENTAL MEASUREMENTS AND THEORETICAL CALCULATIONS

In the following we discuss the final result of this chapter, which is a direct comparison between experimental measurements and theoretical calculations on orbital selectivity. The data obtained in the experiment represents the doublon fraction $D_{at}/N_{at}(\tau)$ and flavor resolved doublon fraction $D_{\alpha\beta}/D_{at}(\tau)$ as a function of τ for $U/D = 2.61$ and is set side by side with the numerical simulation results. In both cases, the plotted quantities are defined in Eqs. (8.1) and (8.2) as averages in the window between 5000 and 35000 particles of the data for double occupancies as a function of the number of particles.
We remind that, as far as the total number of double occupancies is concerned, the experimental probe actualy detects both double occupations and triple occupations, so that the observed quantity is indeed $\tilde{D} = \sum_{\alpha<\beta} D_{\alpha\beta} + T$. However, the theoretical estimates given above show that T is systematically smaller than D and it does not show any specific behaviour as a function of the control parameters, so the discrepancy is not significant.

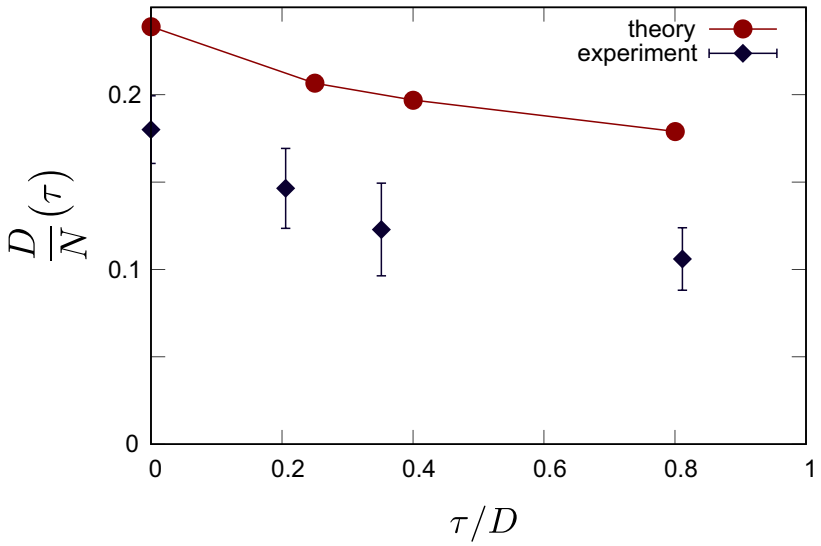

Figure 8.15: **Experimental vs theoretical obtained values on the doublon fraction** The doublon fraction D/N_{at}, the ratio between the number of doublons and the particle number N_{at} as a function of τ/D is shown

Before discussing the final data we recall the results of the model calculations for an ideal homogeneous system. For the chosen interaction value $U/D = 2.61$ the model in the absence of τ is in a metallic state and quite far away from a metal to Mott insulator transition, which takes place at $U_c/D(\tau = 0) \approx 3.5$. (Fig. 8.9) shows a smooth orbital selective Mott transition upon increasing τ/D. The quasi-particle weight for the two coupled components $Z_{\searrow,\downarrow}(\tau)$ starts to approach zero around $\tau/D \approx 0.125$ and is zero at $\tau/D \approx 0.14$, while the weight of the uncoupled flavor $Z_\alpha(\tau)$ saturates to a finite value and does not decrease further increasing τ. From this result it can be concluded that a full Mott state at this specific interaction can not be achieved, even if it is very close, but a very nice orbital selective Mott state is found. Yet, increasing τ always reduces double occupation.

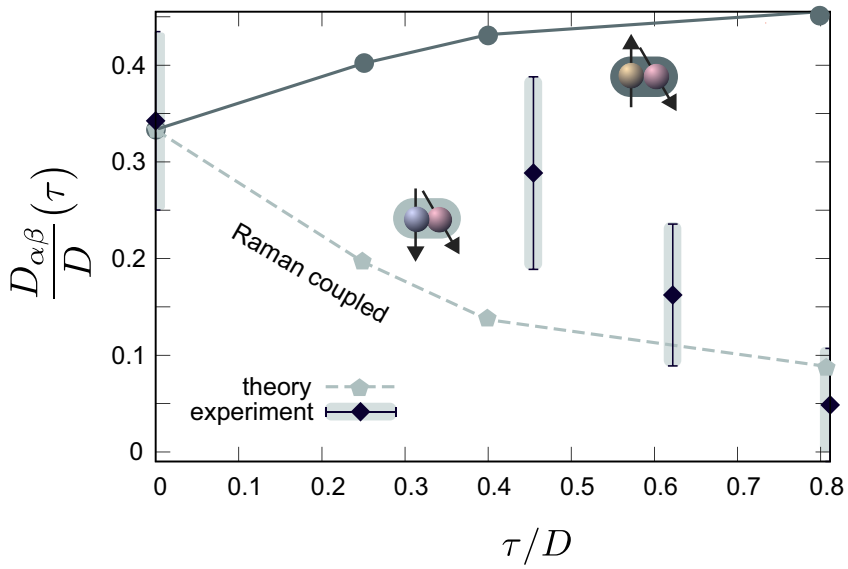

Figure 8.16: **Experimental vs theoretical obtained values on the flavor resolved doublon fractions** The doublon fraction $D_{\searrow\downarrow}/(D_{\searrow\downarrow}+D_{\uparrow\downarrow})$, the ratio between the doublons of the two coupled spins with the doublons with the uncoupled spin as a function of the total particle number for selected τ/D is shown

The two plots Fig 8.15 and Fig 8.16 confirm spectacularly the two non-trivial predictions of our calculations. The total number of double occupancies decreases, both in theory and in experiment as the field τ is increased. This is, to the best of our knowledge, the first experimental evidence in the field of cold atoms of a Raman coupling-induced localization in the presence of strong correlations, which confirms spectacularly the counterintuitive picture where a hopping channel in the synthetic dimension favours localization rather than delocalization.

Furthermore, the orbital-selective double occupancies clearly show that the experiment and the theory agree on the fact that increasing τ favours the orbital selectivity of the correlations, with a significant decrease of the correlators involving the two Raman-coupled species. Again, this result is a first direct realization of orbital-selective correlations introduced by a coupling between two terms. Starting from a triplet of equivalent species, coupling two of them break the degeneracy in the most spectacular way, with the coupled species becoming much more localized than the uncoupled partner.

The qualitative agreement between theory and experiments is clear, but it is almost as clear that at a quantitative level there are still significant differences.

In particular, we observe that the total number of double occupancies is overestimated by the theoretical calculations even if the trend with τ is well reproduced. On the other hand, the fraction of double occupancies involving the two coupled species is smaller in the theory than in the experiment. In other words it appears that the theory overestimates the degree of selectivity of the correlations.

In the following we give some justifications and interpretations of these discrepancy.

The two main source of the difference between theory and experiment are the use of a local-density approximation and the fact that the theoretical calculations, while the experiments are performed at a finite temperature which is not obviously accessible and it can in principle be different for different values of U and τ. We also notice that

these errors can be emphasized by the fact that our system appears close to the Mott boundary.

In the following we focus mainly on the effect of temperature, which is physically more significant. However, the LDA, while it usually captures well local observable, it can have problems to reproduce the properties close to phase boundaries.

We remind that the main reason to perform a complete set of calculations at zero temperature is to provide a complete characterization of the quantum physics in a regime where thermal effects are not present. In this way we isolate the intrinsic physics of the system, at the same time including the experimental constraint of equal population between the species and the effect of the trapping potential (even if within the LDA approximation).

In principle our calculations can be extended to finite temperature but, using our exact diagonalization solver, the finite-temperature calculations require the evaluation of a large number of excited states. For the present results, which require to compute observables for the full range of μ_0 and to find for each μ_0 the correct value of h, this requires a substantial amount of time, which suggested us to postpone these calculations to a later time, opting for obtaining a clear picture of the intrinsic zero-temperature physics of the problem.

Last, but not least, the finite temperature of the experiment is not easily accessible and it can depend on the parameter regime, which would imply to perform calculations in wide range of temperatures. In the following we discuss some phenomenological way to account for the finite-temperature effects to give a qualitative interpretation of the discrepancy between the theory and the experiments.

Given this caveats, in the following we discuss how a finite temperature can explain the discrepancies we found.

. The result on the total number of double occupancies appears at first counter-intuitive as one may expect that the D increases with temperature because the double occupation is minimized at zero temperature in order to minimize the energy and the naive expectation would be an increase of double occupation induced by thermal fluctuations.

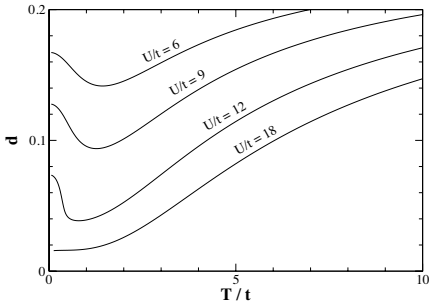

Figure 8.17: shows the double occupation of the SU(2) Hubbard model as a function of temperature T/t and for different interaction strength U/t. The plot is taken from Ref. [160] and is used to explain the smaller doublon fraction in the experiment with respect to the zero temperature theory result.

However, the results for the double occupancy of the SU(2) Hubbard model in Fig. 8.17 show that, in a finite window of temperature the double occupancy decreases with temperature before eventually increasing. This behavior corresponds the Pomeranchuk effect [14] in liquid helium 3 and can be explained by entropy arguments. In a localized state the spin entropy is larger in than in a Fermi liquid and therefore localization is favorable upon heating. Assuming that the experimental temperature lies in the window there the double occupancy is smaller than the $T = 0$ results, we can explain in

these terms the overestimation of the total number of doblons by the zero-temperature theoretical results. This argument can not however explain the discrepancy in the selectivity.
In order to estimate how the temperature can effect the selectivity without performing a demanding finite-temperature calculation we exploited a very powerful feature of Lanczos diagonalization, namely the possibility to extract dynamical (frequency dependent) correlators from a pure groundstate calculation, i.e., without the knowledge of the excited states, but only of the groundstate. The idea is that we could compute a frequency-dependent correlator at zero temperature and infer the finite-temperature values of the related static observables
In particular, we can easily show that the correlator between double occupations at different times

$$\mathcal{C}_{\alpha\beta}(t) = \langle \hat{n}_\alpha(t)\hat{n}_\beta(t)\hat{n}_\alpha(0)\hat{n}_\beta(0)\rangle \tag{8.22}$$

and its Fourier transform $\mathcal{C}_{\alpha\beta}(\omega)$ can be used to estimate the finite-temperature double occupancy according to

$$\mathcal{C}^{\alpha\beta}_T(\omega) \approx \left[\mathcal{C}^{\alpha\beta}_{T=0}(\omega) - \mathcal{C}^{\alpha\beta}_{T=0}(\omega)\right]\left(1+n_B(\omega)\right) + \frac{\eta^2}{\eta^2+\omega^2}\langle \hat{n}_\alpha\hat{n}_\beta\rangle, \tag{8.23}$$

where $\frac{\eta^2}{\eta^2+\omega^2}$ comes from an approximation of the δ-function. Here $n_B(\omega)$ is the Bose-Einstein distribution. This equation is derived under the assumption that we can treat the temperature dependence of this quantity as that of a gas of free bosons with a spectrum obtained by the exact DMFT solution for this propagator. In Appendix A we provide more details on the way this correlator is computed within the exact-diagonalization solution of DMFT.
The integration of the temperature-dependent correlation function gives and estimate of temperature-dependent doublons

$$\langle \hat{n}_\alpha\hat{n}_\beta\rangle_T = \frac{1}{\pi}\int_{-\infty}^{+\infty} \mathcal{C}^{\alpha\beta}_T(\omega) \tag{8.24}$$

This approximation only holds for low enough temperature, when the spectral function is not expected to change significantly when the temperature grows. Particularly, this approximate breaks down for high temperature, since the doublons are treated as free bosons totally neglecting their fermionic nature and the Pauli principle.
In Fig.

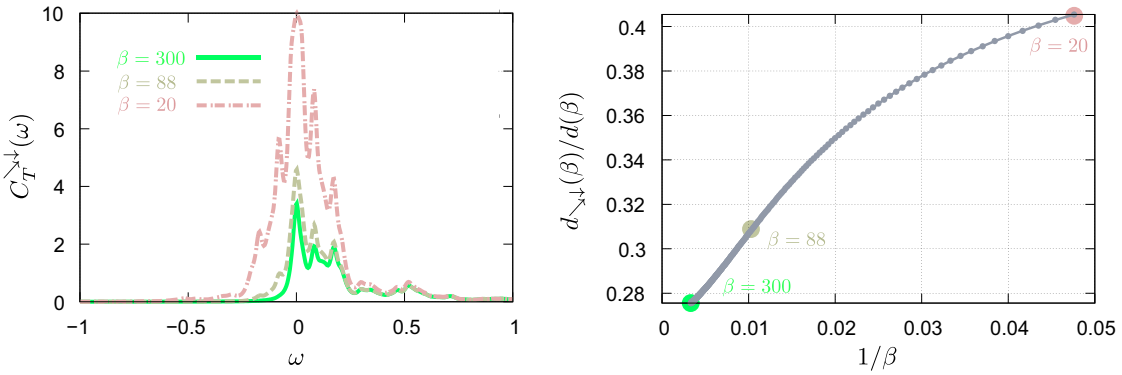

Figure 8.18: **Temperature dependent doublon-doublon correlation function and doublons** The flavor resolved correlation function of the coupled components $\mathcal{C}_{\searrow\downarrow}(\omega)$ is computed for the homogeneous case at $\tau/D = 0.25$ at $U/D = 2.61$ at $\mu/D = 0.725$ close to the density driven Mott point $\langle n \rangle = 2$

In Fig. 8.18 we show the evolution with the temperature of our correlator $\mathcal{C}_{\searrow\downarrow}(\omega)$ and the result for our simple estimate of the temperature dependence of the selective double occupancies.
Finally, we can use these estimates of $D_{\alpha\beta}(T)$ to extract, for every value of τ, the temperature T which reproduces the experimental results for $D_{\searrow\downarrow}/D(\tau)$. This procedure shows that, within this simple approximation, all the experimental data can be fitted using a temperature around $T_{exp} \simeq 0.14t$. While this value is probably an underestimation of the real experimental temperature, we find it promising that a single value of T can explain the whole dependence on τ of the degree of selectivity (Fig. 8.19).

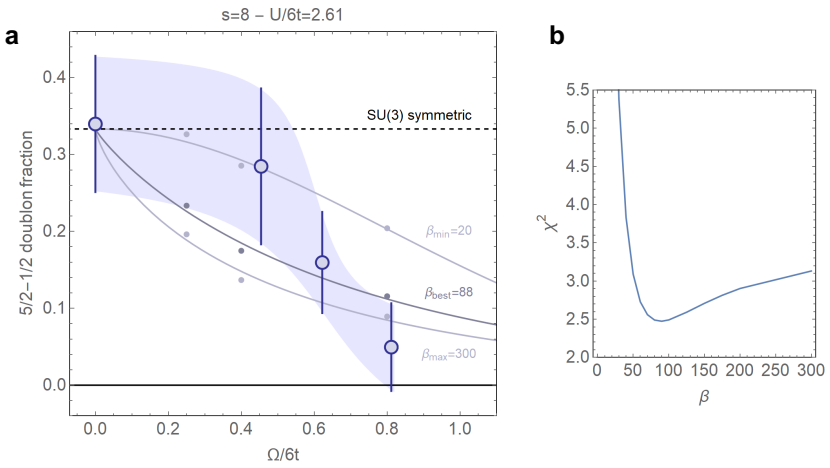

Figure 8.19: **Experimental and theoretical signature of orbital selectivity within interacting Raman coupled SU(3) fermions.** **a** shows the doublon fraction $D_{\searrow\downarrow}/D(\tau) \equiv (D_{5/2} - D1/2)/D$ of the two coupled components as a function of the Raman coupling τ for different estimated inverse temperature regimes β.

9

CONCLUSIONS

This thesis was dedicated to the study of Mott transitions, topology and magnetism of interacting fermions in confined geometries. All the work presented aims at an experimental realization with ultracold atomic experiments, where a harmonic trap is always present in order to confine the particles in a region of space.
The other central aspect of the thesis are strong correlations between particles induced by the interactions and emerging related phenomena. We talk about strong correlations when a large number of particles has a collective behavior which can not be captured by single particle theories. Hence the properties of the single particles are not independent on the others, and we call them correlated. Strongly correlated electrons are one of the most challenging fields in solid-state physics. The present thesis identifies a few open challenges and proposes cold-atom systems which realized a similar physics in a simpler and controlled platform. For one of these phenomena, orbital-selective correlations, we also present a collaboration with experimentalists, which shows a concrete realization of this concept.
In the presence of strong correlations, one can expect interesting phenomena to occur especially when more energy scales are relevant. This interplay of parameter is another main issue we addressed in this thesis, on the one hand trying to find simple description to narrow down the complexity on the other hand the aim was to remain a realistic framework.

The basic model in these studies is the fermionic Hubbard model, that describes interacting particles on a lattice featuring a hopping term and a local repulsion. Throughout the thesis all the numerical simulations were based on Dynamical Mean-Field Theory (DMFT) at zero temperature. Due to the confinement the systems under investigation were intrinsically inhomogeneous and we had to use either a real space extended versions of DMFT (RDMFT) or combine DMFT with a Local Density Approximation (LDA).

The first system we examine (Chapter 5) are strongly interacting spin-1/2 fermions on a honeycomb lattice subject to a harmonic potential. The work was inspired by graphene nanoflakes, which have been widely studied in the solid-state context. Due to the presence of zigzag edges, where correlations are effectively enhanced, nanoflakes host magnetic ordering, contrary to large graphene sheets where magnetic ordering is suppressed. Generally, to realize magnetic states in cold atomic experiments is very challenging since the temperature is typically above the exchange energy needed for magnetism. In previous studies [] it has been demonstrated that the magnetic state of nanoflakes is robust up to rather high temperatures therefore makes them an ideal

candidate to simulate them in optical lattice system. We proposed a cold-atom-based scheme where we use the harmonic trap as a knob to create artificial nanostructures in a large honeycomb system. The idea is to confine the atoms in a limited portion of the lattice thereby forming an effective smaller structure with sharp zigzag edges which can host magnetic ordering.
We demonstrated by means of RDMFT simulations, that indeed a harmonic potential can be used to induce and control the magnetic state in optical lattice experiments starting from a non magnetic system. We find that in addition to becoming magnetic the spin patterns can be highly "fine tuned" by the confinement together with the interaction among fermions. The density distribution which determines the effective structure strongly depends on the interaction and it affects the magnetic state. At very strong interaction a rather uniform distribution can be realized, favoring an antiferromagnetic Mott state, while weak interactions display inhomogeneous density distributions with peculiar magnetic ordering.

In this thesis we demonstrated a route how to induce magnetism in artificial graphene nanostructures formed by optical lattices that are highly tunable. Moreover we expect that the magnetic ordering impacts the transport r [105] properties and can lead to nontrivial spin transport in optical lattice experiments [119, 120].

We extended the above study adding a topologically non-trivial term that models intrinsic spin-orbit coupling (SOC) presented in Chapter 6. This leads to the Kane-Mele model, one of the paradigmatic models for topological insulators. Including also the local repulsion, we obtain the Kane-Mele Hubbard (KMH) model which, for large systems, is expected to display a quantum phase transition from a topologically trivial antiferromagnet to a non-magnetic quantum spin Hall insulator with metallic edge states and insulating bulk.

We provide in this thesis a first analysis of the half-filled uniform flakes of the KMH model. We find that the KMH nanoflakes host topological states that also can coexist with magnetic ordering under specific conditions. In addition we find that suppressing the most stable in-plane magnetic ordering, the topological state can survive to much larger interactions. In this way the state with coexisting topological properties and magnetic ordering is pushed to a region of interactions sufficiently large to create a well-defined effective flake in the presence of the trapping potential.

Therefore we are able to demonstrate that the same trapping protocol which we used to induce magnetism in the honeycomb lattice can be used to generate a topological nanoflake with coexistence magnetic ordering giving rise to a spin-Chern insulator. We also developed a theory describing effective magnetic exchange in the harmonic trap. We discover that at quarter-filling the magnetic state is dominated by Dzyaloshinskii-Moriya anisotropic exchange. Thus we established a theory based on numerical simulation how to govern magnetic order and topology in cold atomic experiments, which paves the pay towards magnetic spin-Chern insulators in cold atoms.

The second part of the thesis (Chapter 7 and Chapter 8) is dedicated to orbital-selective fermionic properties and Mott transition in ^{173}Yb atoms, a study carried out in collaboration with the cold-atom experimental group led by Leonardo Fallani in Lens.

In ^{173}Yb atoms the nuclear spin is essentially decoupled from the electronic state, hence the scattering properties do not depend on it, leading to $SU(N)$ interactions, with $N = 6$. In this way, we have a multicomponent fermionic system which can be connected with multiorbital models for solids.
The general idea is to mimic the elementary mechanism responsible for orbital selective Mott transtion in multi-orbital materials, such as iron-based superconductors, here translated to coherently coupled spin systems, via a controlled breaking of the $SU(N)$ symmetry. The symmetry breaking is realized by Raman transitions connecting different spin states. These terms can be seen as a hopping in a synthetic dimension spanned by the different values of the nuclear spin.
Our study is based on a proposal put forward in Ref. [156], where a minimal system with three spin components was considered at it was shown that the $SU(3)$ breaking leads to a reduced critical value for the Mott transition and to orbital-selective physics, namely a different degree of correlation for different internal spin states, which can even result in an orbital-selective Mott transition where some components are Mott localized and others are not.
In this work we presented a new version of the model adapted to the situation which can be more easily realized in the experiment. The new model is first solved with DMFT assuming a uniform system and then extended to simulate the experimental set up using DMFT and the local-density approximation.
Also for the new model we predict an orbital-selective behavior and a reduction of the critical interaction strength necessary to Mott-localize the fermions. This counterintuitive result where a hopping in the synthetic dimension favours Mott localization is spectacularly confirmed by the experiments, which provide the same qualitative results as our theory.
This work therefore demonstrates the possibility to combine the idea of synthetic dimensions, exploited for artificial gauge field and topological matter, with strong interaction, extending the above result to spin-orbit coupling. In this way one could study the effects of strong correlations on the topological properties of these artificial topological matter, connecting also with the results of the first part of this thesis.
It is expected that the interplay between strong correlation and synthetic dimensions can lead to novel states of matter, such as the fractional quantum Hall effect [30, 161].

Part I

APPENDIX

A

DYNAMICAL DOUBLE OCCUPANCY

A.0.1 *Dynamical response*

Within our numerical simulation, we used a Lanczos based exact diagonalization impurity solver. Within this scheme, dynamical correlation function can be only computed in the following way

$$I(\omega) = -\frac{1}{\pi}\Im[\langle\Psi_0|\,\hat{O}^\dagger \frac{1}{\omega + i\eta + E_0 - \hat{H}}\hat{O}\,|\Psi_0\rangle], \tag{A.1}$$

where $\hat{O}$ is the operator that is analyzed, $|\Psi_0\rangle$ is the ground state of the Hamiltonian $\hat{H}$ with the corresponding ground state energy E_0 and ω the frequency that is made slightly complex with $i\eta$ for shifting the poles of the green function in the complex plane. Within Lanczos we can compute by relating $I(\omega)$ to a continued fraction expansion as follows

$$I(\omega) = -\frac{1}{\pi}\Im\frac{\langle\Psi_0|\,\hat{O}^\dagger\hat{O}\,|\Psi_0\rangle}{z - a_0 - \frac{b_1^2}{z - a_1 - b_2^2/\ldots}}, \tag{A.2}$$

with $z = \omega + E_0 + i\eta$, knowing only the ground state energy of the system, we can compute the desired dynamical response for any value of the the frequency ω, where $a_n = \langle\Phi_n|\,\hat{H}\,|\Phi_n\rangle / \langle\Phi_{n-1}\,|\,\Phi_{n-1}\rangle$, $b_n^2 = \langle\Phi_n\,|\,\Phi_n\rangle / \langle\Phi_{n-1}\,|\,\Phi_{n-1}\rangle$
Therefore, we can not simply compute a correlation function of the type $\langle d_{\alpha\beta}(\omega)\rangle = \langle n_\alpha(\omega) n_\beta(\omega)\rangle$, but we can use a convenient trick, using flavor-flavor correlation functions $\chi^-_{\alpha,\beta}(i\omega_n)$ and density-density $\chi^+_{\alpha,\beta}(\omega)$ correlation functions, which are itself hermitian conjugates and are defined as follows

$$\begin{aligned}\chi^\pm_{\alpha,\beta}(\omega) = \sum_n &\frac{\langle GS|\,\hat{n}_\alpha \pm \hat{n}_\beta\,|n\rangle\,\langle n|\,\hat{n}_\alpha \pm \hat{n}_\beta\,|GS\rangle}{\omega - (E_n - E_0) + i\eta} \\ &- \frac{\langle GS|\,\hat{n}_\alpha \pm \hat{n}_\beta\,|n\rangle\,\langle n|\,\hat{n}_\alpha \pm \hat{n}_\beta\,|GS\rangle}{\omega + (E_n - E_0) + i\eta},\end{aligned} \tag{A.3}$$

combining these two correlation functions we obtain

$$\begin{aligned}\chi_{\alpha\beta}(\omega) &= \chi^+_{\alpha\beta}(\omega) - \chi^-_{\alpha\beta}(\omega) = \\ &= 4\sum_n \langle GS|\,n_\alpha\,|n\rangle\,\langle n|\,n_\beta\,|GS\rangle \times \left(\frac{1}{\omega - (E_n - E_0) + i\eta} - \frac{1}{\omega + (E_n - E_0) + i\eta}\right)\end{aligned} \tag{A.4}$$

Integrating $\chi_{\alpha\beta}(\omega)$ we obtain the flavor resolved double occupation using $\Im\chi_{\alpha\beta}(\omega) = \sum_{n>0} \langle GS|\, n_\alpha \,|n\rangle \langle n|\, n_\beta \,|GS\rangle \left[\delta(\omega + E_n - E_{GS}) - \delta(\omega - E_n + E_{GS})\right]$

$$\begin{aligned} -\frac{1}{\pi}\int_0^\infty d\omega \Im\chi_{\alpha\beta}(\omega) &= -\sum_{n>0} \langle GS|\, n_\alpha \,|n\rangle \langle n|\, n_\beta \,|GS\rangle \times \int_0^\infty d\omega \delta(\omega - E_n + E_{GS}) \\ &= \sum_{n>0} \langle GS|\, n_\alpha \,|n\rangle \langle n|\, n_\beta \,|GS\rangle \\ &= \langle n_\alpha n_\beta\rangle - \langle n_\alpha\rangle\langle n_\beta\rangle \end{aligned} \tag{A.5}$$

We show this type of correlation function in the homogeneous case for a selected value of $\tau = 0.25$ at a chemical potential $\mu/D = 0.725$ close to a density driven Mott state at $\langle n\rangle$. We choose the value because the LDA distribution for the chosen particle number window displays a plateau at this density (Fig. 8.11). The dynamical double occupation $\Im\chi_{\alpha\beta}(\omega)$ displays several peaks at various frequency regime (Fig. A.1 **left**) and as well its constituents $\chi^{\pm}_{\alpha,\beta}(\omega)$((Fig. A.1 **right**). Therefore if several frequency regimes would be excluded and replaced by a cutoff the value of the double occupation upon integration might change and we can conclude that the effect of selectivity comes from several excitation regimes. Cutting of all the lower frequency regime might change the value of the doublons drastically, and selectivity should be washed off. Note that these are just guidelines for a basic understanding and not a solid proof.

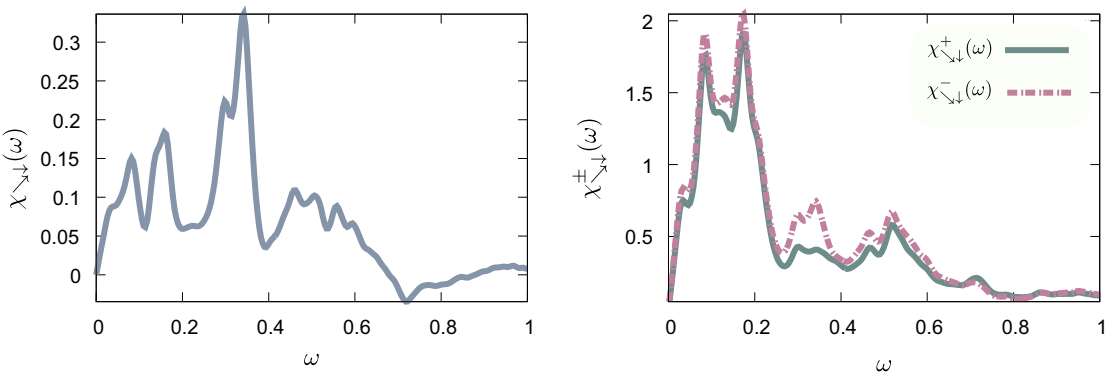

Figure A.1: **Flavor resolved doublon spectral function** The flavor resolved correlation function of the coupled components $\chi_{\searrow\downarrow}(\omega)$ (left) as well as the spin-spin response function $\chi^{-}_{\searrow\downarrow}(\omega)$ and density-density response function $\chi^{+}_{\searrow\downarrow}(\omega)$ and is shown for the homogeneous case at $\tau/D = 0.25$ at $U/D = 2.61$ at $\mu/D = 0.725$ close to the density driven Mott point $\langle n\rangle = 2$.

A.0.2 *Flavor resolved doublon-doublon correlation functions and temperature estimates*

To further gain information on the effects contributing in the experiment on the doublons selectivity, it would be most convenient to have an more precise estimate on temperature effects and the lattice modulation, since we believe that they are the main cause for the quantitative discrepancy in the experiment. Fortunately, we can again use correlation functions to estimate the effect of temperature, but this time not of the type $\langle n_\alpha(t) n_\beta(0)\rangle$, but actually the doublon-doublon correlation function, which can be

understood as time-dependent double occupancies induced by the lattice modulation. This type of correlator has the from

$$\mathcal{C}_{\alpha\beta}(t) = \langle n_\alpha(t) n_\beta(t) n_\alpha(0) n_\beta(0)\rangle \tag{A.6}$$

For this correlator, is interesting to recall the transformation between Raman and physical basis between the flavor resolved double occupancies. $\hat{n}_\uparrow\hat{n}_\searrow = \frac{1}{2}(\hat{n}_1\hat{n}_2 + \hat{n}_1\hat{n}_3 - \hat{n}_1 c_2^\dagger c_3 - \hat{n}_1 c_3^\dagger c_2)$, $\hat{n}_\uparrow\hat{n}_\downarrow = \frac{1}{2}(\hat{n}_1\hat{n}_2 + \hat{n}_1\hat{n}_3 + \hat{n}_1 c_2^\dagger c_3 + \hat{n}_1 c_3^\dagger c_2)$, and $\hat{n}_\searrow\hat{n}_\downarrow = \hat{n}_2\hat{n}_3$. We recall this relation because when we analyzed the doublons these $\hat{n}_1 c_2^\dagger c_3 + \hat{n}_1 c_3^\dagger c_2$ contributions were always zero, however due to the lattice inducing doublons the mixed terms have to be taken into account still under the constrained that each flavor has to be conserved. Then, we obtain

$$\begin{aligned}\mathcal{C}_{\uparrow\downarrow}(t) &= \langle n_\uparrow(t) n_\downarrow(t) n_\uparrow(0) n_\downarrow(0)\rangle \\ &= \frac{1}{4}\langle[(\hat{n}_1(t)\hat{n}_2(t) + \hat{n}_1(t)\hat{n}_3(t) + \hat{n}_1(t)c_2^\dagger(t)c_3(t) + \hat{n}_1(t)c_3^\dagger(t)c_2(t))] \\ &\quad \times [\hat{n}_1(0)\hat{n}_2(0) + \hat{n}_1(0)\hat{n}_3(0) + \hat{n}_1(0)c_2^\dagger(0)c_3(0) + \hat{n}_1(0)c_3^\dagger(0)c_2(0)]\rangle\end{aligned} \tag{A.7}$$

This is a very complicated expression and for the sake of simplicity we introduce and define the Raman correlation functions

$$\begin{aligned}\mathcal{C}_0(t) &= \big\langle\big[n_1\big(n_2+n_3\big)\big](t)\big[n_1\big(n_2+n_3\big)\big](0)\big\rangle \\ \mathcal{C}_+(t) &= \big\langle\big[n_1 c_2^\dagger c_3\big](t)\big[n_1 c_3^\dagger c_2\big](0)\big\rangle \\ \mathcal{C}_-(t) &= \big\langle\big[n_1 c_3^\dagger c_2\big](t)\big[n_1 c_2^\dagger c_3\big](0)\big\rangle\end{aligned} \tag{A.8}$$

With these we obtain

$$\begin{aligned}\mathcal{C}_{\uparrow\downarrow}(t) &= 0.25\big(\mathcal{C}_0(t) + \mathcal{C}_+(t) + \mathcal{C}_-(t)\big) \\ \mathcal{C}_{\uparrow\searrow}(t) &= \mathcal{C}_{\uparrow\downarrow}(t) \\ \mathcal{C}_{\uparrow\downarrow}(t) &= \mathcal{C}_{23}(t)\end{aligned} \tag{A.9}$$

Luckily these correlation functions have the structure $\langle\hat{O}(t)\hat{O}^\dagger(0)\rangle$ and we can use this Lanczos base technique to compute them.
We report on the flavor resolved doublon-doublon correlation function $\mathcal{IC}_{\alpha\beta}(\omega)$ corresponding to Fig. **??** as well as the lattice modulation correlation function $\omega\mathcal{IC}_{\alpha\beta}(\omega)$ presented in Fig. A.2 upper and lower panel respectively. Also these are averaged over the particle number window as doublon fractions etc. The evolution upon increasing $\tau/D = 0.0, 0.25, 0.40, 0.80$

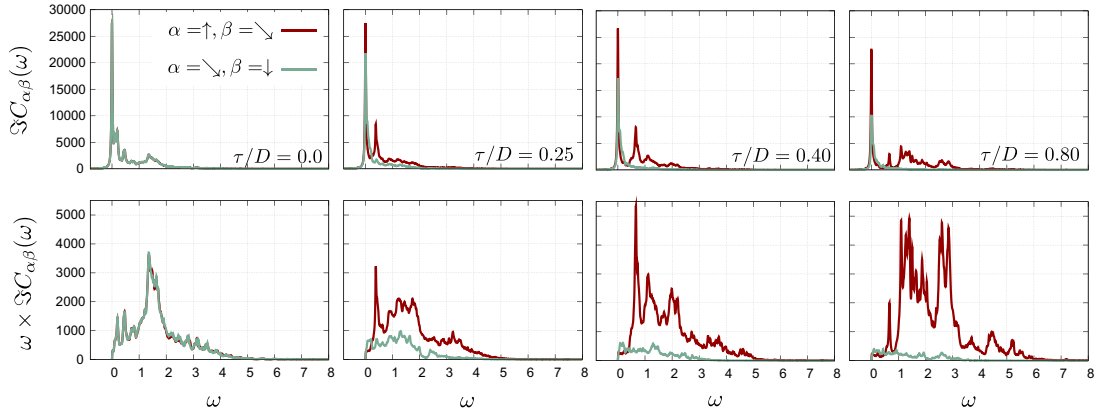

Figure A.2: **Experimental doublon-doublon correlation function induced by lattice modulation** The correlation functions $\mathcal{C}_{\uparrow\downarrow}(\omega)$ and $\mathcal{C}_{\searrow\downarrow}(\omega)$ (upper panel) are computed for $\tau/D = 0.0, 0.25, 0.40, 0.80$ at $U/D = 2.61$ and averaged according to the experimental set up. The lower panel shows the rate of lattice modulation induced doublons

As next step we can also include the effect of temperature by approximating the doublons as free bosons (see appendix [?])

$$\mathcal{C}_T^{\alpha\beta}(\omega) \approx \left[\mathcal{C}_{T=0}^{\alpha\beta}(\omega) - \mathcal{C}_{T=0}^{\alpha\beta}(\omega)\right]\left(1 + n_B(\omega)\right) + \frac{\eta^2}{\eta^2 + \omega^2}\langle n_\alpha n_\beta\rangle, \tag{A.10}$$

where $\frac{\eta^2}{\eta^2+\omega^2}$ comes from an approximation of the δ-function. The integration of the temperature dependent correlation function gives and estimate of temperature dependent doublons

$$\langle n_\alpha n_\beta\rangle_T = \frac{1}{\pi}\int_{-\infty}^{+\infty} \mathcal{C}_T^{\alpha\beta}(\omega) \tag{A.11}$$

This approximation only holds for low enough temperature, when the spectral function is not expected to change significantly. Particularly, this approximate breaks down for high temperature, since the doublons are treated as free bosons and thereby the Pauli exclusion principle gets exceed at some point. We examine the temperature dependent doublon-doublon correlation function and doublons for the coupled flavors at temperature where we expect the approximation to be sufficiently valid.

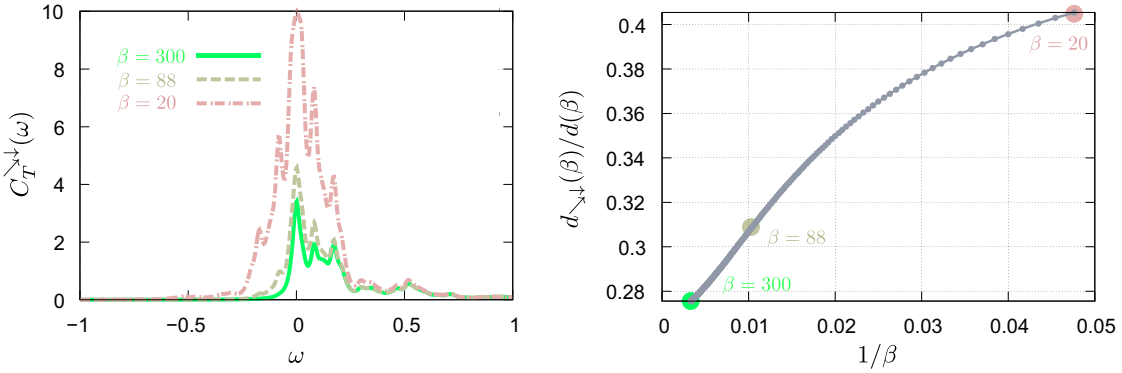

Figure A.3: **Temperature dependent doublon-doublon correlation function and doublons** The flavor resolved correlation function of the coupled components $\mathcal{C}_{\searrow\downarrow}(\omega)$ is computed for the homogeneous case at $\tau/D = 0.25$ at $U/D = 2.61$ at $\mu/D = 0.725$ close to the density driven Mott point $\langle n \rangle = 2$

As expected the doublon-doublon spectral function gains spectral weight upon increasing (decreasing) temperature $T = 1/\beta$ (inverse temperature β). For $\beta = 300$, analogous to zero temperature calculations, $C^{\searrow\downarrow}(\omega)$ displays the largest peak around $\omega = 0$, the lowest energy regime, next to more spectral weight at larger, yet small frequency regime. For $\omega/D > 0.75$, $C^{\searrow\downarrow}(\omega)$ is exactly vanishing. Decreasing β results in a broadening and in a growth of the peak. For $\beta = 88$ this effect is rather small, however the flavor resolved doublon fraction $d_{\alpha\beta}/d(\beta = 88) > d_{\alpha\beta}/d(\beta = 300)$ is already quite larger. For $\beta = 300$ $d_{\alpha\beta}/d \approx 0.275$ while for $\beta = 88$ it decreased already to $d_{\alpha\beta}/d \approx 0.31$. Upon further decreasing β the doublon fraction growths monotonously and the correlation function increases significantly. Though this doesn't necessarily reflect the real temperature achieved in the experiment, it clearly shows that the selectivity is indeed strongly affected by temperature and gives a good explanation for the differences between the zero temperature theory and the cold atom experiment. We can conclude that the selectivity survives larger temperature regimes until it gets washed out, however at zero temperature the effect orbital selective behavior is the clearest.

BIBLIOGRAPHY

[1] J. Hubbard. "Electron correlations in narrow energy bands III. An improved solution." *Proc. R. Soc. Lond.* **281**, pp. 401–419. 1964 (cit. on pp. 11, 49).

[2] N. F. Mott. "The Basis of the Electron Theory of Metals, with Special Reference to the Transition Metals." **62**, pp. 416–422. 1949 (cit. on pp. 11, 36).

[3] N. F. Mott. "Metal-Insulator Transition." *Rev. Mod. Phys.* **40**, pp. 677–683. 1968 (cit. on pp. 11, 31).

[4] P. Fazekas. *Lecture Notes on Electron Correlation and Magnetism*. WORLD SCIENTIFIC. 1999 (cit. on pp. 11, 53, 96, 97).

[5] Y. Kamihara, T. Watanabe, M. Hirano, and H. Hosono. "Iron-Based Layered Superconductor La[O1-xFx]FeAs (x = 0.05-0.12) with Tc = 26 K." *Journal of the American Chemical Society* **130**, pp. 3296–3297. 2008 (cit. on pp. 11, 15).

[6] R. P. Feynman. "Simulating physics with computers." *International Journal of Theoretical Physics* **21**, pp. 467–488. 1982 (cit. on p. 11).

[7] F. Schäfer, T. Fukuhara, S. Sugawa, Y. Takasu, and Y. Takahashi. "Tools for quantum simulation with ultracold atoms in optical lattices." *Nature Reviews Physics*. 2020 (cit. on pp. 11, 15–17).

[8] I. Bloch, J. Dalibard, and S. Nascimbène. "Quantum simulations with ultracold quantum gases." *Nature Physics* **8**, pp. 267–276. 2012 (cit. on pp. 11, 15, 18).

[9] I. Bloch, J. Dalibard, and W. Zwerger. "Many-body physics with ultracold gases." *Rev. Mod. Phys.* **80**, pp. 885–964. 2008 (cit. on pp. 11, 15, 18, 66, 115).

[10] L. Tarruell, D. Greif, T. Uehlinger, G. Jotzu, and T. Esslinger. "Creating, moving and merging Dirac points with a Fermi gas in a tunable honeycomb lattice." *Nature* **483**, 302 EP –. 2012 (cit. on pp. 12, 17, 18, 59, 66, 77).

[11] M. A. Cazalilla, R. Citro, T. Giamarchi, E. Orignac, and M. Rigol. "One dimensional bosons: From condensed matter systems to ultracold gases." *Rev. Mod. Phys.* **83**, pp. 1405–1466. 2011 (cit. on pp. 12, 16).

[12] W. Zwerger. "Mott Hubbard transition of cold atoms in optical lattices." *Journal of Optics B: Quantum and Semiclassical Optics* **5**, S9–S16. 2003 (cit. on pp. 12, 27).

[13] R. W. Helmes, T. A. Costi, and A. Rosch. "Mott Transition of Fermionic Atoms in a Three-Dimensional Optical Trap." *Phys. Rev. Lett.* **100**, p. 056403. 2008 (cit. on pp. 12, 27, 50, 51).

[14] S. Taie, R. Yamazaki, S. Sugawa, and Y. Takahashi. "An SU(6) Mott insulator of an atomic Fermi gas realized by large-spin Pomeranchuk cooling." *Nature Physics* **8**, pp. 825–830. 2012 (cit. on pp. 12, 19, 20, 27–29, 103, 137).

[15] R. Jördens, N. Strohmaier, K. Günter, H. Moritz, and T. Esslinger. "A Mott insulator of fermionic atoms in an optical lattice." *Nature* **455**, 204 EP –. 2008 (cit. on pp. 12, 19, 27).

[16] J. H. Drewes, L. A. Miller, E. Cocchi, C. F. Chan, N. Wurz, M. Gall, D. Pertot, F. Brennecke, and M. Köhl. "Antiferromagnetic Correlations in Two-Dimensional Fermionic Mott-Insulating and Metallic Phases." *Phys. Rev. Lett.* **118**, p. 170401. 2017 (cit. on pp. 12, 19, 27, 77).

[17] M. A. Cazalilla, A. F. Ho, and M Ueda. "Ultracold gases of ytterbium: ferromagnetism and Mott states in an SU(6) Fermi system." *New Journal of Physics* **11**, p. 103033. 2009 (cit. on pp. 12, 13, 19, 27).

[18] R. Jördens, N. Strohmaier, K. Günter, H. Moritz, and T. Esslinger. "A Mott insulator of fermionic atoms in an optical lattice." *Nature* **455**, pp. 204–207. 2008 (cit. on pp. 12, 27).

[19] M. Miranda, R. Inoue, N. Tambo, and M. Kozuma. "Site-resolved imaging of a bosonic Mott insulator using ytterbium atoms." *Phys. Rev. A* **96**, p. 043626. 2017 (cit. on pp. 12, 27).

[20] G. Jotzu, M. Messer, R. Desbuquois, M. Lebrat, T. Uehlinger, D. Greif, and T. Esslinger. "Experimental realization of the topological Haldane model with ultracold fermions." *Nature* **515**, 237 EP –. 2014 (cit. on pp. 12, 17, 77).

[21] M. Aidelsburger, M. Atala, M. Lohse, J. T. Barreiro, B. Paredes, and I. Bloch. "Realization of the Hofstadter Hamiltonian with Ultracold Atoms in Optical Lattices." *Phys. Rev. Lett.* **111**, p. 185301. 2013 (cit. on pp. 12, 16, 77).

[22] T. Chalopin, T. Satoor, A. Evrard, V. Makhalov, J. Dalibard, R. Lopes, and S. Nascimbène. "Exploring the topology of a quantum Hall system at the microscopic level." *arXiv: Quantum Gases*. 2020 (cit. on pp. 12, 25).

[23] J. Dalibard, F. Gerbier, G. Juzeliū, and P. Öhberg. "Colloquium: Artificial gauge potentials for neutral atoms." *Rev. Mod. Phys.* **83**, pp. 1523–1543. 2011 (cit. on pp. 12, 24).

[24] N Goldman, G Juzeliūnas, Pahberg, and I. B. Spielman. "Light-induced gauge fields for ultracold atoms." *Reports on Progress in Physics* **77**, p. 126401. 2014 (cit. on pp. 12, 24).

[25] L. Tagliacozzo, A. Celi, P. Orland, M. W. Mitchell, and M. Lewenstein. "Simulation of non-Abelian gauge theories with optical lattices." *Nature Communications* **4**, p. 2615. 2013 (cit. on pp. 12, 24).

[26] A. Celi, P. Massignan, J. Ruseckas, N. Goldman, I. B. Spielman, G. Juzelinas, and M. Lewenstein. "Synthetic Gauge Fields in Synthetic Dimensions." *Phys. Rev. Lett.* **112**, p. 043001. 2014 (cit. on pp. 12, 24).

[27] H. Zhai. "Degenerate quantum gases with spin–orbit coupling: a review." *Reports on Progress in Physics* **78**, p. 026001. 2015 (cit. on pp. 12, 24).

[28] M. Mancini et al. "Observation of chiral edge states with neutral fermions in synthetic Hall ribbons." *Science* **349**, p. 1510. 2015 (cit. on pp. 12, 24, 103).

[29] T.-S. Zeng, C. Wang, and H. Zhai. "Charge Pumping of Interacting Fermion Atoms in the Synthetic Dimension." *Phys. Rev. Lett.* **115**, p. 095302. 2015 (cit. on pp. 12, 24).

[30] S. Barbarino, L. Taddia, D. Rossini, L. Mazza, and R. Fazio. "Magnetic crystals and helical liquids in alkaline-earth fermionic gases." *Nature Communications* **6**, p. 8134. 2015 (cit. on pp. 12, 24, 143).

[31] C. L. Kane and E. J. Mele. "Quantum Spin Hall Effect in Graphene." *Phys. Rev. Lett.* **95**, p. 226801. 2005 (cit. on pp. 12, 77, 84).

[32] C. L. Kane and E. J. Mele. "Z_2 Topological Order and the Quantum Spin Hall Effect." *Phys. Rev. Lett.* **95**, p. 146802. 2005 (cit. on pp. 12, 77, 84).

[33] A. Vaezi, M. Mashkoori, and M. Hosseini. "Phase diagram of the strongly correlated Kane-Mele-Hubbard model." *Phys. Rev. B* **85**, p. 195126. 2012 (cit. on pp. 12, 77).

[34] M. A. Cazalilla and A. M. Rey. "Ultracold Fermi gases with emergent SU(N) symmetry." **77**, p. 124401. 2014 (cit. on pp. 13, 19, 20, 27).

[35] A. Liebsch. "Mott Transitions in Multiorbital Systems." *Phys. Rev. Lett.* **91**, p. 226401. 2003 (cit. on pp. 13, 103).

[36] L. de'Medici, A. Georges, and S. Biermann. "Orbital-selective Mott transition in multiband systems: Slave-spin representation and dynamical mean-field theory." *Phys. Rev. B* **72**, p. 205124. 2005 (cit. on pp. 13, 103).

[37] A. Koga, N. Kawakami, T. M. Rice, and M. Sigrist. "Orbital-Selective Mott Transitions in the Degenerate Hubbard Model." *Phys. Rev. Lett.* **92**, p. 216402. 2004 (cit. on pp. 13, 103).

[38] P. Werner and A. J. Millis. "High-Spin to Low-Spin and Orbital Polarization Transitions in Multiorbital Mott Systems." *Phys. Rev. Lett.* **99**, p. 126405. 2007 (cit. on pp. 13, 103).

[39] L. de'Medici, S. R. Hassan, M. Capone, and X. Dai. "Orbital-Selective Mott Transition out of Band Degeneracy Lifting." *Phys. Rev. Lett.* **102**, p. 126401. 2009 (cit. on pp. 13, 103).

[40] L. de'Medici, G. Giovannetti, and M. Capone. "Selective Mott Physics as a Key to Iron Superconductors." *Phys. Rev. Lett.* **112**, p. 177001. 2014 (cit. on pp. 13, 103, 105, 106).

[41] A. Georges, L. d. Medici, and J. Mravlje. "Strong Correlations from Hund's Coupling." *Annual Review of Condensed Matter Physics* **4**, pp. 137–178. 2013 (cit. on pp. 13, 103).

[42] A. Georges, G. Kotliar, W. Krauth, and M. J. Rozenberg. "Dynamical mean-field theory of strongly correlated fermion systems and the limit of infinite dimensions." *Rev. Mod. Phys.* **68**, pp. 13–125. 1996 (cit. on pp. 13, 31, 37, 39, 41, 49).

[43] M. Potthoff and W. Nolting. "Surface metal-insulator transition in the Hubbard model." *Phys. Rev. B* **59**, pp. 2549–2555. 1999 (cit. on pp. 14, 46).

[44] S. Florens. "Nanoscale Dynamical Mean-Field Theory for Molecules and Mesoscopic Devices in the Strong-Correlation Regime." *Phys. Rev. Lett.* **99**, p. 046402. 2007 (cit. on pp. 14, 46).

[45] M Snoek, I Titvinidze, C Tőke, K Byczuk, and W Hofstetter. "Antiferromagnetic order of strongly interacting fermions in a trap: real-space dynamical mean-field analysis." *New Journal of Physics* **10**, p. 093008. 2008 (cit. on pp. 14, 46, 67).

[46] M. Buchhold. "Topological Phases of Interacting Fermions in Optical Lattices with Articial Gauge Fields." MA thesis. 2012 (cit. on pp. 14, 46).

[47] A. H. MacDonald, S. M. Girvin, and D. Yoshioka. "$\frac{t}{U}$ expansion for the Hubbard model." *Phys. Rev. B* **37**, pp. 9753–9756. 1988 (cit. on pp. 14, 53, 55, 78, 81).

[48] M. Greiner and S. Fölling. "Optical lattices." *Nature* **453**, pp. 736–738. 2008 (cit. on p. 15).

[49] K. L. Lee, B. Grémaud, R. Han, B.-G. Englert, and C. Miniatura. "Ultracold fermions in a graphene-type optical lattice." *Phys. Rev. A* **80**, p. 043411. 2009 (cit. on pp. 16, 17, 59, 66).

[50] P. Soltan-Panahi, J. Struck, P. Hauke, A. Bick, W. Plenkers, G. Meineke, C. Becker, P. Windpassinger, M. Lewenstein, and K. Sengstock. "Multi-component quantum gases in spin-dependent hexagonal lattices." *Nature Physics* **7**, 434 EP –. 2011 (cit. on pp. 16, 19, 59, 66).

[51] H. Miyake, G. A. Siviloglou, C. J. Kennedy, W. C. Burton, and W. Ketterle. "Realizing the Harper Hamiltonian with Laser-Assisted Tunneling in Optical Lattices." *Phys. Rev. Lett.* **111**, p. 185302. 2013 (cit. on pp. 16, 77).

[52] U. Schneider, L. Hackermüller, S. Will, T. Best, I. Bloch, T. A. Costi, R. W. Helmes, D. Rasch, and A. Rosch. "Metallic and Insulating Phases of Repulsively Interacting Fermions in a 3D Optical Lattice." *Science* **322**, p. 1520. 2008 (cit. on pp. 18, 19, 115).

[53] N. W. *Theoretical Physics 7, Chapter 9 Scattering Theory*. 2017 (cit. on p. 18).

[54] C. Chin, R. Grimm, P. Julienne, and E. Tiesinga. "Feshbach resonances in ultracold gases." *Rev. Mod. Phys.* **82**, pp. 1225–1286. 2010 (cit. on p. 18).

[55] R. Zhang, Y. Cheng, H. Zhai, and P. Zhang. "Orbital Feshbach Resonance in Alkali-Earth Atoms." *Phys. Rev. Lett.* **115**, p. 135301. 2015 (cit. on pp. 18, 19, 27).

[56] G. Pagano, M. Mancini, G. Cappellini, L. Livi, C. Sias, J. Catani, M. Inguscio, and L. Fallani. "Strongly Interacting Gas of Two-Electron Fermions at an Orbital Feshbach Resonance." *Phys. Rev. Lett.* **115**, p. 265301. 2015 (cit. on pp. 18, 19, 27).

[57] M. Höfer, L. Riegger, F. Scazza, C. Hofrichter, D. R. Fernandes, M. M. Parish, J. Levinsen, I. Bloch, and S. Fölling. "Observation of an Orbital Interaction-Induced Feshbach Resonance in ^{173}Yb." *Phys. Rev. Lett.* **115**, p. 265302. 2015 (cit. on pp. 18, 19).

[58] A. V. Gorshkov, M. Hermele, V. Gurarie, C. Xu, P. S. Julienne, J. Ye, P. Zoller, E. Demler, M. D. Lukin, and A. M. Rey. "Two-orbital S U(N) magnetism with ultracold alkaline-earth atoms." *Nature Physics* **6**, pp. 289–295. 2010 (cit. on pp. 19, 103).

[59] F. Scazza, C. Hofrichter, M. Höfer, P. C. De Groot, I. Bloch, and S. Fölling. "Observation of two-orbital spin-exchange interactions with ultracold SU(N)-symmetric fermions." *Nature Physics* **10**, pp. 779–784. 2014 (cit. on pp. 19, 103).

[60] C. Wu, J.-p. Hu, and S.-c. Zhang. "Exact SO(5) Symmetry in the Spin-3/2 Fermionic System." *Phys. Rev. Lett.* **91**, p. 186402. 2003 (cit. on p. 19).

[61] M. A. Perlin and A. M. Rey. "Effective multi-body SU(N)-symmetric interactions of ultracold fermionic atoms on a 3D lattice." **21**, p. 043039. 2019 (cit. on pp. 19, 103).

[62] M. Kitagawa, K. Enomoto, K. Kasa, Y. Takahashi, R. Ciuryło, P. Naidon, and P. S. Julienne. "Two-color photoassociation spectroscopy of ytterbium atoms and the precise determinations of s-wave scattering lengths." *Phys. Rev. A* **77**, p. 012719. 2008 (cit. on p. 20).

[63] Y. N. Martinez de Escobar, P. G. Mickelson, P. Pellegrini, S. B. Nagel, A. Traverso, M. Yan, R. Côté, and T. C. Killian. "Two-photon photoassociative spectroscopy of ultracold ^{88}Sr." *Phys. Rev. A* **78**, p. 062708. 2008 (cit. on p. 20).

[64] L. del Re. "Multicomponent strongly correlated fermions in optical lattices." PhD thesis. 2016 (cit. on pp. 20, 44).

[65] M. Mancini. "Experiments with strongly interacting Yb atoms in optical lattices." PhD thesis. 2015 (cit. on pp. 22, 117).

[66] L. Franchi. "Experiments with strongly interacting Yb atoms in optical lattices." PhD thesis. 2020 (cit. on pp. 22, 116–118, 121, 122).

[67] P. Wang, Z.-Q. Yu, Z. Fu, J. Miao, L. Huang, S. Chai, H. Zhai, and J. Zhang. "Spin-Orbit Coupled Degenerate Fermi Gases." *Phys. Rev. Lett.* **109**, p. 095301. 2012 (cit. on p. 22).

[68] C. J. Kennedy, G. A. Siviloglou, H. Miyake, W. C. Burton, and W. Ketterle. "Spin-Orbit Coupling and Quantum Spin Hall Effect for Neutral Atoms without Spin Flips." *Phys. Rev. Lett.* **111**, p. 225301. 2013 (cit. on p. 22).

[69] B. Song, C. He, S. Zhang, E. Hajiyev, W. Huang, X.-J. Liu, and G.-B. Jo. "Spin-orbit-coupled two-electron Fermi gases of ytterbium atoms." *Phys. Rev. A* **94**, p. 061604. 2016 (cit. on p. 22).

[70] R. Bianco and R. Resta. "Mapping topological order in coordinate space." *Phys. Rev. B* **84**, p. 241106. 2011 (cit. on pp. 27, 78, 84).

[71] J. H. Han, J. H. Kang, M. Lee, and Y. Shin. "Photoassociation spectroscopy of ultracold ^{173}Yb atoms near the intercombination line." *Phys. Rev. A* **97**, p. 013401. 2018 (cit. on pp. 27, 118, 121).

[72] A. A. Abrikosov and I. M. Khalatnikov. "The theory of a fermi liquid (the properties of liquid 3He at low temperatures)." **22**, pp. 329–367. 1959 (cit. on pp. 31, 34).

[73] "Contemporary Physics." *Contemporary Physics* **32**, pp. 341–362. 1991 (cit. on p. 31).

[74] G. Baym and C. Pethick. *Landau Fermi-liquid theory: concepts and applications.* John Wiley and Sons. 2008 (cit. on p. 31).

[75] M. Capone, L. de'Medici, and A. Georges. "Solving the dynamical mean-field theory at very low temperatures using the Lanczos exact diagonalization." *Phys. Rev. B* **76**, p. 245116. 2007 (cit. on pp. 31, 44).

[76] M. Caffarel and W. Krauth. "Exact diagonalization approach to correlated fermions in infinite dimensions: Mott transition and superconductivity." *Phys. Rev. Lett.* **72**, pp. 1545–1548. 1994 (cit. on pp. 31, 44).

[77] C. Weber, A. Amaricci, M. Capone, and P. B. Littlewood. "Augmented hybrid exact-diagonalization solver for dynamical mean field theory." *Phys. Rev. B* **86**, p. 115136. 2012 (cit. on pp. 31, 44).

[78] N. Ashcroft and N. Mermin. *Solid State Physics*. Fort Worth: Saunders College Publishing. 1976 (cit. on p. 32).

[79] E. H. Lieb and F. Y. Wu. "Absence of Mott Transition in an Exact Solution of the Short-Range, One-Band Model in One Dimension." *Phys. Rev. Lett.* **20**, pp. 1445–1448. 1968 (cit. on p. 33).

[80] R. P. N. F. Mott. "Sect A 49, 72." 1937 (cit. on p. 36).

[81] W. Metzner and D. Vollhardt. "Correlated Lattice Fermions in $d = \infty$ Dimensions." *Phys. Rev. Lett.* **62**, pp. 324–327. 1989 (cit. on p. 37).

[82] M. Mézard and G. Parisi. "The Cavity Method at Zero Temperature." *Journal of Statistical Physics* **111**, pp. 1–34. 2003 (cit. on p. 39).

[83] G. Moeller, Q. Si, G. Kotliar, M. Rozenberg, and D. S. Fisher. "Critical Behavior near the Mott Transition in the Hubbard Model." *Phys. Rev. Lett.* **74**, pp. 2082–2085. 1995 (cit. on p. 49).

[84] D. Vollhardt. "Dynamical mean-field theory for correlated electrons." *Annalen der Physik* **524**, pp. 1–19. 2012 (cit. on p. 49).

[85] R. Bulla. "Zero Temperature Metal-Insulator Transition in the Infinite-Dimensional Hubbard Model." *Phys. Rev. Lett.* **83**, pp. 136–139. 1999 (cit. on p. 49).

[86] G. Kotliar and D. Vollhardt. "Strongly Correlated Materials: Insights From Dynamical Mean-Field Theory." **57**. 2004 (cit. on p. 49).

[87] R. Bulla, T. A. Costi, and D. Vollhardt. "Finite-temperature numerical renormalization group study of the Mott transition." *Phys. Rev. B* **64**, p. 045103. 2001 (cit. on p. 50).

[88] A. K. Geim. "Graphene: Status and Prospects." *Science* **324**, pp. 1530–1534. 2009 (cit. on p. 59).

[89] K. S. Novoselov, A. K. Geim, S. V. Morozov, D. Jiang, M. I. Katsnelson, I. V. Grigorieva, S. V. Dubonos, and A. A. Firsov. "Two-dimensional gas of massless Dirac fermions in graphene." *Nature* **438**, 197 EP –. 2005 (cit. on p. 59).

[90] A. H. Castro Neto, F. Guinea, N. M. R. Peres, K. S. Novoselov, and A. K. Geim. "The electronic properties of graphene." *Rev. Mod. Phys.* **81**, pp. 109–162. 2009 (cit. on p. 59).

[91] L. Chen, L. Guo, Z. Li, H. Zhang, J. Lin, J. Huang, S. Jin, and X. Chen. "Towards intrinsic magnetism of graphene sheets with irregular zigzag edges." *Scientific Reports* **3**, p. 2599. 2013 (cit. on p. 59).

[92] K. Nakada, M. Fujita, G. Dresselhaus, and M. S. Dresselhaus. "Edge state in graphene ribbons: Nanometer size effect and edge shape dependence." *Phys. Rev. B* **54**, pp. 17954–17961. 1996 (cit. on p. 59).

[93] J. Fernández-Rossier and J. J. Palacios. "Magnetism in Graphene Nanoislands." *Phys. Rev. Lett.* **99**, p. 177204. 2007 (cit. on pp. 59, 60, 91).

[94] M. Slota et al. "Magnetic edge states and coherent manipulation of graphene nanoribbons." *Nature* **557**, pp. 691–695. 2018 (cit. on p. 59).

[95] L. Duca, T. Li, M. Reitter, I. Bloch, M. Schleier-Smith, and U. Schneider. "An Aharonov-Bohm interferometer for determining Bloch band topology." *Science* **347**, pp. 288–292. 2015 (cit. on pp. 59, 66).

[96] A. Valli, A. Amaricci, A. Toschi, T. Saha-Dasgupta, K. Held, and M. Capone. "Effective magnetic correlations in hole-doped graphene nanoflakes." *Phys. Rev. B* **94**, p. 245146. 2016 (cit. on pp. 59, 60, 67, 75, 85, 91, 100).

[97] C. Koop and S. Wessel. "Quantum phase transitions in effective spin-ladder models for graphene zigzag nanoribbons." *Phys. Rev. B* **96**, p. 165114. 2017 (cit. on p. 59).

[98] M. Kabir and T. Saha-Dasgupta. "Manipulation of edge magnetism in hexagonal graphene nanoflakes." *Phys. Rev. B* **90**, p. 035403. 2014 (cit. on pp. 59, 60, 91).

[99] S. Ganguly, M. Kabir, and T. Saha-Dasgupta. "Magnetic and electronic crossovers in graphene nanoflakes." *Phys. Rev. B* **95**, p. 174419. 2017 (cit. on p. 59).

[100] J. Kang, F. Wu, and J. Li. "Doping induced spin filtering effect in zigzag graphene nanoribbons with asymmetric edge hydrogenation." *Applied Physics Letters* **98**, p. 083109. 2011 (cit. on p. 59).

[101] F. Zou, L. Zhu, and K. Yao. "Perfect spin filtering effect and negative differential behavior in phosphorus-doped zigzag graphene nanoribbons." *Scientific Reports* **5**, 15966 EP –. 2015 (cit. on p. 59).

[102] R. Ortiz, J. L. Lado, M. Melle-Franco, and J. Fernández-Rossier. "Engineering spin exchange in nonbipartite graphene zigzag edges." *Phys. Rev. B* **94**, p. 094414. 2016 (cit. on p. 59).

[103] C. Cao, Y. Wang, H.-P. Cheng, and J.-Z. Jiang. "Perfect spin-filtering and giant magnetoresistance with Fe-terminated graphene nanoribbon." *Applied Physics Letters* **99**, p. 073110. 2011 (cit. on p. 59).

[104] M. B. Lundeberg and J. A. Folk. "Spin-resolved quantum interference in graphene." *Nature Physics* **5**, 894 EP –. 2009 (cit. on p. 59).

[105] A. Valli, A. Amaricci, V. Brosco, and M. Capone. "Quantum Interference Assisted Spin Filtering in Graphene Nanoflakes." *Nano Letters* **18**, pp. 2158–2164. 2018 (cit. on pp. 59, 67, 76, 142).

[106] A. Valli, A. Amaricci, V. Brosco, and M. Capone. "Interplay between destructive quantum interference and symmetry-breaking phenomena in graphene quantum junctions." *Phys. Rev. B* **100**, p. 075118. 2019 (cit. on p. 59).

[107] S. Sorella and E. Tosatti. "Semi-Metal-Insulator Transition of the Hubbard Model in the Honeycomb Lattice." *Eur. Phys. Lett.* **19**, p. 699. 1992 (cit. on pp. 60, 68).

[108] S. Yunoki and S. Sorella. "Two spin liquid phases in the spatially anisotropic triangular Heisenberg model." *Phys. Rev. B* **74**, p. 014408. 2006 (cit. on pp. 60, 68, 91).

[109] G. Z. Magda, X. Jin, I. Hagymási, P. Vancsó, Z. Osváth, P. Nemes-Incze, C. Hwang, L. Biró, and L. Tapasztó. "Room-temperature magnetic order on zigzag edges of narrow graphene nanoribbons." *Nature* **514**, p. 608. 2014 (cit. on p. 60).

[110] A. Mazurenko, C. S. Chiu, G. Ji, M. F. Parsons, M. Kanász-Nagy, R. Schmidt, F. Grusdt, E. Demler, D. Greif, and M. Greiner. "A cold-atom Fermi–Hubbard antiferromagnet." *Nature* **545**, 462 EP –. 2017 (cit. on pp. 66, 77).

[111] B. Tang, T. Paiva, E. Khatami, and M. Rigol. "Short-Range Correlations and Cooling of Ultracold Fermions in the Honeycomb Lattice." *Phys. Rev. Lett.* **109**, p. 205301. 2012 (cit. on p. 66).

[112] B. Tang, T. Paiva, E. Khatami, and M. Rigol. "Finite-temperature properties of strongly correlated fermions in the honeycomb lattice." *Phys. Rev. B* **88**, p. 125127. 2013 (cit. on p. 66).

[113] A. Amaricci, A. Privitera, and M. Capone. "Inhomogeneous BCS-BEC crossover for trapped cold atoms in optical lattices." *Phys. Rev. A* **89**, p. 053604. 2014 (cit. on p. 67).

[114] E. V. Gorelik, I. Titvinidze, W. Hofstetter, M. Snoek, and N. Blümer. "Neel Transition of Lattice Fermions in a Harmonic Trap: A Real-Space Dynamic Mean-Field Study." *Phys. Rev. Lett.* **105**, p. 065301. 2010 (cit. on p. 67).

[115] A. Valli, G. Sangiovanni, O. Gunnarsson, A. Toschi, and K. Held. "Dynamical Vertex Approximation for Nanoscopic Systems." *Phys. Rev. Lett.* **104**, p. 246402. 2010 (cit. on p. 67).

[116] A. Valli, G. Sangiovanni, A. Toschi, and K. Held. "Correlation effects in transport properties of interacting nanostructures." *Phys. Rev. B* **86**, p. 115418. 2012 (cit. on p. 67).

[117] M. Schüler, S. Barthel, T. Wehling, M. Karolak, A. Valli, and G. Sangiovanni. "Realistic theory of electronic correlations in nanoscopic systems." *Eur. Phys. J. Special Topics* **226**, pp. 2615–2640. 2017 (cit. on p. 67).

[118] C. S. Chiu, G. Ji, A. Mazurenko, D. Greif, and M. Greiner. "Quantum State Engineering of a Hubbard System with Ultracold Fermions." *Phys. Rev. Lett.* **120**, p. 243201. 2018 (cit. on p. 67).

[119] M. Greiner, I. Bloch, T. W. Hänsch, and T. Esslinger. "Magnetic transport of trapped cold atoms over a large distance." *Phys. Rev. A* **63**, p. 031401. 2001 (cit. on pp. 76, 77, 142).

[120] O. Mandel, M. Greiner, A. Widera, T. Rom, T. W. Hänsch, and I. Bloch. "Coherent Transport of Neutral Atoms in Spin-Dependent Optical Lattice Potentials." *Phys. Rev. Lett.* **91**, p. 010407. 2003 (cit. on pp. 76, 115, 142).

[121] D. Greif, T. Uehlinger, G. Jotzu, L. Tarruell, and T. Esslinger. "Short-Range Quantum Magnetism of Ultracold Fermions in an Optical Lattice." *Science* **340**, pp. 1307–1310. 2013 (cit. on p. 77).

[122] F. Görg, M. Messer, K. Sandholzer, G. Jotzu, R. Desbuquois, and T. Esslinger. "Enhancement and sign change of magnetic correlations in a driven quantum many-body system." *Nature* **553**, 481 EP –. 2018 (cit. on p. 77).

[123] B. A. Bernevig, T. L. Hughes, and S.-C. Zhang. "Quantum Spin Hall Effect and Topological Phase Transition in HgTe Quantum Wells." *Science* **314**, pp. 1757–1761. 2006 (cit. on pp. 77, 84).

[124] S. Rachel and K. Le Hur. "Topological insulators and Mott physics from the Hubbard interaction." *Phys. Rev. B* **82**, p. 075106. 2010 (cit. on pp. 77, 87).

[125] M. Hohenadler, T. C. Lang, and F. F. Assaad. "Correlation Effects in Quantum Spin-Hall Insulators: A Quantum Monte Carlo Study." *Phys. Rev. Lett.* **106**, p. 100403. 2011 (cit. on pp. 77, 81–83).

[126] M. Hohenadler and F. F. Assaad. "Luttinger liquid physics and spin-flip scattering on helical edges." *Phys. Rev. B* **85**, p. 081106. 2012 (cit. on pp. 77, 78).

[127] J. C. Budich, R. Thomale, G. Li, M. Laubach, and S.-C. Zhang. "Fluctuation-induced topological quantum phase transitions in quantum spin-Hall and anomalous-Hall insulators." *Phys. Rev. B* **86**, p. 201407. 2012 (cit. on p. 77).

[128] M Hohenadler and F. F. Assaad. "Correlation effects in two-dimensional topological insulators." *Journal of Physics: Condensed Matter* **25**, p. 143201. 2013 (cit. on p. 77).

[129] H.-H. Hung, V. Chua, L. Wang, and G. A. Fiete. "Interaction effects on topological phase transitions via numerically exact quantum Monte Carlo calculations." *Phys. Rev. B* **89**, p. 235104. 2014 (cit. on p. 77).

[130] A. Mishra and S. Lee. "Topological multiferroic phases in the extended Kane-Mele-Hubbard model in the Hofstadter regime." *Phys. Rev. B* **98**, p. 235124. 2018 (cit. on p. 77).

[131] A. Amaricci, A. Valli, G. Sangiovanni, B. Trauzettel, and M. Capone. "Coexistence of metallic edge states and antiferromagnetic ordering in correlated topological insulators." *Phys. Rev. B* **98**, p. 045133. 2018 (cit. on pp. 77, 87).

[132] P. Kumar, T. Mertz, and W. Hofstetter. "Interaction-induced topological and magnetic phases in the Hofstadter-Hubbard model." *Phys. Rev. B* **94**, p. 115161. 2016 (cit. on p. 77).

[133] A. Amaricci, L. Privitera, F. Petocchi, M. Capone, G. Sangiovanni, and B. Trauzettel. "Edge state reconstruction from strong correlations in quantum spin Hall insulators." *Phys. Rev. B* **95**, p. 205120. 2017 (cit. on pp. 78, 84, 87).

[134] L. Privitera and G. E. Santoro. "Quantum annealing and nonequilibrium dynamics of Floquet Chern insulators." *Phys. Rev. B* **93**, p. 241406. 2016 (cit. on pp. 78, 84).

[135] S.-L. Yu, X. C. Xie, and J.-X. Li. "Mott Physics and Topological Phase Transition in Correlated Dirac Fermions." *Phys. Rev. Lett.* **107**, p. 010401. 2011 (cit. on p. 81).

[136] J. K. Asbóth, L. Oroszlány, A. Pályi, and J. K. Asbóth. "Berry Phase, Chern Number." *A Short Course on Topological Insulators: Band Structure and Edge States in One and Two Dimensions*. Cham: Springer International Publishing, pp. 23–44. 2016 (cit. on p. 84).

[137] C. Kane and J. Moore. "Topological insulators." *Physics World* **24**, pp. 32–36. 2011 (cit. on p. 84).

[138] Z. Wang and B. Yan. *Topological Hamiltonian as an exact tool for topological invariants*. 2013 (cit. on p. 85).

[139] Z. Wang and S.-C. Zhang. "Simplified Topological Invariants for Interacting Insulators." *Phys. Rev. X* **2**, p. 031008. 2012 (cit. on p. 85).

[140] S. Rachel. "Quantum phase transitions of topological insulators without gap closing." *Journal of Physics: Condensed Matter* **28**, p. 405502. 2016 (cit. on p. 87).

[141] K. Baumann, A. Valli, A. Amaricci, and M. Capone. "Inducing and controlling magnetism in the honeycomb lattice through a harmonic trapping potential." *Phys. Rev. A* **101**, p. 033611. 2020 (cit. on p. 94).

[142] L.-M. Duan, E. Demler, and M. D. Lukin. "Controlling Spin Exchange Interactions of Ultracold Atoms in Optical Lattices." *Phys. Rev. Lett.* **91**, p. 090402. 2003 (cit. on p. 96).

[143] R. C. Brown, R. Wyllie, S. B. Koller, E. A. Goldschmidt, M. Foss-Feig, and J. V. Porto. "Two-dimensional superexchange-mediated magnetization dynamics in an optical lattice." *Science* **348**, pp. 540–544. 2015 (cit. on p. 96).

[144] K. Penc, H. Shiba, F. Mila, and T. Tsukagoshi. "Ferromagnetism in multiband Hubbard models: From weak to strong Coulomb repulsion." *Phys. Rev. B* **54**, pp. 4056–4067. 1996 (cit. on pp. 96, 97).

[145] T. Moriya. "Anisotropic Superexchange Interaction and Weak Ferromagnetism." *Phys. Rev.* **120**, pp. 91–98. 1960 (cit. on p. 98).

[146] F. Keffer. "Moriya Interaction and the Problem of the Spin Arrangements in βMnS." *Phys. Rev.* **126**, pp. 896–900. 1962 (cit. on p. 98).

[147] R. Yu and Q. Si. "Orbital-Selective Mott Phase in Multiorbital Models for Alkaline Iron Selenides $\mathbf{K}_{1-x}Fe_{2-y}Se_2$." *Phys. Rev. Lett.* **110**, p. 146402. 2013 (cit. on p. 103).

[148] M. Yi et al. "Observation of Temperature-Induced Crossover to an Orbital-Selective Mott Phase in $A_xFe_{2-y}Se_2$ (A=K, Rb) Superconductors." *Phys. Rev. Lett.* **110**, p. 067003. 2013 (cit. on p. 103).

[149] M. Ferrero, F. Becca, M. Fabrizio, and M. Capone. "Dynamical behavior across the Mott transition of two bands with different bandwidths." *Phys. Rev. B* **72**, p. 205126. 2005 (cit. on p. 103).

[150] M. Vojta. "Orbital-Selective Mott Transitions: Heavy Fermions and Beyond." *Journal of Low Temperature Physics* **161**, pp. 203–232. 2010 (cit. on p. 103).

[151] L. de'Medici and M. Capone. "The Iron Pnictide Superconductors: An Introduction and Overview, edited by F. Mancini and R. Citro." *Springer International*, pp. 115?185. 2017 (cit. on p. 103).

[152] F. Hardy et al. "Strong correlations, strong coupling, and *s*-wave superconductivity in hole-doped $BaFe_2As_2$ single crystals." *Phys. Rev. B* **94**, p. 205113. 2016 (cit. on pp. 103, 104).

[153] P. O. Sprau, A. Kostin, A. Kreisel, A. E. Böhmer, V. Taufour, P. C. Canfield, S. Mukherjee, P. J. Hirschfeld, B. M. Andersen, and J. C. S. Davis. "Discovery of orbital-selective Cooper pairing in FeSe." *Science* **357**, p. 75. 2017 (cit. on p. 103).

[154] A. Kostin, P. O. Sprau, A. Kreisel, Y. X. Chong, A. E. Böhmer, P. C. Canfield, P. J. Hirschfeld, B. M. Andersen, and J. C. S. Davis. "Imaging orbital-selective quasiparticles in the Hund's metal state of FeSe." *Nature Materials* **17**, pp. 869–874. 2018 (cit. on p. 103).

[155] L. Fanfarillo and E. Bascones. "Electronic correlations in Hund metals." *Phys. Rev. B* **92**, p. 075136. 2015 (cit. on p. 103).

[156] L. Del Re and M. Capone. "Selective insulators and anomalous responses in three-component fermionic gases with broken SU(3) symmetry." *Phys. Rev. A* **98**, p. 063628. 2018 (cit. on pp. 107–110, 112, 116, 117, 122, 125–128, 143).

[157] O. Boada, A. Celi, J. I. Latorre, and M. Lewenstein. "Quantum Simulation of an Extra Dimension." *Phys. Rev. Lett.* **108**, p. 133001. 2012 (cit. on pp. 107, 108).

[158] L. Huang, Z. Meng, P. Wang, P. Peng, S.-L. Zhang, L. Chen, D. Li, Q. Zhou, and J. Zhang. "Experimental realization of two-dimensional synthetic spin–orbit coupling in ultracold Fermi gases." *Nature Physics* **12**, pp. 540–544. 2016 (cit. on pp. 107, 108).

[159] R. Jördens et al. "Quantitative Determination of Temperature in the Approach to Magnetic Order of Ultracold Fermions in an Optical Lattice." *Phys. Rev. Lett.* **104**, p. 180401. 2010 (cit. on p. 118).

[160] F. Werner, O. Parcollet, A. Georges, and S. R. Hassan. "Interaction-Induced Adiabatic Cooling and Antiferromagnetism of Cold Fermions in Optical Lattices." *Phys. Rev. Lett.* **95**, p. 056401. 2005 (cit. on p. 137).

[161] S. Barbarino, L. Taddia, D. Rossini, L. Mazza, and R. Fazio. "Synthetic gauge fields in synthetic dimensions: interactions and chiral edge modes." **18**, p. 035010. 2016 (cit. on p. 143).